FUNDAMENTAL STUDY OF KEY ISSUES RELATED TO ADVANCED sCO_2 BRAYTON CYCLE: PROTOTYPIC HX DEVELOPMENT AND CAVITATION

Report: Final report for NEUP project 14-6670

Technical Point of Contact information:
Devesh Ranjan
Associate Professor
The George W. Woodruff School of Mechanical Engineering
Georgia Institute of Technology, Atlanta
404-384-2922
devesh.ranjan@me.gatech.edu

Table of Contents

Chapter 1 Discontinuous fin style PCHEs for the sCO_2 Brayton cycles

Abstract

Diffusion bonded heat exchangers are the leading candidates for the sCO_2 Brayton cycles in next generation nuclear power plants. Commercially available diffusion bonded heat exchangers utilize set of continuous semi-circular zigzag micro channels to increase the heat transfer area and enhance heat transfer through increased turbulence production. Such heat exchangers can lead to excessive pressure drop as well as flow maldistribution in the case of poorly designed flow distribution headers. The goal of the current project is to fabricate and test potential discontinuous fin patterns for diffusion bonded heat exchangers; which can achieve desired thermal performance at lower pressure drops. Prototypic discontinuous offset rectangular and Airfoil fin surface geometries were chemically etched on to 316 stainless steel plate and sealed against an un-etched flat pate using O-ring seal emulating diffusion bonded heat exchangers. Thermal-hydraulic performance of these prototypic discontinuous fin geometries was experimentally evaluated and compared to the existing data for the continuous zigzag channels. The data generated from this project will serve as the database for future testing and validation of numerical models.

Introduction

The supercritical carbon dioxide (sCO_2) Brayton cycle is an attractive heat-to-power conversion option for the next generation (Gen IV) nuclear power plants. Under Department of Energy (DOE) funding several concepts that involve coupling of liquid metal or molten salt cooled fast reactors to the sCO_2 Brayton cycle rather than the steam Rankine cycle are being developed. Figure 1 shows the schematic and design operating state points for the recompression sCO_2 Brayton cycle coupled to AFR-100 [1].

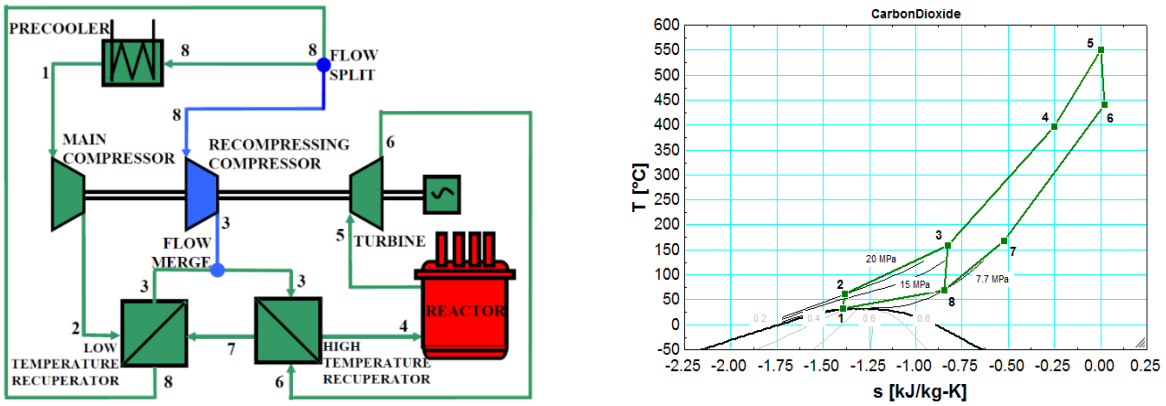

Figure 1: Recompression and recuperated S-CO_2 Brayton cycle layout along with the T-s diagram showing design operating state points [2].

This eliminates the explosive Sodium and Water interactions for the sodium cooled fast reactors (such as AFR-100 being developed at Argonne National Laboratory [1]). In addition, the sCO_2 Brayton cycle also offers higher thermodynamic efficiency within a compact foot print compared to the superheated/supercritical Rankine cycles in the temperature range of interest for the

nuclear power plants [2]. The cycle combines the inherent advantages of the steam Rankine cycles (small back work ratio) and the ideal gas Brayton cycle (single phase fluid) by utilizing CO_2 above its critical pressure and temperature. The specific heat mismatch between high pressure and low pressure sCO_2 streams near the critical point can lead to pinch points inside the recuperator leading to poor heat transfer effectiveness. In order to avoid this issue the internal heat recuperation is accomplished in two stages, which requires that the hot low pressure sCO_2 stream to be split prior to the cooler and compressed (using recompressing compressor) in a parallel fashion and combined with the high pressure sCO_2 stream from the main compressor after the component labelled as the low temperature recuperator in Figure 1. Dostal [2] found out that this configuration leads to the highest efficiency for the temperature range of interest for the nuclear power plants. This configuration requires a significant amount of internal heat recuperation in order to achieve the desired high cycle thermal efficiencies thus requiring numerous, large heat exchangers. Consequently, the total capital cost of the power cycle is dominated by the capital cost of the heat exchangers. An effective way to handle high operating pressures, temperatures as well as to reduce the capital cost is to use compact heat exchangers for the sCO_2 Brayton cycle. Figure 2 presents some of the compact heat exchangers found in literature and discussed extensively by Hesselgreaves [3].

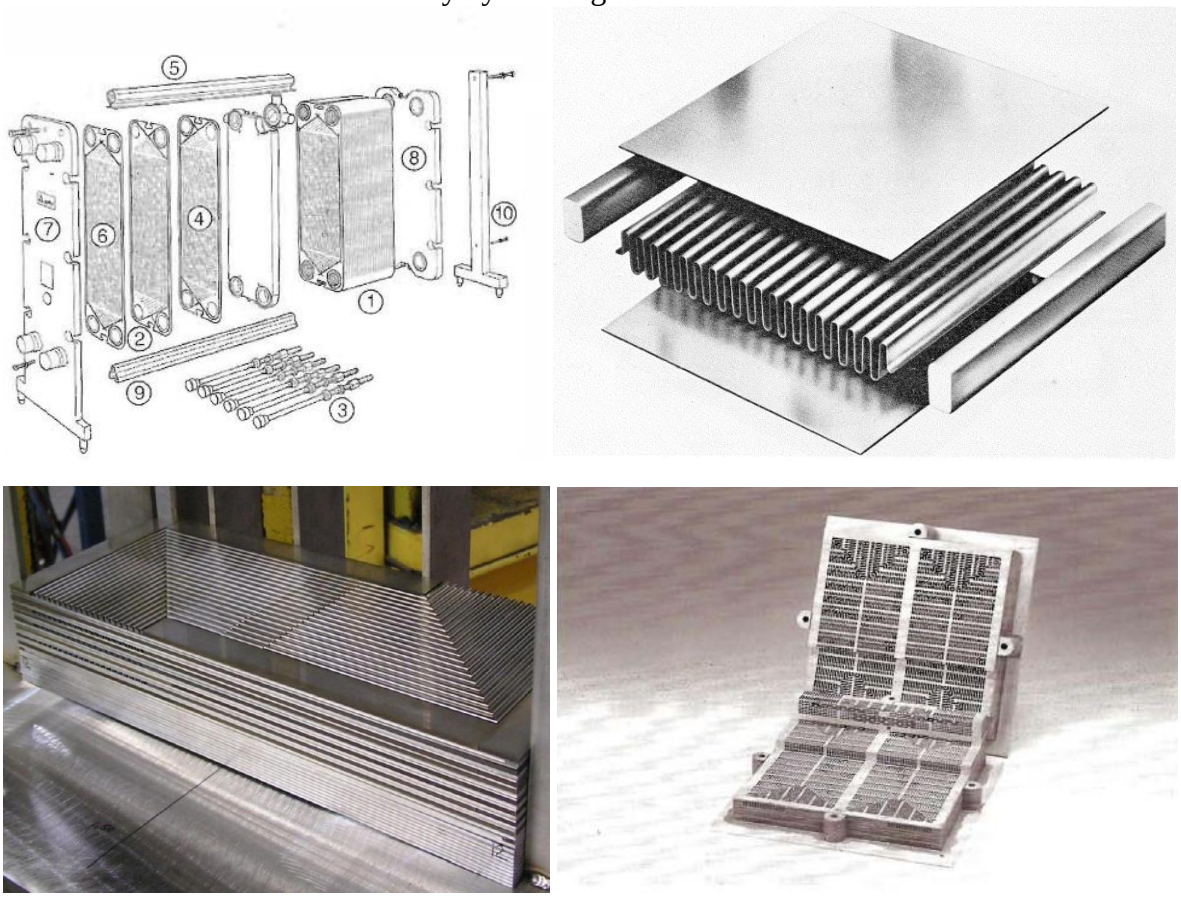

Figure 2: Different types of compact heat exchangers from literature, (a) Plate heat exchanger (PHE) [3], (b) Plate fin heat exchanger (PFHE) [4], (c) Diffusion bonded heat exchanger (such as PCHE) [5], (d) Marbond™ heat exchanger [3]

Compactness of a heat exchanger can be measured/compared using parameters defined by Equations (1) through (3). Equation (1) defines area density which is the ratio of the heat transfer surface area to the volume of heat exchanger. Equation (2) and Equation (3) defines the hydraulic diameter and porosity respectively. The range of these parameters along with the maximum allowable pressure and temperature for the compact heat exchangers presented in Figure 2 are tabulated in Table 1.

$$\beta = \frac{A_s}{V} \tag{1}$$

$$d_h = \frac{4.V_{fluid}}{A_s} \tag{2}$$

$$\Phi = \frac{V_{fluid}}{V} \tag{3}$$

Table 1: Comparison of parameters for various compact heat exchangers from literature [3]

Compact heat exchanger type	Maximum P [MPa]	Maximum T [^{o}C]	β [m^2/m^3]	d_h [mm]
Plate heat exchanger	3.5	250	120 – 660	2 – 10
Brazed plate fin heat exchanger	12	700	800 – 1,500	1 – 2
Diffusion bonded heat exchanger	100	900	200 – 5,000	0.5 – 3
Marbond^{TM} heat exchanger	40	900	< 10,000	0.33 – 1

Plate heat exchanger and brazed fin plate heat exchanger types consist of a series of corrugated plates. These plates are stacked together and alternating plates are either sealed using gasket material or vacuum-brazing depending on whether it is a plate heat exchanger or a brazed fin plate heat exchanger respectively. Different types of corrugation plates, arrangements of the stack into parallel, cross or counter flow for one or more fluid passes are possible. In case of the plate heat exchanger, the plates can be separated and mechanically cleaned whereas the brazed fin plate heat exchanger must be chemically cleaned whenever required. Despite the low cost, high degree of compactness of these compact heat exchangers neither the plate heat exchanger nor the brazed plate fin heat exchangers are suitable for the sCO_2 Brayton cycles due to the maximum pressure and temperature limitations as shown in Table 1. In an effort to reduce the capital cost, footprint, and effectively handle high pressures and temperatures within the cycle use of compact diffusion bonded heat exchangers such as printed circuit heat exchangers, PCHEs marketed by Heatric, U.K. [5] and Marbond^{TM} heat exchanger marketed by Chart industries, U.S.) are proposed. The hydraulic diameters of these diffusion bonded heat exchangers are typically less than 3 mm and can have area density (β) as high as 10,000. A PCHE can be considered as a branch of the plate-fin type heat exchanger family and rely mainly on the two unconventional technologies of photo-chemical etching and diffusion bonding. In the first step, desired flow channels are chemically-etched on to flat metal plates. The etched plates are then stacked and diffusion bonded to form one block of PCHE core as shown in Figure 2(c). Depending on the desired thermal duty multiple PCHE cores can be welded into large assemblies and fitted with nozzles and headers as shown in Figure 3. Sometimes flow distribution headers can also be integrally machined into the plates. The main advantage of PCHEs is that they allow for etching a wide range of surface geometries thus altering the thermal-hydraulic performance of the PCHE core quite easily without adding much to the capital cost. In some cases PCHE and PFHE surfaces can also be combined forming hybrid heat exchangers that can efficiently and compactly transfer heat between two very different fluids such as liquid-to-gas in the case of Na-to-sCO_2 primary heat exchanger (sometimes referred to as an Intermediate heat exchanger) in

sodium cooled fast reactor coupled to the sCO_2 Brayton cycle. Marbond^{TM} heat exchanger is formed by stacking multiple thin plates that are chemically etched through to form slots and then diffusion bonded. The key advantage of Marbond^{TM} heat exchanger is that the flow passages can be almost perpendicular to the plate unlike PCHEs which have inherent three-dimensional rounding and defects due to partial etching as discussed by Black *et al.* [7] and Allen [8]. Both the PCHE and Marbond^{TM} heat exchanger utilize diffusion bonding technology which doesn't utilize foreign material for bonding unlike brazing or welding and the bond strength can be comparable to that of parent material strength. The current project is focused on thermal-hydraulic testing and modeling of the prototypic surface geometries for the printed circuit heat exchangers.

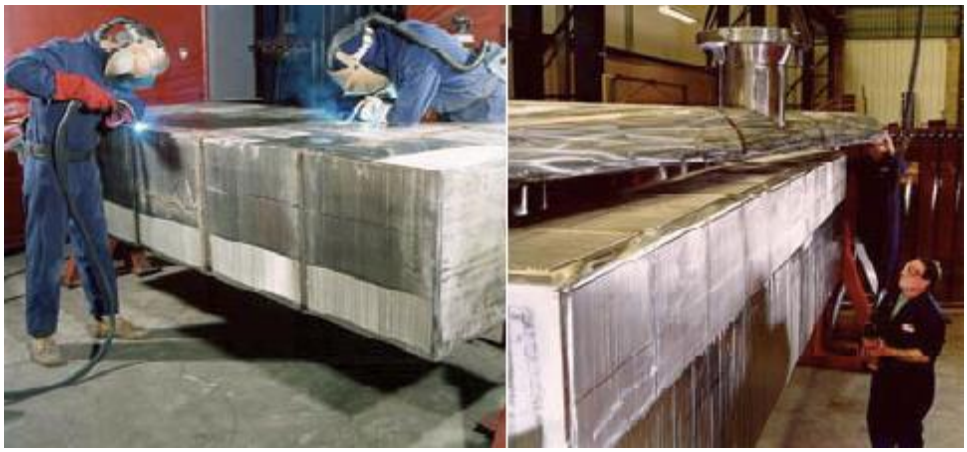

Figure 3: Multiple cores are welded together to meet the desired thermal duty and the flow distribution headers are welded to the assembled cores. Images reproduced from Southall *et al.* [6]

Prior work on PCHEs

Although PCHEs have been around for a while mainly in the oil & gas industry, their use in the nuclear industry gained popularity about a decade ago. Since then decent number of experimental and computational studies have been published in literature to understand the thermal–hydraulic performance of different PCHE surface geometries using mainly Carbon dioxide, air, water or Helium as the working fluid. Based on the literature review, the surface geometries of PCHEs can be categorized as either continuous or discontinuous-fin surfaces. Continuous fin surfaces include straight, sinusoidal, and zig-zag channels, while discontinuous surfaces include louver, S-shaped, and airfoil fin geometries. Most of the studies in the literature are focused on either experimental or numerical investigations into either continuous zig-zag style or straight channels which are commercially available through Heatric. What follows is a compilation of testing and modeling efforts undertaken by different research groups from the literature.

PCHE testing and modeling work at Tokyo Institute of Technology

Some of the earliest work on PCHEs was performed at Tokyo Institute of Technology (TIT), who tested a 3 kW_{th} 316L stainless steel zig-zag channel style PCHE from Heatric for CO_2-to-CO_2 service. Table 2 summarizes the PCHE geometrical parameters and range of operating conditions tested at TIT [9, 10] and Figure 4 provides the description of geometrical parameters for continuous zig-zag channels. The PCHE employed in this work had plates stacked in a double-banking configuration with two hot plates followed by a cold plate and so on (As a result of this

configuration, the number of cold plates is half of number of hot plate, as can be seen in Table 2).

Table 2: 3 kW double-banked 316L stainless steel PCHE parameters tested at TIT [9, 10]

	Hot side (CO_2)	Cold side (CO_2)
Core dimensions (mm^3)	71 x 76 x 896	
Dry mass (kg)	40	
Number of channels	144	66
Number of plates	12	6
Number of channels per plate	12	11
Plate thickness (mm)	1.63	1.63
Channel diameter, w_f (mm)	1.9	1.8
Channel spacing, g_f (mm)	0.6	0.7
Channel angle, θ_b (^{o})	32.5	40
Channel active length (mm)	1000	1100
Fin pitch, p_f^y (mm)	2.964	3.263
Fin pitch, p_f^x (mm)	9	7.24
Heat transfer area, A_s (m^2)	0.697	0.356
Free flow area, A_c (m^2)	0.0002	0.000092
Inlet Pressure range (MPa)	2.2 – 3.2	6.5 – 10.5
Inlet Temperature range (^{o}C)	280 – 300	90 – 108
Flow rate range (kg/h)	40 – 80	

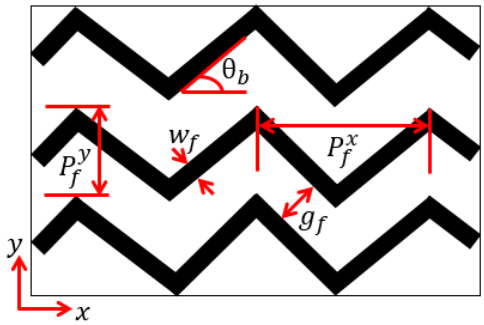

Figure 4: Relevant geometrical parameters for the continuous zig-zag channels

The empirical correlations were proposed for the effective friction factor and the local heat transfer coefficients as shown in Equations (4)-(5). The effective friction factor correlations were developed from the empirical curve fitting to the experimental data. However, the local heat transfer coefficient correlations were reconstructed using Fluent™ and comparing the calculated overall heat transfer coefficients to the experimentally measured overall heat transfer coefficients. An empirical correlation for the overall heat transfer coefficient based on the experimental data was also developed as shown in Equation (6). It should be noted that these empirical correlations don't show any dependence of the Prandtl number because the operating conditions for both the hot and cold fluids are far away from the critical point and hence, the Prandtl number doesn't vary significantly.

$$f_{hot} = (-5.608 \pm 0.348).10^{-6}Re + (0.1798 \pm 0.00152) \quad (4)$$
$$h_{hot} = 2.52Re^{0.681}$$

Where, 2,800 ≤ Re ≤ 5,800

$$f_{cold} = (-6.18 \pm 0.396).10^{-6}Re + (0.37272 \pm 0.0036) \quad (5)$$
$$h_{cold} = 5.49Re^{0.625}$$

Where, 6,200 ≤ Re ≤ 12,100

$$U_{exp} = (18.6 \pm 6.8) + (0.105 \pm 0.002)Re \quad (6)$$

Where, 2,000 ≤ Re ≤ 6,000

Nikitin *et al.* [10] also proposed an alternative way to predict the pressure drop through the zig-zag channels by breaking down the total pressure drop into a combination of frictional losses and form losses as shown in Equation (7).

$$\Delta P = \Delta P_{form} + \Delta P_{friction} \quad (7)$$

$$\Delta P = \sum_m \rho_m K_b \frac{U_b^2}{2} + \sum_m \rho_m f_b \left(\frac{L}{d}\right) \frac{U_b^2}{2}$$

Where,

$$K_b = 0.946 \sin^2\left(\frac{\theta_b}{2}\right) + 2.047 \sin^4\left(\frac{\theta_b}{2}\right)$$

$$f_b = 0.316Re^{-0.25}$$

The PCHE tested at TIT exhibited effectiveness up to 98.7%, maximum power density of 4.4 MW_{th}/m^3 with an area density ratio (β) of 1050 m^2/m^3.

CFD studies conducted by Tsuzuki *et al.* [11] showed that the zig-zag channel enhance the PCHE power density compared to straight channel but at the same time suffers from increased pressure drop due to swirl flows, eddies, and recirculation flows that occur around a zig-zag corner bend. Alternatively, they designed a new surface geometry configuration with discontinuous S-shaped fins, similar to that of sine curve. Figure 5 provides the description of geometrical parameters for discontinuous S-shaped fins.

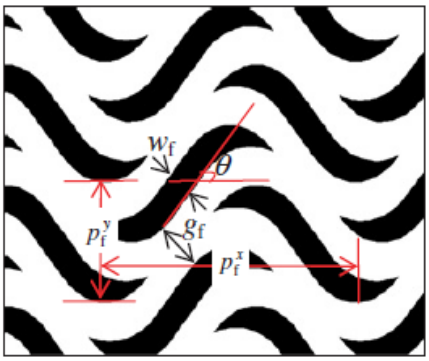

Figure 5: Relevant geometrical parameters for the discontinuous S-shaped fins [11]

For a fin angle (θ_b) of 52°, no local reverse flow or eddies were observed in their CFD studies and the flow distribution along the S-shaped fin is much more uniform compared to that of an equivalent zig-zag channel. Kato [12] compared the thermal-hydraulic performance of different PCHE surface geometries as shown in Figure 6. It can be seen that the S-shaped fin geometry attains about six times lower pressure drop relative to the continuous zig-zag channel while maintaining almost similar heat transfer performance; the continuous sine-curve channel provides almost same low pressure drop as S-shaped fin but at an expense of 20% lower heat transfer performance; the louvered fin results in three times higher pressure drop and 10% lower heat transfer performance compared to the S-shaped fin.

Based on the CFD results of Tsuzuki *et al.* [11], Ngo *et al.* [13] fabricated a new PCHE with S-shaped fins and tested it for CO_2-to-water service, intended for domestic water heating applications. They concluded that the new PCHE with S-shaped fins offered about 3.3 times lower volume and about 37% lower pressure drop compared to the existing domestic hot water suppliers.

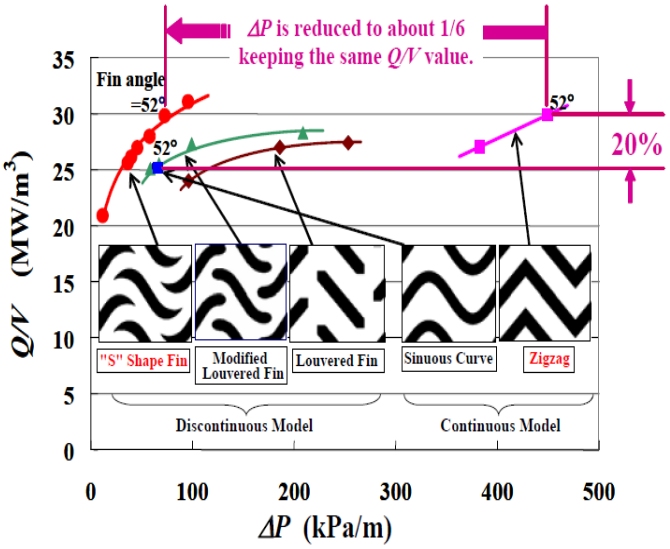

Figure 6: Heat transfer and pressure drop performance of different PCHE surface geometries, reproduced from Kato [12]

Nikitin *et al.* [14] extended the idea of using S-shaped fins for the PCHE style recuperators in gas turbine applications. They experimentally evaluated the thermal-hydraulic performance of PCHE with S-shaped fins and a conventional PCHE with zig-zag channels in the TIT test facility. Table 3 summarizes the geometrical parameters of the two PCHEs along with the range of operating parameters. These tests were conducted for conditions far away from the critical point where the variation of Prandtl number is insignificant. They concluded that the pressure drop of PCHE with S-shaped fins is 4-5 times lower than that of PCHE with zig-zag channels but at the same time Nusselt number is 24-34% lower depending on the Reynolds number. Ngo *et al.* [15] extended the range of operating parameters for both the PCHEs tested by Nikitin *et al.* [14] to study the influence of Prandtl number variation on their thermal-hydraulic performance. They used integral form of log-mean temperature difference (LMTD) to calculate the overall heat transfer coefficients since the operating conditions are closer to the critical point where specific heat varies drastically with the temperature. They proposed Nusselt number and friction factor

empirical correlations for S-shaped fin and zig-zag channel PCHEs as shown in Equations (8)-(9).

S-shaped fin PCHE:

$$Nu = (0.1740 \pm 0.0118)Re^{0.593\pm0.007}Pr^{0.430\pm0.014}, \quad f = (1.818 \pm 0.162)Re^{-0.340\pm0.009} \tag{8}$$

Zig-zag fin PCHE:

$$Nu = (0.1696 \pm 0.0144)Re^{-0.629\pm0.009}Pr^{0.317\pm0.014}, \quad f = (0.7696 \pm 0.1196)Re^{-0.091\pm0.016} \tag{9}$$

Where, 3,500≤*Re* ≤23,000; 0.75≤*Pr*≤2.2

Table 3: Specifications of S-shaped fin and zig-zag channel PCHEs tested in TIT test facility [14, 15]

	Side	S-shaped fins	Zig-zag channels
Core dimensions (mm^3)	-	29 x 76 x 745.2	
Number of channels	Hot/cold	96/44	
Number of plates	Hot/cold	8/4	
Number of channels per plate	Hot/cold	12/11	
Plate thickness (mm)	Hot/cold	1.5/1.5	
Fin width, w_f (mm)	Hot/cold	0.8/0.8	
Fin depth, d_f (mm)	Hot/cold	0.94/0.94	
Fin spacing, g_f (mm)	Hot/cold	1.31/1.31	
Fin pitch, p_f^y (mm)	Hot/cold	3.426/3.426	
Fin pitch, p_f^x (mm)	Hot/cold	7.565/7.565	
Fin angle, θ_b (^{o})	Hot/cold	52/52	
Heat transfer area, A_s (m^2)	Hot/cold	0.5099/0.2559	0.4653/0.2353
Free flow area, A_c (m^2)	Hot/cold	11.82×10^{-5}/5.42×10^{-5}	
Hydraulic diameter, D_h (mm)	Hot/cold	1.09/1.09	
Inlet Pressure range (MPa)	Hot/cold	2.2 – 3.5 /6.5 – 10.5, 6/7.7 – 12	
Inlet Temperature range (^{o}C)	Hot/cold	280/108, 120/35 – 55	
Flow rate range (kg/h)	Hot	30 – 150	

PCHE testing and modeling work at Argonne National Laboratory

Moisseytsev *et al.* [16] tested a 17.5 kW_{th} 316L stainless steel Heatric PCHE for conditions relevant to the low temperature recuperator of the sCO_2 Brayton cycle in Figure 1. Table 4 presents the relevant geometrical parameters and range of testing conditions for PCHE tested at Argonne National Laboratory (ANL) [16]. It should be noted that the parameters provided in the table below are back calculated by ANL based on the information provided to them by Heatric.

Table 4: Specifications of Heatric PCHE tested at Argonne National Laboratory [16]

	Side	Zig-zag Channels
Core dimensions (mm^3)	-	120 x 200 x 1200
Core dry mass (kg)	-	200
Fin width, w_f (mm)	Hot/cold	1.5/1.5
Fin depth, d_f (mm)	Hot/cold	0.75/0.75

Fin angle, θ_b (^{o})	Hot/cold	38/45
Hydraulic diameter, D_h (mm)	Hot/cold	0.9165/0.9165
Inlet Pressure range (MPa)	Hot/cold	7.9 – 8.5 /11.3 – 20
Inlet Temperature range (^{o}C)	Hot/cold	154-161/40.7-48.8
Flow rate range (kg/h)	Hot/cold	306-331/195-233

Southall *et al.* [17] published sample friction factor and colburn j-factor for various etched surface geometries which also included data for straight and three different zig-zag channels (referred to as "plain", "high zig-zag", "medium zig-zag", "low zig-zag" in the original paper without any description of the channel bend angles (θ_b) nor the scales along the y-axis of plots). Moisseytsev *et al.* [16] guessed these values based on well-known straight channel correlations and the data obtained at ANL. They proposed friction factor and j-factor correlations as shown below in Equations (10)-(11) and the corresponding fit curve to the Heatric data [18] is presented in Figure 7.

The friction factor for straight channels (referred to as "plain") is calculated as shown in Equation (10),

$$f_0 = \begin{cases} \frac{16}{Re}, & Re < 1700 \\ \frac{0.0791}{Re^{0.25}}, & Re > 2300 \end{cases} \tag{10}$$

With a linear function for the transition region ($1700 < Re < 2300$).

The zig-zag channel friction-factor enhancement is calculated using the form of Equation (11),

$$\frac{f}{f_0} = \begin{cases} 1 + a_f(Re + 50), & Re < 1300 \\ kRe^c, & Re \geq 1300 \end{cases} \tag{11}$$

Where,

$$c = \frac{\ln\frac{1+223283.a_f^2}{1+a_f.1800}}{\ln\left(\frac{1000}{13}\right)}$$

$$k = \frac{1+a_f.1800}{1300^c}$$

$$a_f = 4.5 \cdot 10^{-3} \tan\theta_b$$

With the a_f values determined to be $1.04 \cdot 10^{-3}$, $2.74 \cdot 10^{-3}$ and $5.76 \cdot 10^{-3}$ for the "high zigzag", "medium zigzag" and "low zigzag" channels respectively. These values result in back calculated channel bend angles (θ_b) as 52^o, 31.33^o, and 13^o for the "high zigzag", "medium zigzag" and "low zigzag" channels respectively.

The j-factor correlations were developed separately for the laminar and turbulent regions as presented in Equation (12).

$$j = \begin{cases} \frac{4.1}{Re}(1 + a_{j,lam}(Re + 50)), & Re < 2300 \\ a_{j,turb}(0.1341)Re^{-0.3319}, & Re \geq 2300 \end{cases} \quad (12)$$

Where the coefficients are defined as follows,

$$a_{j,turb=0.6+0.5\tan\theta_b}$$

$$a_{j,lam=\frac{3.9361.a_{j,turb}-1}{1800}}$$

It was found that the following fit provides better heat transfer prediction for the straight channel in the transition region. As such, no special treatment is necessary for the zig-zag channels.

$$j_{0,trans} = 352Re^{-1.4562}$$

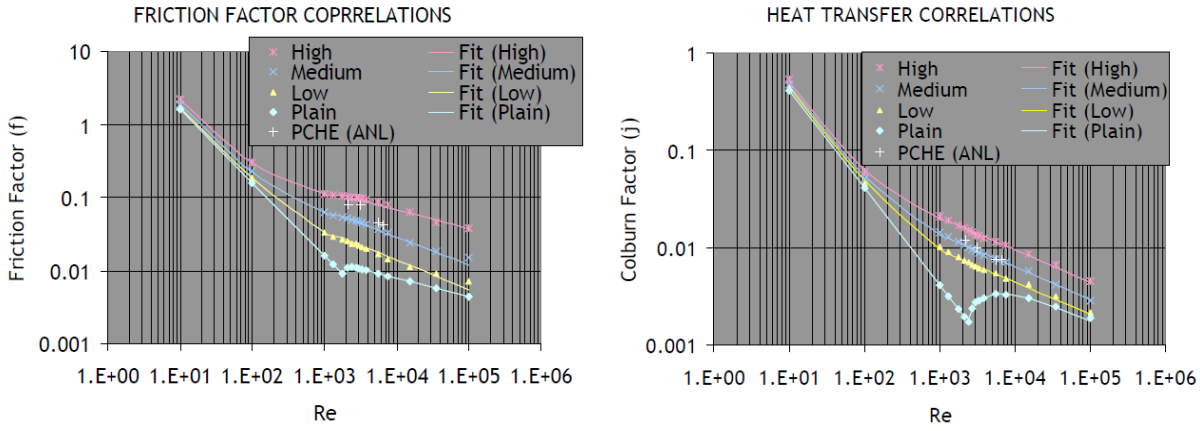

Figure 7: Heat transfer and friction factor correlations proposed by Moisseytsev *et al.* [16] fit curve to the Heatric data for straight and zig-zag channels [17].

PCHE testing and modeling work at Korea Advanced Institute of Science and Technology

I. H. Kim *et al.* [18], [19], [20] tested an Alloy 800H Heatric PCHE for the conditions relevant to the High temperature gas reactors (HGTR). Table 5 presents the geometrical parameters of the PCHE tested at the Korea Advanced Institute of Science and Technology (KAIST) helium test loop.

Table 5: Alloy 800H PCHE parameters tested at KAIST [18]

	Hot side (He or He-CO_2 mixture)/Cold side (He or water)
Core dimensions (mm^3)	150 x 144 x 896
Dry mass (kg)	146
Number of channels	1280/1280

Number of plates	32/32
Number of channels per plate	40/40
Channel diameter, w_f (mm)	1.51/1.51
Channel angle, θ_b (^{o})	15/15
Fin pitch, p_f^x (mm)	24.6/24.6
Hydraulic diameter, D_h (mm)	0.922/0.922
Heat transfer area, A_s (m^2)	3.8/3.8
Free flow area, A_c (m^2)	0.001155/0.001155

They conducted a series of tests for He-to-He, He-to-water, and He+CO_2 mixture-to-water service and proposed global and local averaged friction factor and Nusselt number correlations. In order to obtain local information an experimentally validated Fluent^{TM} CFD model was utilized. Empirical correlations in the form of Equation (13)-(14) were proposed for global averaged friction factor, global and local-pitched averaged Nusselt numbers for the He-to-He tests [18]. The Helium Prandtl number doesn't vary with temperature and pressure for the conditions tested, hence, these correlations show only dependence on the *Re*.

$$f_{ave}.Re_{ave} = 16.51 + 0.01627.Re_{ave} \quad (13)$$

Where, 350 < Re_{ave} < 1200

$$Nu_{ave} = 3.255 + 0.00729.(Re_{ave} - 350) \quad (14)$$

$$Nu_p = 4.065 + 0.00305.Re_p$$

Where, 350 < Re_{ave}, Re_p < 800, Pr_{ave}~0.66

It should be noted that these proposed empirical correlations have physical significance, which can be inferred by comparing Equation (13) and (14) to the following forms.

$$f.Re = b + a.Re$$

$$Nu = d + c.Re$$

The product of $f.Re$ and *Nu* in the case of fully developed laminar flow is independent of *Re* and depends only on the shape of the flow channel cross-section. These numbers are tabulated in Table 6 for semi-circular and circular channels and can be analytically derived for constant temperature and heat flux boundary conditions [18]. The contribution of *Re* in Equations (13) and (14) can be understood as the enhancement in Nusselt number and pressure drop offered by the zig-zag channel.

Table 6: Fully developed friction factor and Nusselt number for laminar flow in straight channel [18]

Channel cross-section	$f.Re$	Nu for constant temperature boundary condition	Nu for constant heat flux boundary condition
Circular	16	3.657	4.364
Semi-circular	15.767	3.323	4.089

I. H. Kim *et al.* [19] pointed out that the constant *b* from their experimental data is equal to 16.51 which is slightly higher than 15.767 from Table 6 as the flow through the PCHE is not fully developed during the testing.

Empirical correlations in the form of Equation (15)-(16) were proposed for local pitch averaged friction factor and Nusselt numbers including the data of He-to-He and He-to-water tests [19]. I. H. Kim *et al.* [19] noted that introduction of correction factor ($C.F$) and the effect of Prandtl number was required in the case of He-to-water tests where the Prandtl number varied significantly and the bulk temperature is much different from the wall surface temperature.

$$f_p.Re_p = 15.78 + 0.004868.Re_p^{0.8416} - C.F \quad (15)$$

$$C.F = 10.939 - 11.014\frac{\nu_s}{\nu_b}$$

$$Nu_p = 4.089 + 0.00365.Re_p.Pr_p^{0.58} \quad (16)$$

Where, $0 < Re_p < 2500$ and $0.66 < Pr_p < 13.41$

Finally, empirical correlations of form Equation (17)-(18) were proposed for local pitch averaged friction factor and Nusselt numbers including the data of He-to-He, He-to-water as well as He and CO_2 mixture-to-water tests [20].

$$f_p.Re_p = 15.78 + 0.00557.Re_p^{0.82} \quad (17)$$

$$Nu_p = 4.089 + 0.00497.Re_p^{0.95}.Pr_p^{0.55} \quad (18)$$

Where, $0 < Re_p < 3500$ and $0.66 < Pr_p < 13.41$

PCHE testing and modeling work at Ohio state university (OSU)

Mylavarapu *et al.* [21] tested two Alloy 617 custom fabricated PCHEs with semi-circular straight channels for conditions relevant to Very high temperature gas reactors (VHTR). Table 7 presents the geometrical parameters of the PCHE tested at the OSU high temperature test facility.

Table 7: Alloy 617 PCHEs parameters tested at OSU [21]

	Hot side (He)/Cold side (He)
Number of channels	120/120
Number of plates	10/10
Number of channels per plate	12/12
Plate thickness (mm)	1.63/1.63
Channel diameter, w_f (mm)	2.0/2.0
Channel gap, g_f (mm)	0.5/0.5
Channel angle, θ_b (^{o})	0/0 (Straight channels)
Hydraulic diameter, D_h (mm)	1.22/1.22
Heat transfer area, A_s (m^2)	0.188/0.168
Free flow area, A_c (mm^2)	188/188

They compared the experimentally determined friction factor and Nusselt numbers to the fully developed, constant-property smooth circular pipe correlations for turbulent and laminar-to-turbulent transition flow regimes. The turbulent flow correlations are listed below in the form of Equations (19)-(21). The laminar flow experimental data are compared with the constant-property fully developed laminar flow correlation for a semicircular duct from Table 6.

$$f = 0.25\left(\frac{1}{1.8logRe-1.5}\right)^2 \quad (19)$$

$$Nu = \frac{\frac{f}{2}(Re-1000)Pr}{1+12.7\left(Pr^{\frac{2}{3}}-1\right)\sqrt{\frac{f}{2}}} \quad (20)$$

Where, 3100<Re<5.10^6 and 0.5<Pr<2000

$$Nu = 3.5239\left(\frac{Re}{1000}\right)^4 - 45.148\left(\frac{Re}{1000}\right)^3 + 212.13\left(\frac{Re}{1000}\right)^2 - 427\left(\frac{Re}{1000}\right) + 316.08 \quad (21)$$

For, 2300<Re<3100 and 0.5<Pr<2000

Mylavarapu *et al.* [21] data suggested that in the case of semi-circular channel, the laminar-to-turbulent flow transition occurred at *Re* of approximately 1700; earlier than *Re* of 2300 for circular channel. This expedited transition is attributed to the rough inlet at the entrance to the PCHE. The data also indicated that the product of $f.Re$ and *Nu* are fairly constant in the laminar region as discussed by Kim *et al.* [18] as well. At higher *Re* (>3000), both the semi-circular channel friction factor and *Nu* data agreed quite well with the correlations of circular pipe by employing equivalent hydraulic diameter concept.

PCHE testing and modeling work at the University of Wisconsin – Madison (UW-Madison)

Kruizenga *et al.* [22] conducted detailed experiments to provide insight into fluid flow and heat transfer characteristics of flow through straight semi-circular and zig-zag flow channels. The geometrical parameters of the PCHEs are provided in Table 8. The experiments spanned several inlet pressures and temperatures dropping through the pseudo-critical temperature for several combinations of heat flux, and orientations including horizontal flow heating and cooling mode, up-flow cooling, and down-flow cooling modes. Local heat removal rates and wall temperature measurements along the channel length were made unlike the previous studies. The local information allowed for more accurate measurement of Nusselt numbers near the pseudo-critical point.

Kruizenga found that the Jackson's correlation shown in Equation (22) worked well for predicting data for semi-circular channel for conditions far away from the pseudo-critical temperature. Near the pseudo-critical temperature (especially for system pressures closer to the critical point), Jackson's correlation consistently over-predicted the *Nu*. In order to improve the prediction near the pseudo-critical region, modified Jackson's correlation shown in Equation (23) was recommended.

$$\mathrm{Nu}_{\mathrm{Jackson}} = 0.0183\mathrm{Re}_b^{0.82}\mathrm{Pr}_b^{0.5}\left(\frac{\rho_w}{\rho_b}\right)^{0.3}\left(\frac{C_{pav}}{C_{pb}}\right)^n \quad (22)$$

Where the subscript n is proposed as,

$$n = 0.4, \text{ for } T_b < T_w < T_{pc} \text{ and } 1.2T_{pc} < T_b < T_w$$

$$n = 0.4 + 0.2\left(\frac{T_w}{T_{pc}} - 1\right), \text{ for } T_b < T_w < T_{pc}$$

$$n = 0.4 + 0.2\left(\frac{T_w}{T_{pc}} - 1\right)\left(1 - 5\left(\frac{T_b}{T_{pc}} - 1\right)\right), \text{ for } T_{pc} < T_b < 1.2T_{pc}$$

$$Nu = Nu_{Jackson}\left(\frac{C_{pb}}{C_{p,IG@T_{pc}}}\right)^{-0.19} \quad (23)$$

Where, $C_{p,IG@T_{pc}}$ is the specific heat is evaluated assuming that fluid behaves as an ideal gas at T_{pc} for a given experimental pressure. The frictional pressure drop data is predicted well by the Colebrook & White friction factor correlation from Equation (24) using measured surface roughness (ε) value of 7.4 μm.

$$\frac{1}{\sqrt{f}} = -2\log_{10}\left(\frac{\varepsilon}{3.7} + \frac{2.51}{Re\sqrt{f}}\right) \quad (24)$$

Kruizenga also found out that the friction factor and *Nu* for zig-zag channels tested ("Hot zig-zag", "Cold zig-zag" from Table 8) are consistently higher than that of straight channels. Based on the least squares fit, Kruizenga suggested empirical correlations of the following form for predicting *Nu*,

$$Nu_{zig-zag} = C_{PCHE}Nu_{Jackson} \quad (25)$$

Where, C_{PCHE} is found out to be 2.8 and 3.8 for the hot and cold zig-zag channels respectively. He also suggested that as an initial estimate for pressure drop, Colebrook & White friction factor correlation could be used in conjunction with effective channel length multiplied by a factor of 4.3 and 5.4 for the hot and cold zig-zag channels respectively.

Carlson [23] continued the work of Kruizenga and compared the thermal-hydraulic performance of different prototypic PCHE test plates, which included the straight and zig-zag channels tested by Kruizenga as well as more prototypic discontinuous NACA0020 airfoil fin geometries. Carlson also showed the importance of measuring the surface geometries after chemical etching and prior to diffusion bonding. It is typically assumed in the literature that the channel profile is nearly semi-circular after etching and diffusion bonding as well as the channel bends are sharp in the case of zig-zag channel. However, due to inherent etching defects it is nearly impossible to have a desired surface geometry as realized by Carlson. Table 8 shows the difference between the designed and measured surface geometrical parameters for the hot and cold zig-zag channels tested at UW-Madison [22, 23]. Figure 9 shows the definition of the geometrical parameters from Table 8. Carlson pointed out that not accounting for these etching imperfections can lead up to >30% error in measurements.

Table 8: Straight and zig-zag channel PCHEs tested at UW-Madison [22, 23]

	Straight (Design)	65ZZ (Hot zig-zag)		80ZZ (Cold zig-zag)	
		Design	Measured	Design	Measured
Number of channels	9	9		9	
Number of plates	1	1		1	
Number of channels per plate	9	9		9	
Length of channels (mm)	500	500		500	
Plate thickness (mm)	6.3	6.3		6.3	

Profile radius, r_s (mm)	0.95	0.95	1.174	0.95	1.334
Channel pitch, p (mm)	2.515	2.972	2.972	3.277	3.277
Channel depth, h (mm)	0.95	0.95	0.864	0.95	0.882
Channel angle, θ_b (^{o})	0	32.5	32.2	40	39.645
Bend-to-Bend length, L_{bb} (mm)	-	5.334	5.322	4.724	4.704
Inner radius, r_i (mm)	-	0	0.796	0	0.583
Outer radius, r_o (mm)	-	0	1.062	0	0.876
Path radius, r_s (mm)	-	0	1.007	0	0.815
Hydraulic diameter, D_h (mm)	1.16	1.135	1.071	1.116	1.096
Free flow area, A_c (mm^2)	1.42	1.42	1.446	1.42	1.62
Relative roughness, ε/D_h	-	7.313e-3		7.227e-3	

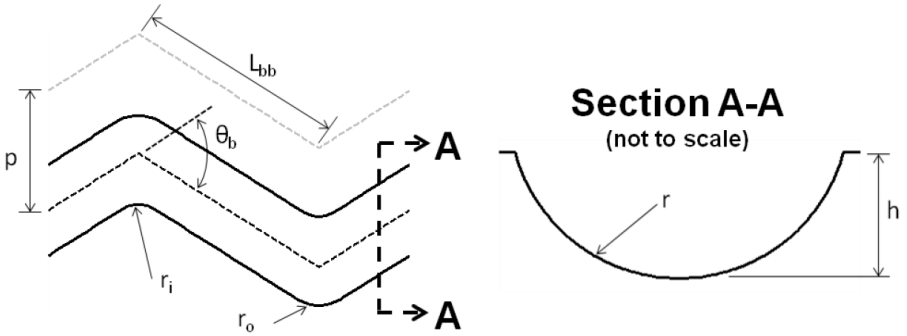

Figure 9: A diagram of an arbitrary rounded zig-zag PCHE channel unit cell [23].

Table 9 presents the design and measured geometrical parameters of the NACA0020 airfoil fin geometries tested by Carlson [23] and Figure 10 shows the definition of these parameters. The idea of utilizing NACA0020 airfoil fin surface geometries for PCHEs seem to be motivated by the CFD study conducted by D. E. Kim *et al.* [24]. Kim *et al.* [24] study showed that the airfoil fin yielded the same heat transfer performance as the zig-zag channel but at significantly lower pressure drop (~1/20) due to the suppression of separated flows. Although not as dramatic as shown by the CFD study, Carlson [23] experiments indeed indicated that the airfoil fin geometries offer significantly lower pressure (almost equal to that of roughened circular tubes with equivalent hydraulic diameter). However, most of these experiments were conducted near the pseudo-critical point (T_b/T_{pc} < 1.2), where the heat transfer is significantly influenced by the thermo-physical property variations rather than the geometrical parameters. This warrants additional experimental/computational investigation into the discontinuous airfoil fin geometries for the diffusion bonded heat exchangers.

Table 9: NACA0020 PCHEs tested at UW-Madison [23]

	4mmNACA0020		8.1mmNACA0020	
	Design	Measured	Design	Measured
Chord width, *c* (mm)	4	3.566	8.1	7.801
Thickness/Chord length	0.2	0.202	0.2	0.205
Fillet radius, *r* (mm)	0	0.795	0	1.091
Channel depth, *h* (mm)	0.95	0.685	0.95	0.774
Axial pitch, *s* (mm)	3.5	3.466	6.9	6.933

Lateral pitch, p (mm)	3.6	3.657	7.3	7.296
Plate thickness, t (mm)	6.3		6.3	
Number of Rows	144		72	
Airfoils per Row	6		3	
Hydraulic diameter, D_h (mm)	1.205	1.112	1.447	1.337
Unit cell heat transfer area, A_s (mm^2)	30.18	24.94	101.8	90.89
Cross-sectional area, A_c (mm^2)	15.96	12.07	16.19	13.23
Measured Relative roughness	7.259e-3		6.285e-3	

Seo *et al.* [25] tested two straight channel 304L stainless steel PCHEs with different number of hot and cold plates for water-to-water service. Table 10 shows the geometrical parameters of the two PCHEs fabricated and tested by Seo *et al.* [25]. They found out that overall heat transfer coefficient is almost similar for both PCHEs and UA scaled according to the total surface heat transfer area. Based on the experimental overall heat transfer coefficient, empirical correlation for the Nusselt number and Colburn j-factor as given in Equations (26)-(27) were proposed using modified Wilson method. Proposed empirical correlation for the friction factor is given in Equation (28).

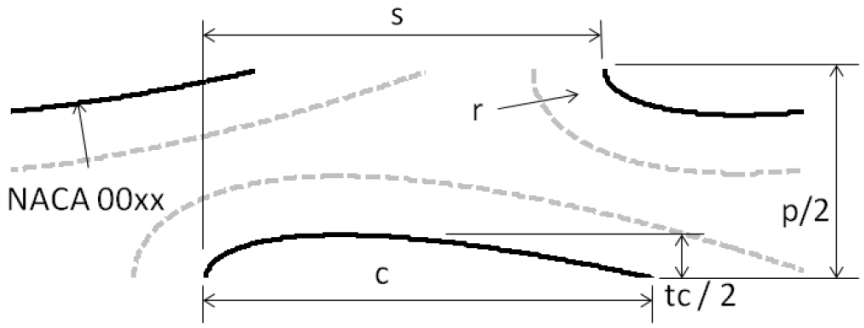

Figure 10: A diagram of an arbitrary rounded symmetrical NACA pillar array PCHE channel unit cell [23]. The dashed grey line represents the outer bottom edge of a depth-wise fillet of radius r which is constructed on the inside bottom edge of the main airfoil profile shown in black.

Table 10: 304L stainless steel PCHEs parameters tested by Seo *et al.* [25]

	Hot side (water)/Cold side (water)	
	PCHE1	PCHE2
Number of channels	66/88	110/132
Number of plates	3/4	5/6
Number of channels per plate	22/22	22/22
Plate thickness (mm)	1.0/1.0	1.0/1.0
Channel width, w_f (mm)	0.8/0.8	0.8/0.8
Channel depth, h (mm)	0.6/0.6	0.6/0.6
Channel gap, g_f (mm)	0.6/0.6	0.6/0.6
Channel angle, θ_b (^{o})	0/0	0/0
Length of flow stream (mm)	137/137	137/137
Hydraulic diameter, D_h (mm)	0.6685/0.6685	0.6685/0.6685
Heat transfer area, A_s (mm^2)	26,037/34,716	43,395/52,074
Free flow area, A_c (mm^2)	31.7/42.2	52.8/63.4

$$Nu = 0.7203Re^{0.1775}Pr^{\frac{1}{3}}\left(\frac{\mu_b}{\mu_w}\right)^{0.14} \quad (26)$$

$$j = 0.706Re^{-0.8208} \quad (27)$$

$$f = 1.3383Re^{-0.5003} \quad (28)$$

Where, 400<Re<3000

Prior work on plate fin Heat exchangers, specifically Offset strip fin patterns

Plate fin heat exchangers have been used in the compact heat exchanger industry (much longer than the PCHEs) and are currently used in a wide range of applications to meet the demand for saving energy and resources. Typically among these are the automobile radiators, air-conditioning, evaporators and condensers, air coolers, and cryogenic exchangers. To reduce weight and size of plate fin heat exchangers, various heat transfer augmentation fin surfaces have been developed to improve the air side heat transfer. Typical fin surfaces used for plate fin heat exchangers are plain fins, wavy fins, offset strip fins, perforated fins, pin fins, and louvered fins. For these surfaces predictive generalized correlations are available [26] along with the monograph database from Kays & London [27], who can be considered as the pioneers of the offset strip fin researches.

Of the many enhanced fin geometries described here, the most common and widely investigated surfaces are the offset strip fins. The Offset strip fins have a high degree of surface compactness and offer substantial heat transfer enhancement as a result of the periodic starting and development of thermal and hydrodynamic boundary layers. Figure 11 shows the relevant geometrical parameters of the Offset strip fin arrangement. The surface geometry can be characterized by the fin length l, fin height h, transverse spacing s, and fin thickness t_{fin}, or by three non-dimensional parameters $\alpha=s/h$, $\delta=t_{fin}/l$, and $\Upsilon=t_{fin}/s$. Apart from these, the fin offset is also an additional parameter and is assumed to be uniform and equal to half-fin spacing. Furthermore, manufacturing defects such as burred edges, bonding imperfections, and plate roughness also influence the flow and heat transfer characteristics in actual heat exchanger cores. What follows is a brief summary of the various thermal-hydraulic correlations proposed for the Offset strip fins in the literature.

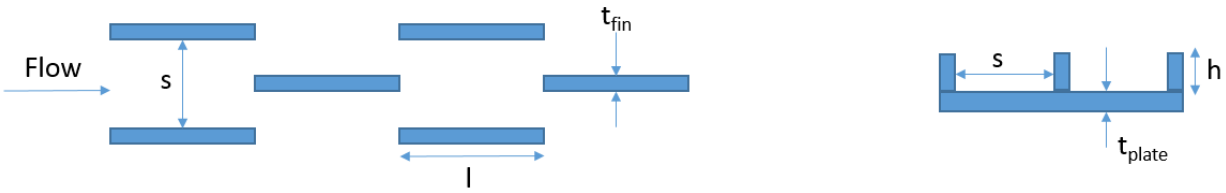

Figure 11: Geometrical parameters of the offset strip fin pattern, fin offset is equal to the half-fin spacing.

Wieting [28] is among one of the earliest researcher to propose friction factor and j-factor empirical correlations based on power law curve fits through data for 22 rectangular offset-fin core geometries using air as the working fluid. These empirical correlations are listed in Equations (29)-(30) for laminar and turbulent regions respectively, where Re<1000 was chosen

as the laminar region. For laminar-to-turbulent transition region, extrapolating these equations until they intersect at a particular *Re* is suggested. However, discrepancy was noticed in the transition region.

$$f = 7.661\left(\frac{l}{D_h}\right)^{-0.384}\alpha^{-0.092}Re^{-0.712} \tag{29}$$
$$j = 0.483\left(\frac{l}{D_h}\right)^{-0.162}\alpha^{-0.184}Re^{-0.536}$$

Where, $Re \leq 1000$ and $Pr \sim 0.7$

$$D_h = \frac{2sh}{(s+h)}$$

$$f = 1.136\left(\frac{l}{D_h}\right)^{-0.781}\left(\frac{t_{fin}}{D_h}\right)^{0.534}Re^{-0.198} \tag{30}$$
$$j = 0.242\left(\frac{l}{D_h}\right)^{-0.322}\left(\frac{t_{fin}}{D_h}\right)^{0.089}Re^{-0.368}$$

Where, $Re \geq 2000$ and $Pr \sim 0.7$

Joshi and Webb [29] attempted to identify the transition from laminar flow based on previous flow visualization studies and their own experiments. As the *Re* increases, oscillating velocities develop in the wakes, leading to vortex shedding which acts as free-stream turbulence for the downstream fins, thereby increasing the heat and momentum transfer. Joshi and Webb observed that the velocity profile in the wake region is affected by the fin geometrical parameters (s, t_{fin}, and l). They recommended an empirical correlation for the onset of transition *Re* (Re^*) based on the data of 21 core geometries. Furthermore, they also readjusted empirical correlations proposed by Wieting to include more appropriate definition of hydraulic diameter and choosing the laminar and turbulent flow limits based on Re^*. These empirical correlations are given in Equations (31)-(32) and Re^* is given in Equation (33).

$$f = 8.12\left(\frac{l}{D_h}\right)^{-0.41}\alpha^{-0.02}Re^{-0.74} \tag{31}$$
$$j = 0.53\left(\frac{l}{D_h}\right)^{-0.15}\alpha^{-0.14}Re^{-0.5}$$

Where, $Re \leq Re^*$ and $Pr \sim 0.7$

$$f = 1.12\left(\frac{l}{D_h}\right)^{-0.65}\left(\frac{t_{fin}}{D_h}\right)^{0.02}Re^{-0.36} \tag{32}$$
$$j = 0.21\left(\frac{l}{D_h}\right)^{-0.24}\left(\frac{t_{fin}}{D_h}\right)^{0.17}Re^{-0.4}$$

Where, $Re \geq 1000 + Re^*$ and $Pr \sim 0.7$

$$Re^* = 257\left(\frac{l}{s}\right)^{1.23}\left(\frac{t_{fin}}{l}\right)^{0.58}D_h\left[t_{fin} + 1.328\left(\frac{Re}{l.D_h}\right)^{-0.5}\right]^{-1} \tag{33}$$

Where, $D_h = \frac{2(s-t_{fin})h}{\left[(s+h)+t_{fin}\cdot\frac{h}{l}\right]}$

Subsequently, Mochizuki *et al.* [30] also proposed a set of friction factor and j-factor correlations as shown in Equations (34)-(35), which are similar to that of the ones proposed by Wieting [28]

with coefficients and exponents modified to fit their own experimental data of five rectangular offset fin cores.

$$f = 5.55\left(\frac{l}{D_h}\right)^{-0.32}\alpha^{-0.092}Re^{-0.67} \quad (34)$$
$$j = 1.37\left(\frac{l}{D_h}\right)^{-0.25}\alpha^{-0.184}Re^{-0.67}$$

Where, $Re \leq 2000$ and $Pr \sim 0.7$

$$D_h = \frac{2sh}{(s+h)}$$

$$f = 0.83\left(\frac{l}{D_h} + 0.33\right)^{-0.5}\left(\frac{t_{fin}}{D_h}\right)^{0.534}Re^{-0.2} \quad (35)$$
$$j = 1.17\left(\frac{l}{D_h} + 3.75\right)^{-1}\left(\frac{t_{fin}}{D_h}\right)^{0.089}Re^{-0.36}$$

Where, $Re \geq 2000$ and $Pr \sim 0.7$

Manglik and Bergles [31] noticed that the empirical correlations presented in Equations (29)-(35) [28, 29, 30] exhibiting discrepancies for certain geometries and also in the transition region. Hence, they considered larger database and 18 different offset fin cores to propose empirical correlations listed in Equations (36)-(37). These correlations are valid for laminar, transition as well as turbulent flow regimes.

$$f = 9.2643Re^{-0.7422}\alpha^{-0.1856}\delta^{0.3053}\gamma^{-0.2659}[1 + 7.669.10^{-8}Re^{4.429}\alpha^{0.92}\delta^{3.767}\gamma^{0.236}]^{0.1} \quad (36)$$

$$j = 0.6522Re^{-0.5403}\alpha^{-0.1541}\delta^{0.1499}\gamma^{-0.0678}[1 + 5.629.10^{-5}Re^{1.34}\alpha^{0.504}\delta^{0.456}\gamma^{-1.055}]^{0.1} \quad (37)$$

Where, *Re* is based on the hydraulic diameter calculated as,

$$D_h = \frac{4A_c}{P} = \frac{4shl}{2(sh+hl+t_{fin}h)+t_{fin}s}$$

And, $0.134 \leq \alpha \leq 1.034$, $0.012 \leq \delta \leq 0.06$, and $0.038 \leq \gamma \leq 0.195$ resulting in $0.646 \leq D_h \leq 3.414$

These correlations are valid for $120 < Re < 10{,}000$.

Hu and Herold [32, 33] tested seven different offset fin geometry cores using liquid coolants (water and polyalphaolefin) to investigate the influence of Prandtl number on the friction factor and j-factor. The Prandtl number was varied from 3 to 150 and they found out that the Prandtl number have a significant effect on the Colburn j-factor. The empirical models developed for air (such as those of Manglik and Bergles [31]) significantly over-predicted (almost by 100%) the j-factor for liquids. However, Prandtl number was found to have very small effect on the friction factor. They proposed a laminar flow model, considering the effects of Prandtl number, *Re*, and fin geometry. Hu and Herold also pointed out that the entry length effects on the heat transfer and pressure drop characteristics is very large especially when the number of offset strip fin rows is small.

Dong *et al.* [34] conducted experimental study to investigate air side heat transfer and pressure drop characteristics of 16 types offset strip fins and proposed the following empirical correlations for the friction factor and j-factor.

$$f = 2.092Re^{-0.281}\alpha^{-0.739}\delta^{0.972}\gamma^{-0.78}\beta^{-0.497} \quad (38)$$

$$j = 0.101Re^{-0.189}\alpha^{-0.488}\delta^{0.479}\gamma^{-0.297}\beta^{-0.315} \quad (39)$$

Comparing the correlations of Dong *et al.* [34] to those of the ones proposed by Manglik and Bergles [31], overall trend of the geometrical parameters appear similar. The key difference is the added term, $\beta = \frac{L}{l}$, the ratio of flow length L and fin length l, to consider the effect of number of offset strip fin rows for shorter cores.

M.S. Kim *et al.* [35] conducted numerical analysis for a total of 39 offset-strip fin surfaces after validating the numerical model against the data of Kays and London [27]. Kim *et al.* [35] compared their numerical data with the empirical model proposed by Manglik and Bergles [31] and noticed that the model underestimated the *f* values and overestimated *j* values for air when blockage ratio is >20%. They proposed f and j-factor correlations for blockage ratios in the range of 5-35% as well as included the effect of Prandtl number in the range of 0.7-50. These correlations are summarized in Equations (41)-(44).

Blockage ratio is defined as,

$$\Phi = \left(1 - \frac{1}{1+\alpha\gamma+\gamma+\alpha\gamma^2}\right).100(\%) \quad (40)$$

For, Φ <20%:

$$f = \exp(7.91)\,\alpha^{-0.159}\delta^{0.358}\gamma^{-0.033}Re^{(0.126lnRe-2.3)} \quad (41)$$

$$j = \exp(1.96)\,\alpha^{-0.098}\delta^{0.235}\gamma^{-0.154}Re^{(0.0634lnRe-1.3)}Pr^{0.00348}$$

For, 20%≤ Φ <25%:

$$f = \exp(9.36)\,\alpha^{-0.0025}\delta^{-0.0373}\gamma^{1.85}Re^{(0.142lnRe-2.39)} \quad (42)$$

$$j = 1.06\alpha^{-0.1}\delta^{0.131}\gamma^{-0.08}Re^{(0.0323lnRe-0.856)}Pr^{0.0532}$$

For, 25%≤ Φ <30%:

$$f = \exp(5.58)\,\alpha^{-0.36}\delta^{-0.552}\gamma^{-0.521}Re^{(0.111lnRe-1.87)} \quad (43)$$

$$j = \exp(1.3)\alpha^{0.004}\delta^{0.251}\gamma^{0.031}Re^{(0.0507lnRe-1.07)}Pr^{0.051}$$

For, 35%≤ Φ <35%:

$$f = \exp(4.84)\,\alpha^{-0.48}\delta^{0.347}\gamma^{0.511}Re^{(0.089lnRe-1.49)} \quad (44)$$

$$j = 0.2\alpha^{-0.125}\delta^{0.21}\gamma^{-0.069}Re^{(0.0005lnRe-0.338)}Pr^{0.0549}$$

In light of above discussion, one can see that there has been a significant amount of work performed and a number of empirical correlations available for design of rectangular Offset strip fin heat exchangers. However, most of these heat exchanger cores used rectangular fins with sharp edges and no pitch in the flow direction. If the concept of offset rectangular fins is to be extended to diffusion bonded heat exchangers, the surface patterns will most likely be photo chemically etched, which allows for mass production of the plates at lower costs. However, unlike previously tested rectangular offset fin heat exchanger cores, chemical etching doesn't provide sharp edges due to inherent manufacturing defects. One of the goals of the current project is to extend the concept of rectangular offset fins to chemically etched plates and compare the thermal-hydraulic aspects with the existing empirical correlations listed here.

Design and fabrication of rectangular offset fin pattern

For this project, we worked with Microphoto (http://microphoto.net/) to understand the photochemical etching limitations and shortlist list of rectangular offset fin patterns that can be fabricated using etching process. Below is the list of guidelines we received from Engineers at Microphoto:

1) Minimum possible fin thickness (t_{fin}) is 0.005".
2) For every 0.001" etch depth, there will be 0.001" lateral etch (In other words, the lateral etch width and length can be expected to be equal to the etch depth). This is known as "etch factor".
3) The etching tolerances are $\pm$0.002" for the etch depth and a best of $\pm$0.005" for the rest of the features.
4) In addition, the best guess for the corner radius at the surface due to etching defects is expected to be in the range of 0.015"-0.02" as shown in Figure 12. Figure 12 is a sample etch for rectangular fin provided by Microphoto upon request.

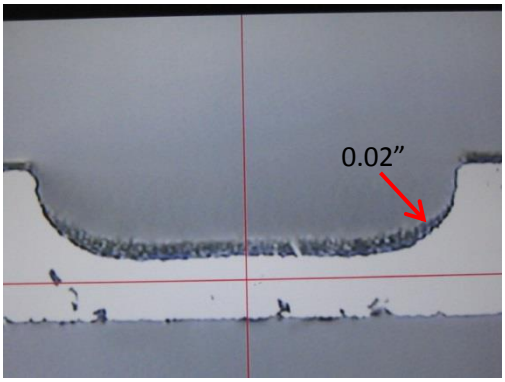

Figure 12: Sample etch for rectangular fin provided by Microphoto upon request. Copyright of Microphoto (http://microphoto.net/)

Using a design fin thickness (t_{fin}) of 0.026" and following the guidelines provided by Microphoto Engineers, the offset fin pattern for etching is designed to be as shown in Figure 13. The fin depth (etch depth) is designed to be equal to that of fin thickness. The fin spacing is

designed to be 3 times that of fin spacing to account for corner etch radius. Figure 14 compares the friction factor, j-factor, and area goodness factor (j/f) of the designed geometrical rectangular offset fin pattern using the correlations proposed by Manglik and Bergles, Equations (36)-(37) against the zigzag channels using the correlations proposed by Moisseytsev *et al.* [16], Equations (10)-(12).

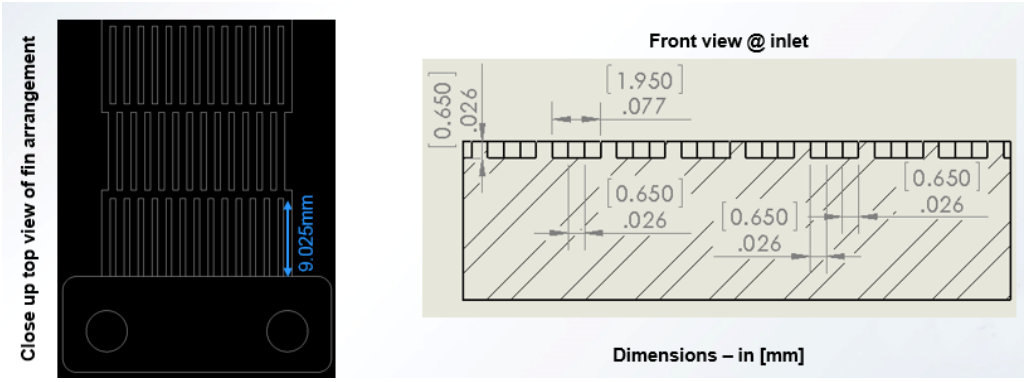

Figure 13: Rectangular Offset fin design geometrical parameters prior to the chemical etching process.

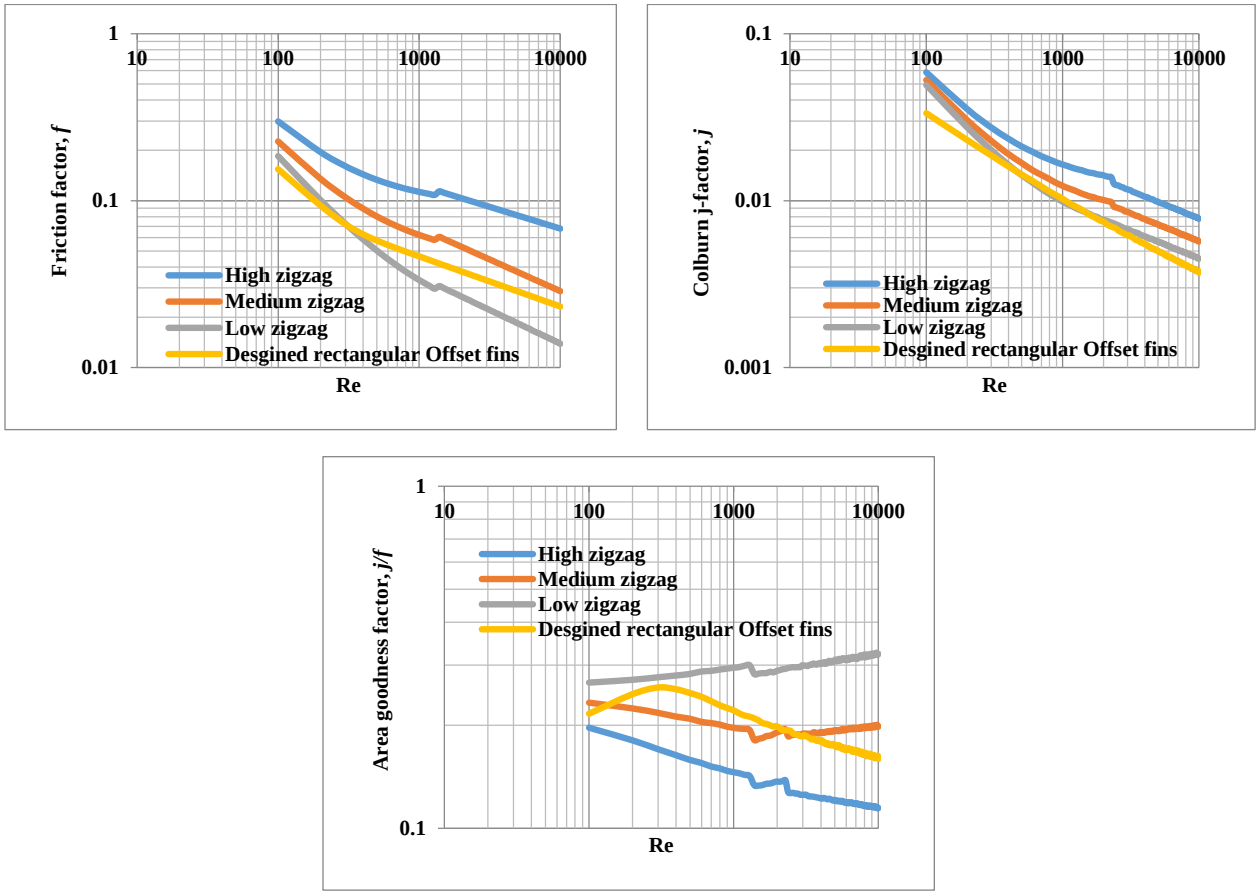

Figure 14: Thermal-hydraulic performance of designed rectangular offset fins compared against the zigzag channel correlations proposed by Moisseytsev *et al.* [16] for different channel bend angles.

As can be seen from Figure 14, the area goodness factor of the designed rectangular offset fin pattern is better than the "high zigzag", "medium zigzag" channels for a wide range of *Re*. However, "low zigzag" channel outperforms the rectangular offset fin pattern both in the laminar and turbulent flow regimes. It should be noted that the rectangular offset fin correlations are proposed based on the experimental data for core geometries with near sharp edges. These sharp edges can increase the pressure drop and the actual fabricated pattern using chemical etching process might benefit from the inherent manufacturing imperfections resulting in blunt/rounded edges. Table 11 compares the designed and measured geometrical parameters of the rectangular offset fin pattern after the chemical etching process. The XYZ point cloud data of the heat exchanger plate has been obtained using laser scanner with an accuracy of ± 0.0005" and the point cloud data has been used to reconstruct generic polymesh file of the pattern. Figure 15 shows a unit cell representation of the rectangular offset fin along with relevant geometrical parameters from Table 11.

Table 11: Design and measured geometrical parameters of the rectangular Offset fin pattern.

	Design	Measured
Fin thickness, t_{fin} (mm)	0.65	0.65
Fillet radius, r (mm)	0	0.47
Fillet radius, r_{fin} (mm)	0	0.18
Fin depth, h (mm)	0.65	0.65
Fin spacing, s (mm)	1.95	1.95
Fin length, l (mm)	9.025	8.63
Lateral pitch, p (mm)	18.05	17.66
Plate thickness, t (mm)	6.3	
Number of unit cells along length (N_x)	28.5	
Number of unit cells per row (N_y)	9	
Hydraulic diameter, D_h (mm)	0.9502	0.9
Unit cell heat transfer area, A_s (mm^2)	82.01	60.9
Cross-sectional area, A_c (mm^2)	11.43	11.09
Measured Relative roughness	7.4e-3	

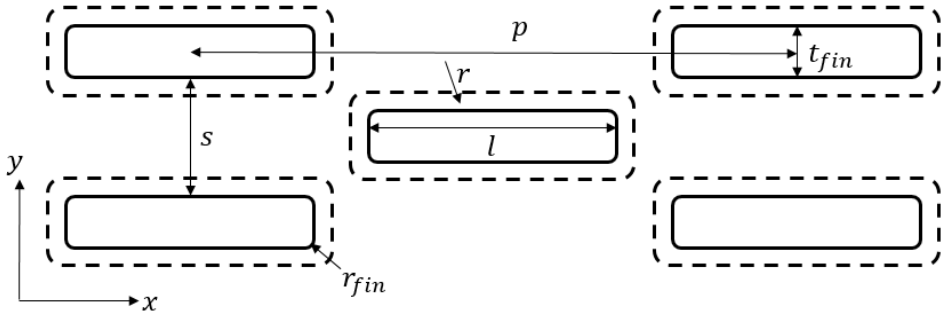

Figure 15: A diagram of a rounded rectangular offset fin array PCHE channel unit cell. The dashed grey line represents the outer bottom edge of a depth-wise fillet of radius r which is constructed on the inside bottom edge of the main rectangular fin profile shown in black.

In light of above discussion and listed shortcomings, research goals for this project are listed as follows:

1) Characterize the thermal-hydraulic behavior of rectangular offset fin patterns fabricated using unconventional chemical etching process, which can lead inherent manufacturing defects.
2) Compare the thermal-hydraulic data to the existing offset strip fin correlations for Plate fin heat exchanger cores and propose new correlations based on the results obtained.
3) Extend the range of testing conditions for the 4.1mmNACA0020 fin geometry and propose thermal-hydraulic correlations.
4) Compare the friction factor and j-factors of the discontinuous airfoil and rectangular fin geometry to the existing correlations/data for the continuous straight and zigzag channels.

Experimental test facility

Since the overall goal of the project is to propose optimal compact heat exchangers for the sCO_2 Brayton cycle, the test facility utilizes CO_2 as the working fluid. In order to test the heat exchanger geometries, the test facility should be able to accommodate multiple heat exchanger configurations and should allow for wide range of operating conditions such as pressures, temperatures as well as flowrates. In addition to these operating requirements, the test facility is designed to allow precise and accurate measurements of all the variables required for data processing. Error propagation analysis was performed a priori in order to identify the large sources of uncertainty and an effort was made to reduce the overall uncertainty in measurements of heat transfer coefficients and pressure drop of the heat exchanger geometries.

Figure 16 shows the schematic and picture of the test rig utilized for this project. The test loop consists of high pressure liquid chromatography (HPLC) pump, circulation gear pump, Coriolis mass flowmeter, pre-heater, test section and an after-cooler.

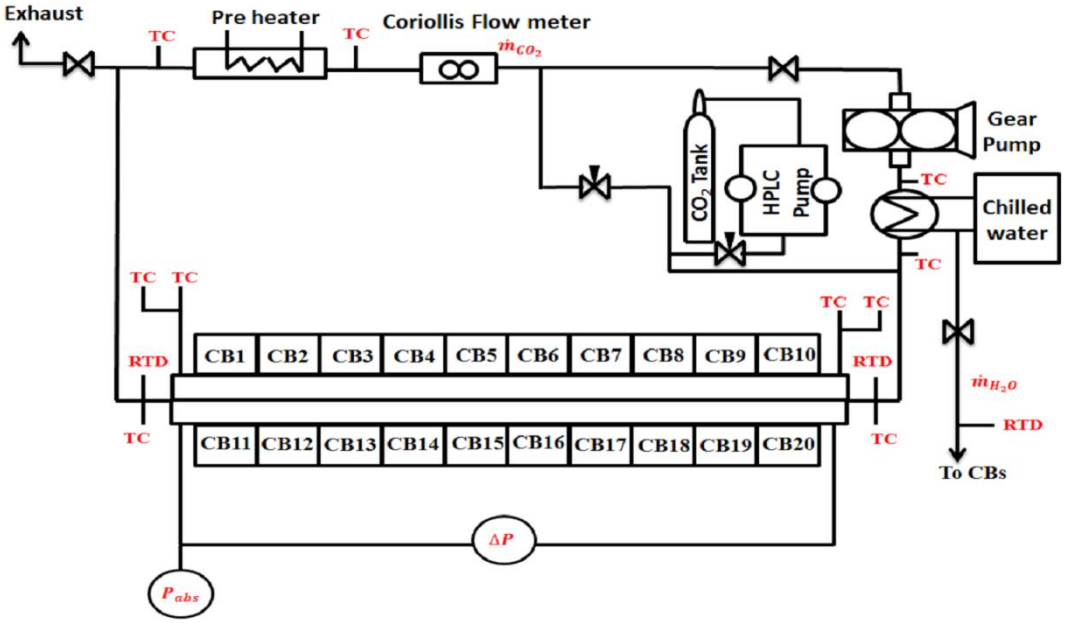

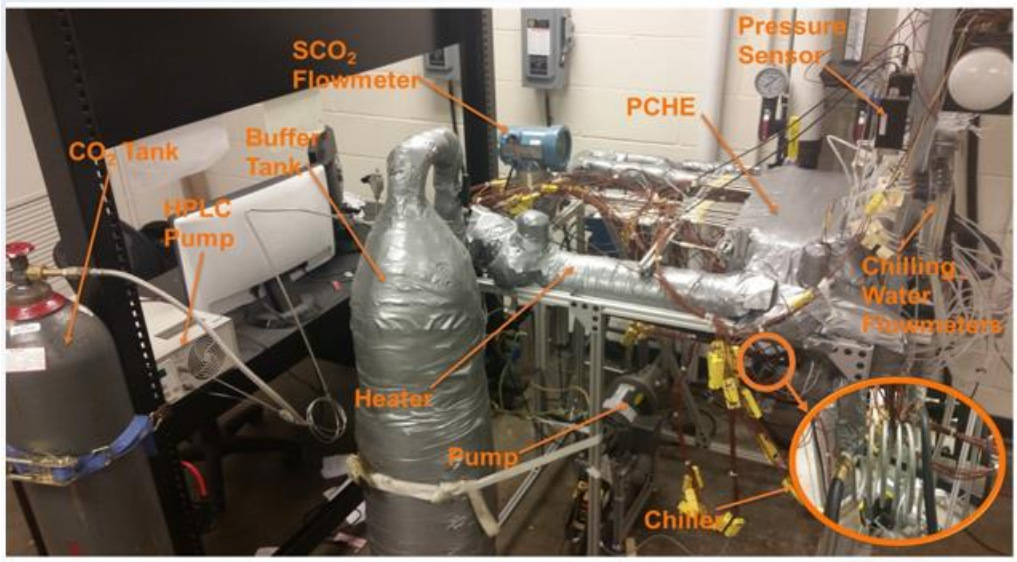

Figure 16: Schematic of the sCO_2 heat exchanger test facility at Georgia Tech.

Prior to the beginning of testing, the test loop is vacuumed and purged with CO_2 to ensure that no foreign contaminants are present in the system. The facility is filled with CO_2 up to desired operating pressures using Scientific Systems, Inc. SFC-24 positive displacement, constant pressure HPLC pump. Once the test loop is at desired operating pressures, Micropump magnetically driven gear pump is used to circulate the fluid in the loop. The pump is coupled to a variable frequency drive (VFD); this in conjunction with a flow bypass valve adjusts and precisely controls the desired mass flowrate through the heat exchanger. A Micromotion Coriolis mass flowmeter and transmitter are used to record the mass flowrate through the test section as well as to provide the feedback to the circulation pump via VFD. The temperature of fluid entering the test section is controlled using a custom fabricated 5.5 kW high pressure cartridge heater. More details of the test facility can be found from Pidaparti *et al.* The prototypic discontinuous heat exchanger patterns for this project are tested in the same manner as Kruizenga [22] and Carlson [23]. The model and sketch of the heat exchanger shown in Figure 17, reproduced from Carlson [23], is a good representation of the heat exchanger, fluid paths, and instrumentation.

The test section of the heat exchanger plate, the mating plate, and the cooling blocks. This design, as described by Kruizenga [22], allows for multiple heat exchanger patterns to be tested by swapping out the heat exchanger plates whenever necessary. In the current project, we tested two different heat exchanger plates (discontinuous rectangular offset fin and 8.1mmNACA0020 geometries described in the previous section). The heat exchanger plate is a 316L stainless steel plate with the desired pattern chemically etched on to it and the total length of the etched pattern is 500 mm. On each end of the plate, entrance and exit manifolds are machined into the plate to distribute and collect the flow entering and leaving the test section. In case of the continuous channel type geometries, it is important to ensure that the manifolds distribute the flow uniformly to avoid any thermal stresses, reduction in effectiveness. However, for the current project since we are focused on testing discontinuous style fin geometries, the flow is expected to be uniformly distributed after certain location downstream.

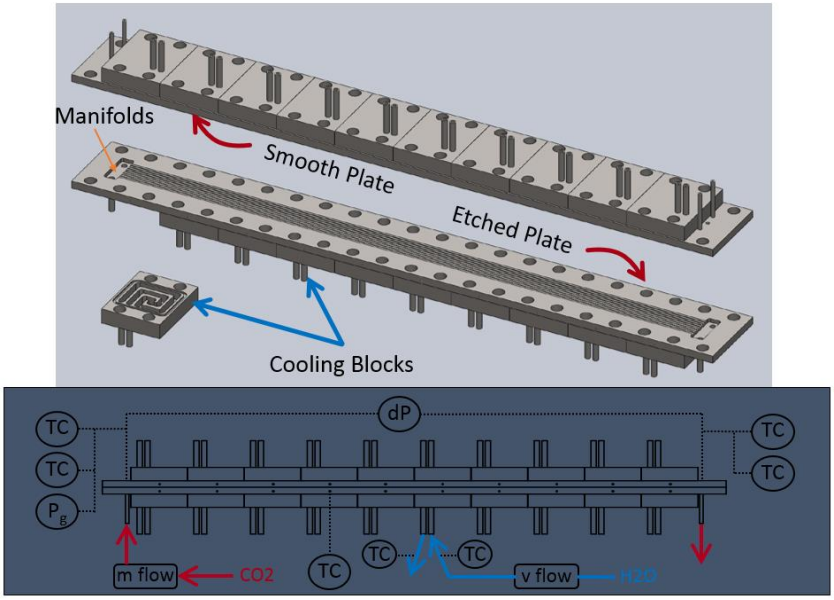

Figure 17: CAD model and Sketch of the heat exchanger showing assembly, fluid paths, and instrumentation [23].

Two RTDs are located in each manifold to measure the inlet and outlet temperatures of the CO_2. The inlet pressure and the differential pressure across the test section are measured using a Meriam ZM1500-GI3000 and ZM1500-DN0415 digital transmitters respectively. The heat exchanger plate is bolted to the mating plate to complete the prototypic heat exchanger emulating the diffusion bonded heat exchangers. Figure 18 shows a section of the two discontinuous fin geometries tested for this project. Detailed design and measured dimensions of the geometrical parameters for each of these plates is provided in Tables (9) and (11). The mating plate is essentially a flat plate with an O-ring groove machined into the surface, along with three holes at each end, two for thermocouples and one for a pressure tap. The O-ring is used to seal the heat exchanger and is made of 1/16" Viton cord stock and that is cut to the length and glued together to form the seal.

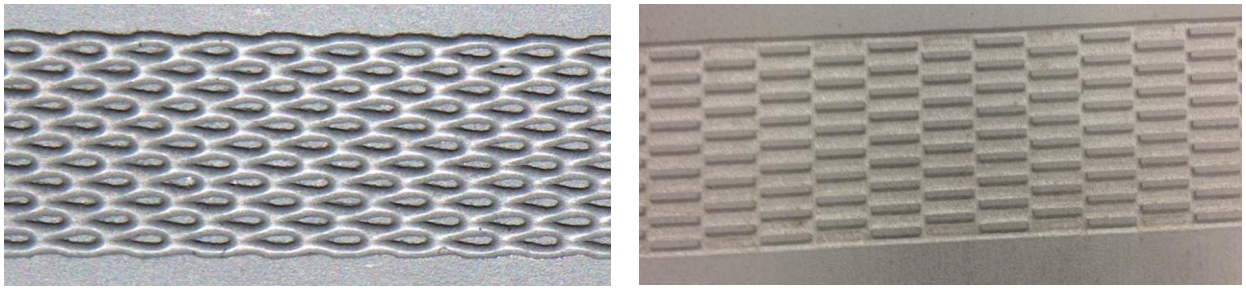

Figure 18: Images representing a section of the 4.1mmNACA0020 airfoil fin (Left) and rectangular Offset fin (Right) geometry heat exchanger plates. Detail design and measured dimensions of the geometrical parameters for each of these plates is provided in Tables (9) and (11).

One of the objective of these tests is to measure local heat transfer coefficients. In order to achieve this, local heat fluxes, wall temperatures and fluid bulk temperatures need to be

accurately determined. Detailed data reduction and uncertainty analysis will be presented in the next section. In order to measure local wall temperatures, a set of ten 1/16" thermocouples are implanted into the side wall of each plate. Since the holes needed for thermocouples have large L/D ratio, the drilling of holes was achieved in two steps. First, a larger hole is drilled to a certain depth followed by drilling using a 1/16" drill bit to the desired location. The locations of thermocouple holes are X-ray scanned after the drilling and we found out that the two step drilling method was more accurate than the electrical discharge machining (EDM). Thermocouples are thermally coupled to the wall and the holes are filled using excess thermal paste which has excellent thermal conductivity and allows for easy cleaning and replacement of thermocouples when needed. This step was necessary to avoid any temperature gradients induced due to the presence of air pockets that could lead to several degrees of error in wall temperature measurement. Attached to the top of the mating plate and bottom of the heat exchanger plate are a set of ten individual cooling blocks that are used to measure local heat removal rate. Each cooling block is supplied with cooling water. Volumetric flowrate of water flowing to each cooling block is measured using turbine type flowmeters. Two K-type thermocouples are installed into the water at the inlet and outlet of each cooling block to measure the temperature of water entering and leaving the cooling block, refer to Figure 17.

Data Acquisition

The data acquisition system consists of NI cDAQ-9178 Chassis interfaced with the data acquisition computer via USB. The Chassis consists of three NI-9213 modules for recording all the thermocouple measurements, one NI-9219 module for recording the mass flowrate and RTDs measurements in the test loop. NI-9476 digital output module is used to provide feedback control for the relay controlling the cartridge heater. NI-9264 analog output module provide the feedback signal to the VFD for pump control. For each operating condition, the system is assumed to be at steady state once all the variables are constant for at least 10 mins. Prior to collecting/recording data, an energy balance between CO_2 and water was performed to ensure that they agree well with each other. Typically the two agree well within $\pm$10%, except for few cases near the pseudo-critical point where the errors can be dominated by small measurement uncertainties. Once the system achieves a steady state, the data is recorded for 500s at a rate of 1 Hz and the average of these data points is used for the data processing.

Heat transfer data Reduction and associated uncertainty

Experimentally measured parameters need to be reduced to heat transfer coefficients (or Nusselt numbers) and friction factors. This section provides the data reduction procedure along with uncertainty associated in each step.

Local and overall heat removal rate calculation

The local heat removal for each cooling block is calculated using the measured inlet and outlet water temperatures and the volumetric flowrate of water. Approximately 3" thick insulation layer is wrapped around the test section and the cooling blocks, therefore, the heat loss to the ambient is assumed to be negligible. Water properties are calculated based on the average of the inlet and outlet temperatures, as the water properties don't vary considerably in the temperature range of

interest. For example, for all the experiments performed, the temperature difference between outlet and inlet to the cooling blocks is between 0.5 – 15°C and the temperatures are far away from boiling point. Therefore, assumption of constant properties for water is quite reasonable. The total heat removal rate can be determined from the water side by summing the local heat removal rates from all 20 cooling blocks (10 on the mating plate and 10 on the heat exchanger plate), as shown in Equation (45).

The total heat removal rate can also be alternatively determined from energy balance on the CO_2 side, as shown in Equation (46).

$$\dot{Q}_{H_2O} = \sum_1^{20} \dot{V}\rho|_{T_{avg}} C_p|_{T_{avg}} [T_{water,out} - T_{water,in}] \quad (45)$$

$$\dot{Q}_{CO_2} = \dot{m}_{CO_2}(i_{in} - i_{out}) \quad (46)$$

Where, i is the enthalpy (J/kg) and is determined from the measured inlet/outlet temperatures and associated pressures. Inlet/outlet temperatures are measured using platinum RTD with an uncertainty of ± 0.15°C. The pressure transducers are calibrated using a deadweight tester and the maximum uncertainty is found to be 0.05% of full scale (equivalent to ± 1.5 psi). All of these uncertainties are used in the overall energy balance for the CO_2 side. Uncertainty in the measurement of local heat removal rate from the cooling blocks is calculated using Equation (47). From Equation (47), the major contributors to the heat removal rate uncertainty are the uncertainty in measurement of water temperature difference and the volumetric flowrate of water.

$$\sigma_{Q_{H_2O}} = \left(\left(\frac{dQ_{H_2O}}{d\dot{V}} \right)^2 \sigma_{\dot{V}}^2 + \left(\frac{dQ_{H_2O}}{d\Delta T} \right)^2 \sigma_{\Delta T}^2 \right)^{0.5} \quad (47)$$

Where, $\frac{dQ_{H_2O}}{d\dot{V}}[i] = \frac{Q_{H_2O}[i]}{\dot{V}[i]}$ and $\frac{dQ_{H_2O}}{d\Delta T}[i] = \frac{Q_{H_2O}[i]}{(T_{out}[i] - T_{in}[i])}$

Volumetric flowrate to each cooling block is measured using turbine type flowmeter with Hall sensor meter. All the flowmeters are connected in series and the cooling water is flown through and collected into a 2000 ml graduated cylinder with an uncertainty of ±20 ml. The frequency output from the flowmeters and the time taken to fill up the cylinder were recorded using Arduino. Following this procedure a linear calibration curve between the frequency and flowrate was generated for each flowmeter with an overall uncertainty of 1.5% in measurement of volumetric flowrates.

Typically, the K-type thermocouples used to measure the water temperature have manufacturer specified uncertainty of 2.2°C or 0.75% of the measured value (whichever is greater). This will lead to extremely large uncertainty in measurement of water temperature difference. In order to reduce this uncertainty, water outlet thermocouples are calibrated against the inlet thermocouples in-situ by flowing water through each block at temperatures ranging from 10-35°C. This method requires that there is no CO_2 flow during the calibration and the maximum estimated uncertainty in measurement of water temperature difference is ±0.15°C.

The overall heat removal rate determined from both water and CO_2 matched well within 10% or less for nearly all the experiments, except for some tests where the inlet/outlet temperature are near the pseudo-critical point.

Bulk fluid temperature calculation

Bulk fluid temperature is calculated at ten axial locations. This was accomplished by an energy balance at each subsection (See Figure 19), which consists of cooling block pairs on the mating and the heat exchanger plate. The measured CO_2 inlet pressure and temperature to the test section are used to calculate the specific enthalpy at the inlet ($i_{in}, i[1]$). Assuming a linear pressure drop across the test section (Equation 48), the local bulk enthalpy at the exit of each cooling block sub-section can be determined as shown in Equation (48). The average enthalpy for each sub-section can then be calculated as in Equation (49).

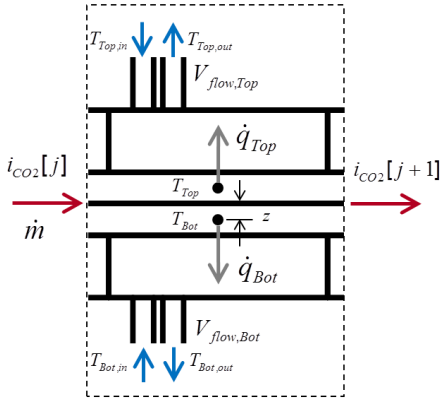

Figure 19: One of the 10-subsections of the heat exchanger showing relevant variables used during data reduction and analysis.

$$P_{j+1} = P_j - \frac{dP}{10} \tag{48}$$

$$i_{j+1} = i_j - \frac{\dot{Q}_{top,j} + \dot{Q}_{bottom,j}}{\dot{m}} \tag{49}$$

$$i = \frac{i_{j+1} + i_j}{2} \tag{50}$$

Finally, the average bulk temperature and any other state-dependent thermo-physical properties can be determined based on the average enthalpy and pressure for each subsection. All the fluid properties are calculated using the NIST REFPROP v9.1 [37] and the uncertainty associated with the calculation of bulk enthalpy and temperature are reported as per Equations (51)-(53).

$$\sigma_i[j] = \left(\sigma_i[j-1] + \left(\frac{di}{dQ}[j]\right)^2 \sigma_Q[j]^2 + \left(\frac{dh}{d\dot{m}_{CO_2}}[j]\right)^2 \sigma_{\dot{m}}^2 \right)^{0.5} \tag{51}$$

$$\sigma_{i_b}[j] = 0.5.\left(\sigma_i[j]^2 + \sigma_i[j-1]^2\right)^{0.5} \tag{52}$$

$$\sigma_{T_b}[j] = \left(\left(\frac{dT_b}{di_b}[j]\right)^2 \sigma_{i_b}[i]^2 + \left(\frac{dT_b}{dP_b}[i]\right)^2 \sigma_P^2\right)^{0.5} \quad (53)$$

Where,

$$\frac{di}{dQ}[j] = \frac{1}{\dot{m}_{CO_2}}$$

$$\frac{di}{d\dot{m}_{CO_2}}[j] = -\frac{Q[j]}{\dot{m}_{CO_2}{}^2}$$

$$\frac{dT_b}{di_b}[j] = \frac{1}{C_p(CO_2, i_b[j], P_b[j])}$$

$$\frac{dT_b}{dP_b}[j] = \frac{T(CO_2, i_b[j], P_b[j]+\sigma_p) - T(CO_2, i_b j, P_b[j]-\sigma_p)}{2.\sigma_p}$$

$$\sigma_Q[j] = \left(\sigma_{Q_{top}}[j]^2 + \sigma_{Q_{bottom}}[j]\right)^{0.5}$$

$$\sigma_{\dot{m}} = \left(\frac{0.5}{100}\right).\dot{m}_{CO_2}$$

Wall temperature calculation

The wall surface temperature on each plate side is calculated according to a plane-wall conductance equation as shown in Equation (54). The two wall surface temperatures as estimated from the top and bottom of the channels are then averaged and used to determine the heat transfer coefficient for each sub-section.

$$T_{w,calc}[j] = T_{w,meas}[j] + \frac{Q[j].z[j]}{k_{ss316}A_{cb}}$$

$$T_w[j] = 0.5.(T_{w,calc,top}[j] + T_{w,calc,bottom}[j]) \quad (54)$$

Where, A_{cb} is the cooling block area actively involved in heat transfer (it is estimated to be 1.39" x 2" from an ANSYS Fluent model, Kruizenga [22]). An uncertainty of 5% is assumed in the usage of this heat transfer area. Uncertainty in the measurement of wall temperature is calculated from Equations (55), (56).

$$\sigma_{T_{w,calc}}[j] = \left(\left(\frac{dT_{w,calc}}{dQ}[j]\right)^2 \sigma_Q[j]^2 + \left(\frac{dT_{w,calc}}{dz}[j]\right)^2 \sigma_z[j]^2 + \left(\frac{dT_{w,calc}}{dk_{ss316}}[j]\right)^2 \sigma_{k_{ss316}}^2 + \left(\frac{dT_{w,calc}}{dA_{cb}}[j]\right)^2 \sigma_{A_{cb}}^2 + \sigma_{T_{w,meas}}^2\right)^{0.5} \quad (55)$$

$$\sigma_{T_w}[j] = 0.5.\left(\sigma_{T_{w,calc,top}}[j]^2 + \sigma_{T_{w,calc,bottom}}[j]^2\right)^{0.5} \quad (56)$$

Where,

$$\frac{dT_{w,calc}}{dQ}[j] = \frac{T_{w,calc}[j] - T_{w,meas}[j]}{Q[j]}$$

$$\frac{dT_{w,calc}}{dz}[j] = \frac{T_{w,calc}[j] - T_{w,meas}[j]}{z[j]}$$

$$\frac{dT_{w,calc}}{dk_{ss316}}[j] = -\left(\frac{T_{w,calc}[j] - T_{w,meas}[j]}{k_{ss316}}\right)$$

$$\frac{dT_{w,calc}}{dA_{cb}}[j] = -\left(\frac{T_{w,calc}[j] - T_{w,meas}[j]}{A_{cb}}\right)$$

All the wall thermocouples are calibrated in-situ with respect to the inlet RTD during isothermal tests (without cooling water flow) and a calibrated uncertainty of ±0.15^{o}C is assumed for uncertainty analysis. The location of thermocouples holes are measured using coordinate measuring machine (CMM) fitted with a dial indicator and vertical caliper as shown in Figure 20. Gauge pins are placed into the holes to accurately measure the locations.

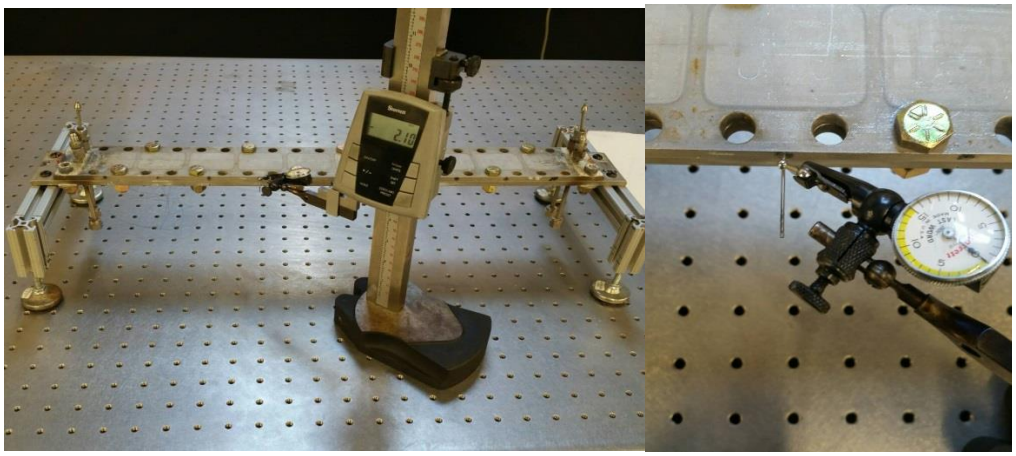

Figure 20: Coodinate measuring machine setup used to measure location of thermcouple holes.

Figure 21 shows that the thermocouple holes depth and angle measured using an X-ray machine are within 98% of the designed values. Uncertainty of 0.002" is used for the measured locations of thermocouple holes. An uncertainty of 5% is assumed for the thermal conductivity of 316 Stainless Steel. From the local heat removal rate, wall temperature, and bulk temperature, the heat transfer coefficient and Nusselt numbers are calculated from Equation (57)-(58).

$$htc[j] = \frac{Q_{top}[j] + Q_{bottom}[j]}{A_s.(T_b[j] - T_w[j])} \quad (57)$$

$$Nu[j] = \frac{htc[j].D_h}{k_b} \quad (58)$$

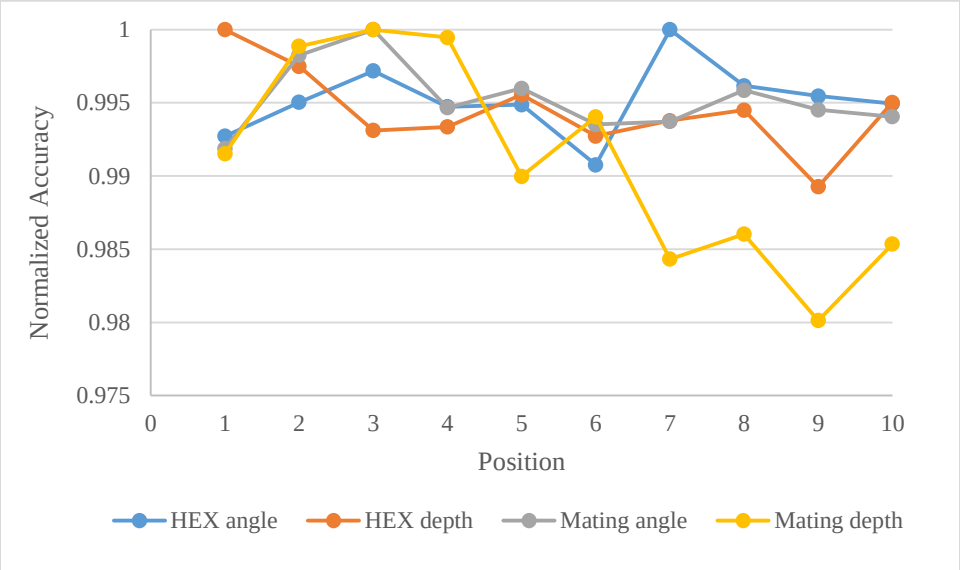

Figure 21: Normalized accuracy of depth and angle of thermocouple holes at 10 positions along with the heat exchanger plate and the mating plate.

The heat transfer surface area and hydraulic diameter required in above equations are tabulated in Table 9 and Table 11 based on laser scanning data of the 4.0mmNACA0020 and rectangular Offset fin surfaces respectively. An uncertainty of 1% is assumed for the measurement of these variables. Uncertainty in the measurement of heat transfer coefficient and Nusselt numbers are calculated using Equation (59)-(60).

$$\sigma_{htc}[i] = \left(\left(\frac{dhtc}{dQ}[i]\right)^2 \sigma_Q[i]^2 + \left(\frac{dhtc}{dA_s}[i]\right)^2 \sigma_{A_s}^2 + \left(\frac{dhtc}{dT_b}[i]\right)^2 \sigma_{T_b}[i]^2 + \left(\frac{dhtc}{dT_w}[i]\right)^2 \sigma_{T_w}[i]^2\right)^{0.5} \quad (59)$$

$$\sigma_{Nu}[i] = \left(\left(\frac{dNu}{dhtc}[i]\right)^2 \sigma_{htc}[i]^2 + \left(\frac{dNu}{dD_h}[i]\right)^2 \sigma_{D_h}^2 + \left(\frac{dNu}{dk_b}[i]\right)^2 \sigma_{k_b}[i]^2\right)^{0.5} \quad (60)$$

Where,

$$\frac{dhtc}{dQ}[i] = \frac{htc[i]}{Q_{top}[i]+Q_{bottom}[i]}$$

$$\frac{dhtc}{dA_s}[i] = -\frac{htc[i]}{A_s}$$

$$\frac{dhtc}{dT_b}[i] = \frac{-htc[i]}{(T_b[i]-T_w[i])}$$

$$\frac{dhtc}{dT_w}[i] = \frac{htc[i]}{(T_b[i]-T_w[i])}$$

$$\frac{dNu}{dhtc}[i] = \frac{Nu[i]}{htc[i]}$$
$$\frac{dNu}{dD_h}[i] = \frac{Nu[i]}{D_h}$$
$$\frac{dNu}{dk_b}[i] = \frac{-Nu[i]}{k_b}$$

Pressure data Reduction and associated uncertainty

The total pressure drop measured across the heat exchanger test section is comprised of four components as shown in Equation (61).

$$\Delta P_{measured} = \Delta P_{friction} + \Delta P_{local} + \Delta P_{accel} + \Delta P_{gravity} \quad (61)$$

Where,

$\Delta P_{friction} = f \frac{L}{D_h} \frac{G^2}{2\rho}$

$\Delta P_{accel} = G^2 \left(\frac{1}{\rho_{out}} - \frac{1}{\rho_{in}}\right)$

$\Delta P_{gravity} = \pm g \left(\frac{i_{out}\rho_{out} + i_{in}\rho_{in}}{i_{out} + i_{in}}\right) Lsin\theta$

All the experiments for this project were performed in horizontal configuration, which eliminates the pressure drop component due to gravity. The acceleration pressure losses due to density changes over the length can be computed from the measured mass flowrate and the inlet and outlet conditions. The local pressure drop arises from the fluid contraction at the inlet, due to the mixing manifold splitting the flow to each channel, and expansion from the channels to the manifold at the outlet. Expansion and contraction pressure losses are well known from published values [38], so the local pressure losses can be determined by the following equations:

$$\Delta P_{local} = \Delta P_{expansion} + \Delta P_{contraction} \quad (62)$$

$$\Delta P_{expansion} = \left[1 - \frac{A_c}{A_{manifold}}\right]^2 \rho_{out} \frac{v_{out}^2}{2}$$

$$\Delta P_{contraction} = 0.5 \left[1 - \frac{A_c}{A_{manifold}}\right]^{0.75} \rho_{in} \frac{v_{in}^2}{2}$$

Where, A_c is the cross-sectional area of the fins and $A_{manifold}$ is the cross-sectional area of the manifolds. Using this procedure, the pressure drop due to friction and the equivalent fanning friction factor can be extracted from the measured pressure drop from the experiments. It should be noted the equivalent frictional pressure drop calculated here includes both pressure drop due to friction as well as the additional pressure drop component due to form losses (due to local flow obstruction from the fins).

Results and discussion

This section presents the exclusive heat transfer and pressure data for the rectangular offset fin and 4.1mmNACA0020 heat exchanger geometries.

Heat Transfer results and Discussion

Figure 22 shows the calculated local average Nusselt numbers along with associated uncertainties determined using the procedure described above. The maximum error in Nusselt numbers farther away from the pseudo-critical point (T_b/T_{pc} > 1.1) was found to be ~5% whereas closer to the pseudo-critical point uncertainty in Nusselt numbers can be as high as ~15% depending on the operating conditions . It can also be noticed that farther away from the critical point (T_b/T_{pc} > 1.1), the Nusselt numbers tend to be constant in the range of 80-100. These values can be used to determine the sizing of high and low temperature recuperators using the current rectangular offset fin PCHE geometry.

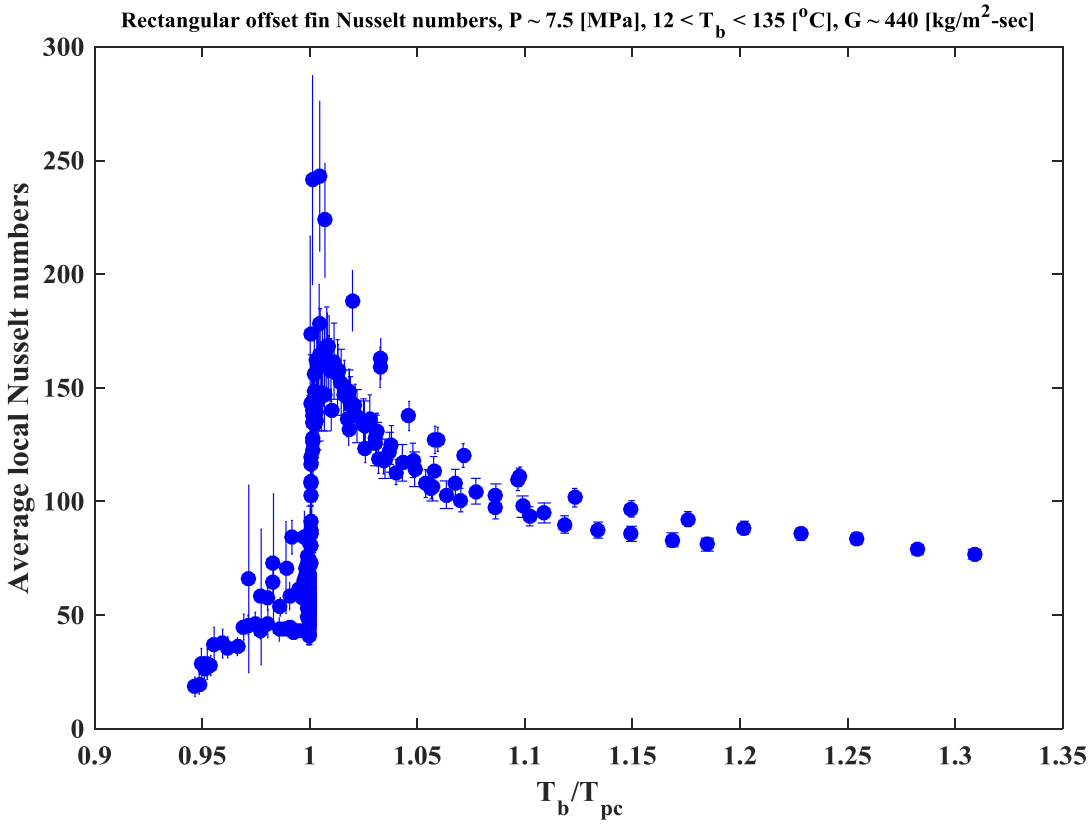

Figure 22: Averaged local Nusselt numbers along with the associated uncertainties for some of the experimental runs. The maximum uncertainty farther away from the pseudo-critical point is 5% and closer to the pseudo-critical point is about 16%.

Figure 23 shows the heat transfer coefficient and Nusselt number of rectangular offset fin heat exchanger as a function of normalized bulk temperature for system pressure of 8.1 MPa (pseudo-critical temperature is ~35.3^{o}C).

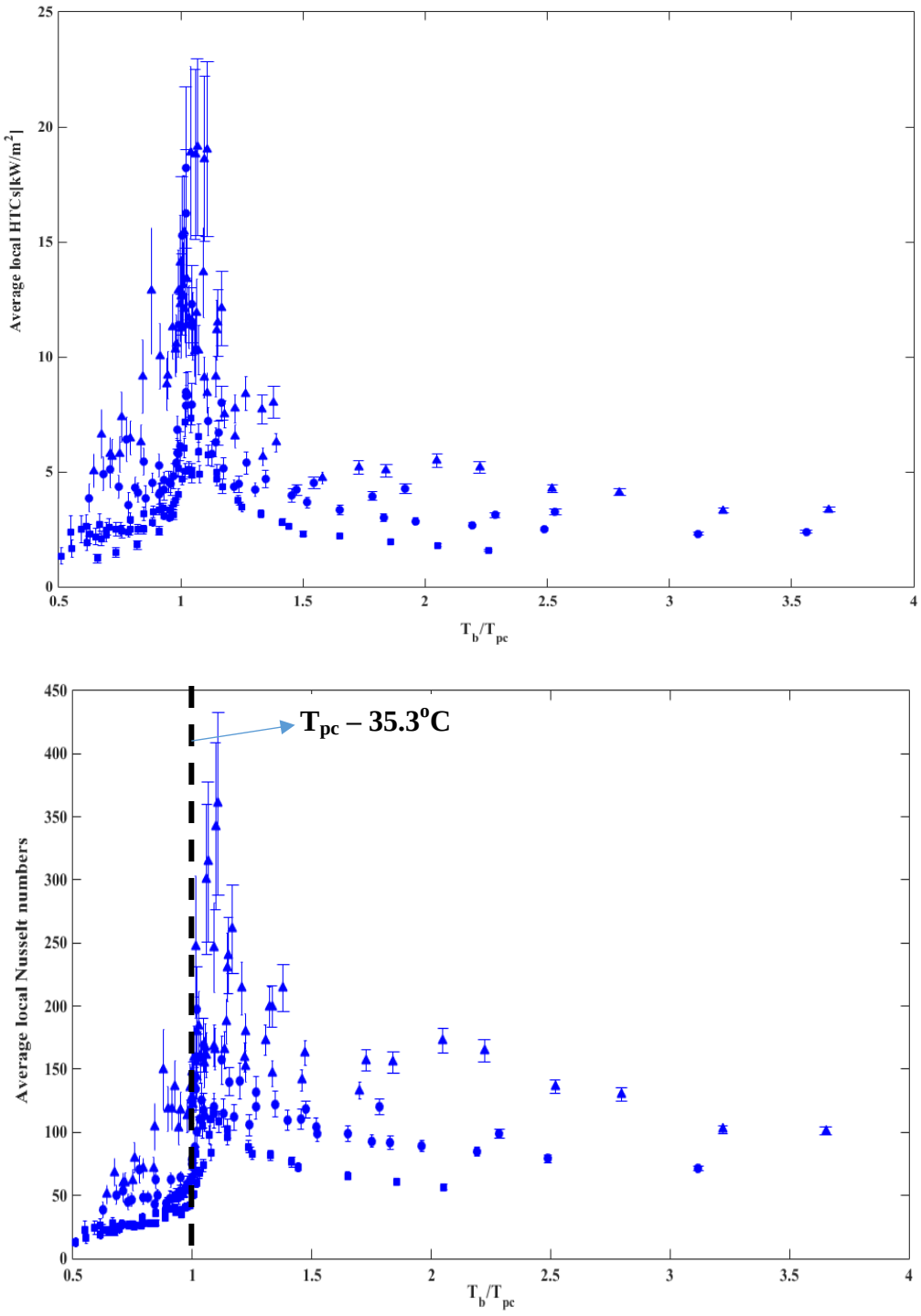

Figure 23: Average local heat transfer coefficients (top) and Nusselt numbers (Bottom) of offset rectangular fin heat exchanger plate versus normalized bulk temperature for a system operating pressure of 8.1 MPa. The square, circular, and triangular symbols represent data for system mass fluxes of 220, 440, 660 kg/m^{2}s respectively.

The square, circular, and triangular symbols in Figure 23 represent data for system mass fluxes of 220, 440, 660 kg/m^{2}s respectively. A drastic-change in thermo-physical properties from gas like to liquid like behavior across the temperature leads to peaks in heat transfer coefficients and Nusselt numbers. As the temperature increases well beyond the pseudo-critical temperature, all the properties decrease gradually to more or less stable ideal gas values, resulting in the lower heat transfer coefficients of gas-like flows. Also, the peak in heat transfer coefficients and Nusselt numbers seem to be much sharper at the higher mass fluxes. In the supercritical region typically temperature variation in the test section has a much more significant effect on heat transfer than the independent variation of mass flux, because it affects thermal properties as well as flow-related Reynolds number substantially.

Figure 24 presents the calculated frictional pressure drop per unit length as a function of average test section temperature. The circular, square, and triangular symbols in Figure 24 represent data for system pressures of 7.5, 8.1, 10.2 MPa respectively. As expected the frictional pressure gradient at the lowest mass flux (G = 220 kg/m^{2}s) is very small. For temperatures greater than the pseudo-critical temperature density of the fluid resembles that of a gas and the frictional pressure gradient is high in this region due to increased flow velocities. As the temperatures falls below the pseudo-critical temperature a steep decrease in the frictional pressure gradient is noticed for all the mass fluxes. This is because the density increases rapidly as the temperature falls below the pseudo-critical temperature.

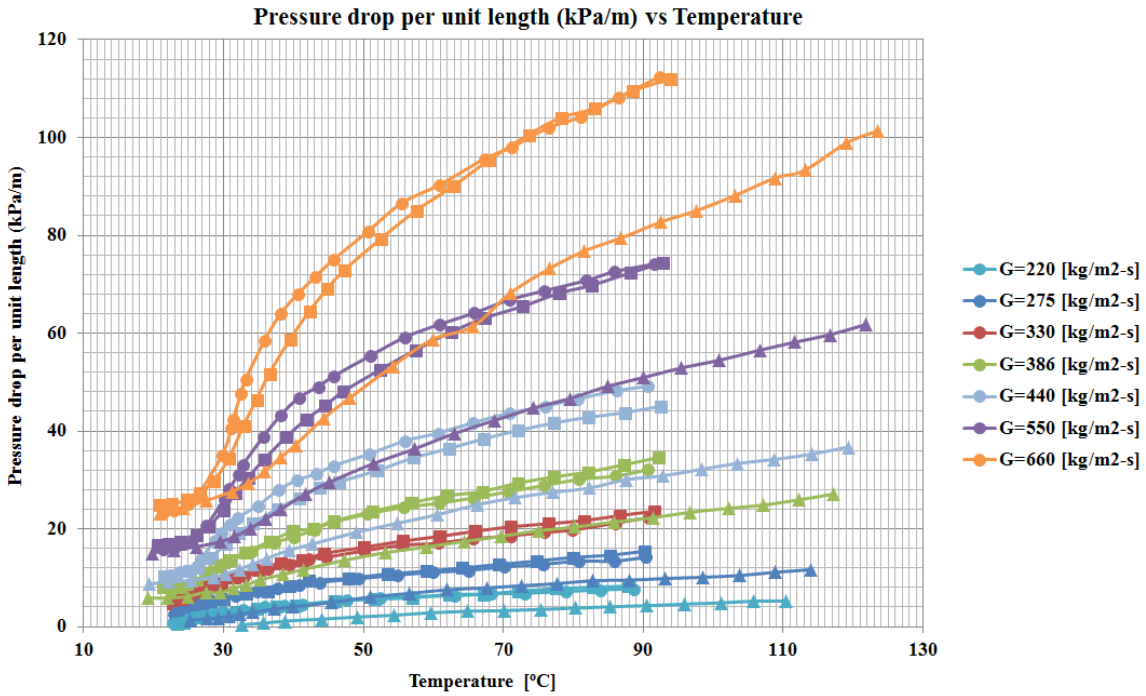

Figure 24: Calculated frictional pressure drop per unit length of offset rectangular fin heat exchanger as a function of average temperature. The circular, square, and triangular symbols represent data for system pressures of 7.5, 8.1, 10.2 MPa respectively.

Based on the variation in thermophysical properties, the supercritical heat transfer and pressure drop data can be divided into three regimes, liquid-like, pseudo-critical transition, and gas-like. These flow regime transition criteria are defined quantitatively based on the specific work of thermal expansion/contraction, E_o, by Kurganov *et al.* as follows:

$$E_o = P.\beta/(\rho C_p)$$

E_o is the ratio of the work done by the fluid during cooling to the heat convected out of it during the flow. Figure 25 shows the plot of E_o with respect to temperature and enthalpy for carbon dioxide for three different operating pressures (same as the collected data) in the critical region. The plot of E_o versus enthalpy shows a gradual increase to a point where $E_o = 0.05$, followed by an abrupt change in the slope until $E_o \sim 0.23 - 0.24$ where the curve reaches a maximum and then decrease with further increase in enthalpy. Based on this, three regimes are defined: (a) a liquid-like (low temperature) regime where the change in E_o with temperature/enthalpy is gradual mostly due to small property variation; For each pressure, temperature where the abrupt change in slope of E_o v/s T occurs is determined. (b) Pseudo-critical transition regime where the change in E_o is rapid with temperature; and (c) the gas-like regime where the E_o starts to decline as temperature increases. The transition from the pseudo-critical transition regime to the gas like were found when $dE_o/dT = 0$. Table 1 shows the corresponding temperature ranges for three different flow regimes described above. The goal is to group all the data sets available for the rectangular offset and airfoil fin heat exchangers based on the flow regime transition criteria described in Table 12. Pressure drop and heat transfer models will be developed for each regime separately.

Table 12: Boundaries determined for the three flow regimes

Pressure [MPa]	Liquid-like regime	Pseudo-critical transition regime	Gas-like regime
7.5	$T < 26.46^oC$	$26.46^oC \leq T \leq 58.79^oC$	$T > 58.79^oC$
8.1	$T < 27.25^oC$	$27.25^oC \leq T \leq 65.76^oC$	$T > 65.76^oC$
10.2	$T < 28.82^oC$	$28.82^oC \leq T \leq 88.44^oC$	$T > 88.44^oC$

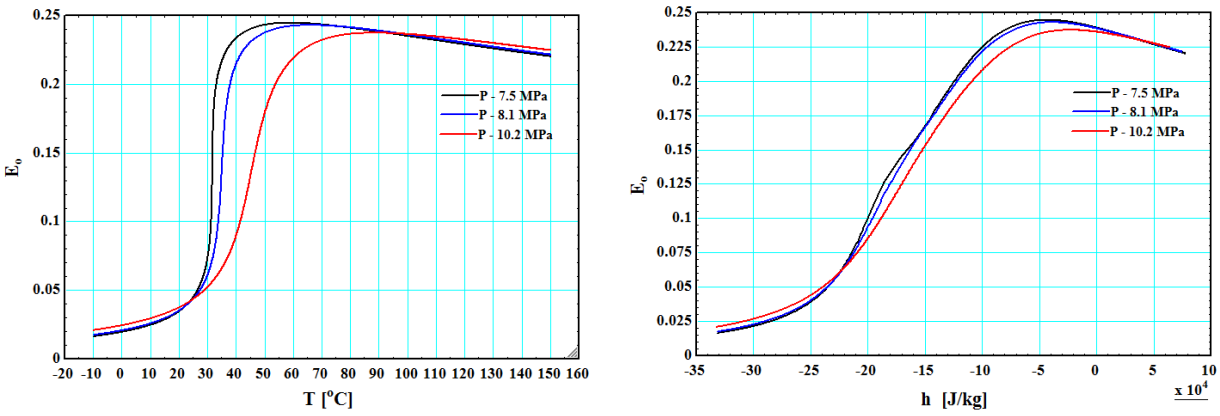

Figure 25: Plot of E_o versus temperature and enthalpy for carbon dioxide in the critical region.

References

[1] Moisseytsev, Anton, and James J. Sienicki. "Investigation of alternative layouts for the supercritical carbon dioxide Brayton cycle for a sodium-cooled fast reactor." *Nuclear Engineering and Design* 239, no. 7 (2009): 1362-1371.

[2] Dostal, Vaclav, Michael J. Driscoll, and Pavel Hejzlar. "A supercritical carbon dioxide cycle for next generation nuclear reactors." PhD diss., Massachusetts Institute of Technology, Department of Nuclear Engineering, 2004.

[3] Hesselgreaves, John E., Richard Law, and David Reay. *Compact heat exchangers: selection, design and operation*. Butterworth-Heinemann, 2016.

[4] Taylor, Mike A. *Plate-Fin Heat Exchangers: Guide to Their Specification and Use*. Heat Transfer and Fluid Flow Services, 1987.

[5] Dewson, S. J., and C. Grady. "Heatric™ Workshop at MIT." *Cambridge, MA, Oct* 2 (2003).

[6] Southall, David, and Stephen John Dewson. "Innovative compact heat exchangers." *Group* 226, no. 212.6 (2010): 583-0.

[7] Black, J. Temple, and Ronald A. Kohser. *DeGarmo's materials and processes in manufacturing*. John Wiley & Sons, 2017.

[8] Allen, David M. "Photochemical machining: from 'manufacturing's best kept secret' to a $6 billion per annum, rapid manufacturing process." *CIRP Annals-Manufacturing Technology* 53, no. 2 (2004): 559-572.

[9] Ishizuka, Takao. "Thermal-Hydraulic Characteristics of a Printed Circuit Heat Exchanger in a Supercritical CO_2 Loop." In *The 11th International Topical Meeting on Nuclear Reactor Thermal-Hydraulics, 2005*. 2005.

[10] Nikitin, Konstantin, Yasuyoshi Kato, and Lam Ngo. "Printed circuit heat exchanger thermal–hydraulic performance in supercritical CO 2 experimental loop." *International Journal of Refrigeration* 29, no. 5 (2006): 807-814.

[11] Tsuzuki, Nobuyoshi, Yasuyoshi Kato, and Takao Ishiduka. "High performance printed circuit heat exchanger." *Applied Thermal Engineering* 27, no. 10 (2007): 1702-1707.

[12] Yasuyoshi Kato. "How New Microchannel Heat Exchanger Reduced Pressure Drop to 1/6 Inheriting High Heat Transfer Performance." Supercritical CO_2 Power Cycle Symposium (2011)

[13] Ngo, Tri Lam, Yasuyoshi Kato, Konstantin Nikitin, and Nobuyoshi Tsuzuki. "New printed circuit heat exchanger with S-shaped fins for hot water supplier." *Experimental Thermal and Fluid Science* 30, no. 8 (2006): 811-819.

[14] Nikitin, Konstantin, Yasuyoshi Kato, and Takao Ishizuka. "Experimental thermal-hydraulics comparison of microchannel heat exchangers with zigzag channels and S-shaped fins for gas turbine reactors." (2007).

[15] Ngo, Tri Lam, Yasuyoshi Kato, Konstantin Nikitin, and Takao Ishizuka. "Heat transfer and pressure drop correlations of microchannel heat exchangers with S-shaped and zigzag fins for carbon dioxide cycles." *Experimental Thermal and Fluid Science* 32, no. 2 (2007): 560-570.

[16] Moisseytsev, A., J. J. Sienicki, D. H. Cho, and M. R. Thomasa. "Comparison of heat exchanger modeling with data from CO_2-to-CO_2 printed circuit heat exchanger performance tests." In *Proceedings of the 2010 International Congress on Advances in Nuclear Power Plants-ICAPP'10*. 2010.

[17] Southall, David, Renaud Le Pierres, and Stephen John Dewson. "Design considerations for compact heat exchangers." In *Proceedings of ICAPP*, vol. 8, pp. 8-12. 2008.

[18] Kim, In Hun, Hee Cheon No, Jeong Ik Lee, and Byong Guk Jeon. "Thermal hydraulic performance analysis of the printed circuit heat exchanger using a helium test facility and CFD simulations." *Nuclear Engineering and Design* 239, no. 11 (2009): 2399-2408.

[19] Kim, In Hun, and Hee Cheon No. "Thermal hydraulic performance analysis of a printed circuit heat exchanger using a helium–water test loop and numerical simulations." *Applied Thermal Engineering* 31, no. 17 (2011): 4064-4073.

[20] Kim, In Hun, and Hee Cheon No. "Thermal–hydraulic physical models for a Printed Circuit Heat Exchanger covering Helium, He–CO_2 mixture, and water fluids using experimental data and CFD." *Experimental Thermal and Fluid Science* 48 (2013): 213-221.

[21] Mylavarapu, Sai K. *Design, fabrication, performance testing, and modeling of diffusion bonded compact heat exchangers in a high-temperature helium test facility*. The Ohio State University, 2011.

[22] Kruizenga, Alan Michael. *Heat transfer and pressure drop measurements in prototypic heat exchanges for the supercritical carbon dioxide Brayton power cycles*. 2010.

[23] Carlson, Matthew D. "Measurement and Analysis of the Thermal Hydraulic Performance of Several Printed Circuit Heat Exchanger Channel Geometries." PhD diss., University of Wisconsin--Madison, 2012.

[24] Kim, Dong Eok, Moo Hwan Kim, Jae Eun Cha, and Seong O. Kim. "Numerical investigation on thermal–hydraulic performance of new printed circuit heat exchanger model." *Nuclear Engineering and Design* 238, no. 12 (2008): 3269-3276.

[25] Seo, Jang-Won, Yoon-Ho Kim, Dongseon Kim, Young-Don Choi, and Kyu-Jung Lee. "Heat transfer and pressure drop characteristics in straight microchannel of printed circuit heat exchangers." *Entropy* 17, no. 5 (2015): 3438-3457.

[26] Shah, R. K., and R. L. Webb. "Compact and enhanced heat exchangers." In *Heat exchangers—theory and practice. International center for heat and mass transfer. Symposium. 14*, pp. 425-468. 1983.

[27] Kays, William Morrow, and Alexander Louis London. "Compact heat exchangers." (1984).

[28] Wieting, Allan R. "Empirical correlations for heat transfer and flow friction characteristics of rectangular offset-fin plate-fin heat exchangers." *Journal of Heat transfer* 97, no. 3 (1975): 488-490.

[29] Joshi, Himanshu M., and Ralph L. Webb. "Heat transfer and friction in the offset strip fin heat exchanger." *International Journal of Heat and Mass Transfer* 30, no. 1 (1987): 69-84.

[30] Mochizuki, S., and Y. Yagi. "Heat transfer and friction characteristics of strip fins." *Heat Transfer-Jpn. Res* 6, no. 3 (1977): 36-59.

[31] Manglik, Raj M., and Arthur E. Bergles. "Heat transfer and pressure drop correlations for the rectangular offset strip fin compact heat exchanger." *Experimental Thermal and Fluid Science* 10, no. 2 (1995): 171-180.

[32] Hu, Sen, and Keith E. Herold. "Prandtl number effect on offset fin heat exchanger performance: experimental results." *International journal of heat and mass transfer* 38, no. 6 (1995): 1053-1061.

[33] Hu, Sen, and Keith E. Herold. "Prandtl number effect on offset fin heat exchanger performance: predictive model for heat transfer and pressure drop." *International Journal of Heat and Mass Transfer* 38, no. 6 (1995): 1043-1051.

[34] Dong, Junqi, Jiangping Chen, Zhijiu Chen, and Yimin Zhou. "Air-side thermal hydraulic performance of offset strip fin aluminum heat exchangers." *Applied Thermal Engineering* 27, no. 2 (2007): 306-313.

[35] Kim, Min-Soo, Jonghyeok Lee, Se-Jin Yook, and Kwan-Soo Lee. "Correlations and optimization of a heat exchanger with offset-strip fins." *International Journal of Heat and Mass Transfer* 54, no. 9 (2011): 2073-2079.

[36] Pidaparti, Sandeep R., Jacob A. McFarland, Mark M. Mikhaeil, Mark H. Anderson, and Devesh Ranjan. "Investigation of Buoyancy Effects on Heat Transfer Characteristics of Supercritical Carbon Dioxide in Heating Mode." *Journal of Nuclear Engineering and Radiation Science* 1, no. 3 (2015): 031001.

[37] Lemmon, Eric W., Marcia L. Huber, and Mark O. McLinden. "NIST reference fluid thermodynamic and transport properties–REFPROP." (2002).

[38] Idelchik, Isaak E., and Erwin Fried. "Handbook of hydraulic resistance" (1986).

Chapter 2 Study of nucleation behavior of CO_2 near the critical point

Abstract

Pressure reduction at the entrance of the compressor in supercritical CO_2 (sCO_2) Brayton cycles may cause nucleation and create a mixture of vapor and liquid droplets due to operation near the saturation conditions. Transient behavior of the flow after nucleation may cause serious issues in operation of the cycle and degrade the materials used in the design. The goal of the current project is to investigate the nucleation behavior of supercritical carbon dioxide inside a venturi nozzle near the critical point and study the impact of two-phase flow on the erosion of materials. A venturi system with optical access has been designed and fabricated to investigate the nucleation behavior and to conduct sample erosion tests. To complement experiments, a transient compressible 3D Navier-Stokes solver, coupled with continuity, and energy equations have been used to perform computational studies [1]. In order to expedite the simulations, Fluid property Interpolation Tables (FIT) based on a piecewise biquintic spline interpolation of Helmholtz energy have been integrated with OpenFOAM to model sCO_2 properties. The mass fraction of vapor created in the venturi nozzle has been calculated using homogeneous equilibrium model (HEM). Nucleation behavior has been shown to be very sensitive to the inlet pressure, inlet temperature, and flow rate. The flow conditions that led to nucleation were identified. Nucleation was observed in the throat area and divergent section of the nozzle for mass flow rates from 0.050 Kg/s to 0.065 kg/s, inlet pressure from 7.8 to 7.4 MPa for fixed exit pressure equal to 7.28 MPa. The inception of high-vapor-content nucleation was first observed in the throat area away from the side walls that remained confined to the throat region in later times. However, near the walls, a high liquid-content two-phase region was detected, first in the divergent section. At later times, the two-phase region was convected downstream toward the nozzle exit. Nucleation in central plane was associated with larger pressure drop and higher vapor-content (higher volume fraction); whereas lower pressure drop and more liquid-content (lower volume fraction) was observed near the walls. Preliminary high speed shadowgraph videos of the flow through the venturi nozzle were recorded for inlet conditions near the critical point. The shadowgraph videos agree qualitatively with the numerical studies and more work is expected to be continued after the end of this project. In addition, short term erosion tests were conducted on the material samples and no noticeable weight changes were measured.

Introduction

Supercritical carbon dioxide (sCO_2) Brayton cycles offer a number of benefits over competing steam Rankine cycles, namely reducing the size of turbomachinery, increased efficiency, reduction of greenhouse gases, and reduced capital cost [2]. The augmented heat transfers and low specific volume of sCO_2 cycles make them a good candidate to replace traditional steam Rankine cycles in future [3, 4]. As the specific volume decreases near the critical point (7.38 MPa, 31°C), the compressor work decreases and thermal efficiency increases. So, the size of the heat exchangers and turbomachinery substantially reduces compared to water or helium Brayton cycles [5, 6]. Despite the recent progress, more research is required to advance the commercialization of sCO_2 power cycles [6]. Power cycles for variety of heat sources, e.g. nuclear, in sodium fast Reactor (SFR) and fluoride high temperature reactor (FHR), solar energy, and fossil fired power plants [7] can benefit from sCO_2 as a working fluid.

There is a pressing need to understand the transition of the working fluid sCO_2 near the critical point. Resolution of issues with cavitation and fluid instabilities operating near and in the two-phase region is of great importance. It is expected that at some degree of pressure reduction where the pressure and temperature are within the vapor dome, nucleation, i.e. either cavitation or condensation or both occur. In rotating machinery this can take place at the end of the turbine blades and at the entrance to the compressor causing loss of power and instability in compressor performance [8]. This is of serious concern with respect to operation and the materials used in designing these systems. Materials erosion, primarily at high temperatures, is an important issue particularly because the expected life times of these components have to be 20 years or more.

The sensitivity of the nucleation behavior to the compressor inlet conditions near the critical point has been demonstrated in Figure 1. We developed a one-dimensional isentropic flow model for a nozzle with inlet to throat area equal to 17 to understand the behavior of the flow by inspecting the phase-change diagram. In this model, by assuming choked flow conditions in the throat region, the inlet pressure has been fixed at 7.40 MPa and the inlet temperature varies from supercritical to subcritical conditions. Red symbols in Figure 1(a) represent the CO_2 stagnation conditions at the venturi nozzle inlet. The blue symbols along the constant entropy line below each red symbol show the corresponding choked flow conditions at the throat. It can be deduced from the *T-s* diagram shown in Figure 1(a) that the nucleation process is extremely sensitive to the inlet stagnation conditions. To the right side of the critical point and approaching the saturated vapor line, i.e. the metastable region, all the inlet stagnation conditions lead to a two-phase mixture with higher vapor volume fraction, i.e. smaller volume fractions of condensate droplets at the throat. The opposite behavior is expected approaching the saturated liquid line from the critical conditions toward subcritical inlet temperatures, i.e. to the left of the critical point. Near the critical pressure, a small variation in inlet temperature compared to the critical temperature may alter the nucleation behavior from condensation to cavitation as evident from the *T-s* and *P-v* diagrams.

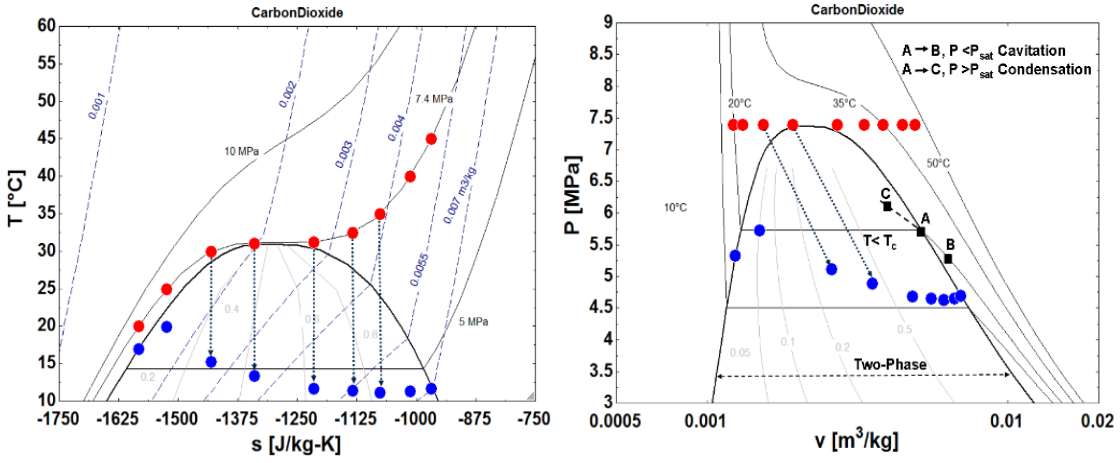

(a) (b)

Figure 1: Predictions of *1D* isentropic model; entering the two-phase region with inlet conditions fixed at 7.40 MPa and subcritical and supercritical temperature on (a) *T-s*, (b) *P-v* diagrams. (The red and blue symbols show the inlet and throat conditions, respectively.)

The nucleation behavior can be assessed by comparing the local pressure to the saturation pressure at the local temperature. This situation has been demonstrated in Figure 1(b), where *A* is located on the saturation vapor line and points *B* and *C* are on the same isotherm. In case the pressure drops below the saturation pressure at the local temperature, i.e. moving from point *A* to *B*, cavitation is expected. On the same isotherm line, by moving from *A* to *C*, the pressure exceeds the saturation pressure and condensation is expected. Distinguishing between these two limits of nucleation and its sensitivity to the inlet conditions near the critical point is significant in designing compressors for supercritical conditions. Cavitation phenomenon is expected to be more detrimental in degrading the compressor blades since the cavitation bubbles burst in a very short time scales near the surface whereas condensation may cause instability in the compressor and energy loss rather than serious erosion. Further experiments are required to identify the effects of cavitation/ condensation on compressors.

It is well documented that the numerical simulations near the critical point can be challenging [8, 9]. Sharp variation of thermodynamic properties near the critical point and their strong deviation from the ideal gas law affects the stability of the numerical simulations/ schemes and highlights the significance of using real gas properties in simulations. The numerical study of sCO_2 flow in the main axial compressor in the neighborhood of the critical point by Takagi [9] demonstrated that the solution did not converge for a few stages of the compressor using real gas properties. Thus, they used modified ideal gas properties to obtain convergence in all stages of the compressor. Therefore, there is a substantial need in performing stable numerical simulations with real gas thermodynamic properties near the critical point and in the two-phase regions. There is lack of knowledge in predicting the transient phase change behavior of sCO_2 near the critical point.

Nucleation of sCO_2 in supersonic flows in converging-diverging nozzles has been experimentally studied by measuring the static pressure drops within the nozzle for the ejectors used in transcritical CO_2 refrigeration cycles [10]. In an ejector, the converging-diverging nozzle gets choked and the pressure of the fluid converts into momentum to energize lower-momentum suction flow. The nucleation process in these nozzles may cause shock and expansion waves since the local speed of sound will change when sCO_2 enters the two-phase region. Computational studies based on real-fluid properties of CO_2 and local mass and energy transfer between phases have been performed and validated against experiments away from the critical point [11]. However, there are very few experimental and numerical studies of subsonic sCO_2 in the converging diverging nozzle near the critical point applicable to the compressor inlet conditions in sCO_2 Brayton cycles. Numerical simulations and experiments of sCO_2 flow in a converging diverging nozzle performed by Lettieri [12] indicated the significance of two-phase effects on the turbomachinery design. A non-dimensional criterion, i.e. the ratio of the nucleation time to residence time was defined to determine the inception of nucleation. Nucleation time is the time required for stable liquid droplets to form which depends on the rate of the expansion of the flow whereas the residence time represents the local flow time scale under saturated conditions. In a recent numerical study, this criterion was applied to the candidate centrifugal S-CO_2 compressor [12, 13]. They predicted that condensation was unlikely in the radial compressors away from the critical point in the sCO_2 power cycles since the nucleation time was much longer than the flow residence time. However, very close to the critical point, the residence time increased and transition from single-phase to two-phase

became more probable. In this study, the nucleation process of sCO_2 in the immediate vicinity of the critical point has been investigated by solving transient 3D Navier-Stokes and energy equations by implementing the real properties of sCO_2 into the computational code. The proposed framework of the nucleation process of sCO_2 in the nozzle serves as a foundation for the definition of the impact of two-phase flows in turbomachinery operating in the vicinity of the critical point. The computational results provide useful information for designing experimental set-up with optical access, which will be described in the later sections of this chapter. For flow visualization, the density gradients on the nozzle walls play a significant role in capturing the flow physics. Therefore, detecting the condensing and cavitation regions inside the nozzle and on the walls via simulations is very helpful to design appropriate optical diagnostics to observe and quantify the number density of the droplets and bubbles in the two-phase regions.

Computational Model & Governing Equations

The flow of sCO_2 in a converging-diverging nozzle with inlet temperature and pressure close to the critical point has been studied. The nozzle has been designed to provide the required pressure drop to initiate the phase change process in the throat area. A schematic of the converging-diverging nozzle used in these simulations has been shown in Figure 2.

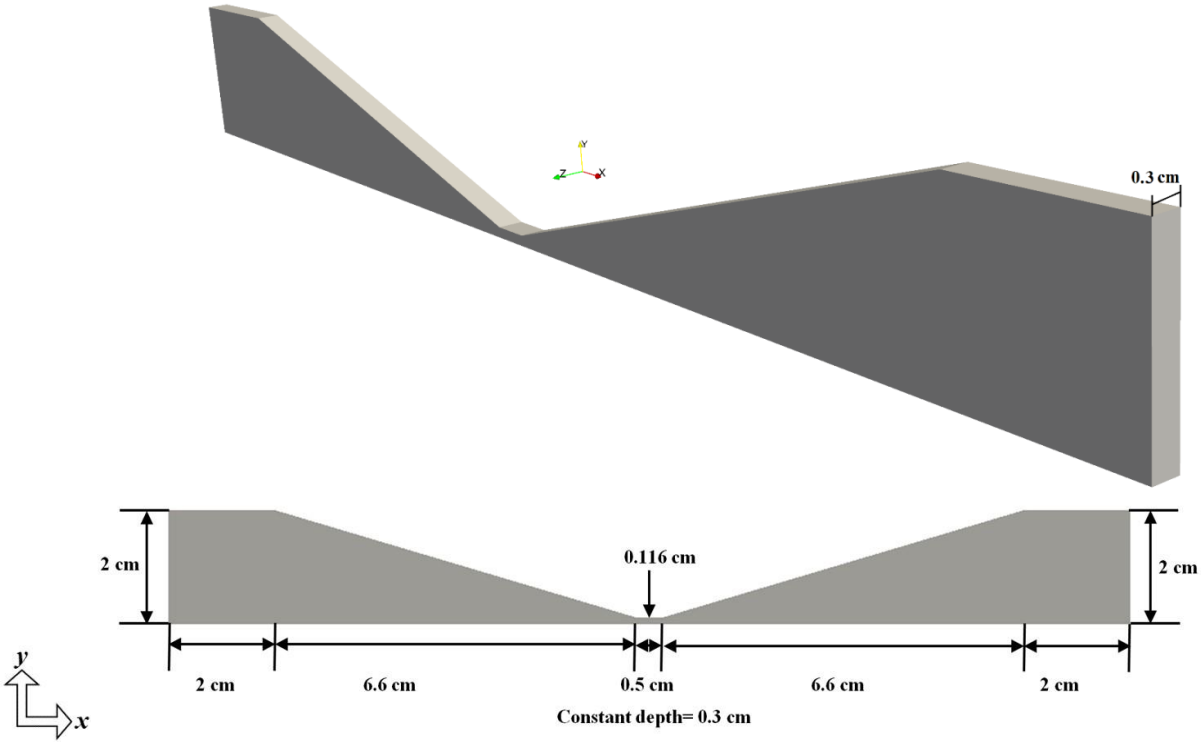

Figure 2: Schematic of the converging-diverging nozzle with rectangular profile with constant depth of 3 mm.

The nozzle has a rectangular *3D* profile with a 3 mm constant depth in the *z* direction perpendicular to the paper. The observations from the phase change process due to local pressure changes as a result of acceleration or deceleration of the flow when surface area

changes within the nozzle have been presented. Based on homogenous mixture assumption, the two phases are considered as one combined mixture of liquid/ vapor in these simulations. The properties of the mixture, i.e. mixture pressure, mixture velocity, saturation temperature at the mixture pressure, and volume fraction have been found from the conservation of mass, momentum, energy, and equation of state.

The density and energy of each discrete phase have been obtained from the equation of state and the mixture density as: $\rho_m = VF\rho_g + (1-VF)\rho_l$ and $e_m = VF\rho_g e_g + (1-VF)\rho_l e_l$, where ρ_m, e_m, and *VF* are the mixture density, mixture energy, and volume fraction and subscripts *l* and *g* refer to liquid and gas phases, respectively. The mass fraction of liquid and vapor created due to nucleation are sought. By interpreting the mixture quantities, the same set of compressible Navier-Stokes and energy equations as for a single-phase flow have been solved. Thus, the velocity has been obtained from a single momentum equation for the mixture. Continuity equation has been solved for each phase to calculate the volume fraction. A closure to these equations is provided by modeling the properties of CO_2. FIT (Fluid property Interpolation Tables), an algorithm which utilizes a modified version of biquintic spline interpolation of Helmholtz free energy and all of its derivatives, have been implemented in OpenFOAM [14] to accurately model the properties of CO_2 required to solve the governing equations near the critical point. The underlying property data of FIT is obtained from REFPROP (Software for fluid properties developed by NIST). However, FIT generates fluid properties much faster than REFPROP within acceptable errors as realized from our previous NEUP project [15].

The governing equations are as follows:

Conservation of mass:
$$\frac{\partial \rho_m}{\partial t} + \frac{\partial}{\partial x_j}(\rho_m u_{m_j}) = 0 \quad (1)$$

Conservation of momentum:
$$\frac{\partial \rho_m u_{m_i}}{\partial t} + \frac{\partial}{\partial x_j}[\rho_m u_{m_i} u_{m_j} + P\delta_{ij} - \tau_{ij}] = 0 \quad (2)$$

Conservation of Energy:
$$\frac{\partial \rho_m e_{0m}}{\partial t} + \frac{\partial}{\partial x_j}[\rho_m e_{0m} u_{m_j} + u_{m_j} P + q_j - u_{m_j}\tau_{ij}] = 0 \quad (3)$$

Where u_m, p, τ_{ij}, δ_{ij}, e_{0m}, and q are mixture velocity, pressure, viscous stress, kronecker delta, total mixture, total mixture energy, and heat flux, respectively and $e_{0m} = e_m + \frac{u_{mi}u_{mi}}{2}$. The standard *k-ε* turbulence model with enhanced wall treatment has been chosen. Transport equations for standard *k-ε* model are as follows:

$$\frac{\partial \rho_m k}{\partial t} + \frac{\partial}{\partial x_j}(\rho_m k u_{mj}) = \frac{\partial}{\partial x_j}\left[(\mu + \frac{\mu_t}{\sigma_k})\frac{\partial k}{\partial x_j}\right] + P_k + P_b - \rho\varepsilon - Y_M + S_k \quad (4)$$

$$\frac{\partial \rho_m \varepsilon}{\partial t} + \frac{\partial}{\partial x_j}(\rho_m \varepsilon u_{m\,j}) = \frac{\partial}{\partial x_j}\left[(\mu + \frac{\mu_t}{\sigma_\varepsilon})\frac{\partial \varepsilon}{\partial x_j}\right] + \frac{C_{1\varepsilon}\varepsilon}{k}(P_k + C_{3\varepsilon}P_b) - \frac{C_{2\varepsilon}\rho\varepsilon^2}{k} + S_\varepsilon \qquad (5)$$

Where μ_t is turbulent viscosity and S_k, S_ε are source terms. σ_k, σ_ε, C_μ, $C_{1\varepsilon}$, $C_{2\varepsilon}$, and $C_{3\varepsilon}$ are model constants. P_k and P_ε are production of kinetic energy and buoyancy term, respectively. Y_M is the contribution of the fluctuating dilation in compressible turbulence to the overall dissipation rate. Based on the equilibrium assumption, an equilibrium speed of sound has been defined to calculate the Mach number for both the single-phase and two-phase regions within the flow. The current simulation code has been validated against experimental data for studying the sCO_2 flow in see-through labyrinth seals [15, 16]. As sCO_2 flows through a labyrinth seal, two-phase behavior is expected similar to the situation in the converging-diverging nozzle. The numerical model predicted the experimental results obtained for labyrinth seals very closely for various tested designs and conditions [15, 16].

Typically, in subsonic compressible flow simulations, exit pressure and inlet mass flow rate are fixed. The inlet pressure is calculated based on these conditions assuming zero gradient conditions for pressure at the inlet. Same boundary conditions have been applied here. For velocity boundary conditions, zero gradient at the outlet and no-slip boundary conditions on all the walls have been applied. Finally, zero-gradient boundary conditions for temperature have been applied at both inlet and outlet. Isentropic *1D* model for the nozzle dimensions shown in Figure 2, has been used to predict the mass flow rate and exit pressure required for transition from single-phase to two-phase at the throat while the inlet condition is at supercritical pressure and supercritical temperature very close to the critical point. The boundary conditions for the simulated cased have been outlined in Table 1. For higher mass flow rate simulations, the exit pressure is fixed that allows for higher inlet pressure and higher velocity compared to lower mass flow rates. The grid independency tests were performed for medium, coarse, and fine mesh corresponding to 5.28e3, 2.64e3, and 1.05e6 cells, respectively. The maximum percent error in velocity and pressure within the nozzle with respect to the medium mesh was equal to 0.9% and 3% for the coarse and fine mesh, respectively. So, the medium mesh was chosen for the entire simulations here. The percent error in predicating the volume fraction and quality with respect to the medium mesh was less than 0.02% for both the coarse and fine meshes. The size of the cells near the walls satisfied the requirement of dimensionless wall distance y^+~1.

Table 1: Inlet and outlet conditions used in simulations.

Mass Flow rate (kg/s)	Inlet Pressure (MPa)	Exit Pressure (MPa)	Inlet Velocity (m/s)	Inlet Temperature (K)
0.050	7.62	7.28	2.71	305.15
0.052	7.68	7.28	2.82	306.78
0.065	7.73	7.28	3.32	307.22

Homogenous Equilibrium Model

Homogeneous equilibrium model (HEM) has been used in this work to predict the flow behavior in the two-phase region. HEM model assumes that the velocities of both phases are equal and thermal equilibrium exists between phases. Neglecting the initial velocity, fluid velocity at any section is simply determined based on an energy balance. In this model, the mass, momentum, and energy is transferred between phases fast enough that equilibrium is reached. HEM is valid when the two phases are sufficiently well mixed; disperse particle sizes are sufficiently small to eliminate any significant relative motion between the two phases. The HEM model is valid if the gas-to-liquid velocity ratio is close to one. It should be noted that physically, there is no discontinuity between the two phases since there is a boundary layer for each phase on either side of the interface. Thus, velocity ratio is an indicator of the relative motion between the two phases. Numerous analytical and empirical correlations exist for the velocity ratio [17]. The simplest definitions in the literature have been defined as Zivi's kinetic energy model for annular flow: $S = \frac{u_g}{u_l} = \left(\frac{\rho_l}{\rho_g}\right)^{\frac{1}{3}}$ [18] and $S = \frac{u_g}{u_l} = \left(\frac{\rho_l}{\rho_g}\right)^{\frac{1}{2}}$ [19], where the former minimizes the specific two-phase mixture kinetic energy and the latter minimizes the specific two-phase momentum based on the momentum flux model. The volume fraction can be defined as:

$$VF = \frac{1}{1+\left(\frac{1-x'}{x'}\right)\frac{\rho_g}{\rho_l}\cdot S} \tag{6}$$

Where x' is the quality; for homogenous equilibrium model, the velocity ratio S is set to one. The density difference between liquid and gas phases in CO_2 near its critical pressure is much smaller than that of the water for the same range of pressure, e.g. the liquid-to-gas density ratio for CO_2 varies between 2 and 3.5 as the pressure varies from 7 to 6 MPa, i.e. the lowest observed pressure in the current simulations. Therefore, the velocity ratio based on Zivi's model for this condition varies between 1.25-1.51. So, the HEM model is most likely valid for the existing problem and the slip velocity between the two phases will not affect the predictions. However, further validation with experimental results is required to investigate the non-equilibrium behavior of nucleation near the critical point.

Computational results and discussion

The converging-diverging nozzle in this study has been designed so that the pressure drops below critical pressure at the end of the converging section by fixing the exit pressure at P= 7.28 MPa that is well below the critical pressure (see Figures 7-9). In this study, the volume fraction (*VF*) has been defined based on Equation 6. *VF* equal to one represents single-phase supercritical fluid if the local pressure is higher than the critical pressure at that local temperature that occurs upstream of the throat region. If the local pressure is less than the critical pressure at that local temperature, *VF*= 1 corresponds to saturated vapor. This situation is expected downstream of the throat and in the diverging section of the nozzle. *VF* less than one corresponds to the existence of a two-phase fluid. *VF* approaching zero means that the two-

phase mixture contains more liquid than vapor, i.e. condensation prevails. *VF* close to one implies more vapor than liquid exists in the mixture, i.e. cavitation dominates.

Figure 3 and 4 show the transient behavior of nucleation in *xy*-2D plane at two different planes in the *z*-direction, i.e. near the wall, at z = -1.5 mm and at the central plane at z = 0, respectively. The contours of *VF* indicate that cavitation initiates in the divergent section first with a higher content of vapor, i.e. *VF* = 0.998 at z = -1.5 mm. Then, the two-phase region extends upstream and more liquid forms due to condensation. However, the cavitation initiates in the throat area in the nozzle at the central plane, i.e. z = 0 as the black arrows show in Figure 4 at t = 1 ms. As Figure 3 indicates, at t = 1.6 ms, condensation occurs at the sharp corners in the throat area as well as the divergent section and *VF* approaches zero in those areas. However, the two-phase region remains confined to the throat area in the central plane as Figure 4 demonstrates. The nucleation in the central plane produces more vapor than liquid since *VF* is much larger than that of the near wall at all times. Thus, liquid droplets are expected to form near the walls and vapor tend to occupy the throat area in the central plane of the nozzle. This result is critical for designing experiments and choosing the appropriate optical diagnostics since the liquid droplets on the walls might impede the optical access to the throat area.

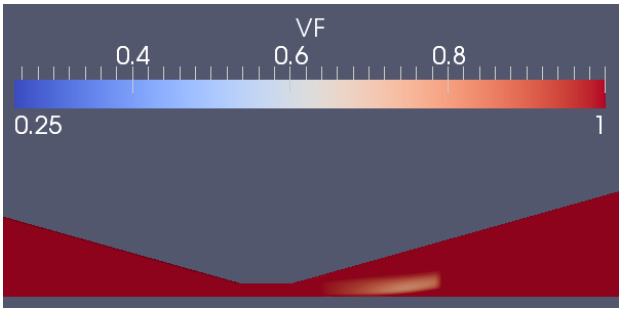

t =1.0 ms

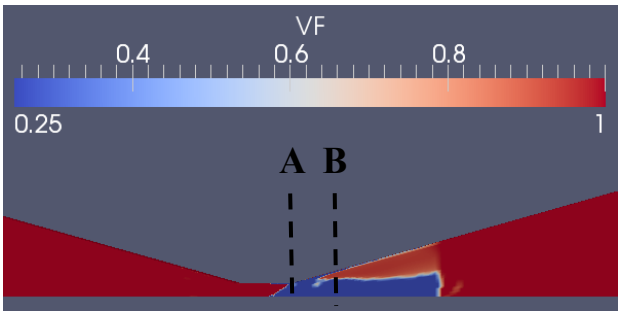

t =2.0 ms

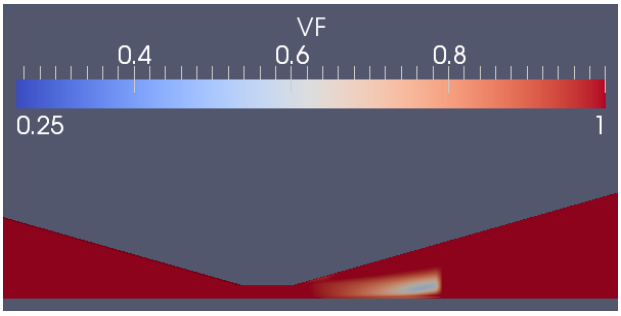

t =1.2 ms

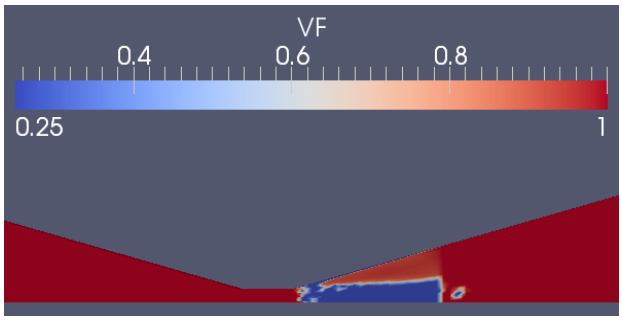

t =2.2 ms

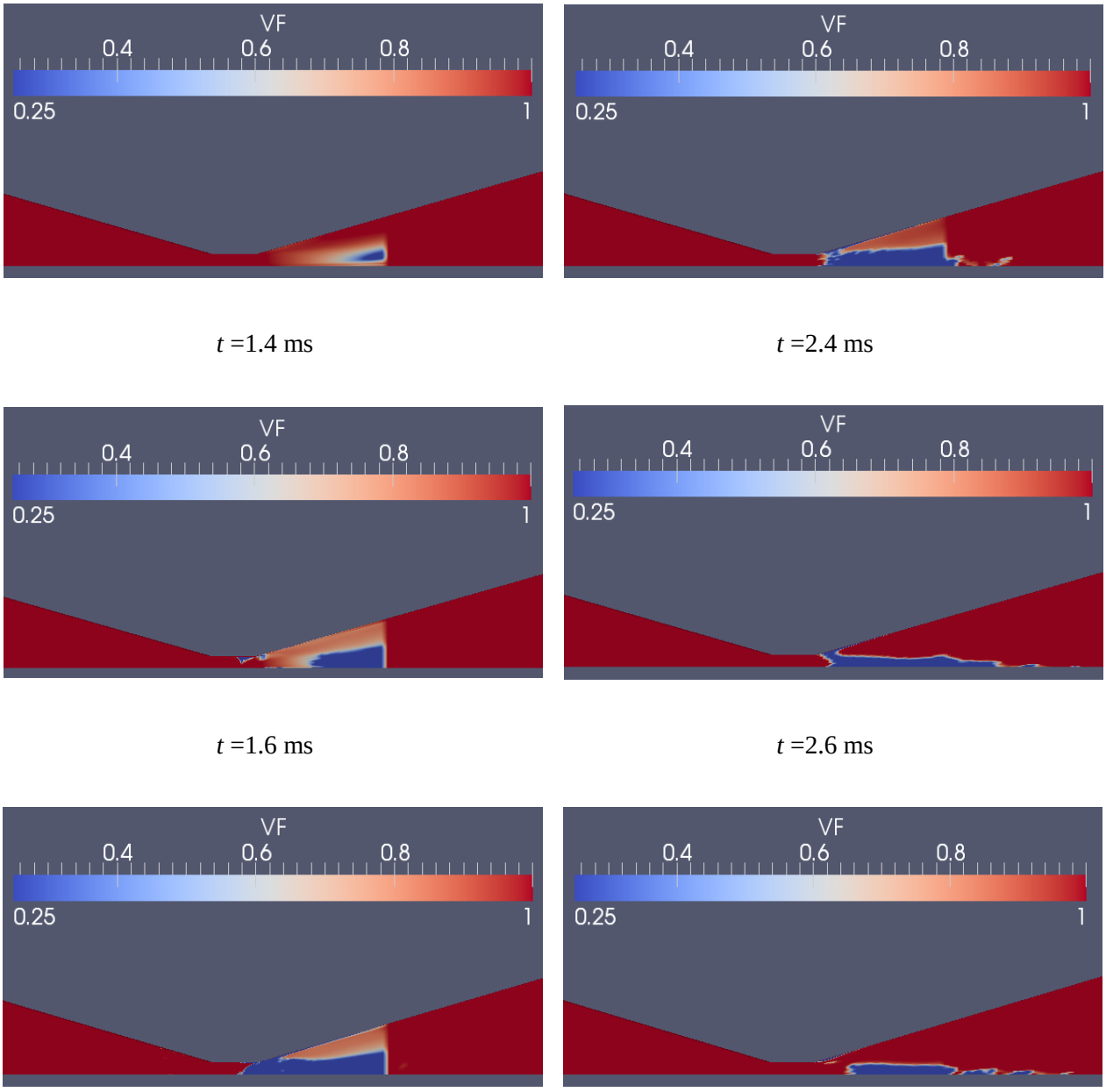

Figure 3: Contours of *VF* in the *xy* plane indicating the transient behavior of the nucleation of S-CO_2 in the nozzle near the wall (*z*= -1.5 mm) for $\dot{m}$ = 0.065 kg/s, (Flow is from left to right).

The comparison between the pressure drops in the central plane compared to that of near the wall versus the local saturation pressure is responsible for this change of behavior in the *z*-direction as will be discussed later in this section.

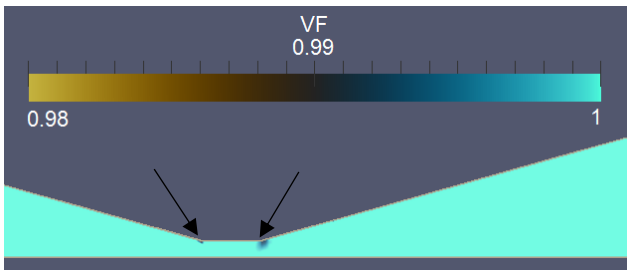

t =1.0 ms

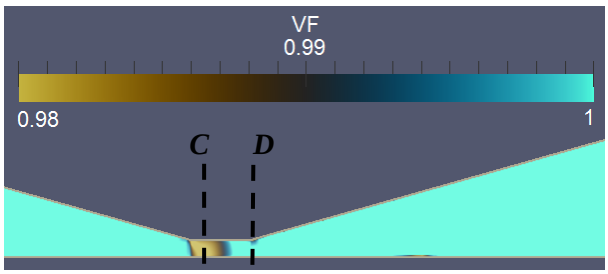

t =2.0 ms

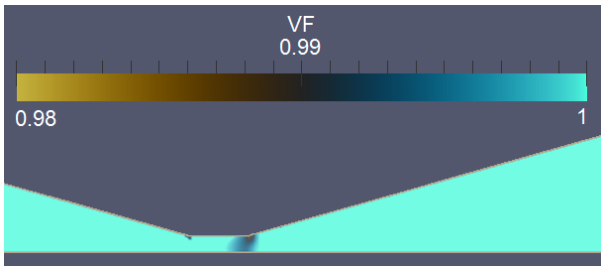

t =1.2 ms

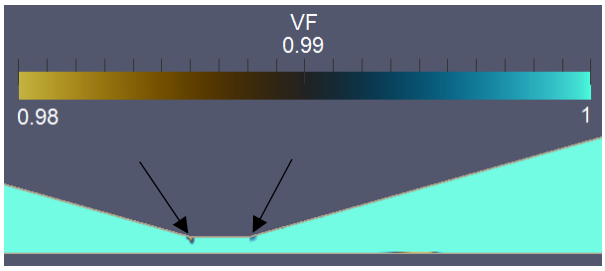

t =2.2 ms

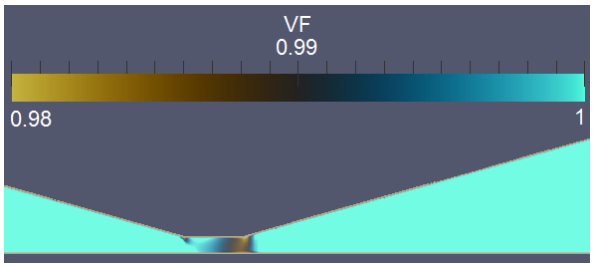

t =1.4 ms

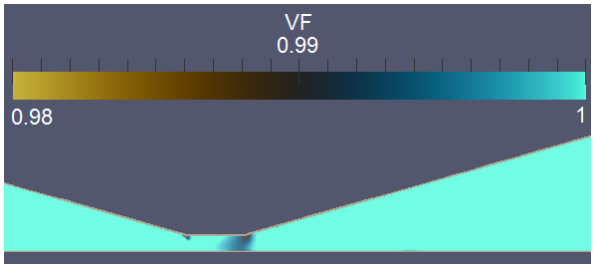

t =2.4 ms

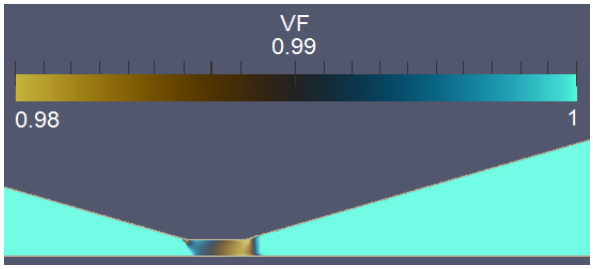

t =1.6 ms

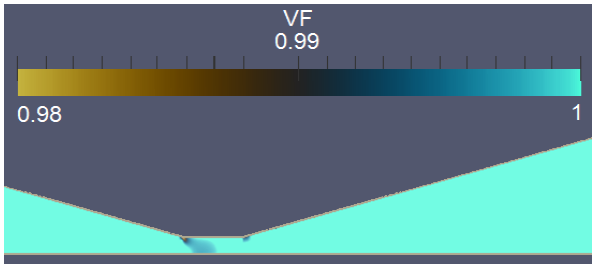

t =2.6 ms

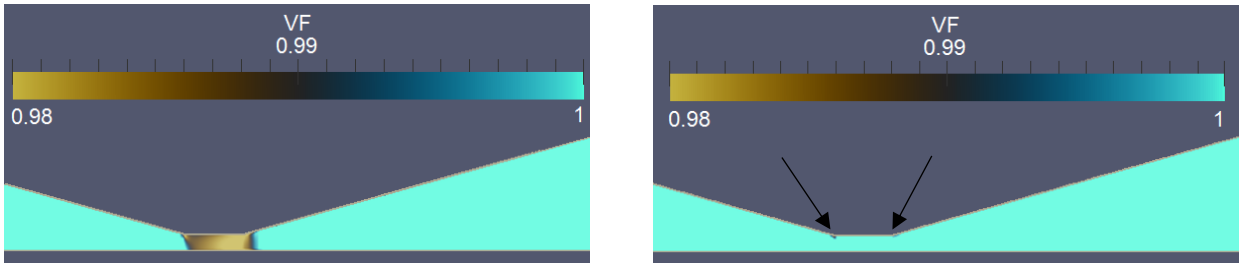

t =1.8 ms t =2.8 ms

Figure 4. Contours of VF in the *xy* plane indicating the transient behavior of the nucleation of S-CO2 in the central plane (z = 0 mm) for $\dot{m}$ = 0.065 kg/s. (Flow is from left to right.)

Figure 3 indicates that the two-phase region has been confined at nearly a constant distance downstream of the throat in the divergent section up to t = 2 ms after which the two-phase region moves downstream, mostly in the liquid form. At the same time, small liquid patches detach from the bulk liquid near the throat and move downstream of the throat. At t = 2.8 ms, a small two-phase region near the throat area with VF > 0.9 is observed and a stream of high liquid-content mixture i.e. VF= 0.25 travels downstream and exits the nozzle in later times (not shown here). This phenomenon can be very detrimental to the rotating parts of the compressor in actual Brayton cycles when higher liquid-content fluid moves with the swirling flow and the liquid droplets impinge on the solid parts of the cycle. Figure 4 shows that the nucleation in the throat area at z = 0 is more prominent at early times, i.e. t < 2 ms after which the high vapor-content two-phase region becomes very small and remains confined to the sharp corners of the throat area as the black arrows show. In conclusion, condensation is more critical than cavitation near the walls for S-CO_2 at near critical conditions.

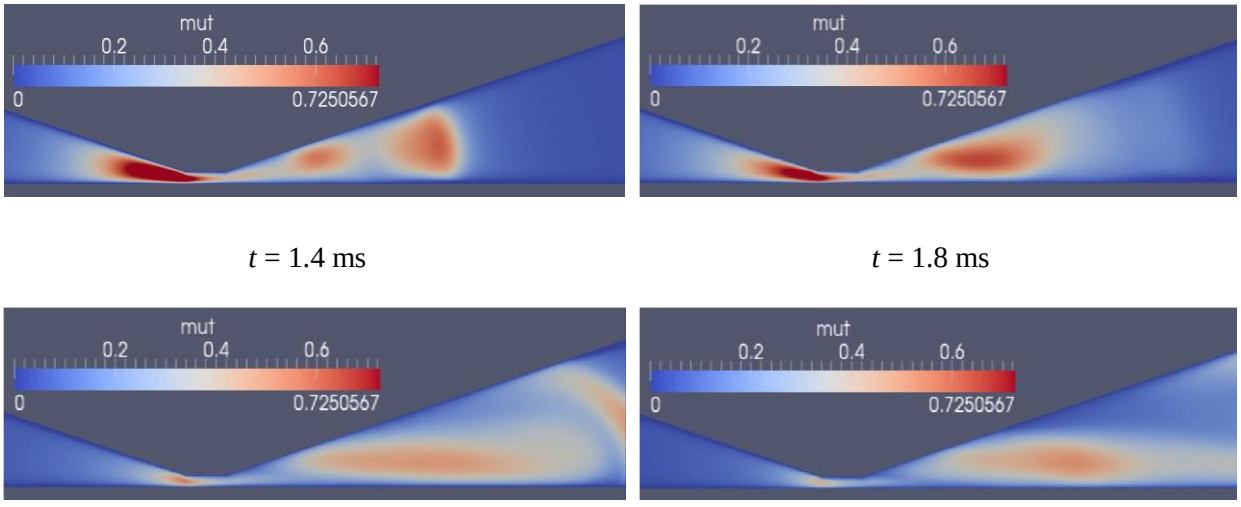

t = 1.4 ms t = 1.8 ms

t = 2.2 ms t = 2.8 ms

Figure 5: Contours of turbulent viscosity (kg/m.s) in the *xy* plane and z = 0 indicating the development of the re-circulation region in the divergent section with time for $\dot{m}$ = 0.065 kg/s. (Flow is from left to right.)

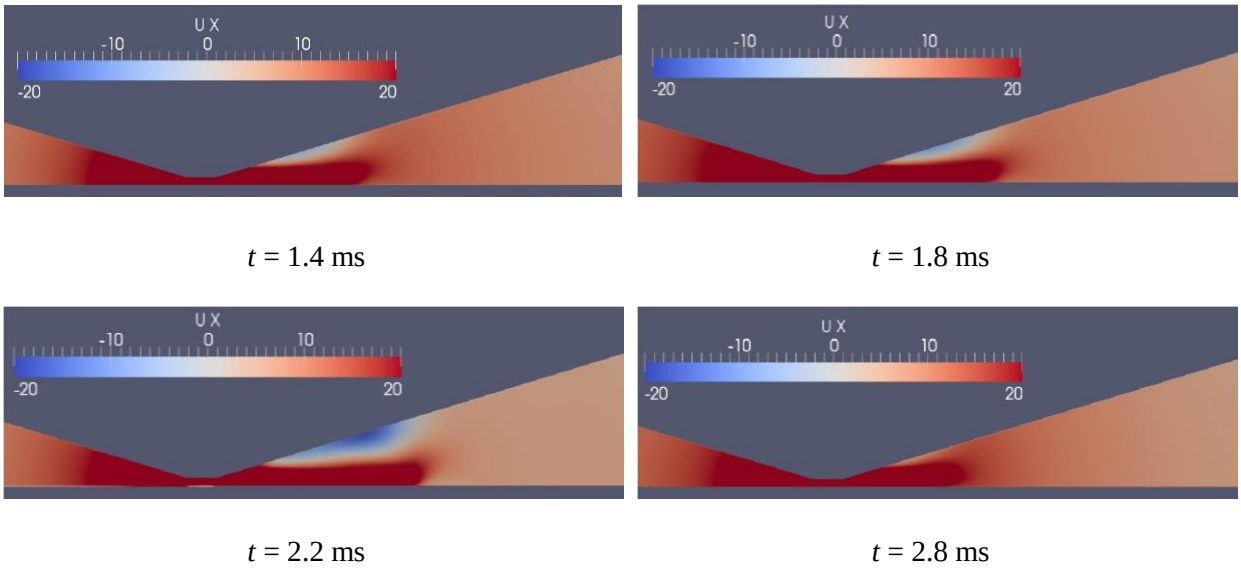

t = 1.4 ms t = 1.8 ms

t = 2.2 ms t = 2.8 ms

(a)

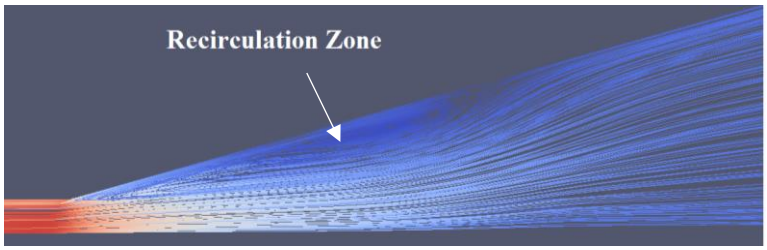

(b)

Figure 6: (a) Contours of axial velocity (m/s), and (b) streamlines in the divergent section in the *xy*-plane and *z* = 0 indicating the development of the recirculation region in the divergent section with time for $\dot{m}$ = 0.065 kg/s. (Flow is from left to right.)

The contours of turbulent viscosity in Figure 5 demonstrate the evolution of the re-circulation area after the flow separation in the divergent section. The location of the two-phase region in the divergent section is related to the development of the flow re-circulation with time. The recirculation region in the divergent section confines the two-phase mixture in the throat region and parts of the divergent section shown in Figure 3 at t = 2.0 ms. Later, as the re-circulation region moves downstream, the two-phase region occupies the divergent section and moves downstream and exit the nozzle as observed in Figure 3 at t = 2.8 ms. The turbulent viscosity is larger near the bottom wall and smaller on the top wall in the divergent section. This explains our earlier observation that more vapor was seen near the top wall and more liquid-content mixture formed near the bottom wall. The contours of axial velocity as a function of time in Figure 6 also indicates the location of the inception and expansion of the re-circulation zone downstream of the throat, supporting the nucleation behavior observed in Figure 3. The velocity contours have been re-scaled to better portray the re-circulation region in the divergent section. Nucleation behavior on the back wall, i.e. z = 1.5 mm, not shown here, is similar to the front wall; so, only front wall has been demonstrated here.

Figure 7 explains the different behaviors observed near the front wall and central plane in Figure 3 and 4 at t = 2 ms, respectively. In this figure, the pressure and temperature obtained from the simulations have been averaged in the y-direction at different locations downstream of the venturi nozzle and plotted for both the front wall, i.e. z = - 1.5 mm and central plane, i.e. z = 0. The saturated pressure at the calculated average temperature and average quality at the same downstream locations have been demonstrated in Figure 7 (a). A schematic of the venturi nozzle has been shown at the bottom of the figure to indicate the location of interest within the nozzle. The pressure drop is larger in the convergent section and the throat area at the central plane compared to the walls since the velocity is higher near the throat and reaches minimum near the wall due to the no-slip boundary condition. At x = 0.085 m where the convergent section ends and throat region begins, corresponding to Section *C* in Figure 4, the average pressure falls below the saturation pressure at that location. The corresponding value of the average *VF* at that location is equal to 0.998. Therefore, high-vapor content mixture is expected near the throat at the center of the nozzle. The same behavior is seen at the end of the throat region and entrance to the divergent section at x = 0.095 m that is associated with Section *D* in Figure 4. At x = 0.09 m, located in the throat region and downstream of the divergent section at x = 0.1 m, corresponding to Section *A* and *B* shown in Figure 3 respectively, the obtained pressure on the front wall is larger than the value of the saturation pressure leading to more condensation on the front wall compared to the central plane. Cavitation conditions on the central plane continue in the divergent section due to the re-circulation effects near the top wall. Figure 7 (b) demonstrates the variation of temperature averaged along the y-direction with respect to the axial location in the nozzle. This figure shows that the temperature decreases from supercritical to sub-critical condition with the maximum drop in the throat area and in the central plane of the nozzle.

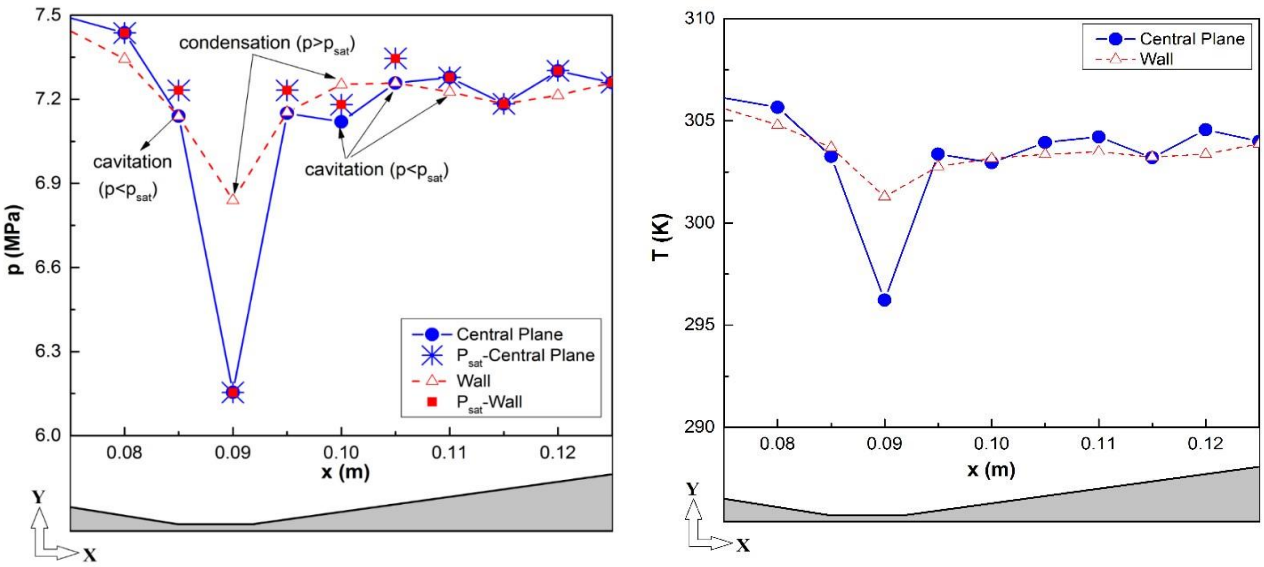

(a) (b)

Figure 7: (a) Average pressure in *y*-direction and saturation pressure vs. *x*, (b) average temperature in *y*-direction for central plane and front wall at *t* = 2.0 ms for $\dot{m}$ = 0.065 kg/s.

Figure 8 (a) demonstrates the contours of *VF* on the top wall of the venturi nozzle, as the height, i.e. *y* varies. The pressure and temperature have been shown for the same downstream locations as that of Figure 7 at t = 2.0 ms for $\dot{m}$ = 0.065 kg/s. The top wall is of great interest due the formation of a relatively large re-circulation region in the divergent section and its effects on the phase change behavior.

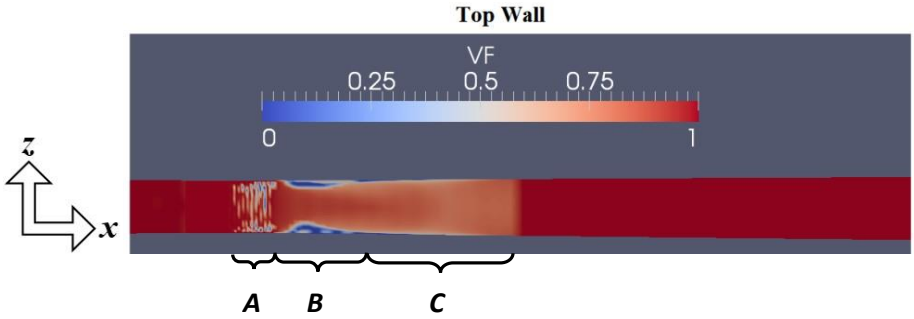

(a)

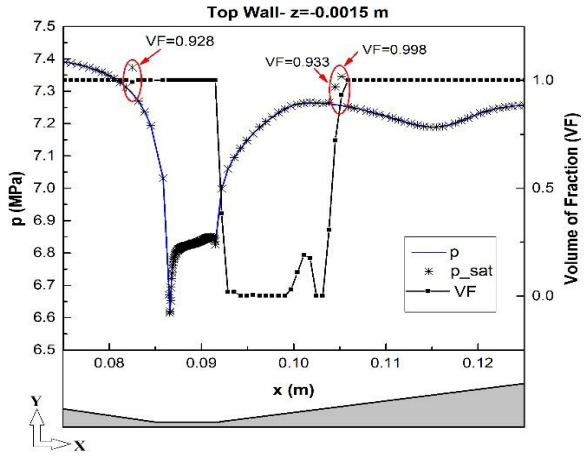

(b)

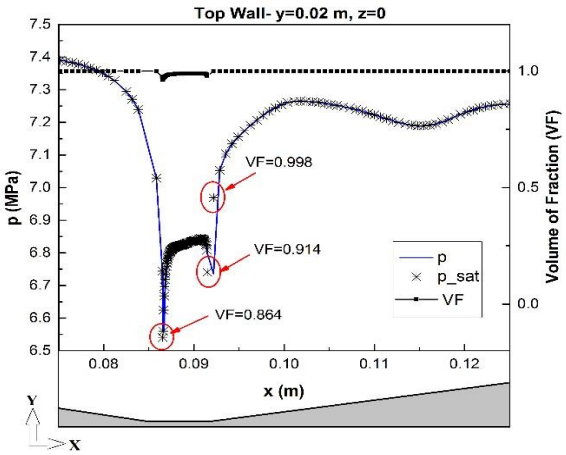

(c)

Figure 8: (a) Contours of *VF* on the top wall at t = 2.0 ms, $\dot{m}$ = 0.065 kg/s; average pressure, saturation pressure, and *VF* vs. downstream direction for the top wall on (b) z = -1.5 mm, (c) z = 0.

As shown in Figure 8 (a), the two-phase region is extended from the throat down to the divergent section where the re-circulation region ends, after which the flow is single phase, i.e. *VF* = 1 and stays as saturated vapor since the pressure remains sub-critical (p < 7.38 MPa) in the divergent section of the nozzle. As expected, condensation occurs on the two sides of the wall while cavitation takes place near the center of the nozzle as observed earlier. From the left to right in Figure 8 (a), in the region associated with a large density gradient in the throat area (shown as *A*), both liquid and vapor phases exist. A drastic drop of *VF* is observed at the end of the throat region and entrance to the divergent section indicating large volume of liquid droplets associated with region *B* in Figure 8 (a). Region *C* is associated with the divergent section of the nozzle where a high-vapor content mixture prevails. Downstream of region *C*, the flow becomes single-phase saturated vapor. Figure 8 (b) and (c) show the pressure in the downstream location

on the top wall along z = -1.5 mm and z = 0 lines, respectively. *VF* at each downstream location is plotted on the second vertical axis on the same figure. As Figure 8 (b) indicates, *VF* is equal to 0.928 at the center of the throat region (x = 0.085 m). At this location, the average pressure is smaller than both the saturation pressure at the average temperature and the average quality obtained from the simulation. This region is the associated region *A* of Figure 8 (a). As Figure 8 (c) shows, *VF* remains larger on z = 0 compared to z = -1.5 mm in Figure 8 (b) and drops to 0.0864 and 0.914 in the throat region. Downstream of the throat area in the re-circulation region, high vapor-content mixture persists in the center of the nozzle. The re-circulation region causes pressure variations in the downstream of the throat, i.e. x > 0.1 m as shown in Figure 8 (b) and (c). Drastic pressure drop is observed in the vicinity of the two sharp corners in the throat area, especially at z = 0.

Figure 9 (a) shows the contours of *VF* for the bottom wall, i.e. y = 0 in the *xz*-plane at t = 2.0 ms for $\dot{m}$ = 0.065 kg/s.

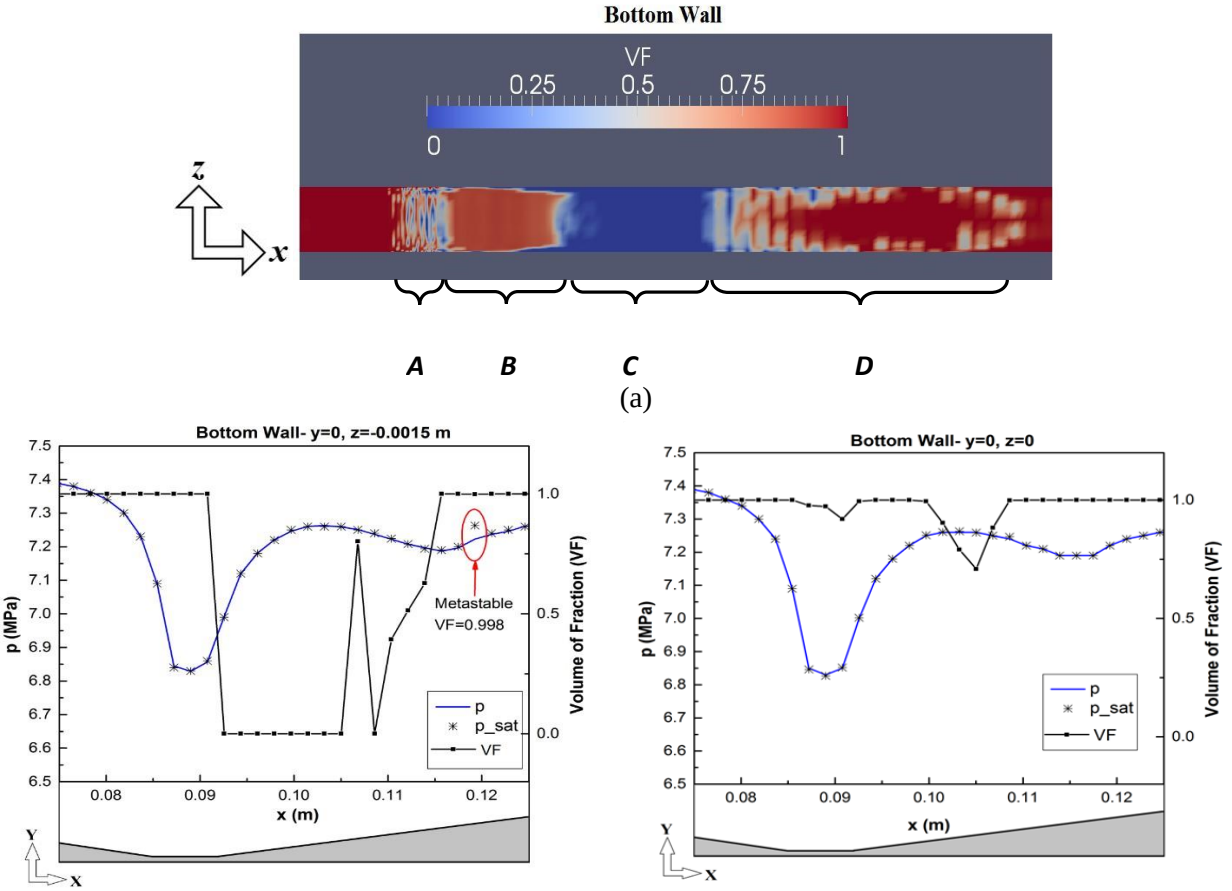

(a)

(b)

(c)

Figure 9: (a) Contours of *VF* on the bottom wall at t = 2.0 ms for $\dot{m}$ = 0.065 kg/s; average pressure, saturation pressure, and *VF* vs. downstream direction for the bottom wall on (b) z = -1.5 mm, (c) z = 0.

Region *A* corresponds to the throat region where a mixture of vapor and liquid exists. Capturing the density gradients in this region might be a very challenging task experimentally. These results will help designing experiments and choosing the right optical diagnostic that can resolve the obtained density gradients in the throat region. In region *B*, more vapor forms in the middle of the channel and liquid droplets occupy the regions near the wall similar to region *B* in Figure 8 (a). Region *C*, shows a very high-liquid content mixture in contrast to Figure 8 (a) where a high-vapor content mixture formed at that region. Finally, in region *D*, a high vapor-content mixture followed by a single-phase mixture is observed. Therefore, the two-phase mixture occupies a larger volume of the nozzle downstream of the throat compared to the top wall and is associated with a higher liquid-content mixture near the bottom wall. As Figure 9 (b) and (c) demonstrate, *VF* is smaller, i.e. higher liquid-content exists in regions *B* and *C* on both z = -1.5 mm and z = 0 planes compared to the top wall shown in Figure 8 (b) and (c). As expected, *VF* is smaller on the bottom wall at z = -1.5 mm. The average pressure is equal to the saturation pressure at all axial locations on the bottom wall except for x = 0.12 m associated with region *D* in Figure 9 (a) where a gas-liquid mixture is observed. Some fluctuations of *VF* can be seen downstream of the throat on the bottom wall due to the flow re-circulation downstream of the throat on the top wall. As a result, liquid regions have been convected downstream near the wall as was shown in Figure 3. The pressure drop is less significant on the bottom wall for both z = -1.5 mm and z = 0 since the bottom wall is at a distance with respect to the sharp corners in the throat. However, the re-circulation effects are still active on the bottom wall as the pressure jumps for x > 0.1 m indicates.

Figure 10 shows the entropy variation in the nozzle at t= 2 ms for $\dot{m}$ = 0.065 kg/s on the central plane. Entropy at each downstream location has been calculated as a function of the average temperature, average pressure, and average quality in the *y*-direction. As this graph shows, except for around the throat region and the divergent section of the nozzle, i.e. 0.08 m < x < 0.125 m, associated with the location of the two-phase mixture, the flow can be assumed isentropic. As discussed earlier, Table 1 outlines the inlet temperature, pressure, and velocity magnitude for mass flow rates equal to 0.050, 0.052, and 0.065 kg/s. Note that the exit pressure is fixed at 2.28 MPa for all cases. Thus, by increasing the mass flow rate, the inlet pressure and temperature increase and inspecting the results for different mass flow rates reveals the sensitivity of the nucleation process to the inlet conditions for the same nozzle geometry as is shown in Figures 11 and 12.

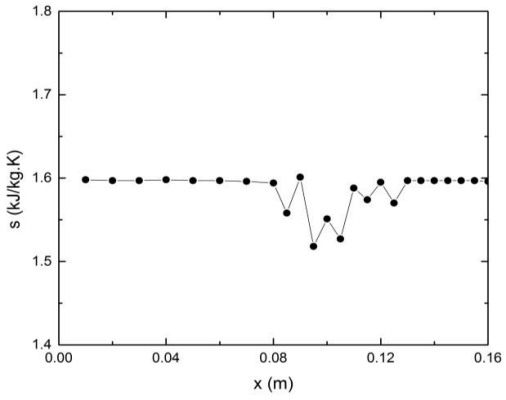

Figure 10: Entropy variation vs. downstream location for at t = 2.0 ms and $\dot{m}$ = 0.065 kg/s on the central plane, z = 0.

Figure 11 (a) and (b) demonstrate the Mach number and volume fraction variations vs. *x* for different mass flow rates with the fixed exit pressure. The speed of sound for the mixture has been calculated for homogenous frozen conditions, i.e., $\frac{1}{c^2} = \left(\rho_l VF_l + \rho_g VF_g\right) \times \left[\frac{VF_l}{\rho_l c_l^2} + \frac{VF_g}{\rho_g c_g^2}\right]$ [20], where *c* and *VF* are the speed of sound and volume fraction and subscripts *l* and *g* refer to the liquid and gas phases, respectively.

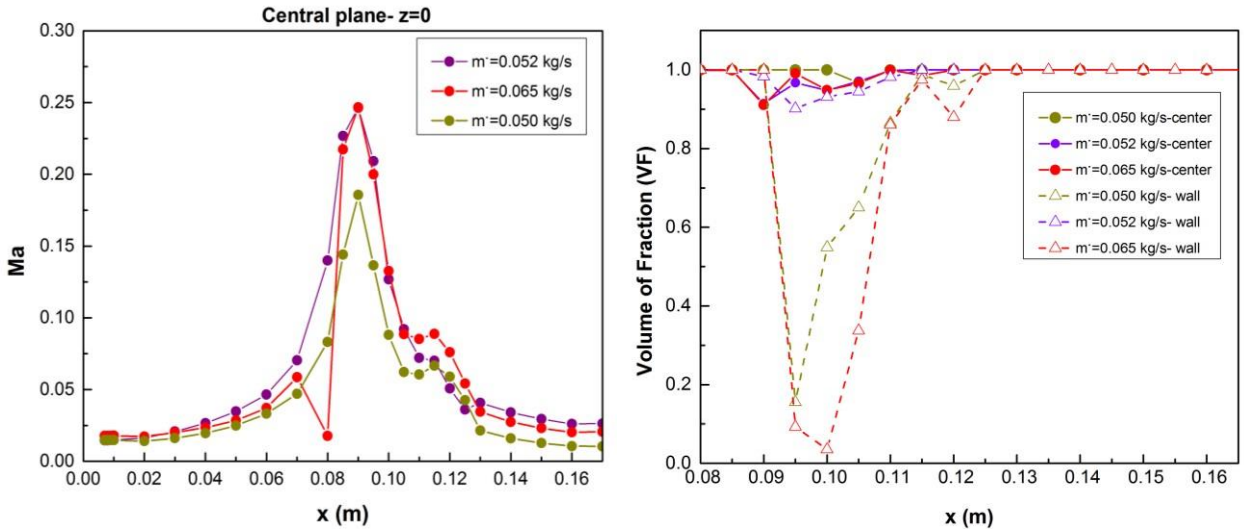

(a) (b)

Figure 11. (a) Mach number vs. *x* for different mass flow rates at the central plane, i.e. *z* = 0 (b) *VF* vs. *x* for different mass flow rates for *z* = 0 and *z* = -1.5 mm.

The homogenous frozen expression of speed of sound is based on the assumption of no mass-exchange between the two phases. As Figure 11 (a) shows, *Ma* increases to its maximum value near the throat and decreases downstream as was expected for subsonic flows. By increasing the mass flow rate, *Ma* increases due to the fixed exit pressure boundary conditions in these simulations that allows larger inlet pressure for higher mass flow rates and higher velocity within the throat area to reach to the same exit pressure for all mass flow rates. The drop in *Ma* for mass flow rate equal to 0.065 kg/s near *x*= 0.08 m is due to larger content of liquid, i.e. smaller *VF* as indicated in Figure 11 (b). *Ma* increases slightly downstream of the throat in the divergent section, i.e. *x*= 0.11 m, since *VF* increases (more vapor is formed) and the speed of sound decreases in vapor phase. As Figure 11 (b) indicates, *VF* decreases drastically near the walls for all mass flow rates compared to that of the central plane. This is consistent with the conclusion obtained earlier that significant condensation occurs near the walls. *VF* decreases by increasing the mass flow rate near the walls. Simulations with higher mass flow rates up to 0.095 kg/s (not shown here), indicated that the flow remained subsonic throughout the nozzle since there was not significant vaporization downstream of the throat and throat region. The high liquid-content mixture causes a relatively low *Ma* in the two-phase regions as it increases the speed of sound and decreases *Ma*.

Figure 12 shows the state of CO_2 within the nozzle with respect to the vapor dome in *P-v* diagram for mass flow rates equal to 0.065 kg/s and 0.050 kg/s for the central plane (*a* and *c*) and near the wall (*b* and *d*), respectively. Each point on these plots represent different locations within the nozzle, i.e. inlet, throat, divergent section, and outlet at $t = 2.0$ ms. As Figure 12 (b) and (d) indicate, the pressure drop from the near-critical conditions to sub-critical is smaller near the wall for both mass flow rates. However, the mixture changes from saturated liquid to saturated vapor. As observed in Figure 11 (b), *VF* is smaller for larger mass flow rates within the two-phase region. On the contrary, the pressure drop is larger at the center of the nozzle since the velocity drop is larger for both mass flow rates as indicated in Figure 12 (b) and (d). For these conditions, *VF* remains close to one, i.e. more vapor than liquid exists compared to that of the near walls. The higher pressure drop observed for higher mass flow rates leads to lower *VF* and quality on the central plane as the comparison between Figure 12 (a) and (c) shows. Therefore, it can be emphasized again that cavitation effects are not as significant as condensation near the walls for the near-critical inlet conditions.

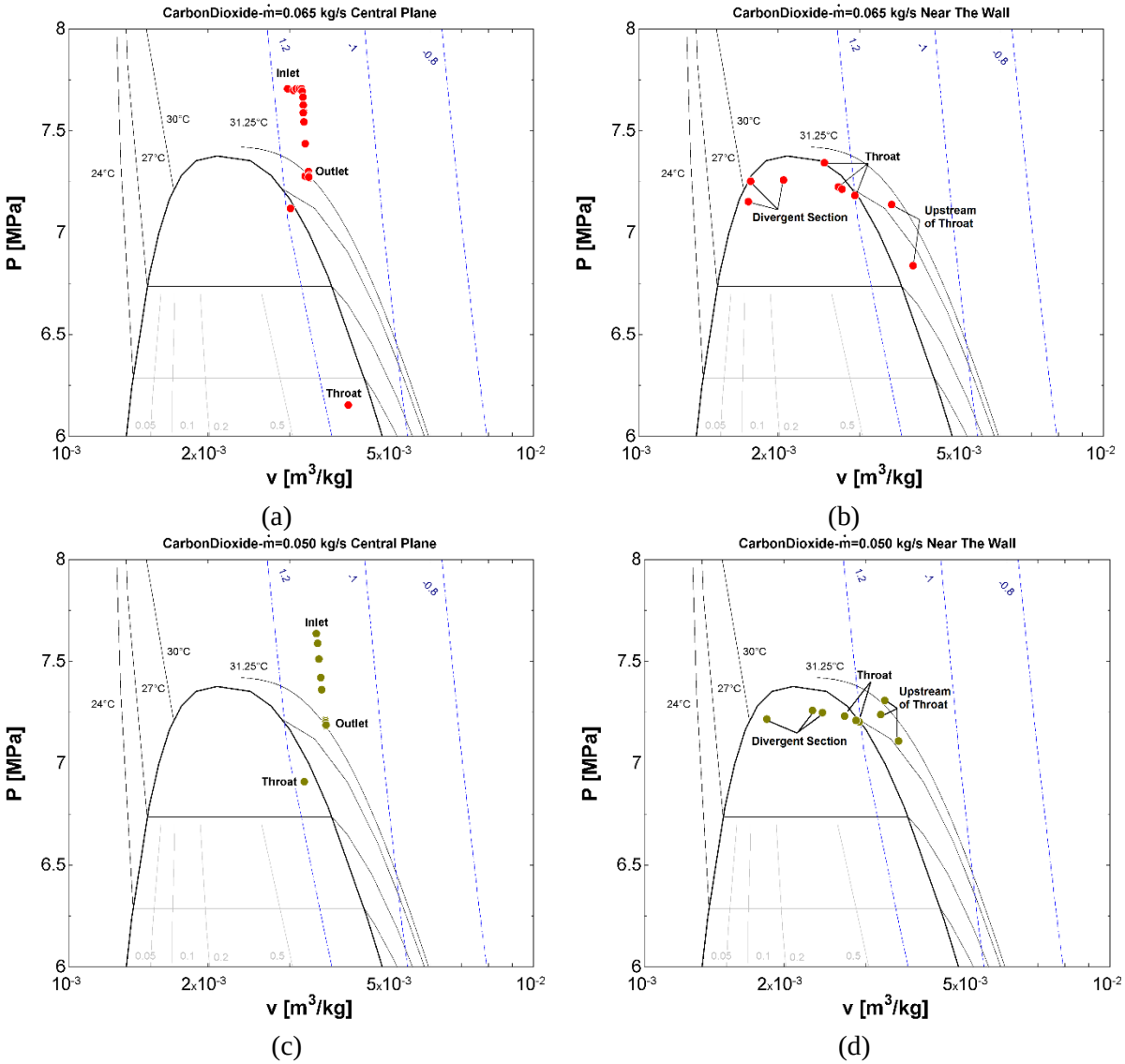

Figure 12: *P-v* diagrams for (a) $\dot{m}$ = 0.065 kg/s on the central plane (*z* = 0); (b) $\dot{m}$ = 0.065 kg/s near the wall (*z* = -1.5 mm.); (c) $\dot{m}$ = 0.050 kg/s on the central plane; (d) $\dot{m}$ = 0.050 kg/s near the wall.

The simulation results for different mass flow rates, i.e. pressure, quality, and temperature have been averaged along the nozzle height (*y*-direction) at each axial location *x*, and the averaged values have been used to calculate the nucleation rate at each axial location for the central plane and near the walls of the nozzle. It is noted that since homogenous equilibrium model has been assumed in our simulations, at each cell, equilibrium between the two phases is expected; thus, the nucleation rate is zero before averaging the results. However, to compare the nucleation behavior for different mass flow rates and at different axial locations within the nozzle, the averaged values have been used. Therefore, for the conditions where the average pressure is smaller or larger than the saturation pressure and *VF* at that average temperature is very close to one, the nucleation rate is not zero. Obtaining nucleation rate at different locations within the nozzle will be helpful to study the nucleation process as is shown below.

Nucleation of a new phase forms the non-equilibrium conditions depends on the nucleation work, i.e. the Gibbs free energy barrier [21]. A relative time scale ratio $t_{cr} = t_r/t_n$ can be defined based on the classical nucleation theory, where $t_r = l/u_{avg}$ is the residence time and l and u_{avg} are the length of the condensing volume and the average flow velocity, respectively [12]. $t_n = (J_{max}\mathrm{V})^{-1}$ is the nucleation time and J_{max} is the maximum nucleation rate obtained from Equation 7. The critical radius of the condensed droplets and limiting energy barrier for nucleation can be obtained from Equation 8 and 9 and the Gibbs free energy can be calculated from Equation 10.

Nucleation Rate
$$J_{\max} = \left[\sqrt{\frac{2\sigma}{\pi m^3}\frac{\rho_v^2}{\rho_l}}\right] e^{\left(-\frac{\Delta G^*}{\kappa T}\right)} \tag{7}$$

Critical Radius
$$r^* = \frac{2\sigma}{\rho_l[g(p_v,T) - g(p_s,T)]} \tag{8}$$

Limiting Energy Barrier
$$\Delta G^* = \frac{4}{3}\pi r^{*2}\sigma \tag{9}$$

Gibbs free energy
$$g(p_v,T) - g(p_s,T) = [h(p_v,T) - Ts(p_v,T)] - [h(p_s,T) - Ts(p_s,T)]; \tag{10}$$

Where σ, ρ_v, ρ_l, m, κ, G, T, p_s, and r^* are surface tension coefficient, gas-phase density, liquid-phase density, molecular weight, Boltzmann's constant, Gibbs free energy, temperature, saturation pressure at the given temperature, and critical radius, respectively. The time scale determines whether the deviation from the equilibrium conditions in an internal flow is large enough for stable droplets to form. Ratios below one indicate that the nucleation time is larger than the residence time, implying that condensation cannot occur. For our base calculation, the obtained resident and nucleation time were $t_r = \frac{l}{u_{avg}} \approx 10^{-5} s$ and $t_n \approx 10^{-30} s << t_r$ showing that

very close to the critical point nucleation occurs. The condensation length in these calculations is associated with the location where $VF < 1$ in the simulations results.

Figure 13 shows the nucleation rate as a function of x for mass flow rates equal to 0.050, 0.052, and 0.065 kg/s for central plane and near the wall, i.e. $z = 0$ and $z = -1.5$ mm, respectively. In the throat area (0.085 m < x < 0.095 m), nucleation on the central plane is larger than the wall for mass flow rates equal to 0.065 and 0.052 kg/s, and larger for 0.065 kg/s. This is consistent with the contours of VF for the central plane shown in Figure 4.

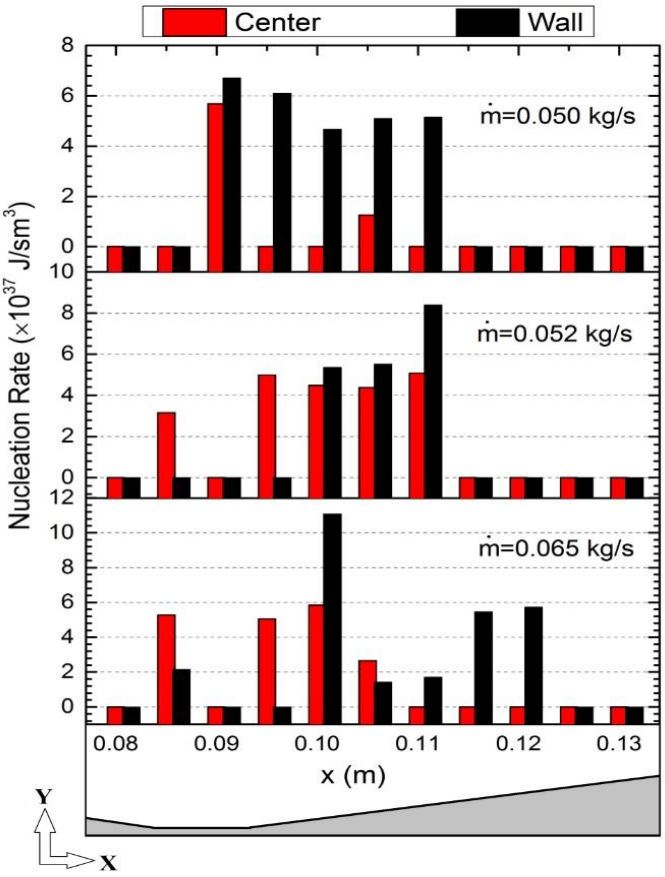

Figure 13: Nucleation rate vs. x for central plane and wall for $\dot{m}$ = 0.050, 0.052, and 0.065 kg/s.

In the divergent section, i.e. $x \geq 0.10$ m, nucleation on the wall is larger than that of the center for all cases. Further downstream, i.e. 0.10 m < $x \leq$ 0.12 m for 0.065 kg/s, the average velocity is higher; therefore, the pressure drop is sufficient to initiate the phase change. For mass flow rate equal to 0.050 kg/s, nucleation occurs downstream in the throat area, i.e. x = 0.095 m compared to larger mass flow rates, i.e. m= 0.052 and 0.065 kg/s since the lower pressure drop in the throat area prevents nucleation upstream of the throat at x = 0.085 m. The pressure drop required for phase change is obtained at x = 0.095 m for this lower mass flow rate. However, more condensation occurs near the wall than cavitation due to the lower velocity and higher pressure near the wall, leading to higher nucleation rates compared to the central plane throughout the nozzle for mass flow rate equal to 0.050 kg/s. Previous studies of radial

compressor operating with supercritical CO_2 at realistic cycle conditions showed that away from the critical point, i.e. inlet pressure equal to 7.69 MPa, condensation occurred at very small regions near the blade tip and blade trailing edge [8]. Their studies showed that for higher rotational speeds (leading to higher pressure drop at the compressor inlet) and higher mass flow rates the regions in which condensation was predicted were considerably larger. The presented computational conditions are of relevance to the real compressor inlet conditions as stated above; indicating that even a small pressure drop near the critical point leads to a large volume of liquid (with respect to the size of the nozzle) downstream of the throat that moves downstream of the nozzle and cavitation in the sharp corners of the throat. Thus, we predict that condensation and cavitation at conditions near the critical point affect compressor performance; especially, at higher mass flow rates, the nucleation is more likely to occur due to larger pressure drops. Further experimental data are required to demonstrate the effects of nucleation on compressor performance near the critical point.

Experimental facility to study nucleation behavior

One can only represent the two-phase flow by quality distribution using the homogeneous equilibrium model described in the previous section. More details about the flow, such as droplet sizes, count, phase distribution etc. can only be resolved using advanced two-phase flow models. Such advanced models are generally formulated by modeling the nucleation process as source terms in the Navier-Stokes equations and closure to these source terms is typically derived from nucleation theories and growth rate models [22]. However, the nucleation theories and growth rate models need careful experimental validation for nucleation of sCO_2 near the critical point. To achieve this task, a 2-D venturi system with optical access was designed and fabricated which allows for testing of various upstream stagnation conditions.

The venturi system is comprised of the main body, window flange, bottom flange, sapphire windows, and the converging-diverging (C-D) profile as shown in Figure 14. Figure 14 (a) presents the cross-section view of the assembly and the fluid flow path is formed by squeezing a 3 mm thick C-D profile between two sapphire windows and the windows are secured in place using the window flange. The C-D profile is positioned and secured in place with the aid of the dowel positioning pins shown in Figure 14 (b). The bottom wall of the flow path is formed by the bottom flange which is shown in Figure 15 (a).

The bottom flange is equipped with the material sample holders which can hold material samples for the erosion tests. Four material samples; 6061 Aluminum, 625 Inconel alloy, 304 stainless steel, and 316 stainless steel are prepared for the erosion tests. Set of ten 1/16” holes are wire eroded on the bottom flange for measurement of the local static pressure along the C-D profile. The schematic in Figure 15 (b) presents the dimensions of the C-D profile along with the locations of 1 mm pressure sample ports along the profile. Four pressure sampling ports are positioned in the throat region for better resolution of the local static pressure measurements. The C-D profile has been designed based on the CFD study reported in the previous sections [1]. This venturi system design has an added capability of accepting multiple C-D profiles to study the nucleation process for different expansion rates.

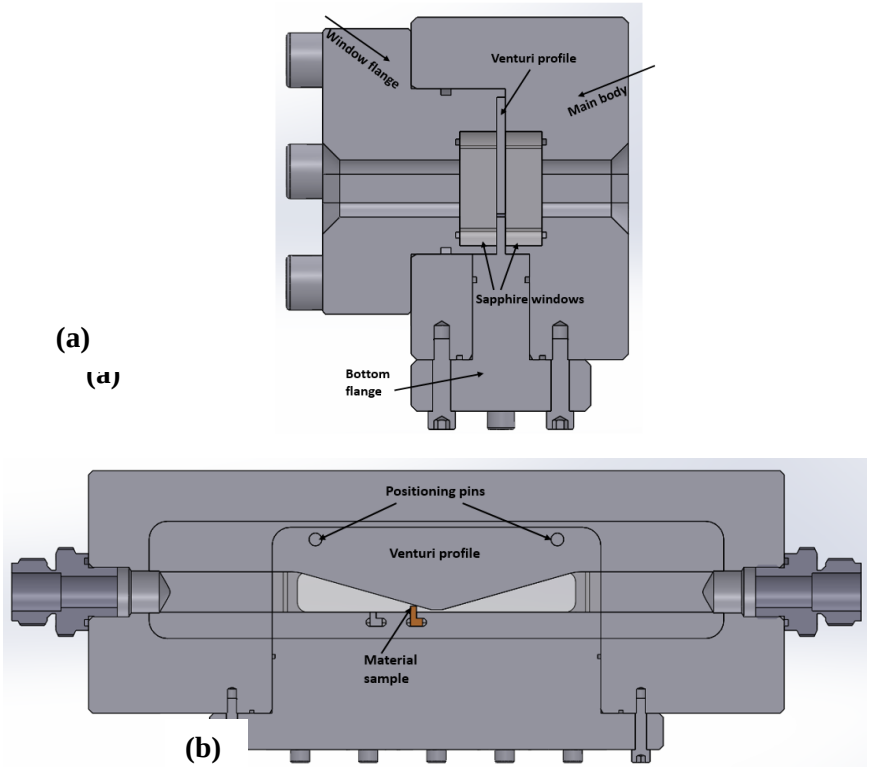

Figure 14: CAD model representing (a) Cross-sectional view of the internal details of the assembly process, and (b) Cross-sectional view of the converging-diverging profile along with the positioning pins and the erosion tests material sample.

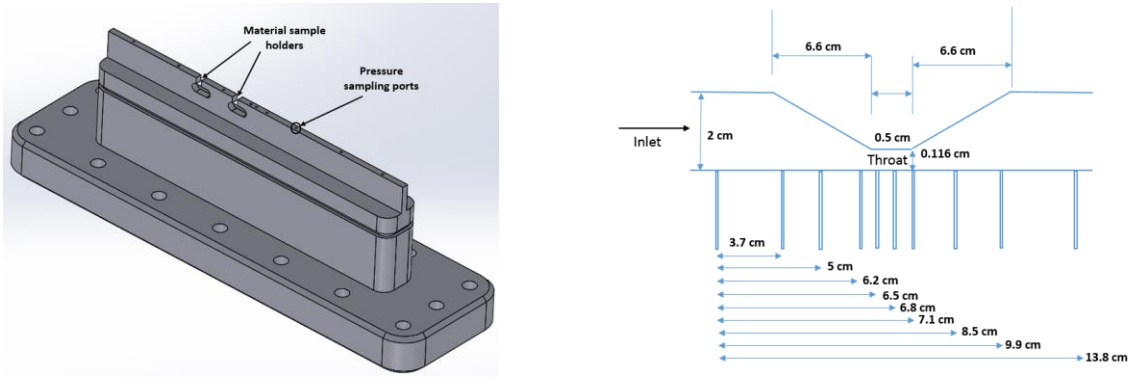

Figure 15: (a) CAD model of the bottom flange showing the pressure sampling ports and material sample holders (b) Converging-diverging profile dimensions along with the locations of the pressure sample ports.

The venturi system was fabricated by Marine Technology (http://www.marinetechnology.ie/) and hydro pressure tested up to 26 MPa before installing in the test facility. Figure 16 represents the bottom view of the assembled test section and shows the 1/16" ports for pressure measurements along the converging-diverging (C-D) profile. 1/16" OD 316 stainless steel tubes are laser welded to these ports and the tubes will be connected to Meriam M1500-GI3000 gauge pressure transmitters for local static pressure measurements. Figure 17 shows the disassembled view of the venturi test section along with the important inner details. One sapphire window fits into the slot on the main body as can be seen in the figure below. The C-D venturi profile is bolted to the windows retainer via two machine screws and is fitted with male dowel pins to accurately position inside the main body. The second sapphire window sits inside the slot in windows retainer as can be seen in the picture below.

Figure 16: Assembled test section showing the static pressure ports

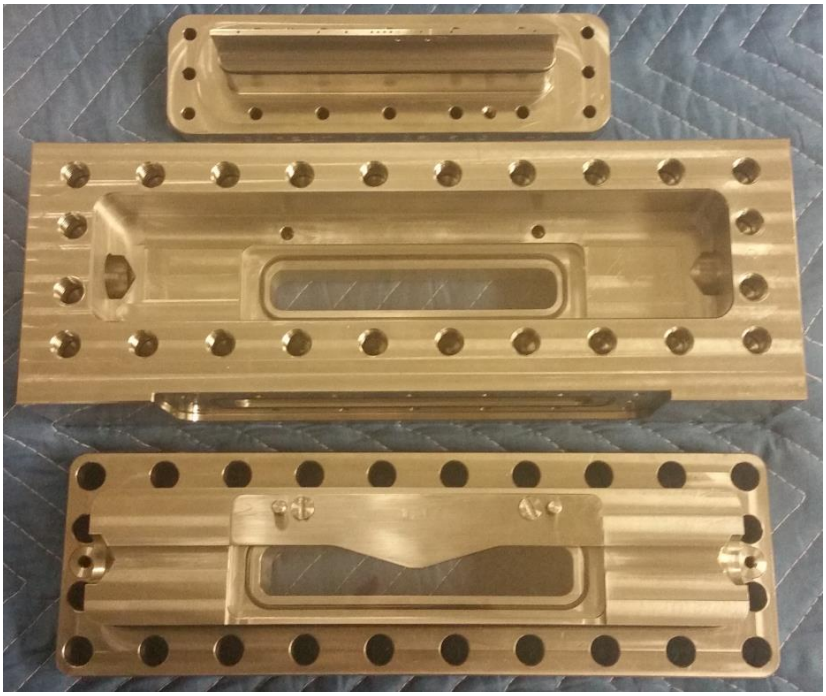

Figure 17: Disassembled venturi test section showing inner details

Figure 18 (a), (b) shows the schematic and the picture of the experimental facility that has been constructed to achieve stable upstream conditions and longer experimental times. The facility is equipped with two 10 kW high pressure cartridge heaters. Therefore, in order to achieve the desired fluid temperature at the venturi inlet (limited to < 50^{o}C), the mass flowrate through the test section is limited to 0.1 kg/s which is within the capability of Hydro-Pac CO_2 compressor used in the facility. The high pressure cartridge heaters in combination with a high pressure cooler precisely control the inlet stagnation temperature. The compressor has a maximum discharge pressure of 2400 psi (~17.23 MPa) and allows for achieving wide range of inlet stagnation pressures. A large heated buffer tank in the facility dampens flowrate oscillations due to the compressor cycling and can handle pressures up to 2750 psi (~25.85 MPa). The local static pressure measurements might reveal presence of density oscillations when nucleation occurs in the venturi. The local saturation pressure will be calculated assuming that the flow is isentropic and using the measured stagnation properties at the inlet. Comparison of the calculated local saturation pressure and measured local static pressure will provide a qualitative indication of the nucleation rate. In addition to the local static pressure measurements the optical access to the flow allows for use of optical techniques such as shadowgraph, schlieren photography, and interferometry. These optical techniques can be used for qualitative/quantitative resolution of the density field when the nucleation occurs within the venturi. With good enough resolution, features such as local droplet sizes, droplets count etc. are parameters of interest for calculation of the nucleation rate as a function of the upstream stagnation conditions. This data can be used to check the validity of nucleation theories from literature and study presence of any flow instabilities near the critical point.

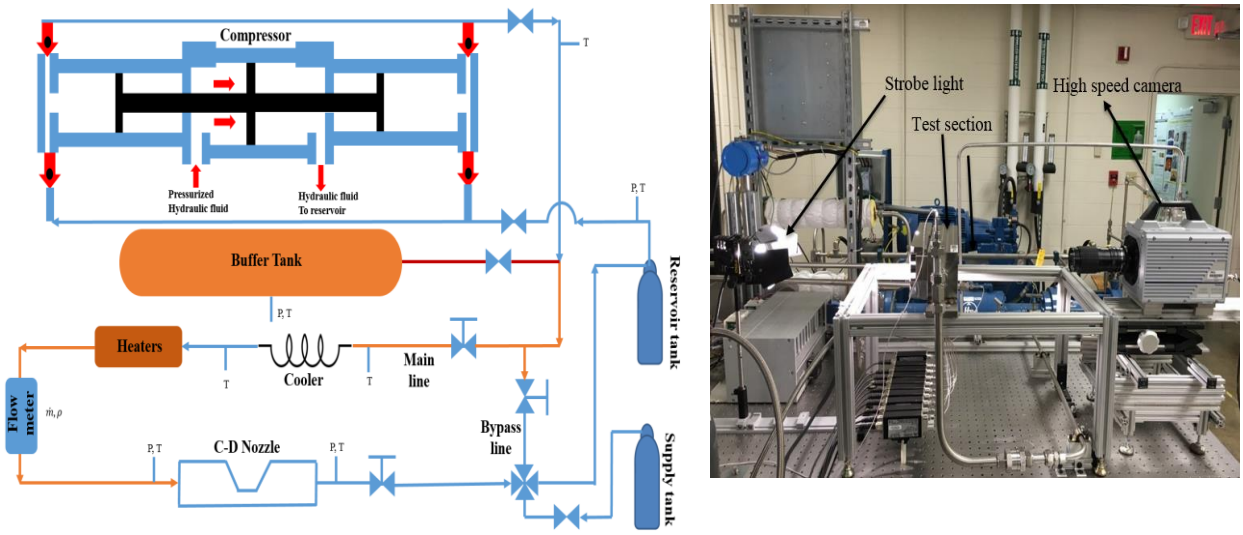

(a) **(b)**

Figure 18: (a) Schematic representation of the venturi test facility indicating various components (b) Picture of the assembled test section with the venturi test section installed

Test facility operating procedure

Prior to filling the system will CO_2, the system is vacuumed to ~1 psia and is purged with

CO_2 gas couple of times to ensure that the system is free of foreign gases, contaminants. After filling the system with CO_2, following steps describe the standard operating procedure followed during the nucleation tests:

- Heat the buffer tank up to ~80^oC (limit to <100^oC), at which point the pressure inside the buffer tank is typically in the range of 1800-2000 psi.
- Turn on the cooling water supply to the cooler as well as the compressor. The Hydro-Pac compressor is fitted with CO_2 aftercooler as well as Hydraulic oil cooler, both of these components require cooling water supply.
- Close the bypass valve completely and partially open the inlet and outlet flow control valves to the test section. These valves set the desired flow resistance at the inlet and outlet of the test section.
- Turn on the compressor motor and provide a voltage signal to control the mass flowrate and pressure of CO_2 exiting the compressor. Generally, it is a good idea to start with a low value and increase the voltage signal as needed. The compressor takes 0-10V signal, where 0 corresponds to no flow and 10V corresponds to maximum flow and pressure of 2500 psi. In between these two limits, the compressor outlet pressure scales linearly with the voltage signal.
- Set and control the desired fluid inlet temperature to the test section using relay controlled from the LabVIEW or external temperature controller.
- Adjust the inlet, outlet, and/or bypass control valve settings to achieve the desired pressure, mass flowrate in the test section. Generally, the system responds slowly and it is recommended to change the valve settings slowly and wait for a while for the system to respond.
- At this point, the pressure generally fluctuates by $\pm$30-40 psi due to compressor pistons cycling. Open the valve to heated buffer tank and the pressure fluctuations should drop down to $\pm$1-2 psi.
- Generally, the operating conditions change significantly after opening the buffer tank as the tank is heated up to 80^o and is at significantly higher pressure than generally required.
- If at any point the pressure inside the reservoir tank pressure drops below 200 psi, open the valve to CO_2 supply tank to make for the CO_2 lost through leaks in the system.

Once the system reaches the desired operating conditions, data was recorded in NI Labview as well as at the same time high speed camera (Photron fastcam SA-Z) starts collecting the videos of the flow through the venturi nozzle. Lowel Pro 250 W strobe focusing light is used as the light source for illuminating the flow field. Figure 19 shows a snapshot of one such video recorded by the high speed camera for flow of liquid CO_2 jet at inlet pressure of 6.2 MPa, inlet temperature of 25^oC and recorded mass flowrate of 0.125 kg/s. This video was recorded during initial testing phase and we observed very high CO_2 leak rate between the walls of the C-D profile and the sapphire windows as can be seen in Figure 19. This is probably due to the machining tolerances resulting in larger than designed gaps between the C-D profile and sapphire windows. Because of the high leakage flow between the walls, it was extremely hard to quantify the actual mass flowrate through the C-D profile itself. In other words, for the example video snapshot presented here, the mass flowrate is recorded

to be 0.125 kg/s but the actual mass flowrate through the C-D profile itself can be significantly lower than the value recorded because of the leakage between the walls. The actual mass flowrate can only be accurately be quantified only if the leakage flow is accurately quantified or leakage flow is prevented altogether. Additionally, because of the excessive flow into the test section, it was difficult to achieve the desired operating pressure and temperature. For example, the thermal capacity of heaters (<20 kW) is not sufficient to raise the temperature of CO_2 from 10^oC to above critical temperature for such high mass flowrates.

In an effort to reduce the leakage flow, stainless steel shim stocks of varying thicknesses were cut in the shape of the venturi profile and placed between the walls to reduce the clearance gaps. One such cut shim stock of thickness 0.004" is shown in Figure 20. These shim stocks in combination with RTV-106 (http://www.skygeek.com/momentive-rtv106.html) were expected to reduce the leakage flow between the walls. However, during actual testing it was realized that the leakage still was still very significant.

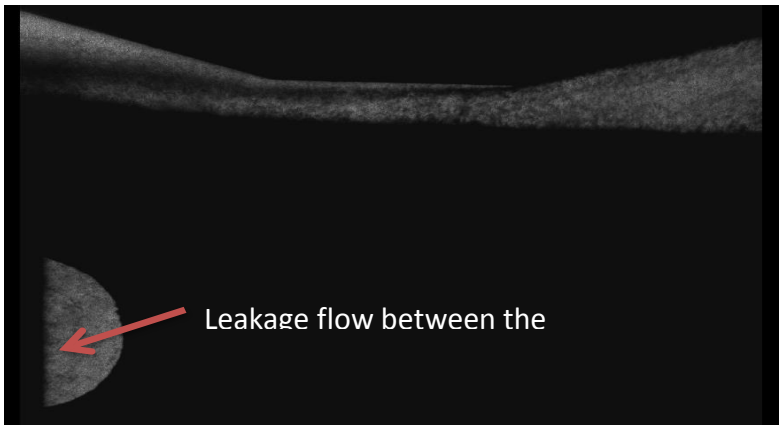

Figure 19: Snapshot of a shadowgraph video showing leakage flow between the walls of venturi profile and the sapphire window

Figure 20: 316 stainless steel shim stocks cut in shape of the venturi profile

In order to completely eliminate the leakage flow, 1/32" O-ring groove path is machined on the bottom flange and C-D profile on both sides to seal the fluid leakage path against the sapphire windows. Figure 21 represents a CAD model showing the O-ring groove path in blue.

Figure 22 shows the picture of the assembled test section with O-rings grooves installed (Note that the O-rings are installed on both the front and back). Custom stock cut to length 1/32" Viton O-ring was installed into the O-ring grooves.

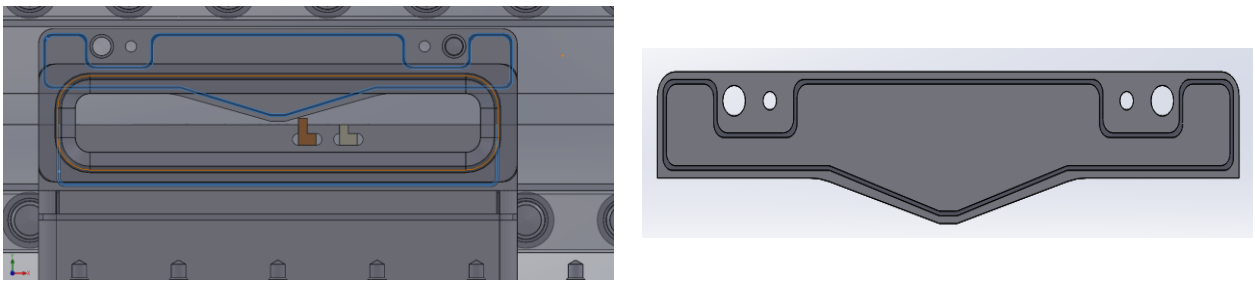

Figure 21: CAD model showing O-ring groove paths machined into the C-D profile and bottom flange on either sides.

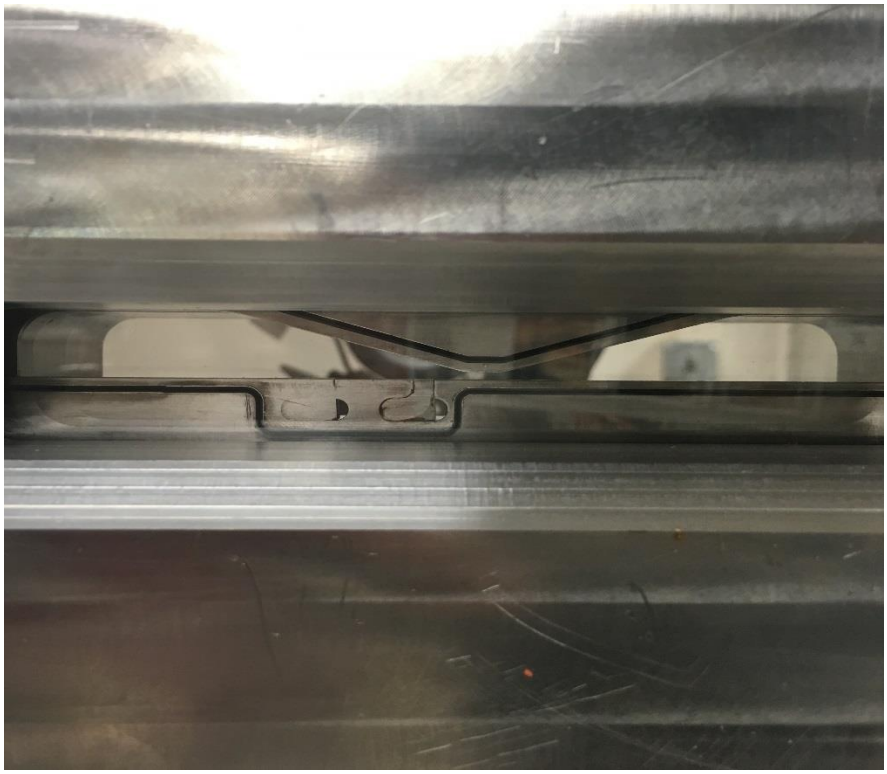

Figure 22: A photograph of the assembled section partially showing one of the installed O-rings between walls of the C-D profile and the sapphire window.

Table 2 presents a list of video cases recorded after installing the O-ring grooves along with the corresponding inlet temperature and pressures to the venturi test section. For all these cases, mass flowrate of ~0.049 kg/s was recorded using Coriolis mass flowmeter. It should be noted be noted that, for the cases A & C inlet temperature is below the critical pressure but the pressure is above the critical pressure; Whereas for the cases B, D, & E both the inlet temperature and pressure are above the critical values for CO_2. Figure 23 presents the static pressure profile

recorded for each of these cases. These pressure profiles are recorded using Meriam 1500 pressure transducer with uncertainty of ±0.025% of full scale (or equivalent of 0.75 psi).

Table 2: List of experiments performed after installing the O-ring grooves between walls to prevent the excess leakage rate.

	Inlet Temperature [^{0}C]	Inlet pressure [MPa]
Case A	30.56	1071.8
Case B	31.14	1082.1
Case C	30.97	1077.2
Case D	31	1081.75
Case E	30.98	1082.73

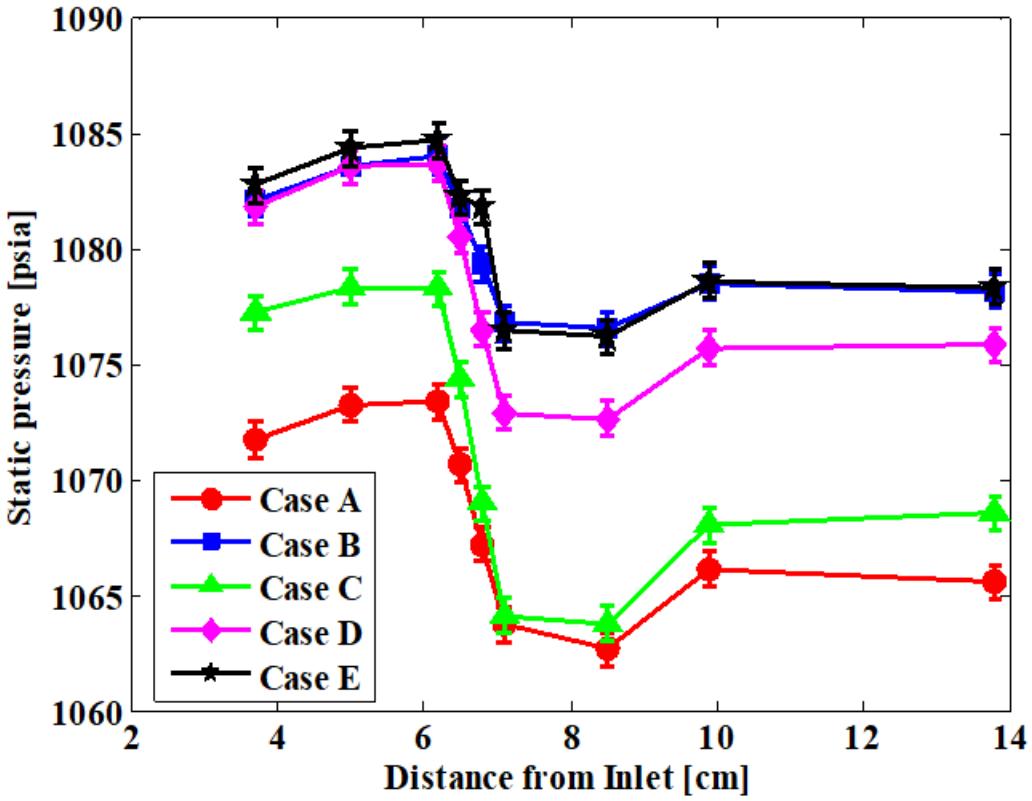

Figure 22: Static pressure profiles recorded for all the cases presented in Table 2.

By comparing cases Case B, D, & E from Figure 22, it can be seen that the static pressure profiles can vary significantly depending even when the inlet pressure and temperature are nearly similarly. This is because the data presented in Figure 22 is averaged data for a period of 30 seconds, whereas the instantaneous static pressure fluctuates significantly (sometimes up to ±10 psi) even in presence of the heated buffer tank. Figure 23 presents three different snapshots of video recorded for Case A. It should be noted these videos were recorded using a standard phone camera due to lack of availability of high speed camera during the time these experiments were conducted, nevertheless, these videos provide qualitative information for each of these cases. The snapshots presented below for Case A show that the upstream of the throat region is clear

indicating supercritical CO_2 flow; whereas in the throat and downstream of the throat regions are opaque and cloudy, indicating presence of condensation in these regions. Comparing the top picture from Figure 23 and some of the CFD results presented in previous section, one can clearly see presence of a recirculation zone downstream of the throat.

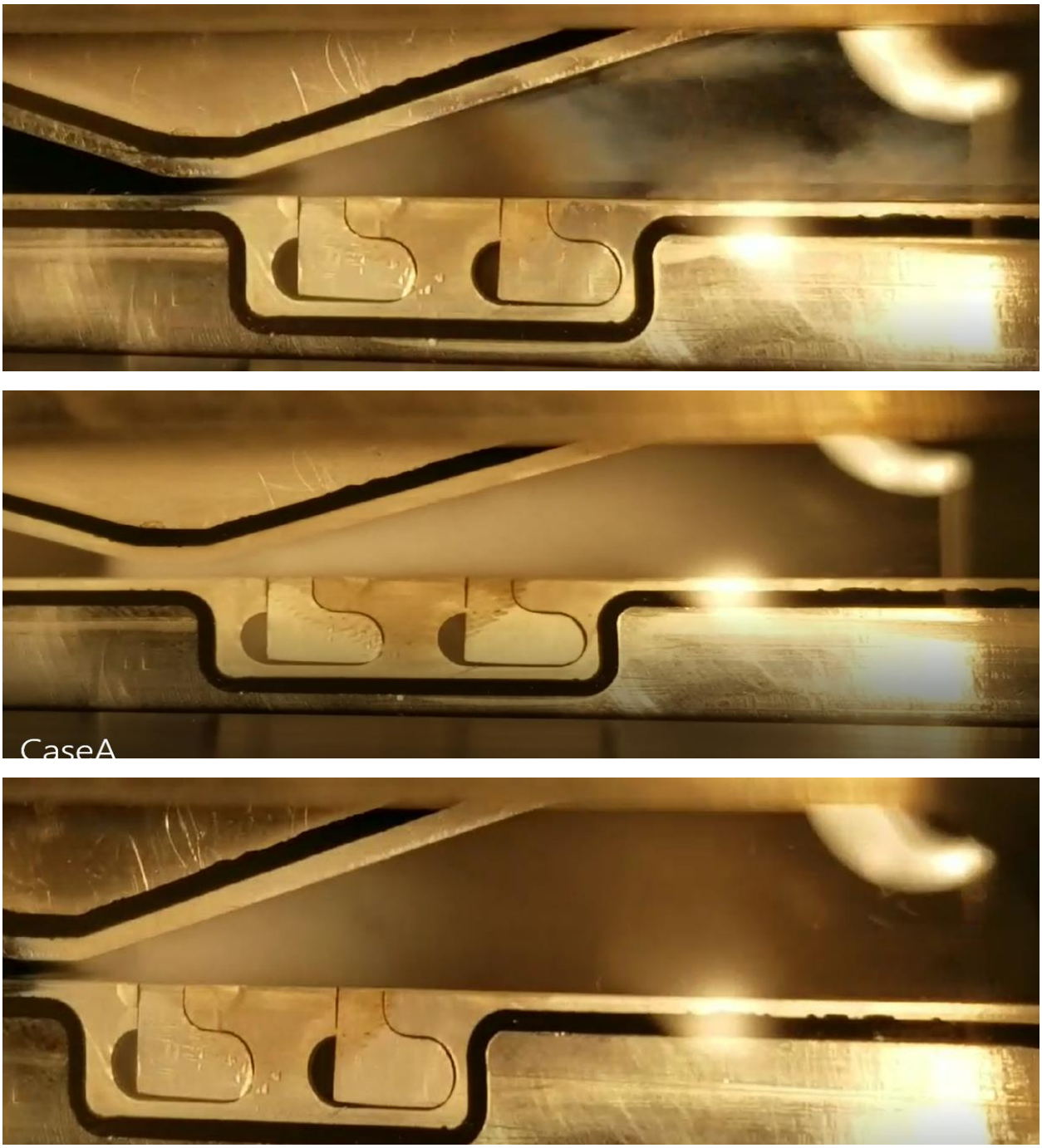

Figure 23: Snapshots at different times from the video recorded for Case A) in Table 2. These pictures clearly show the transition from the supercritical phase to two-phase region due to reduction in pressure in the throat region. Some of the condensation zones formed in the throat region are convected downstream of the throat.

Videos recorded for other cases will be analyzed to obtain qualitative understanding of nucleation behavior and the conditions leading to it. More videos will be recorded in the near future when the high speed camera is available for use. In addition, we fabricated and installed a new C-D profile (with smaller throat area) to lower the mass flowrate requirements to initiate condensation in the throat region. Figure 24 shows the new C-D profile installed in the venturi system along with O-ring to seal flow of fluid between the walls.

Figure 24: New converging-diverging nozzle profile fabricated and installed in the venturi test section. The new C-D profile lowers the mass flowrate requirement by a factor of 2, increasing the range of operating conditions that can be investigated.

Another objective of the current project is to assess impact of the condensation on erosion behavior of different material samples. Material samples are prepared using wire cut EDM technology and these samples are shown in Figure 25.

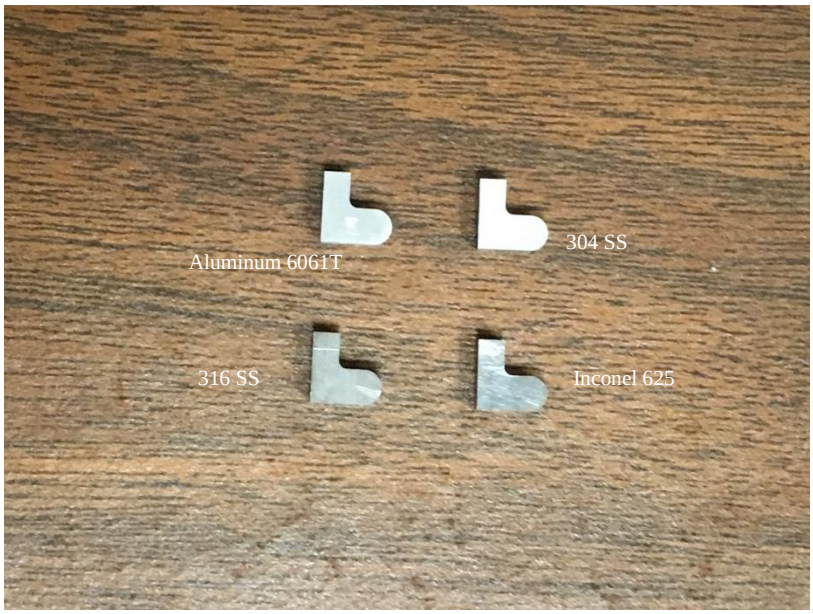

Figure 25: Fabricated samples for the erosion tests.

Two samples of each material (Aluminum 6061T, 316 stainless steel, 304 stainless steel, and Inconel 625) are prepared. Table 3 presents the initial weights of each of the sample measured by SCALE-METTLER TOLEDO AG245 weighing scale. Short term erosion tests (<20 hours) were conducted for each of these samples, without any noticeable weight changes. Longer term erosion tests are planned in the near future.

Table 3: Initial weight measurements of the erosion test samples

Sample	Aluminum 6061T	304 SS	316 SS	Inconel 625
Weight (mg)	332.8	993.7	1008.9	1064.3

Summary & Conclusions

Nucleation of S-CO_2 very close to the critical pressure and temperature flowing through a converging-diverging nozzle was computationally studied. 3D transient compressible Navier-Stokes and energy equations were solved in OpenFOAM. Developed fluid property interpolation tables (FIT) based on a piecewise biquintic spline interpolation of Helmholtz energy was integrated with OpenFOAM to model S-CO_2 properties. The mass fraction of vapor created in the venturi was calculated using homogeneous equilibrium model (HEM). The proposed nozzle geometry provided the required pressure drop to develop two-phase flow by keeping the inlet at supercritical pressure and temperature in the vicinity of the critical point. *1D* isentropic model of the nozzle indicated that nucleation process was very sensitive to the initial conditions. The 3D simulations demonstrated that the nucleation first occurred in the throat area in the center of the channel. However, the nucleation took place in the divergent section near the wall and then convected downstream later in time. Nucleation in central plane was associated with larger pressure drop and higher vapor-content (higher *VF*); whereas lower pressure drop and more liquid-content (lower *VF*) was observed near the walls. The two-phase mixture was convected downstream and pushed away from the walls due to re-circulation region near the top wall. Nucleation rate, *Ma*, and *VF* increased with increasing the mass flow rate at constant exit pressure. For the smallest mass flow rate tested, i.e. $\dot{m}$= 0.050 kg/s, the pressure drop required for nucleation was obtained downstream of the throat and the nucleation rate was larger near the wall everywhere. It was observed that condensation, i.e. formation of stable liquid droplets near the walls due to deceleration were more significant than cavitation in near-critical conditions. The presented computational conditions are of relevance to the real compressor inlet conditions; indicating that even a small pressure drop near the critical point leads to a large volume of liquid (with respect to the size of the nozzle) downstream of the throat that moves downstream of the nozzle and cavitation in the sharp corners of the throat. Thus, we predict that condensation and cavitation near the critical point might affect compressor performance; especially, at higher mass flow rates, the nucleation is more likely to occur due to larger pressure drops. To complement computational studies and to validate CFD models, a 2-D venturi system with a converging-diverging (C-D) profile and optical access was designed, constructed and installed in an experimental test facility. Throughout the project numerous issues were encountered and changes were constantly made to lower the leakage flow in the test section. Towards the end of the project, O-rings were installed between wall of C-D profile and sapphire windows to eliminate leakage flow. Some videos were recorded for inlet

conditions around the critical point to obtain qualitative information of the condensation behavior. More high speed videos and advanced diagnostics will be conducted in the near future to obtain quantitative information regarding the flow field during condensation. Erosion samples were prepared and short term (<20 hours) erosion tests were conducted. None of the material samples (6061T, 316 Stainless Steel, 304 Stainless Steel and Inconel 625) exhibiting any noticeable weight changes before and after the erosion tests. More long term erosion tests will be conducted in the near future.

References

[1] Jarrahbashi, Dorrin, S. R. Pidaparti, and Devesh Ranjan. "Nucleation of super-critical carbon dioxide in a venturi nozzle" *Nuclear Engineering and Design* 310 (2016): 69-82.

[2] Feher, E. G., 1968, "The supercritical thermodynamic power cycle", Energy Conversion, 8, pp. 85-90.

[3] Dostal, V., Hejzlar, P., and Driscoll, M. J., 2006, "High performance supercritical carbon dioxide cycle for next generation nuclear reactors", Nuclear Technology, 154(3), pp. 265–282.

[4] Dostal, V., Hejzlar, P., and Driscoll, M. J., 2006, "The supercritical carbon dioxide power cycle: Comparison to other advanced power cycles", Nuclear Technology, 154(3), pp. 283–301.

[5] Ma, Z., Turchi, C. "Advanced supercritical carbon dioxide power cycle configurations for use in concentrating solar power systems", Proceedings of Supercritical CO_2 Power Cycle Symposium 24, pp. 24-25.

[6] Persichilli, M., Kacludis, A., Zdankiewicz, E. and Held, T., 2012, "Supercritical CO2 Power Cycle Developments and Commercialization: Why sCO2 can Displace Steam", Power-Gen India & Central Asia 2012, 19-21 April, 2012, Pragati Maidan, New Delhi, India.

[7] Muto, Y., Ishiyama, S., Kato, Y., Ishizuka, T., & Aritomi, M., 2010, "Application of Supercritical CO2 Gas Turbine for the Fossil Fired Thermal Plant", Journal of Energy and Power Engineering, 4(9), pp.7-19.

[8] Pecnik, R., Rinaldi, E., and Colonna, P., 2012, "Computational fluid dynamics of a radial compressor operating with supercritical CO_2", Journal of Engineering for Gas Turbines and Power, 134(12), pp. 1223011-1223018.

[9] Takagi, K., Muto, Y., Ishizuka, T., Kikura, H., and Aritomi, M., 2010, "Research on flow characteristics of supercritical CO_2 axial compressor blades by CFD analysis", Journal of Power and Energy Systems, 4(1), pp. 138–149.

[10] Nakagawa, M., Berana, M. S., and Kishine, A., 2009, "Supersonic two-phase flow of CO_2 through converging-diverging nozzles for the ejector refrigeration cycles", International Journal of Refrigeration, 32(6), pp. 1195–1202.

[11] Yazdani, M., Alahyari, A., and Radcliff, T., 2014, "Numerical modeling and validation of supersonic two-phase flow of CO_2 in converging-diverging nozzles", Journal of Fluid Engineering, 136, pp. 0145031-6.

[12] Lettieri, C, Yang, D., and Spakovszky, Z., 2015, "An investigation of condensation effects in supercritical carbon dioxide compressors", Journal of Engineering for Gas Turbines and Power, 137, pp. 0826021-8.

[13] Baltadjiev ND, Lettieri C, and Spakovszky Z., 2015, "An investigation of real gas effects in supercritical CO_2 centrifugal compressors", ASME Journal of Turbomachinery, 137(9), pp. 0910031-13

[14] OpenFOAM, 2012, "User Guide 2.1.1". [Online]

[15] Yuan, H., Pidaparti, Wolf, M., Edlebeck, J., Anderson, M., 2015, "Numerical modeling of supercritical carbon dioxide flow in see-through labyrinth seals", Nuclear Engineering and Design, 293, pp. 436-446.

[16] Pidaparti, Sandeep R. "A Computational Study on the Leakage of Supercritical Carbon Dioxide through Labyrinth Seals." M.S thesis, 2013

[17] Ghiaasiaan, S. Mostafa, 2007, "Two-phase flow, boiling, and condensation: in conventional and miniature systems", Cambridge University Press

[18] Zivi, S. M. 1964. "Estimation of steady-state steam void-fraction by means of the principle of minimum entropy production", Transactions ASME, Journal of Heat Transfer, Series C, 86, pp. 247-252

[19] Smith, S. L. 1969, "Void fractions in two-phase flow: a correlation based upon an equal velocity head model", Proceedings of the Institution of Mechanical Engineers, 184(1), pp. 647-664.

[20] Brennen, C. E., 2005, "Fundamentals of multiphase flow", Cambridge University Press, New York.

[21] McDonald, J. E., 1962, "Homogeneous nucleation of vapor condensation. I. thermodynamic aspects," American Journal of Physics, 30(12), pp. 870–877

[22] Dykas, Sławomir, and Włodzimierz Wróblewski. "Numerical modelling of steam condensing flow in low and high-pressure nozzles" *International Journal of Heat and Mass Transfer* 55, no. 21 (2012): 6191-6199.

Chapter 3 Techno-economic analysis of heat rejection options for the sCO_2 Brayton cycles

Abstract

Techno-economic feasibility of dry air cooling the supercritical carbon dioxide (S-CO_2) Brayton cycle has been investigated. A radiator type CO_2-to-air heat exchanger has been identified in the current market in an attempt to reduce the capital cost of the power plant. A quotation for the same is obtained and the heat exchanger was modeled in engineering equation solver (EES) to confirm the quoted heat exchanger performance and sizing. A cost-based optimization procedure was employed to identify the cycle optimum operating conditions with the goal of minimizing the plant capital cost per unit electrical output ($/kWe) for the Advanced Fast reactor (AFR) with 250 MW_{th} heat input. Cycle operating conditions such as minimum temperature, minimum pressure, and maximum pressure are chosen as the parameters to be optimized. Minimum pressure and minimum temperature are selected to be in the vicinity of pseudo-critical line to take advantage of the high fluid density near the pseudo-critical point while an increasing minimum CO_2 temperature is dictated by the ambient air temperature. The cycle maximum pressure is varied from 18 to 30 MPa. The mechanical design of the cycle heat exchangers (reactor intermediate sodium-to-CO_2 heat exchanger, high temperature recuperator, and the low temperature recuperator) and the piping are modified as per ASME code requirements to withstand the higher cycle design pressures. The associated change in the cost of components is also taken into account. All the calculations are performed using the Argonne National Laboratory Plant Dynamics Code (PDC) in conjunction with newly developed air cooler model assuming that the air is at an ambient temperature of 30^{o}C. The air cooler model calculations take into account the tradeoff between the cooler size and the required air pumping power. The calculations show that the optimum cycle conditions correspond to a minimum CO_2 pressure of 8.2 MPa, minimum CO_2 temperature of 35^{o}C, and a maximum CO_2 pressure of 25 MPa. Corresponding to these conditions, the plant $/kWe is only about 1% higher than that of a water cooled plant utilizing a compact diffusion-bonded CO_2-to-water heat exchanger technology. Finally, the effect of higher ambient air temperatures on the power consumption and the plant $/kWe is investigated.

Introduction

The recompression supercritical carbon dioxide (S-CO_2) Brayton cycle has been gaining a lot of interest for energy conversion in nuclear power, and concentrated solar power (CSP) systems because of higher plant efficiency than the traditional Rankine superheated steam cycle, especially, as the turbine inlet temperature is increased past 500^{o}C. For sodium cooler fast reactors (SFRs) use of S-CO_2 cycle for power conversion will also eliminate dangerous sodium-water interactions. The cycle achieves high efficiency by utilizing the high fluid density near the pseudo-critical point during compression process, thereby, reducing the back work ratio of the cycle. The high energy density of S-CO_2 reduces the size of turbomachinery which leads to a compact footprint when combined with the compact diffusion bonded technology for the heat exchangers. The cycle is also attractive because of the ability to dry air cool the cycle, thereby, completely eliminating the need for water cooling. This is particularly important for the CSP plants which are most likely to be set up in a desert where water resources are extremely scarce.

Therefore, it is important to investigate the techno-economic feasibility of using air as the ultimate heat sink for sCO_2 cycles. Previous study at Argonne National Laboratory (ANL) [1] in this regard, concluded that the air cooling option is technically feasible provided that the penalty is paid in terms of both reduced plant efficiency and increased plant capital cost. The study focused on reducing the approach temperature in the cooler (and hence, cooler volume) by increasing the minimum temperature in the cycle and operating the main compressor inlet close to the pseudo-critical line. The calculations showed that increasing the minimum temperature of the cycle to 40^{o}C lead to least plant capital cost per unit electrical output ($/kWe). The previous study made two assumptions which are subject to change in this report.

1) The CO_2-to-air cooler was assumed to be based on Heatric hybrid heat exchanger technology (H^2X – FPHE configuration on the air side) [2]. This will allow for raw material savings over the printed circuit heat exchanger (PCHE) technology but the cost of such a cooler is still significantly higher compared to CO_2-to-water cooler. This is primarily due to the fact that the properties of air and water as a heat transfer media are quite different. Hence, the first goal of the current study is to identify alternative CO_2-to-air cooler designs in an attempt to reduce the cooler cost.

2) The cycle maximum pressure was assumed to be 20 MPa. With recent developments in Heatric diffusion bonding technology, PCHEs which can withstand pressures up to 40 MPa can be fabricated. Therefore, by increasing the cycle maximum pressure some of the cycle efficiency lost due to increase in cycle minimum temperature (dictated by ambient air temperature for air cooled cycle) can be recovered, thereby, reducing the plant $/kWe. This will of course increase the cost of heat exchangers, piping etc. which has to be taken into account during calculation of the plant $/kWe.

With these modifications the cycle conditions are re-optimized to minimize the plant $/kWe in comparison to the reference water cooled plant.

Reference water cooled cycle conditions and heat exchangers design

For the current study, the cycle optimization is performed for the S-CO_2 cycle developed for 100 MWe sodium cooled Advanced Fast Reactor (AFR-100) applications. In order to have a direct comparison between the air and water cooled cycles, the operating conditions and the plant $/kWe of the water cooled cycle are used as reference conditions for the optimization study. Figure 1 shows the operating conditions of the reference water cooled AFR-100 plant. The boundary conditions for the air are assumed to be same as the water boundary conditions i.e. 30^{o}C inlet temperature and 0.101 MPa (1 atm) outlet pressure. The reference dimensions for reactor heat exchanger (RHX), high temperature recuperator (HTR), low temperature recuperator (LTR) are shown in Table 1. These dimensions are based on the previous cost-based optimization study [3] of water cooled S-CO_2 cycle for the reference conditions (cycle minimum pressure of 7.4 MPa, cycle minimum temperature of 31.25^{o}, and cycle maximum pressure of 20 MPa). When any of the cycle operating conditions are changed, it is required to re-optimize the flow split fraction between compressors as well as the heat exchangers design. For example, split fraction of 0.68 and the heat exchangers designs in Table 1 may not lead to optimum $/kWe if cycle maximum pressure is changed to let's say, 25 MPa. Another important mechanical design

aspect to keep in mind is that as the cycle maximum pressure is changed the cycle piping have to be-redesigned to withstand the pressure at the design temperature which will affect the capital cost of the plant. Hence, the goal of the current study is to investigate the effect of cycle minimum pressure, minimum temperature, and maximum pressure on the power plant $/kWe and find the optimum cycle conditions to minimize $/kWe.

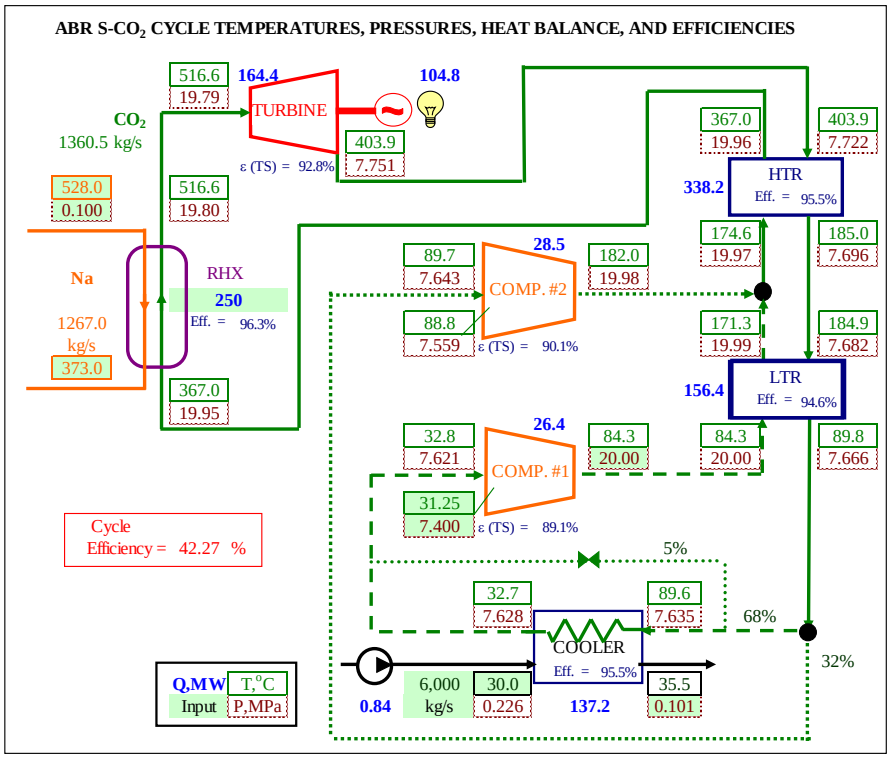

Figure 1: Reference AFR-100 water cooled S-CO_2 cycle calculations

Table 1: Heat exchangers design for the reference cycle conditions

Reference design of the RHX

Type	Z/I PCHE	
Number of units	96	All parameters below are per unit
Heat transfer capacity	2.6 MW_{th}	
Hot side fluid	Na	
Hot side temperature inlet	528°C	
Hot side temperature outlet	373°C	
Hot side pressure inlet	0.1 MPa	
Hot side pressure outlet	0.1 MPa	
Hot side pressure drop	0.0 kPa	
Hot side flow rate	13.2 kg/s	
Cold side fluid	CO_2	
Cold side temperature inlet	367°C	
Cold side temperature outlet	516.5°C	
Cold side pressure inlet	19.931 MPa	
Cold side pressure outlet	19.786 MPa	
Cold side flow rate	14.2 kg/s	
Effectiveness	96.3%	

Efficiency (CO_2 side)	92.9%	
Unit width	0.6 m	
Unit height	0.6 m	
Unit length	1.5 m	
Plate material	SS316	
Number of plates	84	Each side
Hot side channel diameter	6.0 mm	Semi-Circular channel
Hot side channel pitch	6.5 mm	
Hot side plate thickness	5.1 mm	
Hot side channel length	1.5 m	
Hot side number of channels	87	Per plate
Hot side channel angle	0^o	
Cold side channel diameter	2.0 mm	Semi-Circular channel
Cold side channel pitch	2.6 mm	
Cold side plate thickness	1.6 mm	
Cold side channel length	1.732 m	
Cold side number of channels	189	
Cold side channel angle	60^o	
Void fraction	60.5%	From channels
Metal mass	1.701 tonnes	Dry
Plate mass	2.268 tonnes	Dry
Properties		
Hot side – inlet		
Density	828.1 kg/m^3	
Specific heat	1260.1 J/kg-K	
Hot side – outlet		
Density	863.9 kg/m^3	
Specific heat	1289.1 J/kg-K	
Cold side – inlet		
Density	165.8 kg/m^3	
Specific heat	1226 J/kg-K	
Cold side – outlet		
Density	128.9 kg/m^3	
Specific heat	1234.8 J/kg-K	

Reference design of the HTR

Type	PCHE	
Number of units	48	All parameters below are per unit
Heat transfer capacity	7.06 MW_{th}	
Hot side temperature inlet	404^oC	
Hot side temperature outlet	185^oC	
Hot side pressure inlet	7.721 MPa	
Hot side pressure outlet	7.695 MPa	
Hot side flow rate	28.4 kg/s	
Hot side pressure drop	26.2 kPa	
Cold side temperature inlet	174.7^oC	
Cold side temperature outlet	367.1^oC	
Cold side pressure inlet	19.971 MPa	
Cold side pressure outlet	19.962 MPa	
Cold side flow rate	28.4 kg/s	
Cold side pressure drop	9.5 kPa	
Effectiveness	95.5%	

Heat transfer area	311.7 m^2	
Unit width	1.5 m	
Unit height	0.6 m	
Unit length	0.6 m	
Heat transfer length	0.38 m	
Plate material	SS316	
Number of plates	283	Each side
Hot side channel diameter	1.3 mm	Semi-Circular channel
Hot side channel pitch	1.7 mm	
Hot side plate thickness	1.0 mm	
Hot side number of channels	751	Per plate
Hot side channel angle	60^o	
Hot side channel length	0.439 m	
Cold side channel diameter	1.3 mm	Semi-Circular channel
Cold side channel pitch	1.7 mm	
Cold side plate thickness	1.0 mm	
Cold side number of channels	751	
Cold side channel angle	60^o	
Cold side channel length	0.439 m	
Void fraction	38.4%	From channels
Metal mass	2.653 tonnes	Dry
Properties		
Hot side – inlet		
Density	60.5 kg/m^3	
Specific heat	1159.2 J/kg-K	
Hot side – outlet		
Density	96.4 kg/m^3	
Specific heat	1137.9 J/kg-K	
Cold side – inlet		
Density	287.6 kg/m^3	
Specific heat	1482.7 J/kg-K	
Cold side – outlet		
Density	128.9 kg/m^3	
Specific heat	1226.1 J/kg-K	

Reference design of the LTR

Type	PCHE	
Number of units	48	All parameters below are per unit
Heat transfer capacity	3.26 MW_{th}	
Hot side temperature inlet	185^oC	
Hot side temperature outlet	89.8^oC	
Hot side pressure inlet	7.68 MPa	
Hot side pressure outlet	7.664 MPa	
Hot side pressure drop	15.9 kPa	
Hot side flow rate	28.4 kg/s	
Cold side temperature inlet	84.3^oC	
Cold side temperature outlet	171.3^oC	
Cold side pressure inlet	19.995 MPa	
Cold side pressure outlet	19.986 MPa	
Cold side flow rate	19.3 kg/s	

Cold side pressure drop	8.5 kPa	
Effectiveness	94.6%	
Heat transfer area	311.7 m^2	
Unit width	1.5 m	
Unit height	0.6 m	
Unit length	0.6 m	
Heat transfer length	0.38 m	
Plate material	SS316	
Number of plates	283	Each side
Hot side channel diameter	1.3 mm	Semi-Circular channel
Hot side channel pitch	1.7 mm	
Hot side plate thickness	1.0 mm	
Hot side number of channels	751	Per plate
Hot side channel length	0.439 m	
Hot side channel angle	60^o	
Cold side channel diameter	1.3 mm	Semi-Circular channel
Cold side channel pitch	1.7 mm	
Cold side plate thickness	1.0 mm	
Cold side number of channels	613	
Cold side channel length	0.537 m	
Cold side channel angle	90^o	
Void fraction	38.4%	From channels
Metal mass	2.653 tonnes	Dry
Properties		
Hot side – inlet		
Density	96.2 kg/m^3	
Specific heat	1137.6 J/kg-K	
Hot side – outlet		
Density	142 kg/m^3	
Specific heat	1372 J/kg-K	
Cold side – inlet		
Density	566.6 kg/m^3	
Specific heat	2579 J/kg-K	
Cold side – outlet		
Density	292.4 kg/m^3	
Specific heat	1500 J/kg-K	

Selection of CO_2-to-air cooler

As mentioned in the previous section, use of compact diffusion bonded heat exchangers as CO_2-to-air cooler significantly increases the capital cost of the cooler. In an effort to reduce the plant $/kWe, alternative options for the CO_2-to-air cooler were explored. In this section, details of the selected cooler design and the cooler calculations for the reference cycle conditions are summarized. Figure 2 shows the CAD model of a cooler module selected for the current study. As can be seen, the CO_2 and air are setup in cross flow arrangement with CO_2 flowing inside the finned tubes and the fans blow air over the tubes in a fashion similar to that of a car radiator. For each cooler module, CO_2 undergoes three passes with two mixing chambers to ensure uniform flow temperature between the passes. The design uses three fans per module and

it is assumed that these fans distribute air flow uniformly throughout the cooler module. This assumption is required for modeling of the cooler module and the calculations later confirmed that it was indeed a fair assumption.

A quotation for this cooler was obtained from Harsco Industrial Air-X-Changers for the reference cooler conditions in Figure 1 and a model was developed in Engineering Equation Solver (EES) to confirm the performance and sizing of the cooler. The EES code in conjunction with the ANL PDC is used for the cost-based optimization that will be described in the following sections. The following section presents the details of the modeling methodology of the CO_2-to-air cooler developed based on the quote obtained from Harsco Industrial Air-X-Changers (http://www.harscoaxc.com/).

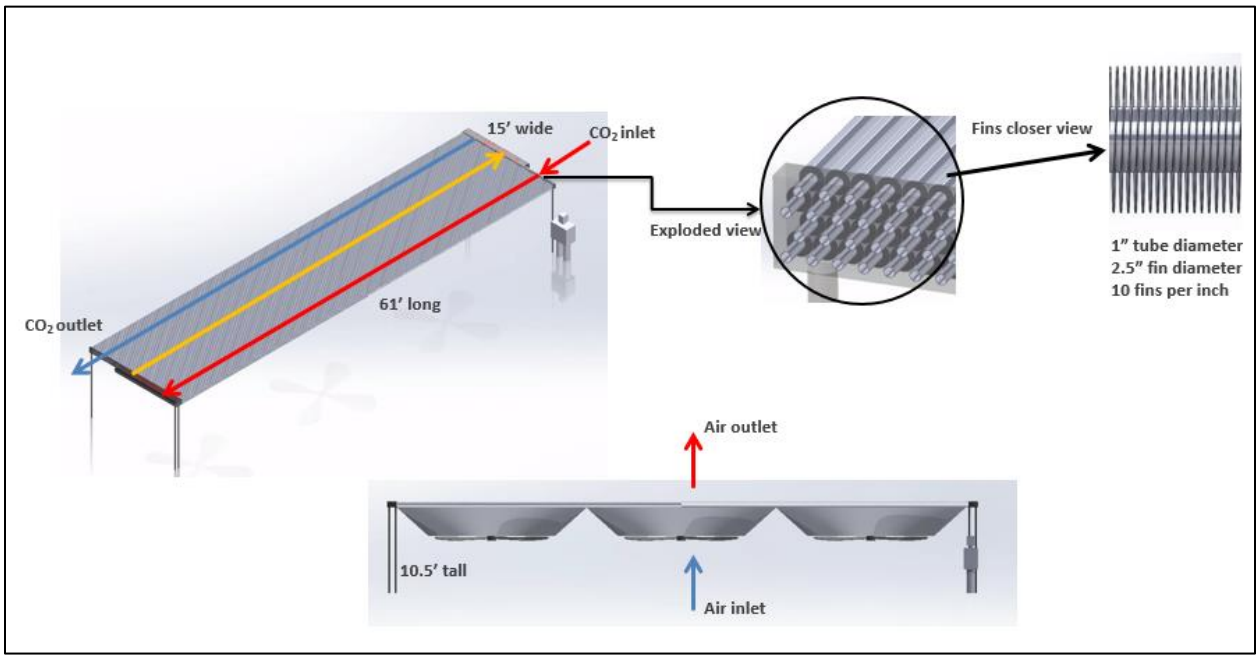

Figure 2: CAD model of the selected CO_2-to-air cooler. A six-foot tall person is shown for reference

Modeling of CO_2-to-air cooler

This section presents the modeling methodology of the CO_2-to-air cooler presented in Figure 2. Table 2 depicts the inputs that were regularly adjusted during the plant optimization study. The last column in the table is labelled as the "base case" which represents the cooler conditions that the heat exchanger was designed for by Harsco.

Table 2: Model inputs taken from overall cycle model. The base case values represent the design parameters for the modeled heat exchanger.

Model Input	Description	Base Case Values
$\dot{m}_C$	Mass flow of sCO2 that passes through the cooler (Given as cycle mass flow and split fraction)	$878.9\,\frac{kg}{s}$
T_{in}	Inlet Temperature of sCO2	$89.6\ C$
P_{in}	Inlet Pressure of sCO2	$7.635\ MPa$
T_{out}	Outlet Temperature of sCO2	$32.657\ C$
T_{air}	Ambient Air Temperature	$30\ C$
N_{HX}	Number of cooler units	86

Table 2 represents the design of the heat exchanger. Each parameter corresponds to a physical dimension described by the Harsco quoted design. The fan efficiency is a parameter that was calculated based on the correlations described in later sections and the manufacturer's given fan power and air flow rates.

Table 3: Cooler design parameters (per unit) used from Harsco quoted design.

Cooler Design Parameters	Description	Value
FF	Fouling factor for tubing used in resistance network	$0.000176 \frac{m^2 K}{W}$
SA_{bare}	Bare tubing surface area.	$456.3\ m^2$
$SA_{extended}$	Extended tubing and fins surface area	$9765\ m^2$
Tube Material$	Material of tubing	Stainless Steel 316
Fin Material$	Material of fins	Aluminum
fin_{pitch}	Fin pitch	$393.7 \frac{fins}{m}$ $(10 \frac{fins}{in})$
th_{fin}	Fin thickness	$0.406\ mm\ (0.016\ in)$
D_{fin}	Fin outer diameter	$57.15\ mm\ (2.25\ in)$
h_{tubes}	Distance between tube rows	$49.49\ mm$
w_{tubes}	Distance between tube columns	$57.15\ mm\ (2.25\ in)$
D_o	Tube outer diameter	$25.4\ mm\ (1\ in)$
th_{tubes}	Tube wall thickness	$1.65\ mm\ (0.065\ in)$
N_{pass}	Number of passes along cooler	3
N_{rows}	Number of tube rows	4
N_{tubes}	Total number of tubes	322
$N_{tubes}[pass]$	Number of tubes in each pass	$107, 108, 107$
N_{cols}	Number of tube columns in each row	$81, 80, 81, 80$
$Length$	Length of cooling unit (tube length).	$18.29\ m$
η_{fan}	Fan efficiency (Based on calculations from design fans and CHX geometry)	0.41

Air side thermal-hydraulic correlations

The air side correlations required for this analysis are the average heat transfer coefficient and the pressure drop. The heat transfer coefficient is used in the resistance network between the air and the sCO2. The pressure drop is used to determine the required fan power.

The difficulty with modeling compact heat exchangers (finned tubes spaced close together) is that the heat transfer coefficient and the pressure drop are largely dependent on the geometry of the finned tubes. The correlations for the heat transfer coefficient and pressure drop that are used in EES have a limited selection of finned tube geometry. This leads to possible error in the heat transfer coefficient determined for these calculations. The geometry chosen for modeling the Harsco design is classified as finned circular tubes with surface CF-8.8-1.0J, tube configuration (a). Table 3 shows a comparison for the finned tube geometries of the Harsco design and the tubes used for the correlation.

Table 4: Finned tube geometry comparison between the Harsco design and the compact heat exchanger used in EES correlations.

Variable	Harsco Design	EES CHX
Fin Thickness	0.4064 mm	0.3048 mm
Fin Pitch	393.7 per m	346 per m

Fin Diameter	57.15 mm	44.12 mm
Tube Diameter	25.4 mm	26.01 mm
Horizontal Spacing	57.15 mm	52.4 mm
Vertical Spacing	49.49 mm	49.76 mm

The compact heat exchanger correlations used in EES are calculated based on the Colburn j factor as described by Kays and London (1984) [4]. The Colburn j factor is a function of the Reynolds number. Table 4 shows values of the Colburn j factor for different values of Reynolds number.

$$j_H = F(Re)$$

$$Re = \frac{GD_h}{\mu_a}$$

$$G = \frac{\dot{m}_a}{\sigma A_{fr}}$$

Where j_H is the Colburn j factor, Re is the Reynolds number, G is the product of the maximum mass velocity and the density of the fluid, D_h is the hydraulic diameter of the flow, μ_a is the dynamic viscosity of the air, $\dot{m}_a$ is the mass flow of air, σ is the ratio of the freeflow area to the frontal area, and A_{fr} is the frontal area perpendicular to the flow.

The hydraulic diameter for flow over a bank of tubes normalized by the flow length is defined as four times the cross sectional area divided by the total heat transfer area.

$$\frac{D_h}{L} = 4\frac{A_c}{A}$$

Where L is the length in the flow direction, A_c is the cross sectional area of the flow, and A is the total heat transfer surface area.

The heat transfer coefficient is calculated from the definition of the Colburn j factor being a function of the Stanton number. The equation for the heat transfer coefficient reduces down to:

$$\bar{h}_a = \frac{j_H G c_{P,a}}{Pr^{2/3}}$$

$$Pr = \frac{c_{P,a}\mu_a}{k_a}$$

Where $\bar{h}_a$ is the air side heat transfer coefficient, $c_{P,a}$ is the specific heat of air, Pr is the Prandtl number, and k_a is the conductivity of air.

The pressure drop is calculated with correlations used in EES as described by Kays and London (1984) [4]. The correlation is simplified using the assumption that the inlet air density is equal to the outlet density. Table 4 shows values of the friction factor for different values of Reynolds number.

$$f = F(Re)$$

$$\Delta P_a = \frac{G^2}{2\rho_a} f \frac{\alpha * Height}{\sigma}$$

$$Height = (N_{rows} - 1) * h_{tubes} + D_{fin}$$

Where, ΔP_a is the air side pressure drop considered for the entire unit, f is the friction factor, α is the heat transfer area per total volume, and $Height$ is the flow distance of the air; The friction factor is determined in EES by interpolating experimental data presented by Kays and London (1984) [4].

The correlations represented in Table 5 can be determined using curves of best fit. The equations for the Colburn j factor and the friction factor as functions of Reynolds numbers are best represented by the following power laws.

$$j_H = 0.0109 \left(\frac{Re}{1000}\right)^{-0.37}$$

$$f = 0.0276 \left(\frac{Re}{1000}\right)^{-0.244}$$

These best fit curves are shown in Figure 2.

Table 5: Table used in EES for interpolation of the Colburn j factor and friction factor for a given Reynolds number. These values are taken from the experimental data described by Kays and London (1984) [4].

Re (10^{-3})	j_H	f
1.5	0.009397	0.02513
1.623	0.009132	0.02466
1.757	0.008869	0.02418
1.901	0.008592	0.02369
2.058	0.008344	0.02316
2.227	0.0081	0.02275
2.41	0.007859	0.02229
2.609	0.007657	0.02184
2.823	0.007409	0.02143
3.055	0.007199	0.02101
3.307	0.006983	0.02058
3.579	0.006794	0.02011
3.873	0.006597	0.01969
4.192	0.00639	0.01939
4.536	0.006207	0.01898
4.909	0.006021	0.0186
5.313	0.005846	0.01823
5.75	0.005679	0.01793
6.223	0.005497	0.01754
6.735	0.00534	0.01727
7.289	0.005176	0.017
7.889	0.005057	0.01674
8.538	0.00494	0.01648
9.24	0.004826	0.01623
10	0.004714	0.01598

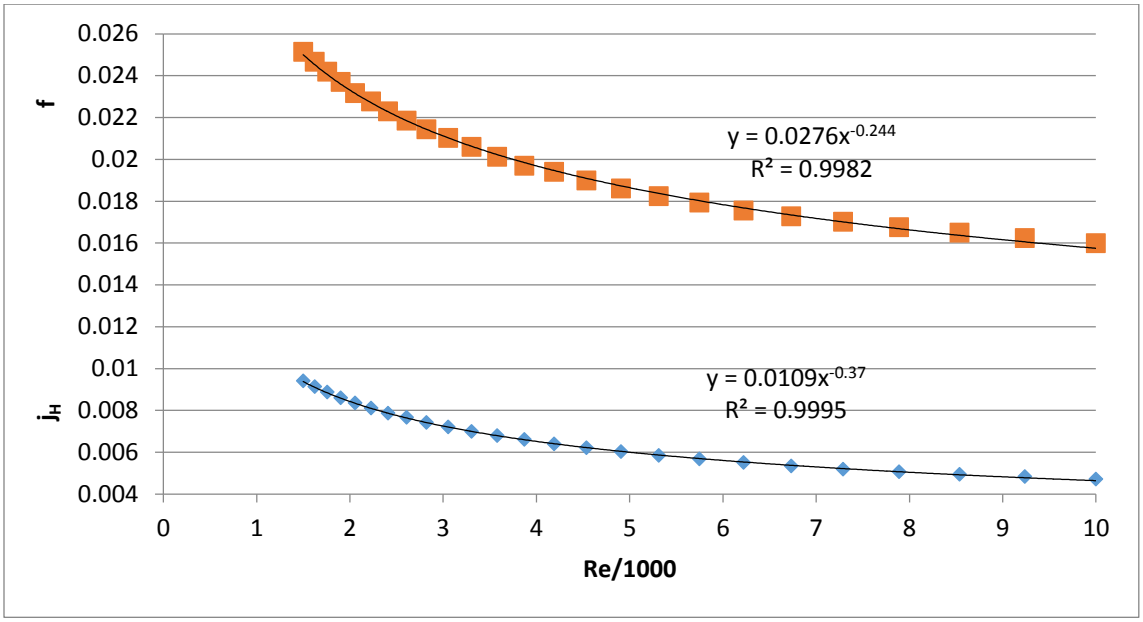

Figure 3: Plotted correlations for the Colburn j factor and friction factor as a function of the Reynolds number.

The air side pressure drop is used to determine the total fan power. The fan power is defined as the product of the volumetric flow of air and the pressure drop seen by the air.

$$\dot{W}_{fan} = \frac{\dot{m}_a \Delta P_a}{\rho_a \eta_{fan}}$$

Where, $\dot{W}_a$ is the fan power, ρ_a is the inlet air density, and η_{fan} is the fan efficiency.

The fan efficiency is calculated based on the Harsco design parameters and is correlated to using the compact heat exchanger geometry used from EES. The Harsco design uses a total of 3 fans per cooler unit, each with a rated power of 32.95 horsepower. The air-side performance from Harsco has a flow rate of 557,814 standard cubic feet per minute. This air flow rate is converted to actual cubic feet per minute by using a standard state of 293 K and 1 atmosphere. The air side pressure drop for these conditions along with the given dimensions of the designed unit is calculated using the correlation in EES. The fan efficiency is then calculated.

$$\eta_{fan} = \frac{\dot{V}_{air} \Delta P_a}{N_{fans} \dot{W}_{HARSCO}}$$

For this analysis, the fan efficiency was calculated to be 41%.

The last correlation used for air side calculations is for the surface efficiency of the finned tubes. This surface efficiency is used in the resistance network for convection from the air to the finned tubes. The overall surface efficiency is a function of the fin efficiency and the ratio of finned surface area to the total surface area exposed to the air.

$$A_{fin}/_{A} = \frac{SA_{extended} - SA_{bare}}{SA_{extended}}$$

Where, $A_{fin}/_{A}$ is the ratio of the finned surface area to the total surface area exposed to the air.

The fin efficiency is calculated from a built-in procedure in EES. The procedure is a function of the fin dimensions, the air side heat transfer coefficient, and the conductivity of the fin material.

$$\eta_{fin} = eta\_fin\_annular\_rect\left(fin_{th}, \frac{D_o}{2}, \frac{D_{fin}}{2}, \bar{h}_a, k_{fins}\right)$$

Where, η_{fin} is the fin efficiency and k_{fins} is the conductivity of aluminum at the average temperature between the air and sCO_2 inlet states. The function calculates a non-dimensional parameter that is in turn used to calculate the fin efficiency through a series of Bessel functions.

$$mR_{out} = \frac{D_{fin}}{2}\sqrt{\frac{2\bar{h}_a}{k_{fins} th_{fin}}}$$

$$\eta_{fin} = \frac{2D_o}{D_{fin}} \frac{BesselK\left(1, mR_{out}\frac{D_o}{D_{fin}}\right) BesselI(1, mR_{out}) - BesselI\left(1, mR_{out}\frac{D_o}{D_{fin}}\right) BesselK(1, mR_{out})}{\frac{BesselK\left(0, mR_{out}\frac{D_o}{D_{fin}}\right) BesselI(1, mR_{out}) + BesselI\left(0, mR_{out}\frac{D_o}{D_{fin}}\right) BesselK(1, mR_{out})}{mR_{out}\left(1 - \left(\frac{D_o}{D_{fin}}\right)^2\right)}}$$

Where, mR_{out} is the non-dimensional parameter used for the annular rectangular fin geometry and $Bessel$ is the Bessel function call. $BesselI(x, y)$ returns the value of the x[th]-order Modified Bessel function of the first kind for the argument y. $BesselK(x, y)$ returns the value of the x[th]-order Modified Bessel function of the second kind for the argument y. The fin efficiency correlations are as discussed by Nellis and Klein (2009) [5].
The surface efficiency is calculated from these two parameters.

$$\eta_o = 1 - A_{fin}/_{A}\left(1 - \eta_{fin}\right)$$

Where, η_o is the overall surface efficiency used in the resistance network.

Table 6 shows the calculated values for the air-side correlations using the base case of input conditions shown in Table 1.

Table 6: Air side parameter values calculated in the base case model

Parameter	Description	Base Case Value
$\bar{h}_a$	Air side heat transfer coefficient	$80.76 \frac{W}{m^2 K}$
$\dot{W}_{fan}$	Fan power per unit	$65758\ W$
η_{fan}	Fan efficiency	0.41
ΔP_a	Air side pressure drop	$96.76\ Pa$

η_{fin}	Fin efficiency	0.8294
η_o	Overall surface efficiency	0.8373

CO_2 side thermal-hydraulic correlations

This section describes the procedure used to find the heat transfer coefficient and the pressure drop for the sCO_2. Even though there are no indices, these calculations are used for each discrete sub-section of the cooler as an internal procedure to the model.

The correlations for the supercritical carbon dioxide are for fully developed, turbulent, internal pipe flow as discussed by Nellis and Klein (2009) [5]. The heat transfer coefficient and the pressure drop are related to the Reynolds number and Prandtl number.

$$Re = \frac{\rho U D_i}{\mu}$$

$$Pr = \frac{\mu}{\rho \alpha}$$

Where, ρ is the density of the sCO_2, U is the average flow velocity, D_i is the internal tube diameter, μ is the dynamic viscosity of the sCO_2, and α is the thermal diffusivity of the sCO_2.

The friction factor used to determine the pressure drop is an explicit correlation developed by Zigrang and Sylvester (1982) [6] for fully developed, turbulent flow through a duct.

$$f = \left[-2.01 \log_{10}\left(\frac{2\varepsilon}{7.54 D_i} - \frac{5.02}{Re}\log_{10}\left(\frac{2\varepsilon}{7.54 D_i} + \frac{13}{Re}\right)\right)\right]^{-2}$$

Where, ε is the surface roughness of the tubing. The tubes are considered to be smooth, so $\frac{e}{D_i}$ is considered to be negligible by using a value of 1e-6.

The Nusselt number is then calculated using a correlation developed by Gnielinski (1979) [7] for fully developed, turbulent flow.

$$\bar{N}u = \frac{\left(\frac{f}{8}\right)(Re-1000)Pr}{1+12.7\left(Pr^{\frac{2}{3}}-1\right)\sqrt{\frac{f}{8}}}$$

The average heat transfer coefficient is calculated from the Nusselt number and the pressure drop is calculated from the friction factor.

$$\bar{h} = \frac{\bar{N}u\, k}{D_i}$$

$$\Delta P = f L \frac{\rho U^2}{2 D_i}$$

Where, k is the thermal conductivity of the sCO_2 and L is the length of tubing.

Discrete sub-section Modeling

The cooler unit is numerically modeled as several smaller heat exchangers that are considered to have constant properties throughout. This approach is used for fluids that have large variation in thermal properties and there is no analytical solution to describe the change in flow properties.

The model breaks the cooler into a total of 120 sub-sections. The length of tubing is broken in 10 sub-sections of equal length in the direction of the sCO_2 flow.

$$N_{sub} = 10$$

$$dL = \frac{Length}{N_{sub}}$$

Where, dL is the length of each sub-section and N_{sub} is the number of sub-sections. The direction of the air flow is broken up to contain a single row of tubes (4 rows). The same breakdown of sub-sections occurs in each pass (3 passes), creating a pseudo 3-dimensionsal aspect to the numerical analysis.

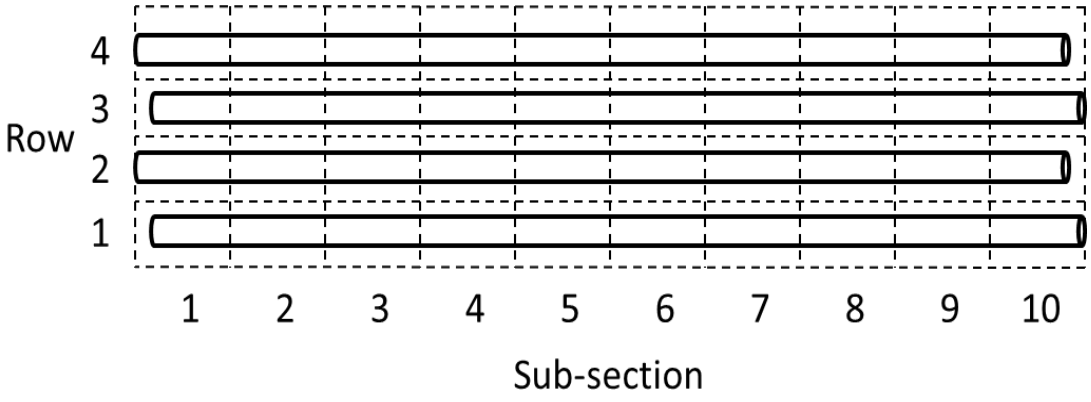

Figure 4: The discrete sub-sectioning for an example column of tubes is shown. The tubes along the same row contained in the same pass (i.e. all 27 tubes in the bottom row of the first pass) are assumed to be in the same state. (NOT shown to scale)

In order to keep track of the sub-sectioning in the model, an array methodology is implemented. This allows for a simple index notation to be used to specify the state of each sub-section. Each sub-section is represented as a node, with one additional node at the end to represent the exit conditions. The index notation used is as follows:

$$X[i][j][k]$$

The X represents the variable of interest at the given node (i.e. temperature or pressure). i (1-11) represents the node along the sCO_2 flow direction. The 11^{th} node represents the exit conditions for the sCO_2 along a row of tubes. j (1-5) represents the row of tubes with 1 being the bottom row (i.e. the row exposed to the ambient air temperature). The 5th node represents the exit

conditions for the air. k (1-3) represents the pass number. Not all three indices are used for every variable (i.e. the total number of tubes in each pass is $N_{tubes}[k]$ where k still represents the pass number).

The advantage of using this pseudo 3-dimensional approach, the temperature distributions in the sCO_2 and the air can be captured throughout the heat exchanger. Figure 5 shows an example temperature distribution. One should notice that the significant amount of CO_2 temperature reduction happens in the first two passes of the module. As the bulk temperature of CO_2 approaches the pseudo-critical temperature (defined as the temperature at which specific heat reaches a maximum value for a given pressure), significant increase in the number of cooler modules or flow rate of air is needed in order to remove rest of the waste heat from the CO_2. This means that even a 0.5°C increase in the minimum temperature of the cycle at reference minimum pressure (7.4 MPa) would reduce the number of cooler units by roughly 33%. Of course by doing this one would have to pay penalty in the form of reduced cycle efficiency. Hence, the $/kWe metric needs to be more carefully investigated around the pseudo-critical point for any potential savings.

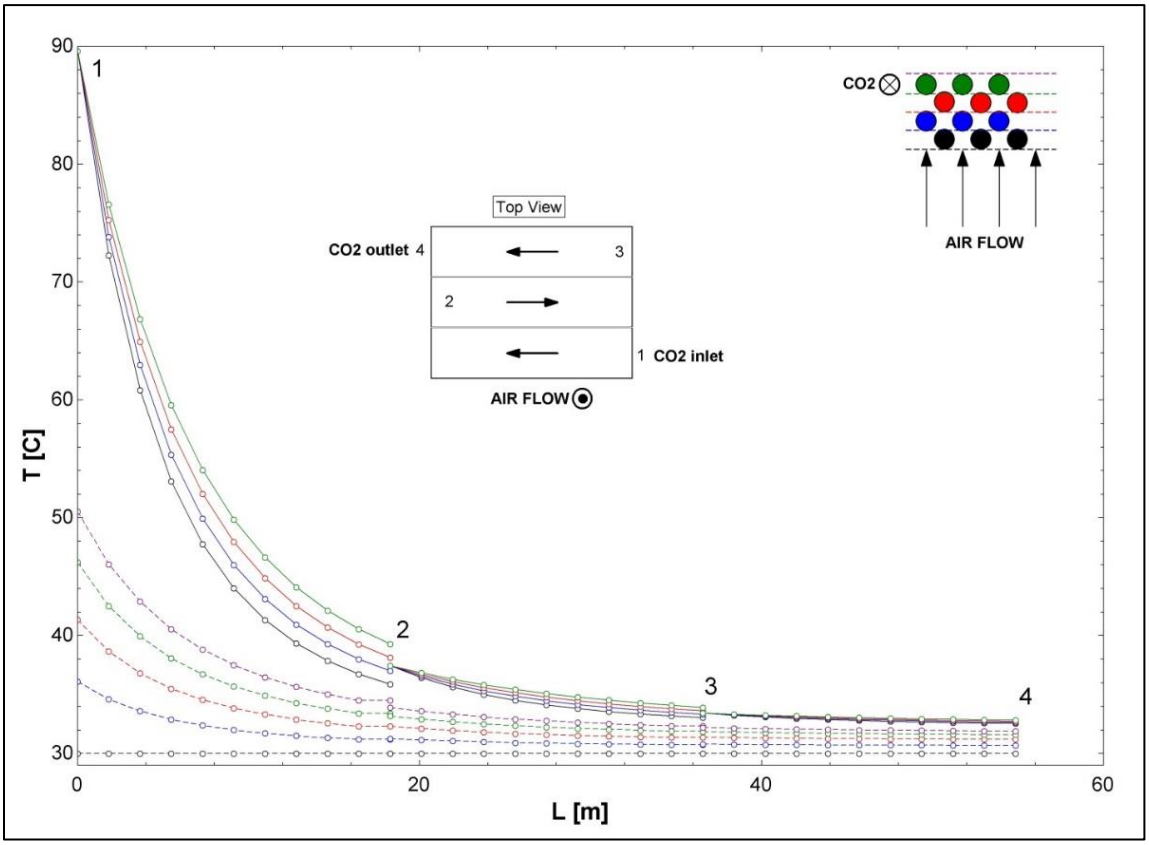

Figure 5: An example of sCO_2 and air temperature profiles in each cooler module, solid lines represent sCO_2 and dashed lines represent air

Energy balance and Conductance Calculations

This section explains the set of equations that are used on each sub-section in the model. The equations are set up in EES using "duplicate" statements that are used as loops. This makes is so each equation only needs to be written once, and EES will compute as if each equation is written for each index in the model simultaneously. The equations in this section are embedded in the appropriate duplicate statements for i from 1 to N_{sub}, for j from 1 to N_{rows}, and for k from 1 to N_{pass}.

The first part of this section performs an energy balance on the sCO_2 and the air. This is also where the sCO_2 internal flow correlations explained in section 2 are used. The energy balance for the sCO_2 occurs between each node along the tube length.

$$q_{sub}[i][j][k] = \dot{m}_c[j][k] * (h_c[i][j][k] - h_c[i+1][j][k])$$

Where $q_{sub}[i][j][k]$ is the heat transfer that occurs in each sub-section, $\dot{m}_c[j][k]$ is the mass flow of sCO_2 through the given row and pass, $h_c[i][j][k]$ is the specific enthalpy of the sCO_2 at each node. In order to define each node, one more property needs to be known. The internal flow correlations are used to calculate the pressure drop. With the inlet pressure known, the pressure at each node is determined.

$$call\ P\_pipeflow(C\$, T_c[i][j][k], P_c[i][j][k], \frac{\dot{m}_c[j][k]}{N_{cols}[j][k]}, D_i, dL, \frac{e}{D} : \bar{h}_c[i][j][k], \Delta P_c[i][j][k])$$

$$P_c[i+1][j][k] = P_c[i][j][k] - \Delta P_c[i][j][k]$$

Where, $\bar{h}_c[i][j][k]$ is the average heat transfer coefficient for the sCO_2 and $\Delta P_c[i][j][k]$ is the pressure drop along each sub-section. $\frac{\varepsilon}{D}$ is the relative surface roughness which is considered negligible, so a value of 1e-6 is used. The call function for the internal procedure takes the variables to the left of the colon as inputs and returns the variables to the right of the colon as outputs. This internal procedure is described in previous sections. The energy balance for the air occurs between each row of tubes.

$$q_{sub}[i][j][k] = \dot{m}_a \left(\frac{dL * Width[k]}{A_{fr}}\right) cp_a (T_a[i][j+1][k] - T_a[i][j][k])$$

$$Width[k] = Width * \frac{N_{tubes}[k]}{N_{tubes}}$$

Where, cp_a is the specific heat of the air and $Width[k]$ is the width of the pass. The total air mass flow along with the dimensional terms represent the mass flow of air through the given sub-section.

The next part of this section uses a correlation for cross flow heat exchangers to determine the effectiveness and number of transfer units in each sub-section. Using the number of transfer units, the conductance is determined. The effectiveness is defined as the actual heat transfer rate over the maximum possible heat transfer rate.

$$\epsilon[i][j][k] = \frac{q_{sub}[i][j][k]}{q_{max}[i][j][k]}$$

Where, $\epsilon[i][j][k]$ is the effectiveness and $q_{max}[i][j][k]$ is the maximum possible heat transfer rate for each sub-section. The maximum possible heat transfer is defined as the product of the minimum capacitance rate and the maximum temperature difference. The capacitance rate of both flows is the product of the mass flow and the specific heat of the fluid. The specific heat of the sCO_2 is calculated using the definition of specific heat; the change in enthalpy over the change in temperature.

$$cp_c[i][j][k] = \frac{h_c[i][j][k] - h_c[i+1][j][k]}{T_c[i][j][k] - T_c[i+1][j][k]}$$

$$\dot{C}_c[i][j][k] = \dot{m}_c[j][k] * cp_c[i][j][k]$$

$$\dot{C}_a[k] = \dot{m}_a \left(\frac{dL * Width[k]}{A_{fr}}\right) cp_a$$

$$\dot{C}_{min}[i][j][k] = MIN\left(\dot{C}_c[i][j][k], \dot{C}_a[k]\right)$$

$$q_{max} = \dot{C}_{min}(T_c[i][j][k] - T_a[i][j][k])$$

Where, $cp_c[i][j][k]$ is the specific heat of the sCO_2, $\dot{C}_c[i][j][k]$ is the capacitance rate of the sCO_2, and $\dot{C}_a[k]$ is the capacitance rate of the air flow per sub-section for the given pass.

The effectiveness is used to calculate the number of transfer units using a built-in function from EES. The correlation used for this cooler model is a cross flow configuration with one unmixed fluid. The air is considered unmixed from being separated by the fins and the sCO2 is considered mixed because the heat exchanger in each sub-section is a single finned tube where the sCO2 is allowed to mix inside the tube.

$$NTU[i][j][k] = HX('crossflow\_one\_unmixed', \epsilon[i][j][k], \dot{C}_a[k], \dot{C}_c[i][j][k], 'NTU')$$

Where, $NTU[i][j][k]$ is the number of transfer units. The function requires the first capacitance rate input to be the unmixed flow. The equation used for crossflow with one unmixed flow depends on if the unmixed flow capacitance rate is less than or greater than the mixed flow capacitance rate.

$$NTU = -ln\left(1 + \frac{1}{C_R} ln(1 - \epsilon C_R)\right) \; if \; \dot{C}_1 < \dot{C}_2$$

$$NTU = -\frac{1}{C_R} ln(C_R ln(1 - \epsilon) + 1) \; if \; \dot{C}_1 > \dot{C}_2$$

$$C_R = \frac{\dot{C}_{min}}{\dot{C}_{max}}$$

Where, C_R is the capacitance ratio. In this case, $\dot{C}_1$ represents the air side flow (unmixed flow) and $\dot{C}_2$ represents the supercritical carbon dioxide flow (mixed flow). The equations used for the heat exchangers in this function are taken from Nellis and Klein (2009) [5].

The conductance is calculated as the product of the number of transfer units and the minimum capacitance rate.

$$UA[i][j][k] = NTU[i][j][k] * \dot{C}_{min}$$

Where, $UA[i][j][k]$ is the conductance of each sub-section. The conductance calculated from this part is determined from the fluid internal thermal properties and flow configuration.

The final part of this section is the resistance network going from the air flow to the sCO_2 flow. This method allows for the conductance to be calculated for a second time in the model by using the physical size of the heat exchanger as well as the heat transfer coefficients associated with the flows. Equating the conductance values calculated using the two methods allows for the heat transfer for each sub-section to be determined.

The resistance network is constructed of four thermal resistances in series; sCO_2 resistance to convection, $R_{conv,c}$, tubing resistance to conductance, R_{cond}, fouling resistance R_{foul} (taken from Harsco design), and air resistance to convection, $R_{conv,a}$. The resistance network is shown visually in Figure 6.

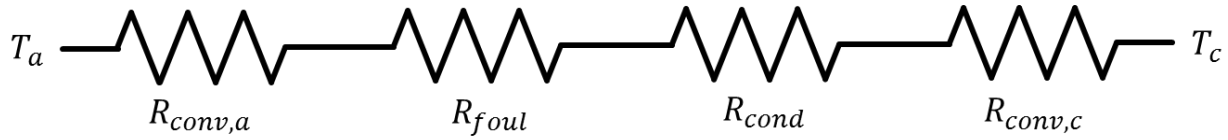

Figure 6: Resistance network between the air flow temperature and the sCO_2 flow temperature.

$$R_{conv,c}[i][j][k] = \frac{1}{\bar{h}_c[i][j][k]\,\pi\,D_i\,dL\,N_{cols}[j][k]}$$

$$R_{cond}[i][j][k] = \frac{ln\left(\frac{D_o}{D_i}\right)}{2\pi k_{tubes}\,dL\,N_{cols}[j][k]}$$

$$R_{foul}[i][j][k] = \frac{FF}{\pi D_i\,dL\,N_{cols}[j][k]}$$

$$R_{conv,a}[i][j][k] = \frac{1}{\eta_o \bar{h}_a\,SA_{air}/_{tube}\left(\frac{dL}{Length}\right)N_{cols}[j][k]}$$

Where, k_{tubes} is the conductivity of the tubing material at the average temperature between the fluid inlet states. $SA_{air}/_{tube}$ is the surface area exposed to the air flow per tube.

$$SA_{air}/_{tube} = \left(\frac{\pi}{2}\left(D_{fin}^2 - D_o^2\right) + \pi D_o\left(\frac{1}{fin_{pitch}} - th_{fin}\right)\right) * Length * fin_{pitch}$$

The total resistance is the sum of all four resistances since they are in series.

$$R_{tot}[i][j][k] = R_{conv,c}[i][j][k] + R_{cond}[i][j][k] + R_{foul}[i][j][k] + R_{conv,a}[i][j][k]$$

Where, $R_{tot}[i][j][k]$ is the total resistance. The conductance is defined as the inverse of the total resistance.

$$UA[i][j][k] = \frac{1}{R_{tot}[i][j][k]}$$

This conductance is equivalent to the conductance calculated using the effectiveness and number of transfer units method.

Other calculations and consideration of additional thermal resistances

The mass flow through each row of tubes is determined by setting the sum of the sub-section's pressure drops for each row of tubes to be equal along each pass, while keeping the sum of the mass flows for each pass equal to the total mass flow. The total cooler pressure drop is calculated as the sum of the pressure drops along each pass as well as the pressure drop associated with the headers. The header pressure drop was set to an arbitrary 500 Pa per header in order to attempt to match the Harsco designed pressure drop.

$$\Delta P_c[k] = \sum_{i=1}^{N_{sub}} \Delta P_c[i][j][k]$$

$$\Delta P_c = \sum_{k=1}^{N_{pass}} \Delta P_c[k] + \left(N_{pass} - 1\right)\Delta P_{header}$$

$$\dot{m}_c = \sum_{j=1}^{N_{rows}} \dot{m}_c[j][k]$$

Where, $\Delta P_c[k]$ is the pressure drop along the given pass and ΔP_c is the total sCO_2 pressure drop in the cooler.

The header mixing is also considered in the model. It is assumed that the flow out of pass 1 is fully mixed before entering pass 2, same with pass 2 to pass 3. To account for this mixing, the state at the final node of each pass is determined from the mass flow weighted average from each row. These equations are used for passes 2 and 3, not pass 1.

$$h_c[1][k] = \frac{\sum_{j=1}^{N_{rows}} (\dot{m}_c[j][k-1] h_c[N_{sub}+1][j][k-1])}{\dot{m}_c}$$

$$P_c[1][j][k] = P_c[N_{sub} + 1][j][k - 1] - \Delta P_{header}$$

The enthalpy and the pressure define the state entering each pass.

Lastly, the total fan power and the total cooler cost are calculated. The total fan power that is required for the cooler is calculated as the product of the fan power in each unit and the number of cooler units.

$$\dot{W}_{fan,total} = \dot{W}_{fan} * N_{HX}$$

The total cooler cost is calculated based on the Harsco quoted design. The total cost for the cooler in this model uses a linear relationship between number of coolers and total cost.

$$Cost = {}^{Cost[\$]}/_{unit} * N_{HX}$$

The resistance network considered for this model was constructed with the assumption that the dominating resistances would be the convective components on the sCO_2 and air sides as well as conduction through the tubing material. In addition to these resistances, a fouling resistance was added to the model in order to stay consistent with the Harsco design. Table 7 shows the magnitudes of each of these four resistances as well as the magnitude of the total resistance for each sub-section as described in previous section.

Table 7: The magnitude of each resistance used in the cooler model is shown along with the magnitude of the total resistance. All resistance values are based on a single sub-section

Resistance	Value (K/W)
Convection from Air to Outer Surface	1.8×10^{-4}
Conduction through Tubing Material	3.2×10^{-5}
Fouling	5.1×10^{-5}
Convection from sCO_2 to Inner Surface	5×10^{-5} to 7×10^{-4}
Total Resistance	3×10^{-4} to 7×10^{-4}

The largest determining resistance is the resistance to convection between the sCO_2 and the inner tube walls. This convective resistance largely determines the total resistance; however, the other resistances used in the analysis are shown to be on the same order of magnitude as the total resistance. This shows that all of these resistances are important to the resistance network between the air and the sCO_2.

Something to consider for further improving the model would be to include additional resistances in the network. The resistances that have been further considered are the contact resistance between the fins and the tubing material as well as conduction through the fin material due to the L-tension design of finned tubes. L-tension fins use additional fin material to provide spacing for the fins and rely on the tensioning from winding the fins to provide good contact.

The resistance to conduction through the additional fin material is calculated using the same correlation as the conduction through the tubing material.

$$R_{cond,fins}[i][j][k] = \frac{ln\left(\frac{D_o + 2fin_{th}}{D_o}\right)}{2\pi k_{fins}\, dL\, N_{cols}[j][k]}$$

The contact resistance is calculated using a correlation described by Kern and Kraus (1972) [8]. The correlation breaks the total contact resistance into two parts; the solid to solid contact and the resistance to conduction through the voids.

$$\frac{1}{R_c''} = \frac{k_a}{\gamma_{tubes} + \gamma_{fins}} + \frac{4P_c k_{tubes} k_{fins}}{c'\pi R_i \sigma_B (k_{tubes} + k_{fins})}$$

Where R_c'' is the contact resistance per unit contact area. The first term is the resistance to conduction through the voids where k_a is the fluid inside the voids, assumed to be air, and γ_{tubes} and γ_{fins} are the surface roughness of the tubes and fins respectively. The tubes and fins are assumed to be smooth 1 μm is used for both surface roughness values. The second term is the solid to solid contact resistance where P_c is the contact pressure, c' is a coefficient that has been found to be 3 for most materials according to Kern and Kraus, and R_i is the radius of the contact spot that is taken to be 0.001 in according to Kern and Kraus. The contact resistance is calculated similarly to the fouling resistance as described in previous section.

$$R_{contact}[i][j][k] = \frac{R_c''}{\pi D_o \, dL \, N_{cols}[j][k]}$$

Table 8 shows the magnitudes of both the conduction resistance through the fin material and the contact resistance.

Table 8: The magnitude of additional resistances is shown for possible consideration.

Resistance	Value (K/W)
Conduction through Fin Material	4.3×10^{-7}
Contact Resistance	1.9×10^{-5}

As can be seen, the resistance to conduction through the additional fin material is far below any of the other resistance value due to aluminum having a large conductivity and the fin material being very thin. The contact resistance, however, is on the same order of magnitude as the other resistances taken into account for this model. Although it has the same order of magnitude as the other resistances, the contact resistance would account for only 6% of the total resistance. This leaves room for debate on whether the contact resistance should be taken into account in this analysis. With the contact resistance being strongly related to the surface roughness of the two materials, this representation of the contact resistance may be off to the actual resistance associated with the L-tension fins.

Alternative flow configuration

Another consideration that has been explored for this model is to have vertical passes of the supercritical carbon dioxide rather than the designed horizontal passes. The vertical pass design would create a larger pinch point between the sCO_2 and the ambient air by having the bottom row of tubes, where the lowest sCO_2 temperatures occur, be exposed to ambient conditions directly. One problem that occurs for the horizontal design is that the pinch point that occurs at the end of the heat exchanger is smaller than designed due to air flowing over three rows of tubes before encountering the final row. This additional pinch point can be seen in Figure 5.

In order to avoid this, a vertical pass design was considered using the same physical heat exchanger design; however, the headers would need to be adjusted appropriately. The new temperature distribution between the sCO_2 and the air can be seen in Figure 7. The base case for the quoted Harsco design was selected in order to compare the horizontal pass design with the vertical pass design. The horizontal pass design calculated the total fan power required for 86 total cooler units, and using the same fan power per unit the vertical pass design calculated the required number of units to produce the same outlet temperature.

Table 9: Comparison for the number of units and total fan power between the horizontal pass design and the vertical pass design.

	Horizontal Passes	Vertical Passes
sCO_2 mass Flow	878.9 kg/s	
Inlet Temperature	89.6 C	
Outlet Temperature	32.657 C	
Outlet Pressure	7.630 MPa	
Fan Power per Unit	65.758 kW	
Number of Cooler Units	86	77.75
Total Heat Transfer	137.8 MW	137.9 MW
Total Fan Power	5.655 MW	5.113 MW
Inlet Pressure	7.635 MPa	7.643 MPa
Average Air Outlet Temperature (Peak)	34.92 C (50.54 C)	35.44 C (38.13 C)

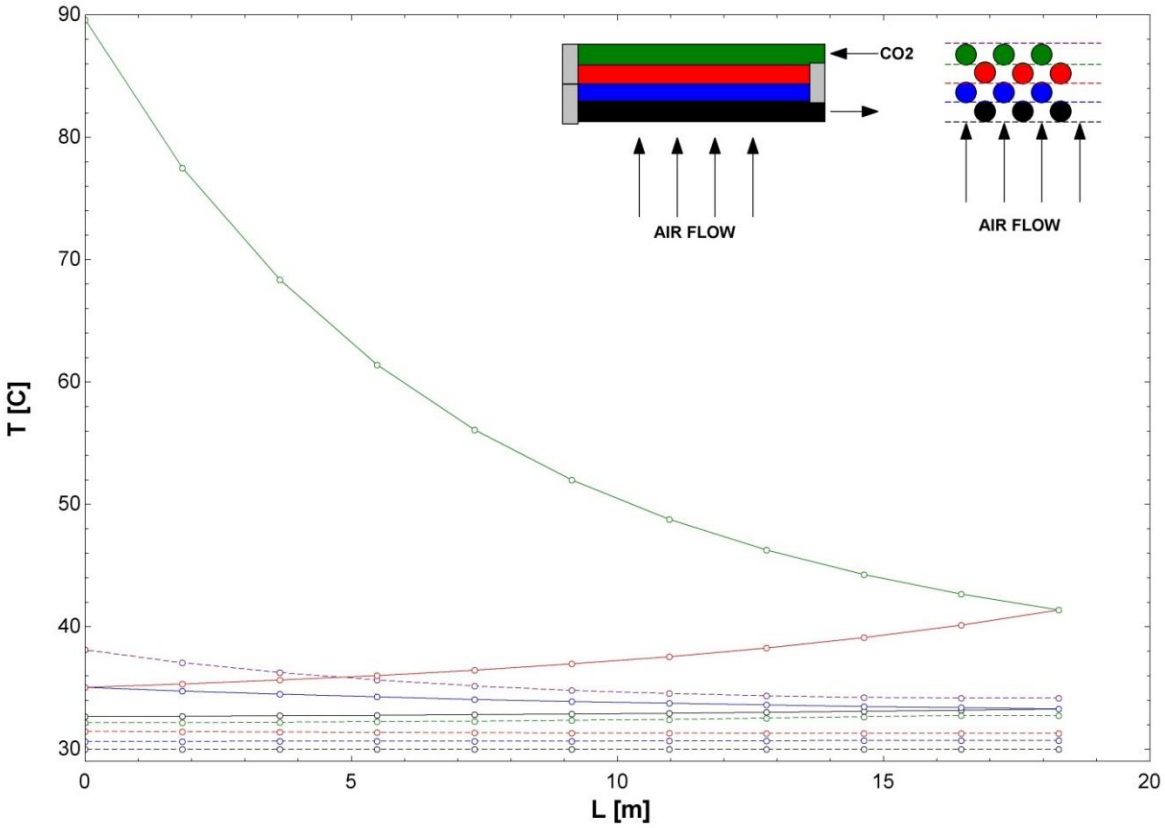

Figure 7: Temperature distribution of a vertical pass design. The solid lines represent the sCO_2 temperature and the dashed lines represent the air.

The fan power per unit is calculated based on the designed heat exchanger design. This value was held constant in order to create a comparison for the horizontal pass design and the vertical pass design. As can be seen in Table 8, the vertical pass design would require 8 less heat exchanger units to produce the same outlet condition as the horizontal design. This corresponds to an approximately 10% decrease in capital cost as well as total fan power required. The reason this design isn't used is due to the manufacturability of the headers that would be required for the vertical pass design. It would require precision with the header walls between tube rows as well

as introduce additional pressure drop that isn't accounted for in this model. These additional costs could easily overtake the 10% decrease in capital cost and prove to be less feasible than considered above.

Effect of number of nodes

The effect of the number of nodes along the supercritical carbon dioxide flow direction on the accuracy of the model as well as the time for the model to converge was investigated. In general, a numerical model is more accurate when using more nodes, but it also takes longer to solve. Table 10 shows the effect of the number of nodes on the run time for the model in addition to the calculated fan power for the base case. All of the results shown previously have been for a 10 node model, which corresponds to a total of 30 nodes along the supercritical carbon dioxide flow direction.

Table 10: Time to solve for different number of nodes along a single pass for the base case of conditions. Fan power difference is calculated on the fan power calculated using 30 nodes.

# Nodes	1	5	10	20	30
Single Run Time	0.2 s	2.9 s	**5.9 s**	11.8 s	18.1 s
Parametric Table (26 Runs)	18.8 s	158 s	**330 s**	711 s	1052 s
Fan Power (Base Case)	6.729 MW	5.916 MW	**5.655 MW**	5.516 MW	5.468 MW
Fan Power Difference	23.1%	8.1%	**3.4%**	0.9%	0%
Optimal # Coolers	122	118	**116**	116	116

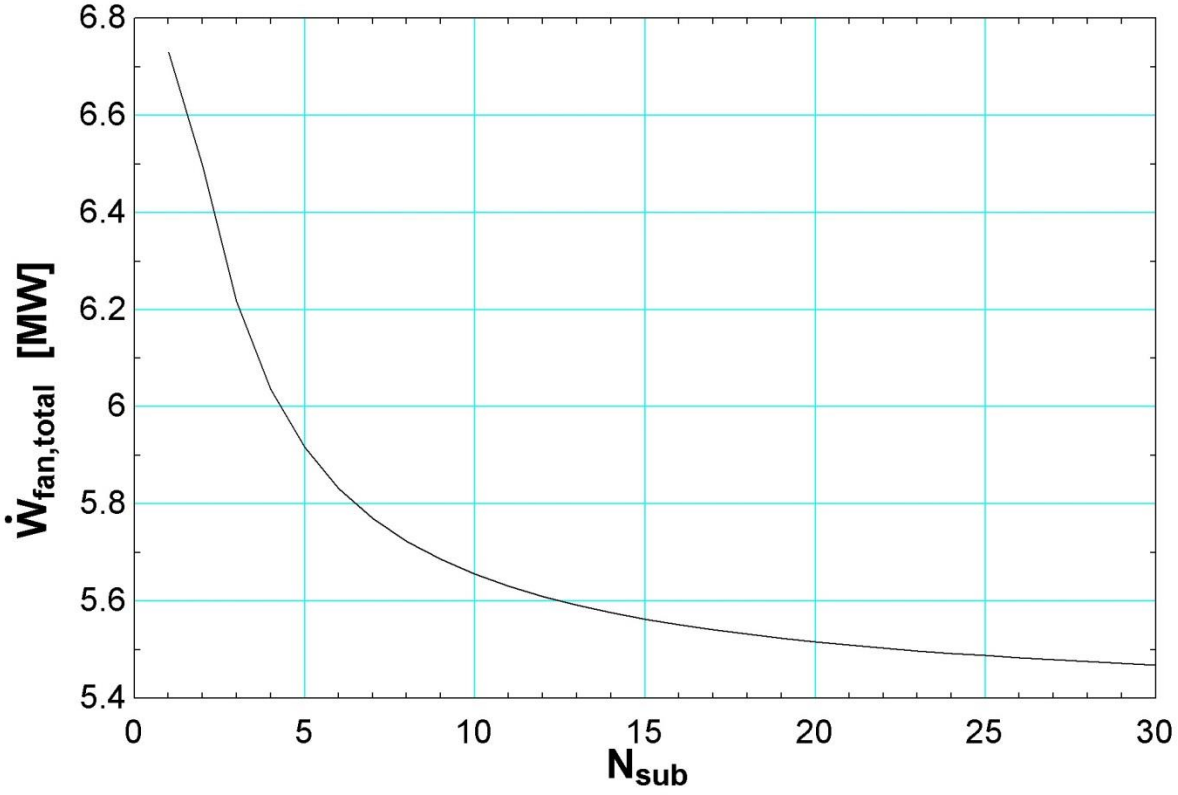

Figure 8: Calculated required fan power plotted as a function of number of nodes for the base case.

The most important value calculated for this model is the fan power due to its large effect on plant efficiency. The fan power for dry cooling typically requires between 1-5% of the total net cycle output power. Also, the other parameters that are important to the performance of the cycle are more often than not set in the model while the fan power is being calculated. Figure 8 shows the calculated fan power plotted versus the number of sub-sections (i.e. number of nodes) for each pass for the base case of cycle conditions.

It can be seen that the fan power doesn't fully plateau by 30 sub-sections, however, it doesn't have a large slope which corresponds to the change in fan power past 30 nodes would be small. In general, it is good practice in numerical models to use 90% of the infinite value (i.e. the value of fan power for an infinite number of sub-sections). An exponential best fit curve shows what the infinite value of the fan power would be according to the following approximation.

$$W_{fan} = Ae^{-bN_{sub}} + \dot{W}_{fan,total,\infty}$$

Where W_{fan} is the adjusted fan power, A and b are arbitrary constants, and $\dot{W}_{fan,total,\infty}$is the infinite value for fan power. Figure 9 shows the best fit curve with a root mean squared value of 0.9875.

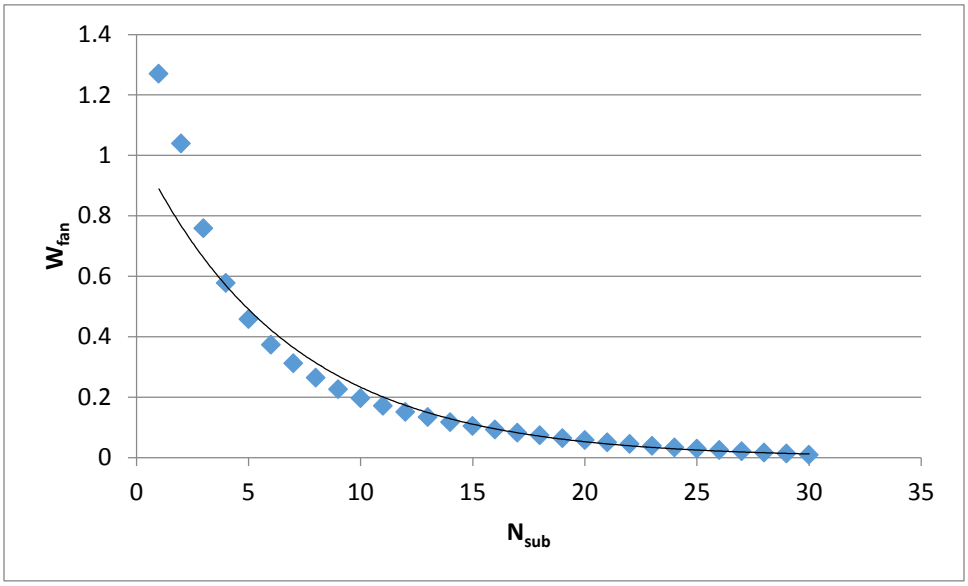

Figure 9: Best fit curve for the fan power plotted versus the number of nodes.

The equation for this best fit curve is:

$$W_{fan} = 1.0322e^{-0.149N_{sub}} + 5.459$$

For an infinite value of N_{sub}, the fan power goes to 5.459 MW. According to the 90% rule, or $\pm$10%, the sufficient value of fan power would be 6.005 MW. The model presented in this paper uses 10 nodes, which calculates the fan power to be 5.655 MW. This value is well inside the typical limits, being 3.6% off of the infinite value of fan power.

Table 11 compares the vendor quoted cooler specifications and the calculations from the EES model for the reference cooler conditions. It is evident that the EES calculations overall matches well with the vendor quotation with small differences in calculated air and CO_2 outlet temperatures.

Table 11: Comparison of manufacturer specifications and model calculations for reference cooler conditions

	Variable	Harsco Industrial Air-X-Changers	Calculated (EES model)	Calculated (EES model)
Inputs	Number of cooler units	86	86	86
	CO_2 flow rate per unit [kg/s]	10.22	10.22	10.22
	CO_2 inlet temperature [^oC]	89.61	89.61	89.61
	CO_2 inlet pressure [MPa]	7.736*	7.736*	7.635
	Air flow rate per unit [kg/s]	317.2	317.2	317.2
	Air inlet temperature	30	30	30
Outputs	Heat transfer capacity [MW_{th}]	1.691	1.696	1.61
	CO_2 outlet temperature [^oC]	32.7	33.12	32.64
	CO_2 pressure drop [kPa]	6.895	6.645	6.802
	Air outlet temperature [^oC]	52	51.2	51.11
	Air pressure drop [kPa]	Not provided	-	0.1112

*The CO_2 inlet pressure provided in the Harsco quotation didn't match the reference inlet pressure

For the calculations presented in Table 11, number of cooler units is used as the input and the CO_2 outlet temperature is calculated for verification of the code. However, for rest of the analysis, the developed EES code is used to calculate number of required cooler units ($N_{cooler,units}$) using CO_2 inlet temperature and pressure, CO_2 outlet temperature as the inputs. The cost of a Harsco heat exchanger unit, $cost_{cooler,unit}$ is obtained from the manufacturer quote and is assumed to be constant in further calculations in this chapter. Once the number of required cooler units is calculated, power consumption for the cooler and total cost of the cooler are calculated using Equations (2) and (3) respectively.

$$P_{fans} = 3 \cdot \dot{W}_{per,fan} \cdot N_{cooler,units} \tag{2}$$

$$cost_{cooler} = cost_{cooler,unit} \cdot N_{cooler,units} \tag{3}$$

Rest of the cycle Components design and cost methodology

As mentioned in the introduction chapter, the cycle minimum pressure, minimum temperature and maximum pressure are chosen as the variables for optimization of the S-CO_2 cycle using modified CO_2-to-air cooler design described in previous sections. For an air cooled cycle, cycle minimum temperature is generally dictated by the ambient air temperature of the power plant location. For a given minimum temperature, the cycle minimum pressure is selected near the pseudo-critical pressure to exploit the high fluid density during compression process. For cycle minimum temperatures > 31.25^{o}C, the current study showed that it is more economical (lower \$/kWe) to select the cycle minimum pressure that is slightly greater than the pseudo-critical pressure. The cycle maximum pressure is limited by the pressure containment capability of the cycle heat exchangers and piping. All the cycle heat exchangers excluding the air-to-CO_2

cooler are envisioned to be diffusion bonded compact heat exchangers from Heatric [9]. Figure 10 is reproduced from the Heatric website and shows the pressure containment capabilities of the current Heatric PCHEs as a function of the operating temperature. As can be seen, for a maximum operating temperature of 500°C, PCHEs can handle pressure differentials as high as 400 bar (40 MPa). For the current study, 300 bar (30 MPa) was chosen as the upper limit for the cycle maximum pressure and Table 12 summarizes the selected conditions for the cost-based optimization study.

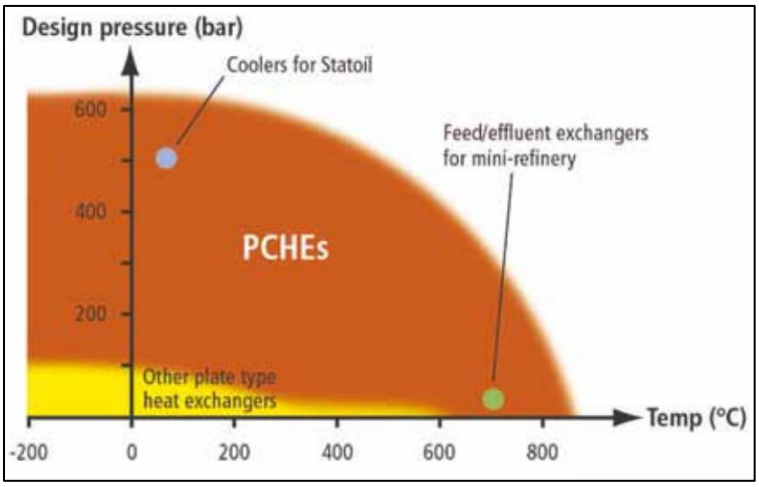

Figure 10: Pressure containment capability of Heatric PCHEs as a function of operating temperature [Reproduced from Heatric Website [9]]

Table 12: Selected cycle conditions for the optimization study

Minimum pressure (MPa)	Pseudo-critical pressure (MPa)	Minimum temperature [°C]	Maximum pressure [MPa]
7.4	7.422	31.25	18 – 30
7.628	7.628	32.5	18 – 30
8	8.040	35	18 – 30
8.864	8.864	40	19 – 30
9.688	9.688	45	20 – 30

As the cycle maximum pressure is increased, the mechanical design of the following components needs to be changed to withstand the design pressure.

- Reactor heat exchanger (RHX)
- High temperature recuperator (HTR)
- Low temperature recuperator (LTR)
- S-CO_2 cycle piping
- Turbomachinery components (compressors and turbine) – Not implemented in the current study

PCHE mechanical design methodology and cost estimation

Design modifications to be heat exchangers (RHX, HTR, and LTR) are implemented as per the ASME 13-9 code requirements and the design equations presented here are summarized in the

Heatric paper [9]. The commercially available Heatric PCHE units are fabricated by chemically etching semicircular channels with zig-zag pattern on a substrate plate and the plates are then diffusion bonded together to form a monolithic block. In order to simplify the mechanical design process, the channels are approximated as rectangular channels. Figure 11 shows the approximated rectangular channels along with the nomenclature. In the figure, t_2 represents the thickness of the plate after etching, t_3 represents the ridge width, $W=d$ is the channel width, $H=d/2$ is the channel depth assuming that the channels are semi-circular, and t_1 is the edge thickness. Where, d is diameter of the semicircular channels.

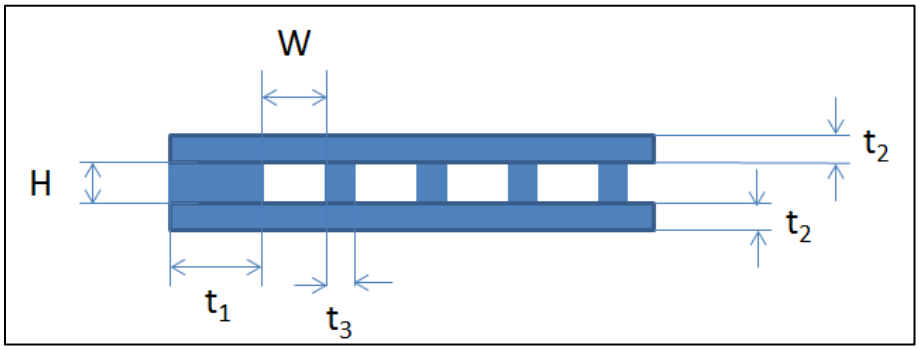

Figure 11: Approximated PCHE channels for mechanical design and the associated nomenclature

The procedure for calculation of the edge thickness (t_1), plate thickness (t_2), and ridge thickness (t_3) involves calculation of the membrane stress (S_m) and bending stress (S_b) experienced by these members when subjected to the design pressure. These equations can be found in either ASME section 13-9 or Heatric paper [9]. Once the membrane stress and bending stress are calculated, the total tress is known from Equation (4).

$$S_T = S_m + S_b \tag{4}$$

Design pressure used to calculate the stresses is selected to be 10% greater than the cycle maximum pressure to ensure safety margin at a particular design temperature. For the current study, the dimensions of the channels for all the heat exchangers are kept same as their respective reference designs in Table 1. The mechanical design is considered to be successful when the following criteria are met.

$$S_m \leq SE \tag{5}$$

$$S_T \leq 1.5SE \tag{6}$$

Where, E is the joint factor and is 0.7 for the diffusion bonded block based on Heatric's conservative assumption, S is the maximum allowable stress of the heat exchanger material (in this case it is 316 stainless steel) and is a function of the design temperature.

Figure 12 shows the maximum allowable stress as a function of the temperature for SS316. The allowable stress data for different materials can be found in ASME B&PV Code Section I, Part D. For operating temperatures in between the data points, maximum allowable stress is calculated using linear interpolation method. Table 13 shows the design parameters for the PCHEs relevant to the current study. As mentioned earlier, the channel dimensions, and design temperature are kept constant for all the conditions and the plate thickness, and ridge thickness (hence, channel pitch-to-diameter ratio) are calculated as a function of the design pressure.

Channel pitch is equal to the sum of ridge thickness and the channel diameter. Channel pitch-to-diameter ratio and the plate thickness are plotted as a function of design pressure in Figure 13 for the RHX, HTR, and LTR. These values are updated in ANL PDC inputs as the cycle maximum pressure is changed. Please note that the plate thickness in Table 13 is the original plate thickness before etching and is assumed continuous throughout the layer.

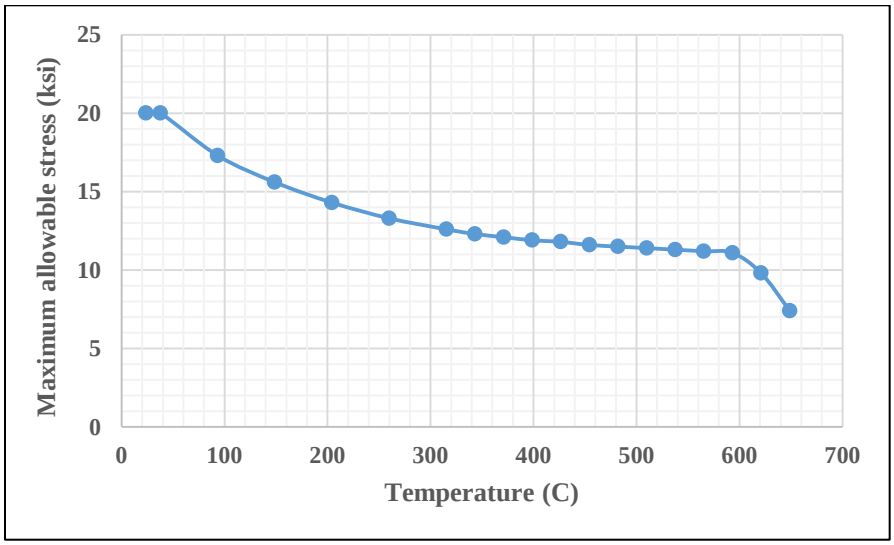

Figure 12: Maximum allowable stress vs temperature for 316 stainless steel (Data obtained from ASME B&PV Code Section I, Part D)

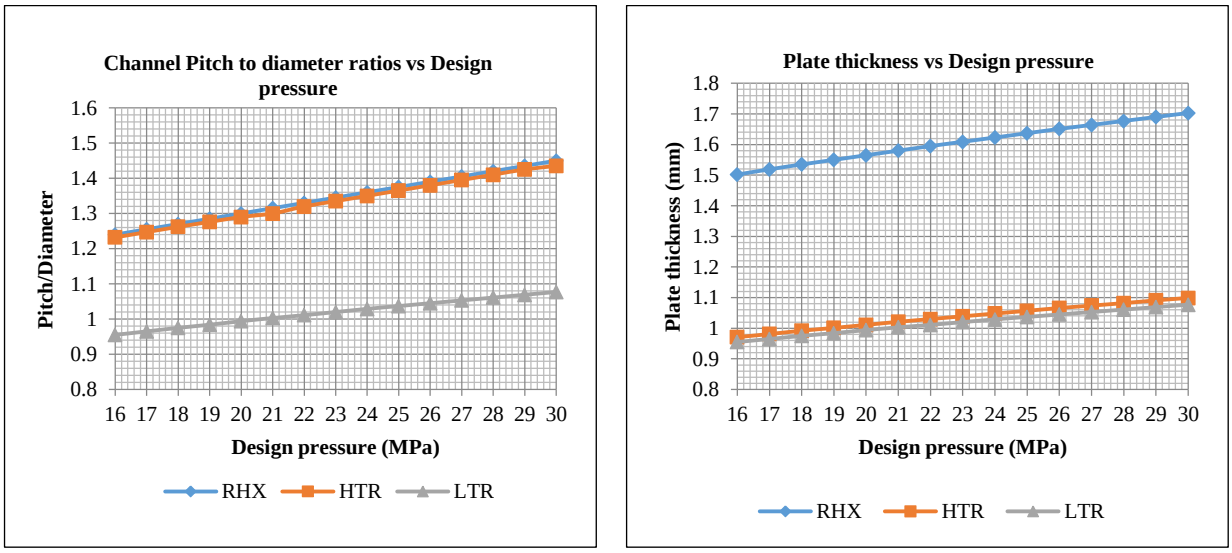

Figure 13. Channel pitch to diameter ratios and plate thickness as a function of design pressure

Table 13: Design parameters for the S-CO_2 cycle PCHEs

Parameters	RHX	HTR	LTR
HEX type	Z/I PCHE	Platelet PCHE	Platelet PCHE
Unit length (m)	1.5	0.6	0.6
Unit width (m)	0.6	1.5	1.5

Unit height (m)	0.6		0.6		0.6	
Design temperature (°C)	550		450		300	
Design pressure (MPa)	18 – 30		18 – 30		18 – 30	
	Hot side (Na)	Cold side (CO_2)	Hot side (CO_2)	Cold side (CO_2)	Hot side (CO_2)	Cold side (CO_2)
Channel diameter (mm)	6.0	2.0	1.3	1.3	1.3	1.3
Channel depth (mm)	4.0	1.0	0.65	0.65	0.65	0.65
Pitch to diameter ratio	1.083	Variable	Variable	Variable	Variable	Variable
Plate thickness (mm)	Variable	Variable	Variable	Variable	Variable	Variable

A proper capital cost estimation for the PCHEs is needed for the cost-based optimization technique that will be described in the next chapter. A simplified capital cost estimate procedure for the cycle PCHEs is as follows [3].

- The mass of raw material required for fabrication of each PCHE unit is calculated from the volume of the PCHE unit and the material density

$$M_{block} = V_{block} \cdot \rho_{ss316(@20^0C)}$$

- The material cost of SS316 is chosen as 7.64 $/kg in order to be consistent with previous optimization studies performed at ANL and the total material cost of one PCHE block is calculated. Please note that the current market material cost for SS316 might be different and the cost of the cycle heat exchangers (including cooler) can be different depending on when the purchase is made.

- The fabrication cost to perform chemical etching and diffusion bonding depends on the type of PCHE. For example, Z/I PCHE as in the case of RHX is less expensive than the platelet PCHE as in the case of HTR and LTR.

- The total cost of each PCHE block is the sum of material cost and fabrication cost. The capital cost of full PCHE is calculated as,

$$cost_{PCHE} = cost_{PCHE,block} \cdot N_{blocks}$$

Note that PCHE in the above equation can be either RHX, HTR, LTR, or water cooler. The additional costs such as costs associated with welding of blocks and headers, as well as engineering and shipping costs are neglected as they are considered to be small compared to the fabrication and material costs.

Piping design methodology and cost estimation

Plant piping is designed as per ASME B31.1 process piping guidelines and the design equations are summarized in this section. The design process involves calculation of minimum required wall thickness for a known pipe inner (or outer) diameter, design pressure, and design temperature. The required minimum wall thickness is calculated using Equation (7).

$$t_{min} = \frac{PD_i}{2(SEW+PY)(1-UTP-CA)-P} \quad (7)$$

Where,

t_{min} = minimum wall thickness.
D_i = inner diameter of the pipe
E = quality factor and is equal to 1 for seamless pipes (ASME B31.3 Table 302.3.4)
W = weld joint quality factor and is equal to 0.975 (ASME B31.3 Cl. 302.3.5)
Coefficient Y is equal to 0.4 (ASME B31.3 Table 304.1.1)
P = internal pipe pressure or the design pressure
S = maximum allowable stress and is a function of design temperature (see Figure 12)
UTP = Under tolerance allowance to account for manufacturing tolerances
CA = Corrosion allowances in percentage

Under tolerance and corrosion allowances are selected to be 12.5% each. When Equation (7) is applied for a pipe bend an additional factor, I (ASME B31.3 Cl. 304.2.1) has to be taken into account. Depending on the bend radius, the required minimum thickness for a pipe bend is slightly greater than that of a straight section. However, the difference is not significant in the current study and all the pipe bends in the plant layout are ignored and treated as straight pipe sections. The piping inner diameters are selected based on previous optimization study to keep the pressure drop in the piping to reasonable values [3]. The pipe lengths are selected from the S-CO_2 plant layout for AFR-100 developed at ANL [10] and is shown in Figure 14. A total of 25 pipe sections are identified and Figure 15 shows the numbering of nodes, and sections in a schematic of the layout as used in the PDC. The lengths (L_{pipe}) and inner diameters of each pipe section are summarized in Table 14. The wall thickness for these pipe sections are calculated based on the design pressure and design temperature for that particular section. Design temperature is chosen to be the temperature expected in that section based on the PDC steady-state calculations for design conditions. The pipe lengths in the PDC are left unchanged from previous settings because it requires re-optimization of the pipe inner diameters to ensure that the cycle efficiency is unaffected by the choice of pipe inner diameters.

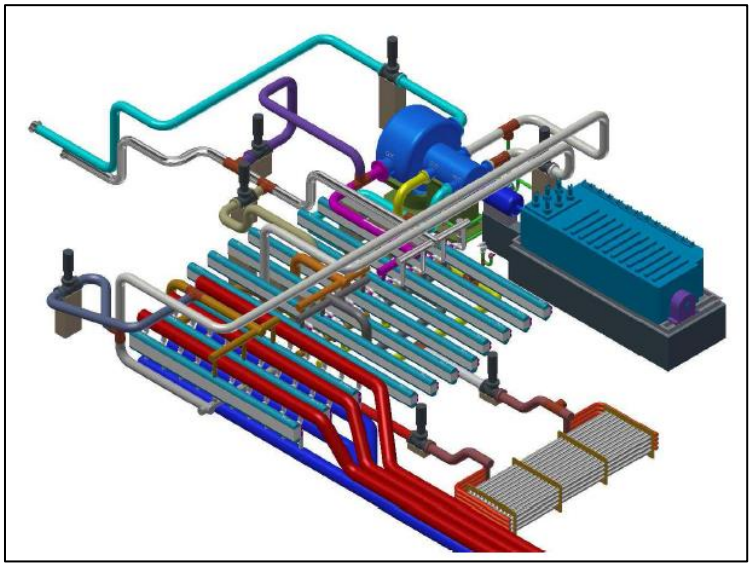

Figure 14: S-CO_2 Brayton cycle layout for AFR-100 developed at ANL [8], Aqua pipe is the inlet line from Na-to-CO_2 heat exchanger and Silver pipe is the return line to Na-to-CO_2 heat exchanger

Table 14: S-CO_2 cycle piping inner diameters and lengths, based on AFR-100 layout

Section	D_i (m)	L_{pipe} (m)
1	0.68302	29
2	0.68302	2
3	0.68302	12
4	0.68302	30
5	0.5	9.25
6	0.5	5.5
7	0.5	13
8	0.5	9.25
9	0.5	5
10	0.5	55
11	0.5	21
12	0.5	5
13	0.5	10
14	0.5	10
15	0.68302	10
16	0.68302	15
17	0.68302	2
18	0.5	12
19	0.45	38
20	0.25	17
21	0.25	21
22	0.25	11
23	0.25	11
24	0.25	12
25	0.25	25

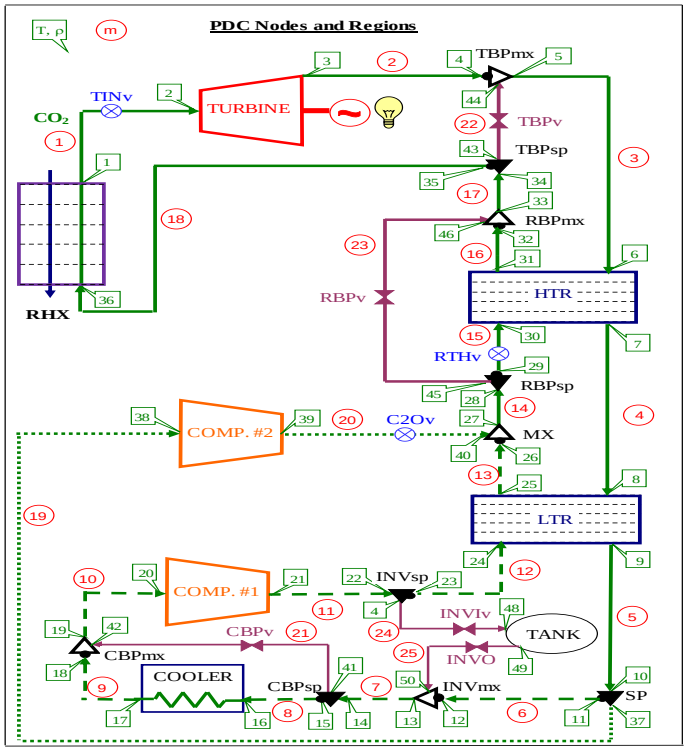

Figure 15: PDC Nodes and regions for identifying pipe sections in S-CO_2 cycle

Figure 16 presents an example of pipe thickness calculations as a function of the cycle maximum pressure, minimum pressure, and minimum temperature for two of the pipe sections. The plot on the left is for the pipe connecting the RHX outlet and the turbine inlet (Aqua pipe in Figure 8) and the plot on the right is for the pipe connecting turbine outlet and the HTR inlet (Magenta pipe in Figure 14). Please note that the legends in the Figure 16 are for compressor inlet conditions and not the conditions in the pipe section. The thickness of the pipe connecting turbine outlet and HTR decreases as the cycle minimum pressure decreases and is independent of the high pressure side. Whereas, the thickness of the pipe connecting RHX and turbine inlet is independent of the cycle minimum pressure and increases as cycle maximum pressure increases.

The cost of each pipe section is calculated as follows,

$$D_o = D_i + 2t_{min}$$

$$V_{pipe} = \frac{\pi}{4}.(D_o^2 - D_i^2).L_{pipe}$$

$$cost_{pipe} = V_{pipe}.\rho_{ss316(@20^0C)}.cost_{ss316}$$

The material cost of SS316 ($cost_{ss316}$) is 7.64 $/kg. The total capital cost of the piping ($cost_{piping}$) is simply calculated as sum of cost of all the 25 pipe sections. It should be noted that the fabrication cost, costs associated with welding of pipe sections are ignored in the piping cost estimation as these costs are hard to estimate.

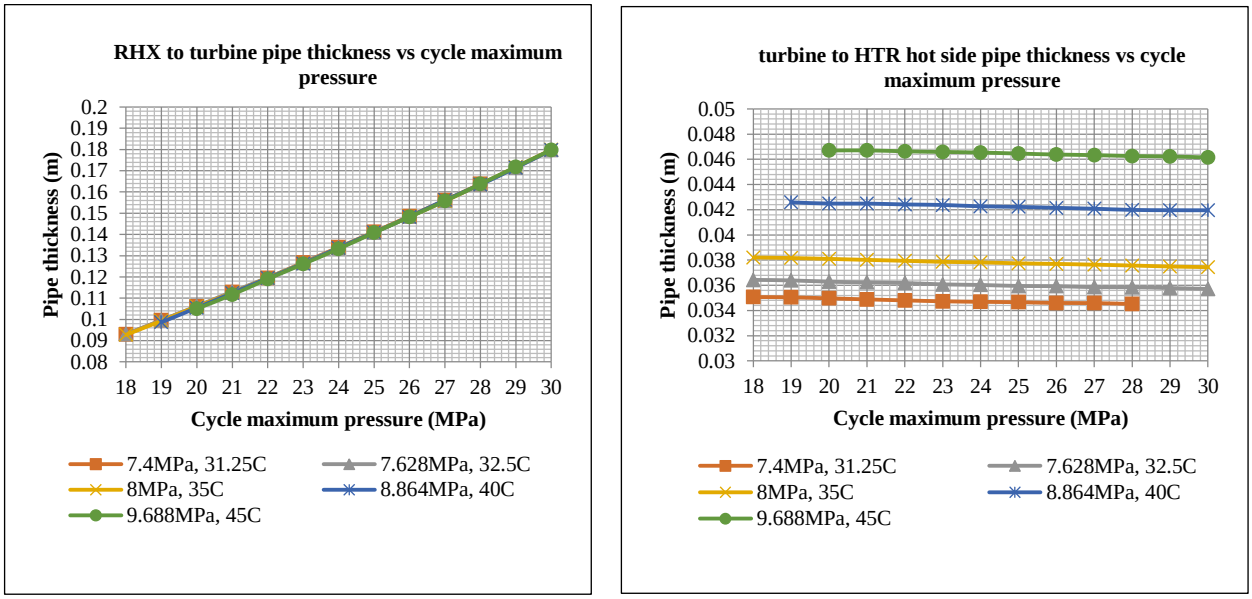

Figure 16: Example of pipe thickness calculations as a function of the cycle conditions

Turbomachinery components design methodology and cost estimation

Design procedure for the turbomachinery components is not straight forward and requires attention to lot of details. For example, the blade dimensions are not just a function of cycle maximum pressure but also depends on other details like number of stages, hub diameter etc. Moreover, the casing to withstand the high pressure will have to be designed according to the

calculated blade dimensions. Due to lot of complications involved, no changes were made to the PDC turbomachinery inputs. The turbomachinery inputs to the PDC are based on previous optimization study at the ANL [3]. Consequently, cost estimation for the turbomachinery components is difficult and these costs are treated as constant in the cost-based optimization procedure described in the next section.

Cost-based Optimization

For a power plant it is important to take into account the plant net electrical output as well as the capital cost of the plant. Usually, there is a trade-off between these two and a cost-based optimization method is employed to find the optimum operating conditions. This section summarizes details of the cost-based optimization technique employed to perform the plant optimization. The plant capital cost per unit electrical output ($/kWe) is calculated using Equation (8) and takes into account the changes in cost of heat exchangers, piping for different cycle conditions.

$$\frac{\$}{kWe} = \frac{cost_{rest}+cost_{RHX}+cost_{HTR}+cost_{LTR}+cost_{air\ cooler}+cost_{piping}}{P_{elec}-P_{fans}} \quad (8)$$

Where, $cost_{rest}$ is the capital cost of the rest of the plant, i.e. excluding the components being optimized here: RHX, HTR, LTR, cooler, and the piping. And $cost_{RHX}$, $cost_{HTR}$, $cost_{LTR}$, $cost_{air\ cooler}$, $cost_{piping}$ is the cost of reactor heat exchanger, high temperature recuperator, low temperature recuperator, CO_2-to-air cooler, plant piping respectively. P_{elec} is the work output from the cycle, and P_{fans} is the work input to operate the CO_2-to-air cooler fans.

Several assumptions are made in the process of calculating the $/kW$_e$ and these assumptions are as follows:

- The plant capital cost per unit electrical output, including the cost of heat exchangers and piping costs, is assumed to be equal to 4,780 $/kWe for the reference water cooled S-CO_2 plant with net electrical output of 104.8 MWe (see Figure 1).

- Rest of the plant capital cost ($cost_{rest}$) is calculated by excluding the cost of heat exchangers and piping costs for the reference plant and is assumed to be constant throughout the optimization study. This value is $4,480 $/kWe for net electrical output of 104.8 MWe.

- The model for CO_2-to-air cooler design (described in previous sections) is not yet implemented in the PDC, hence, the optimization is performed assuming that the cooler is reference PCHE design. The number of cooler units is kept constant at 72 throughout the optimization. After the optimization is complete, the cooler operating conditions are exported to the CO_2-to-air cooler EES model to calculate the required fan power (P_{fans}) and cost of the cooler ($cost_{cooler}$) as a function of the number of cooler units.

A Matlab code was developed to automate the calculations during the process of optimization for different cycle operating conditions. Ideally the optimization process for all the components should be performed simultaneously, but such a process would require enormous amount of computational time. In order to reduce the computational effort and simplify the optimization

process, a sequential optimization method was used. This allows for optimization of individual components. The flow chart of the Matlab code is shown in Figure 17. For the calculation of $/kWe during optimization, the code replaces fan power with pump power for CO_2-to-water cooler.

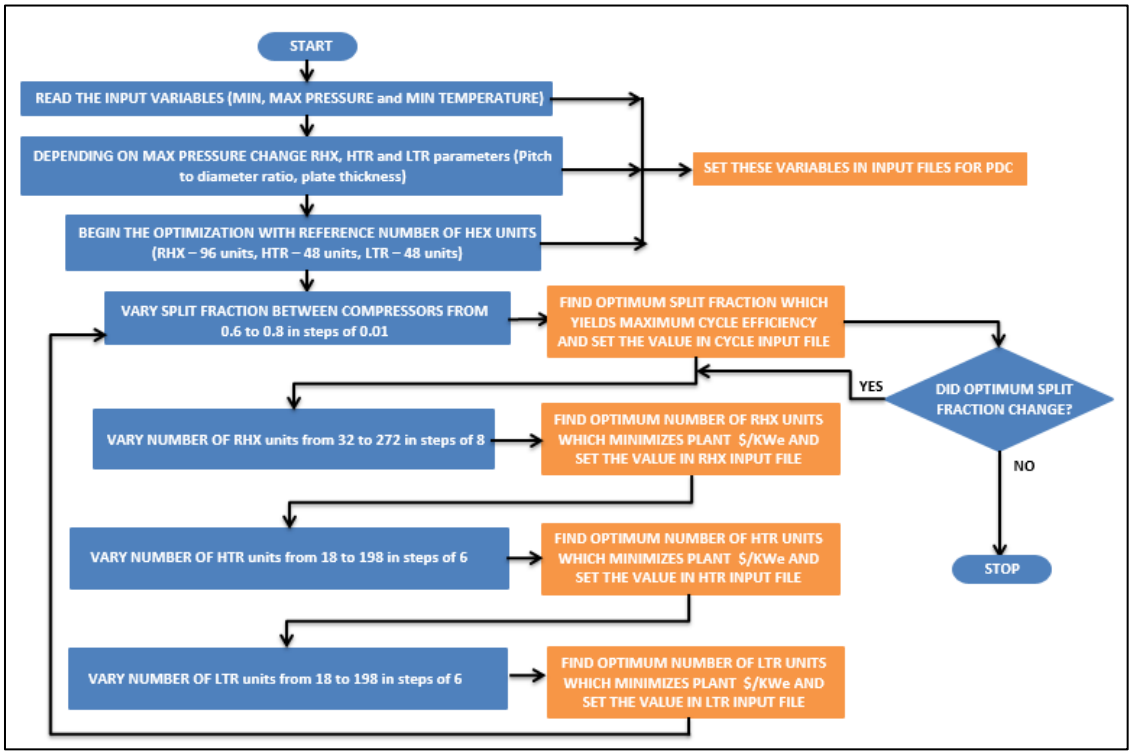

Figure 16: Matlab optimization code flow chart

Prior to beginning of the optimization, the cycle minimum pressure, minimum temperature, and maximum pressure are set as inputs to the code and the channel pitch-to-diameter ratio, and plate thickness of the PCHE heat exchangers are modified in the PDC input files. The number of heat exchanger units for each heat exchanger is reset to the reference values mentioned in Table 1 (96 RHX units, 48 HTR units, 48 LTR units) to start the optimization with the same initial condition for all the cases. The next few subsections explains each step of the flow chart in more detail along with sample calculations. The sample calculations correspond to cycle minimum pressure of 8 MPa, cycle minimum temperature of 35^{o}C, and cycle maximum pressure of 24 MPa.

Optimization of split fraction between the compressors

Depending on the cycle conditions the specific heats of cold and hot streams in the LTR can be significantly different which in turns affects the LTR effectiveness. Therefore, the split flow needs to be adjusted in order to find a balance between the increase in LTR effectiveness and increase in re-compressor work due to compression of uncooled fluid. Consequently, the first step of the optimization process is to find this optimum split fraction between the main compressor and re-compressor. With the number of heat exchanger units for all the heat exchangers set to reference values, the flow split fraction is varied from 0.6 to 0.8 in steps of 0.01. The cycle efficiency is calculated as a function of the flow split fraction and the optimum split fraction corresponds to the maximum cycle efficiency. An example of this step is shown in Figure 17 where cycle efficiency, work input to the compressors, and LTR effectiveness are

plotted as a function of the split fraction. As can be noted, the decrease in work input to the main compressor is small as the split fraction decreases but the work input to the re-compressor increases significantly for the lower split fractions. On the other hand, the LTR effectiveness increases as the split fraction is increased resulting in optimum split fraction (0.7 for the current example) and maximum cycle efficiency (42.32% for the current example). Once the optimal split fraction is calculated, the split fraction is updated in the PDC input file (Cycle_dat.txt) and the Matlab code proceeds to optimization of the RHX.

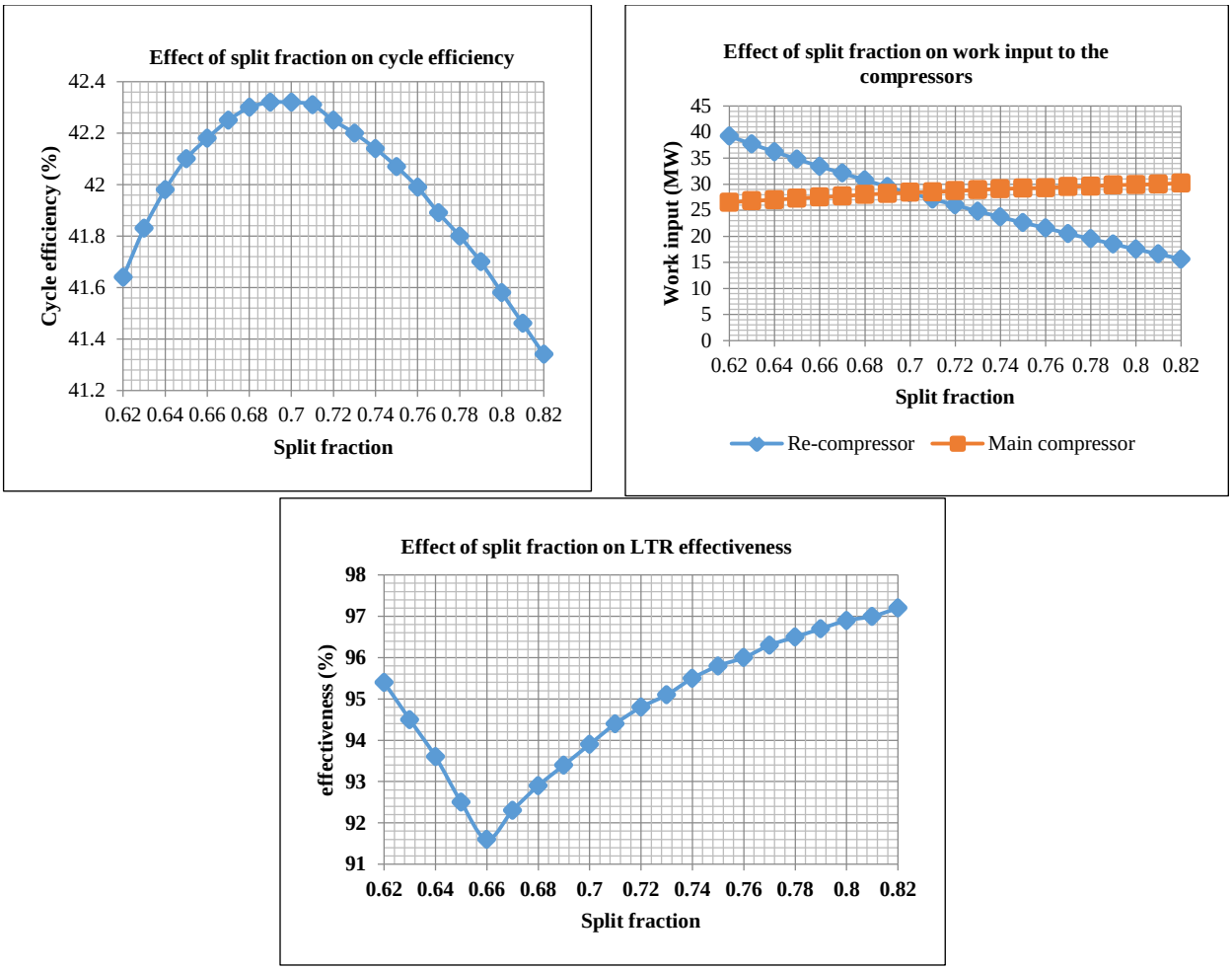

Figure 17: Optimization of the split flow fraction between main and re-compressors

Optimization of Reactor heat exchanger

Increasing the number of RHX units (hence, RHX effectiveness) increases the CO_2 turbine inlet temperature and reduces the CO_2 pressure drop in RHX which in turn increases the cycle efficiency. On the down side, capital cost of the RHX increases as well. Therefore, for the changing cycle conditions it is important to find the optimum number of RHX to minimize plant unit capital cost ($/kWe). In the second step of optimization, the number of RHX units is varied from 32 to 272 in steps of 8 and the cycle efficiency, and $/kWe are calculated. An example of these calculations is shown in Figure 18. For this particular example, the optimum number of RHX units changed from 96 (reference value) to 80.

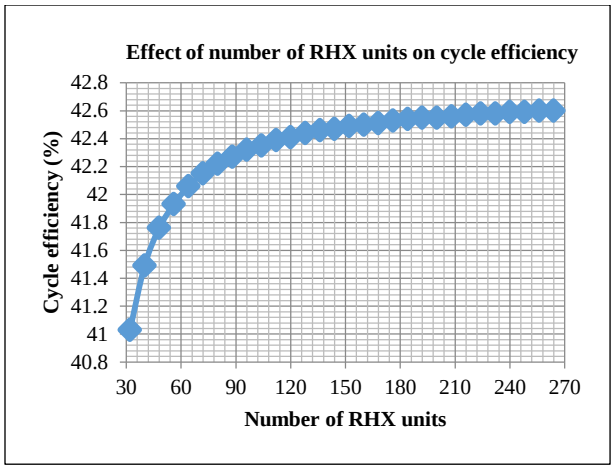

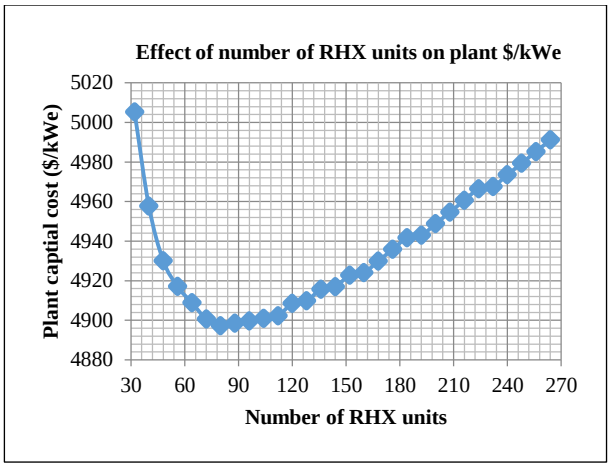

Figure 18: Example of cost-based optimization of the RHX

It should be noted these calculations are performed with the number of HTR and LTR units set to reference values (48 each) and the $/kW$_e$ can be represented as,

$$\frac{\$}{kWe} = \frac{cost_{rest}+cost_{RHX}+cost_{HTR,ref}+cost_{LTR,ref}+cost_{water\ cooler}+cost_{piping}}{P_{elec}-P_{pump}}$$

Once the optimum number of RHX units is calculated, the value is updated in the PDC input file (RHX_dat.txt) and the Matlab code proceeds to the optimization of the recuperators.

Optimization of recuperators

Similar to the RHX, increasing the number of HTR, and LTR units will increase both the cycle efficiency (due to increased recuperation, reduced pressure drop) and cost of the recuperators. In the third step of optimization, the number of HTR units is varied from 18 to 198 in steps of 6 to find the optimum number of HTR units resulting in least $/kWe. For the HTR optimization, $/KW$_e$ can be represented as,

$$\frac{\$}{kWe} = \frac{cost_{rest}+cost_{RHX,optimum}+cost_{HTR}+cost_{LTR,ref}+cost_{water\ cooler}+cost_{piping}}{P_{elec}-P_{pump}}$$

It should be noted that for the HTR optimization, the number of RHX units is set to optimum value found in previous section and the number of LTR units is set to the reference value. Figure 19 shows an example of cycle efficiency and plant $/kWe as a function of number of HTR units. For this particular example, the number of HTR units changed from 48 (reference value) to 42. Once the optimum number of HTR units is calculated, the value is updated in the PDC input file (HTR_dat.txt) and the code proceeds to the LTR optimization. In the fourth step of optimization, the number of LTR units is varied from 18 to 198 in steps of 6 to find the optimum number of LTR units and minimize the $/kWe. For the LTR optimization, the plant $/kWe can be represented as,

$$\frac{\$}{kWe} = \frac{cost_{rest}+cost_{RHX,optimum}+cost_{HTR,optimum}+cost_{LTR}+cost_{water\ cooler}+cost_{piping}}{P_{elec}-P_{pump}}$$

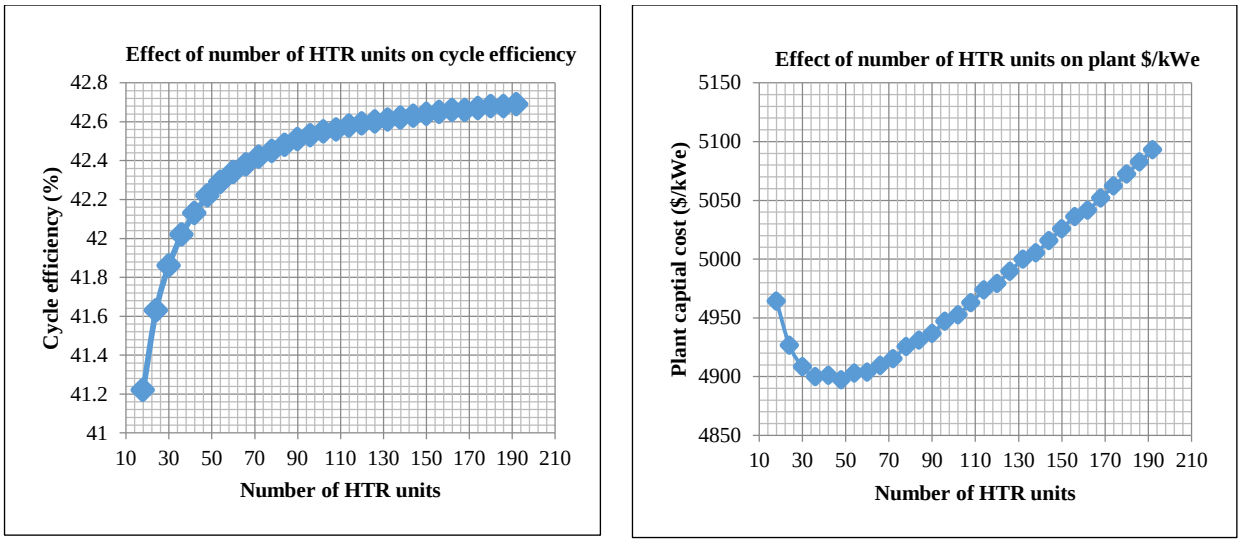

Figure 19: Example of cost-based optimization of the HTR

It should be noted that for the LTR optimization, the number of RHX and HTR units are set to optimum values found above. An example of cycle efficiency and plant $/kWe for LTR optimization is shown in Figure 20.

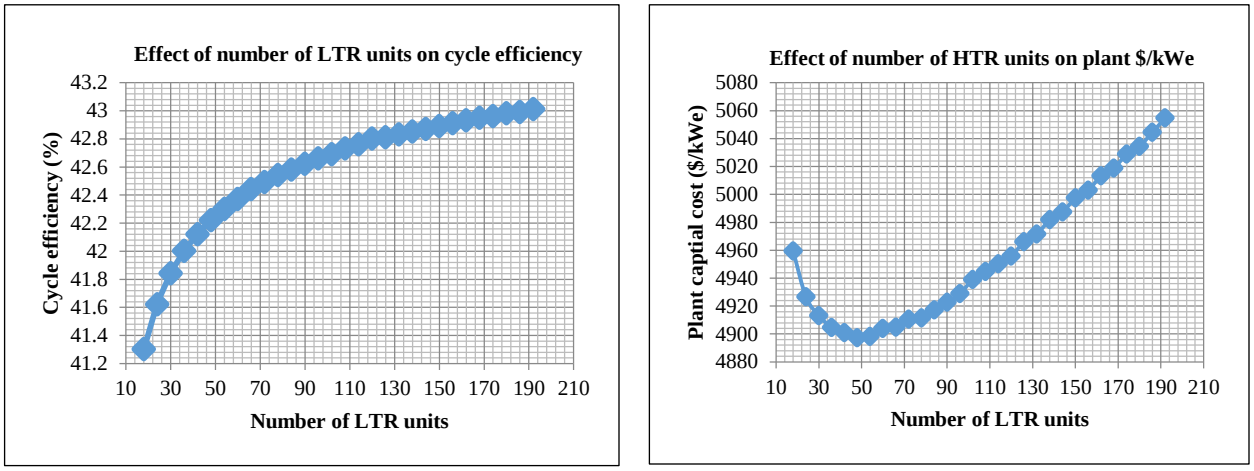

Figure 20: Example of cost-based optimization of the LTR

For this particular example, the optimum number of LTR units is unchanged from the reference value. In fact, for almost all of the cycle conditions the optimum number of LTR units remained roughly about the same as reference value. A possible reason for this is that the optimum split fraction in the first step of optimization is calculated by setting the number of LTR units to reference value. In cases where the optimum number of the LTR units is different from the reference value, the value is updated in the PDC input file (LTR_dat.txt) and the Matlab code proceeds to the optimization check.

In the optimization check step, the number of units for all the heat exchanger are set to optimum values, and the cycle efficiency as a function of the split flow is calculated similar to the procedure mentioned in previous section. If the optimum split fraction remains the same, then the optimization is complete otherwise the number of units for each heat exchanger is re-optimized again as indicated in the flow diagram in Figure 16. Figure 21 shows an example of the optimum

split fraction before and after the cost-based optimization. It is evident that the cycle efficiency changes slightly but the optimum split fraction remains nearly the same indicating that the optimization is complete. As mentioned earlier, all the PDC calculations presented above used CO_2-to-water cooler and the final step of optimization is to export the cooler conditions to the CO_2-to-air cooler EES code and find the optimum number of cooler units to minimize the $/kWe. The detailed cycle calculations after cost-based optimization of the heat exchangers (excluding the cooler) are shown in Figure 22 for the example case.

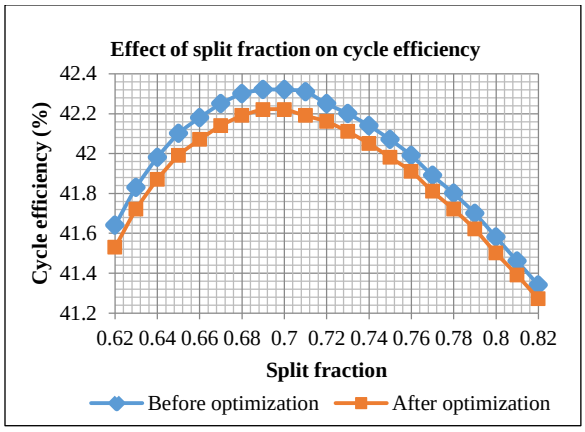

Figure 21: Optimum split fraction before and after cost-based optimization

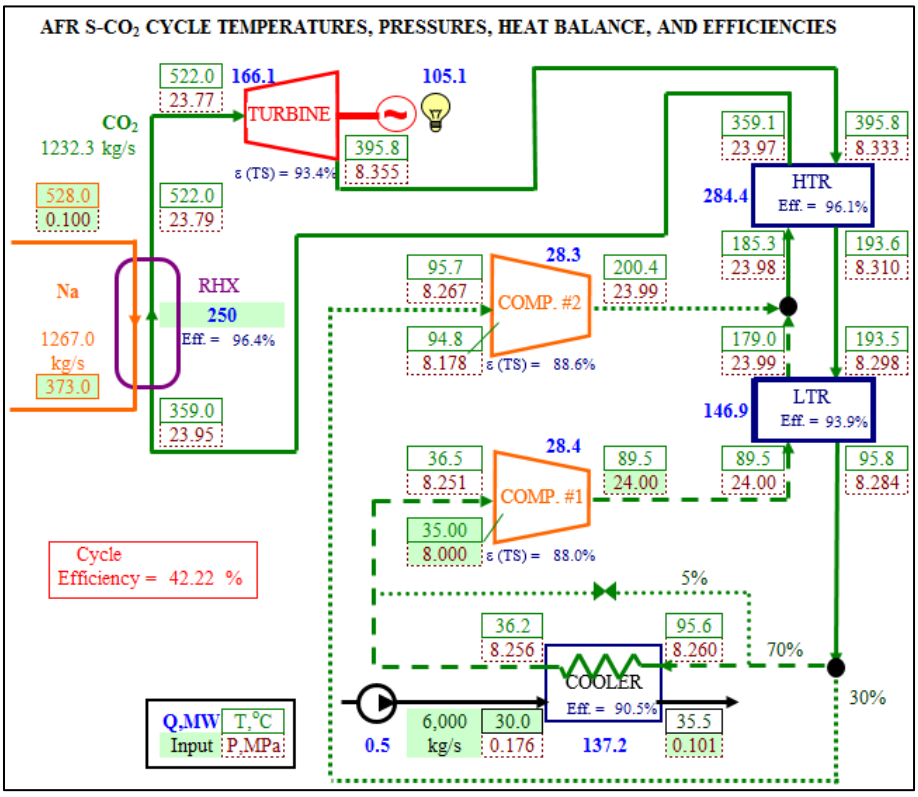

Figure 22: Cycle calculations after cost-based optimization using reference water cooler design

Optimization of CO_2-to-air cooler

For the CO_2-to-air cooler optimization, the cooler conditions after optimization of other components (split fraction, RHX, HTR, and LTR) are exported from the PDC to the EES code for CO_2-to-air cooler. The code uses the CO_2 inlet temperature and pressure as well as, CO_2 outlet temperature as inputs to calculate the required fan power, the cooler cost, and the CO_2 pressure drop for a given number of cooler units. For the current example case, the CO_2 inlet temperature, and pressure are 95.6^{o}C, and 8.26 MPa respectively and the CO_2 outlet temperature is 36.2^{o}C (see Figure 22). All the calculations are performed for fixed ambient air temperature of 30^{o}C and air outlet pressure of 0.101 MPa in order to be consistent with the water cooled cycles. Using smaller number of air cooler units will decrease the cooler cost but increases the required fan power (for the required heat removal rate) and vice versa. Therefore, the number of cooler units is varied and the $/kWe is calculated to find the optimum number of cooler units. Figure 23 presents an example to show the effect of number of cooler units on the plant $/kWe. For this particular case the optimum number of air cooler units is 58 resulting in a plant capital cost of 4892 $/kWe. There are couple of drawbacks of performing the air cooler calculations outside the PDC as listed here,

- The CO_2 pressure drop calculated for the air cooler doesn't match the CO_2 pressure drop calculated in the PDC using water cooler. For example, the CO_2 outlet pressure calculated in the PDC is 8.256 MPa (see Figure 22) whereas the CO_2 outlet pressure from the air cooler is 8.248 MPa for optimum number of air cooler units. This increased pressure drop of CO_2 in the air cooler would slightly reduce the cycle efficiency. For the example presented here, the cycle efficiency decreases from 42.22% to 42.20% due to increased pressure drop in the cooler. This is not expected to affect the $/kWe calculations significantly.

- The cost of reference water cooler used during the cost-based optimization (in the PDC) is different from the cost of air cooler. In this example, the cost of air cooler is 16.29 M$ whereas the cost of reference water cooler used for cost-based optimization in the PDC is 16.86 M$. Although the cost difference is not much for this particular case, the cost of air cooler can be higher as the minimum pressure and temperature get closer to the critical point.

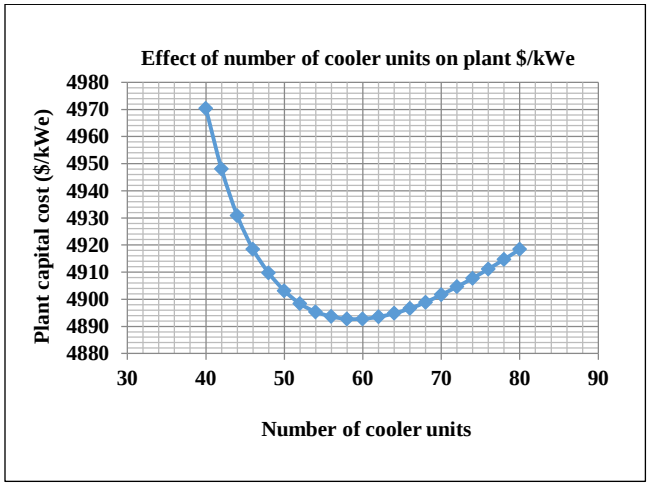

Figure 23: Example of cost-based optimization of the CO_2-to-air cooler

Results and Discussion

The cost-based optimization technique introduced in previous sections is applied for different cycle conditions and the results are presented in this section along with a brief discussion. The calculations are performed for two scenarios as described below.

- In the first scenario, the PDC inputs to the turbomachinery components (turbine and compressors) are left unchanged. For this scenario, depending on the cycle conditions the isentropic efficiency of the compressors and turbine can drop significantly.

- In the second scenario, the turbine design part of the PDC is skipped and a constant static-to-static efficiency (called turbine efficiency from hereon) of 93.4% is assumed for the turbine. Please note that this corresponds to total-to-static efficiency of 92.8% for the reference conditions (see Figure 1). The PDC inputs to the compressors is left unchanged. To achieve a constant turbine efficiency of 93.4% for different operating conditions, it is required to either increase/decrease the number of turbine stages or implement other modifications to the turbine. These modifications will have significant amount of cost associated with them which are not accounted for during calculation of the plant $/kWe.

In the next two subsections the calculations for both these scenarios will be presented, followed by cost-based optimization results to investigate the sensitivity of cycle minimum pressure on the plant $/kWe near the pseudo-critical pressure.

Plant optimization for fixed turbomachinery inputs

The cycle efficiency and the net plant efficiency as a function of the cycle maximum pressure are plotted in Figure 24 for different cycle minimum pressures and temperatures listed in Table 12. The net plant electrical output (calculated based on the cycle electrical output minus the fan power consumption) is used to calculate the plant efficiency in Figure 24. The fluid density decreases as the cycle minimum temperature increases which increases the work input to the compressor, thereby, decreasing the cycle and plant efficiency as can be seen in the figure below.

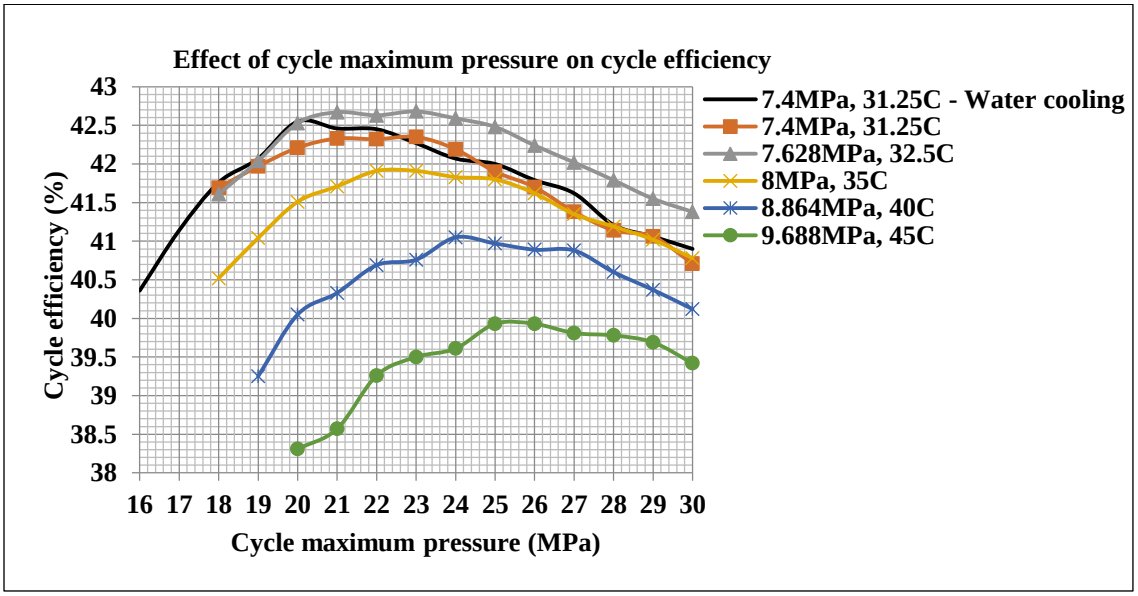

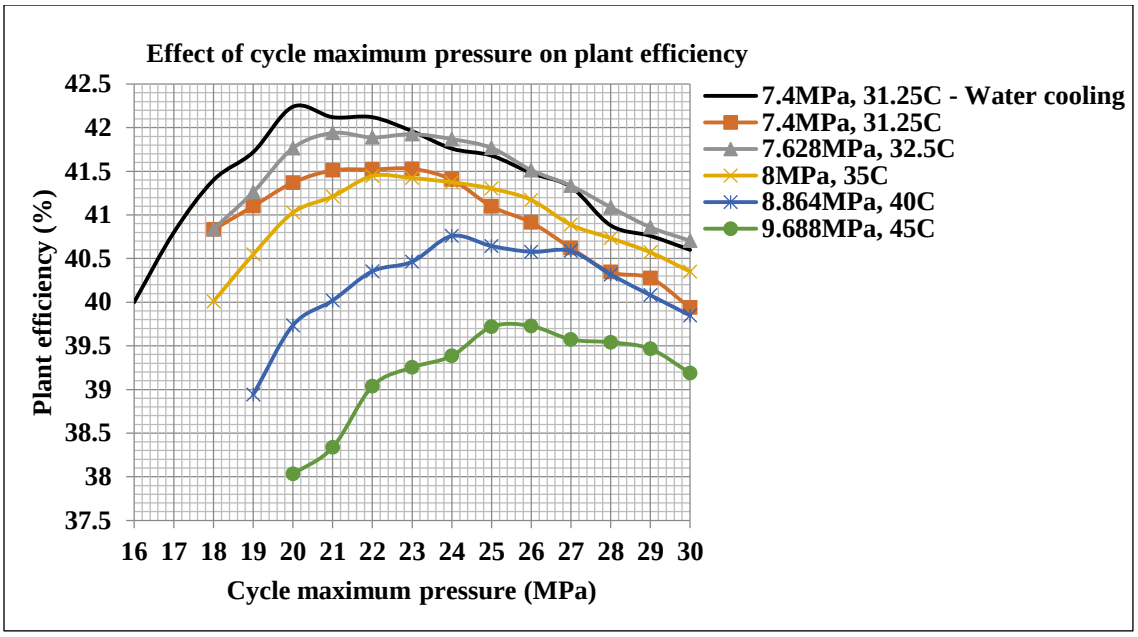

Figure 24: Effect of cycle maximum pressure on cycle and plant efficiency for fixed turbomachinery inputs

An exception to this is that the plant efficiency for 7.628 MPa, 32.5°C case is higher than that of 7.4 MPa, 31.25°C case. The reason for this is that the selected cycle minimum pressure is equal to the pseudo-critical pressure for the 32.5°C whereas the cycle minimum pressure for 31.25°C case is lower than the pseudo-critical pressure (see Table 12). Also plotted in the figure are the cycle and plant efficiencies for the reference water cooled cycle. The plant efficiency of the air cooled cycle (for 7.4 MPa, 31.25°C case) is lower than that of the water cooled cycle due to an increase in the fan power consumption for the CO_2-to-air cooler. For the cost-based optimization described in the previous Chapter, the optimization parameters (split fraction, and number of heat exchanger units) are changed in steps. This is the reason for rugged nature of the curves in Figure 24. Choosing smaller step sizes during the optimization will make these curves smoother but will increase the computational time. The plant capital cost ($/kWe) calculations are presented in Figure 25 for both air cooled and water cooled cycles. For 7.4MPa, 31.25°C case the optimum cycle maximum pressure is around 22 MPa and the plant capital cost for the air cooled cycle increased to 5054 $/kWe. This corresponds to about 6% increase in the capital cost compared to the capital cost of the reference water cooled cycle (4780 $/kWe). For the ambient air temperature of 30°C, the plant $/kWe benefits greatly by increasing the cycle minimum temperature from 31.25°C to 32.5°C and selecting the cycle minimum pressure as the pseudo-critical pressure (7.628 MPa for 32.5°C). For this case the optimum cycle maximum pressure is around 24 MPa and the plant capital cost decreases to 4967 $/kWe. This corresponds to nearly 2% decrease in the capital cost when compared to the capital cost of the 7.4 MPa, 31.25°C case. Out of all the conditions in Figure 25, the optimum case for the air cooled cycle is noted to be 8 MPa, 35°C case with maximum cycle pressure of 24 MPa. For this optimum case, the plant capital cost is 4934 $/kWe which is only about 3% increase in the plant $/kWe compared to the reference water cooled cycle. This is a significant improvement in the air cooled S-CO_2 plant economics when compared to the previous PCHE air cooler technology which resulted in about 40% increase in the $/kWe [1]. In this section, we have noticed a drop in plant efficiency for

higher cycle pressures which can be either related to the drop in turbomachinery efficiency or might be a result of the cost-based optimization.

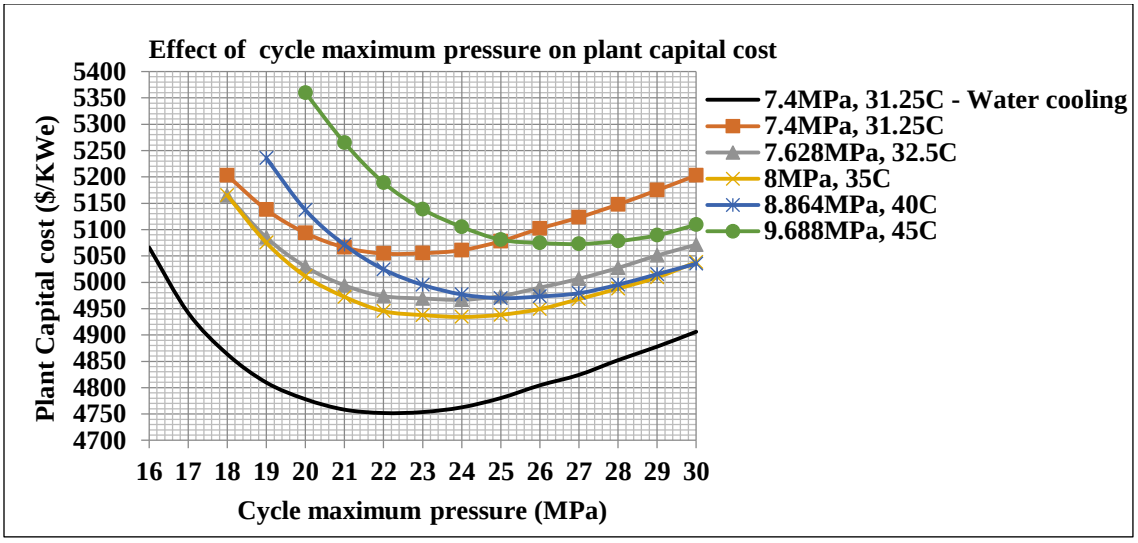

Figure 25: Effect of cycle maximum pressure on the plant $/kWe for fixed turbomachinery inputs

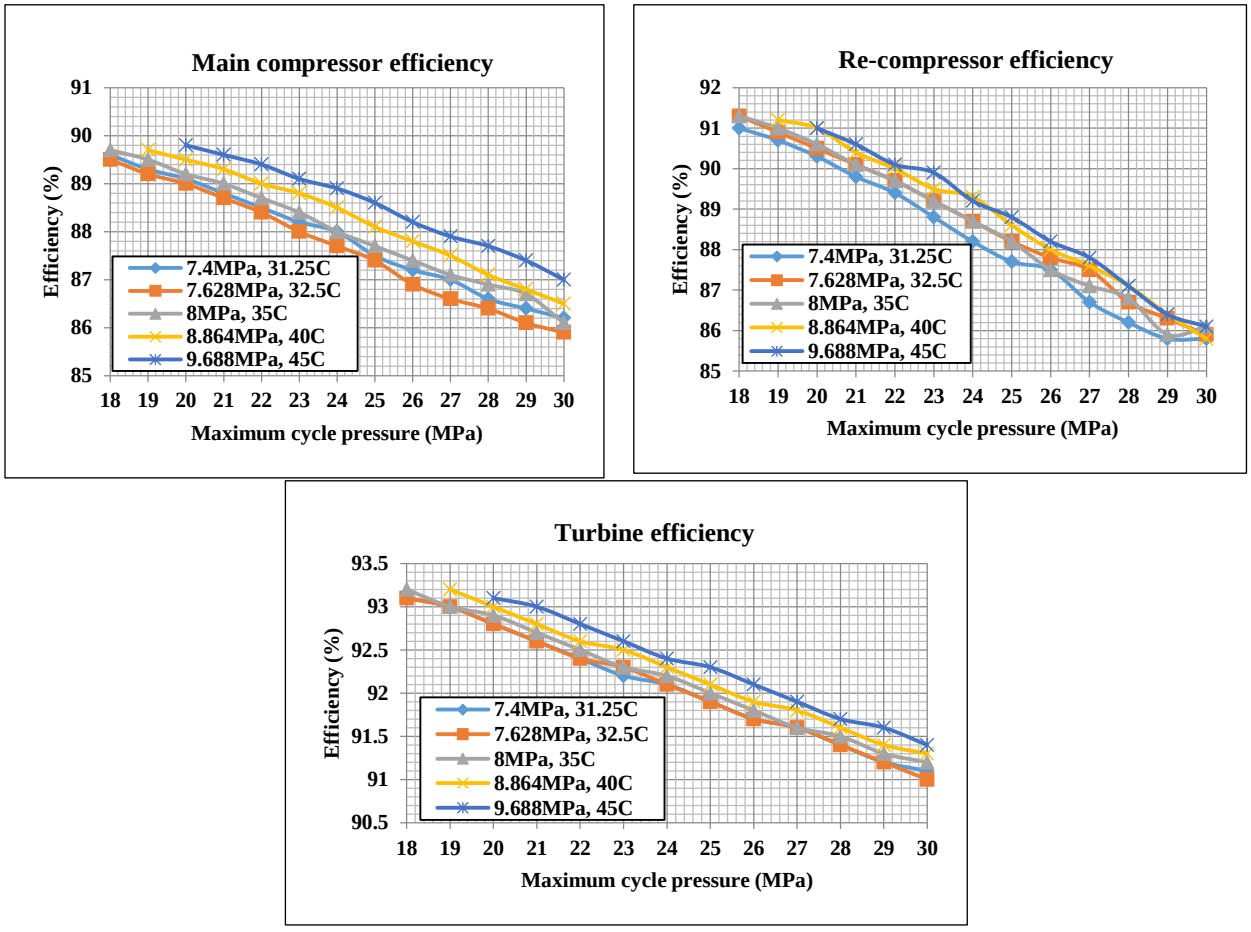

Figure 26: Drop in isentropic efficiency of compressors and turbine for fixed turbomachinery inputs

In the results presented above, one would guess that the plant efficiency will increase as the cycle maximum pressure increases, however, it is clearly evident that the plant efficiency decreases for higher maximum cycle pressure for all the conditions (see Figure 24). There are two possible factors to this observation as listed below.

- One reason might be related to the drop in total-to-static efficiency of the compressors and the turbine as the cycle maximum pressure is increased as can be seen in Figure 26. By increasing the cycle maximum pressure from 18 MPa to 30 MPa, the turbine efficiency drops by almost 2% and the compressors efficiency drops by almost 4%.

- Also, the decrease in plant efficiency might be a result of the cost-based optimization. For higher cycle pressures, it is more economical to use fewer number of the heat exchanger units (to reduce the capital cost of the heat exchangers) and compromise on the cycle efficiency.

In order to investigate the influence of these factors on the plant efficiency (also $/kWe), the static-to-static efficiency of the turbine is fixed constant and the calculations are repeated again. These calculations are presented in the next section.

Plant optimization for fixed static-to-static turbine efficiency

Since, the turbine power output is almost 4 times that of the power input to the compressors (see Figure 22), a 2% drop in turbine efficiency in the previous section is expected to have larger impact on the plant efficiency than that of the drop in compressors efficiency. For this reason, the turbine design part of the PDC is skipped and the cost-based optimization calculations are repeated with a fixed turbine efficiency. Figure 27 presents the cycle and the plant efficiency calculations for a fixed static-to-static turbine efficiency of 93.4%.

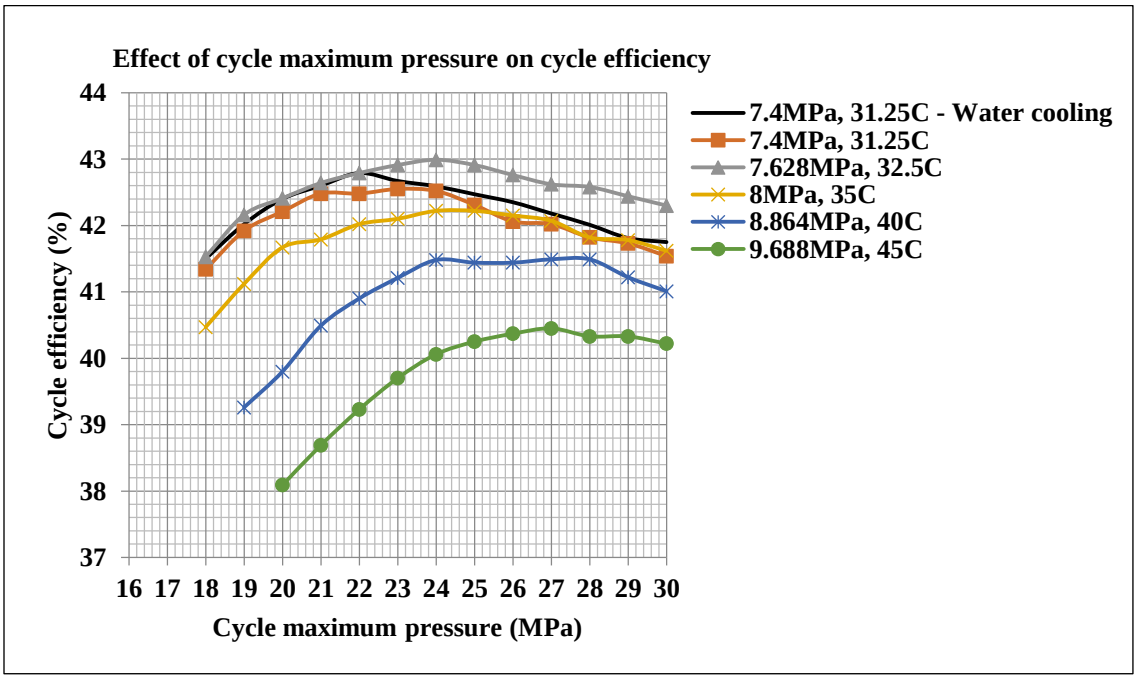

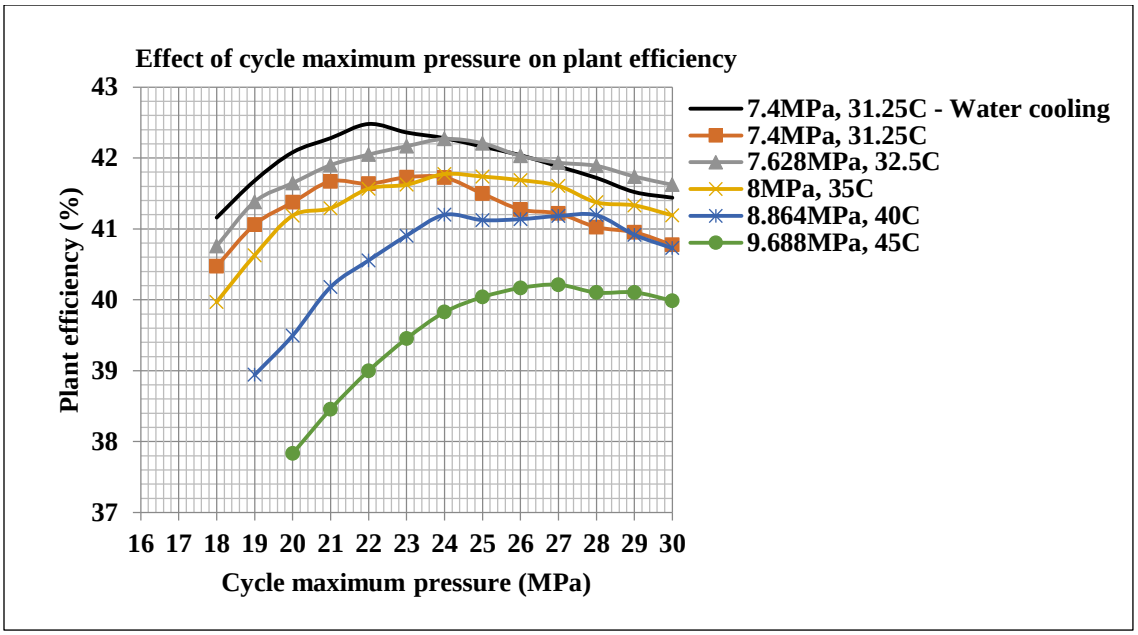

Figure 27: Effect of cycle maximum pressure on cycle and plant efficiency for fixed turbine efficiency

Similar to the previous section, there plant efficiency drops for higher cycle maximum pressures. However, drop in plant in plant efficiencies for this particular case occurs at higher pressures than the previous case. In Figure 28, the $/kWe calculations are presented for the fixed turbine efficiency.

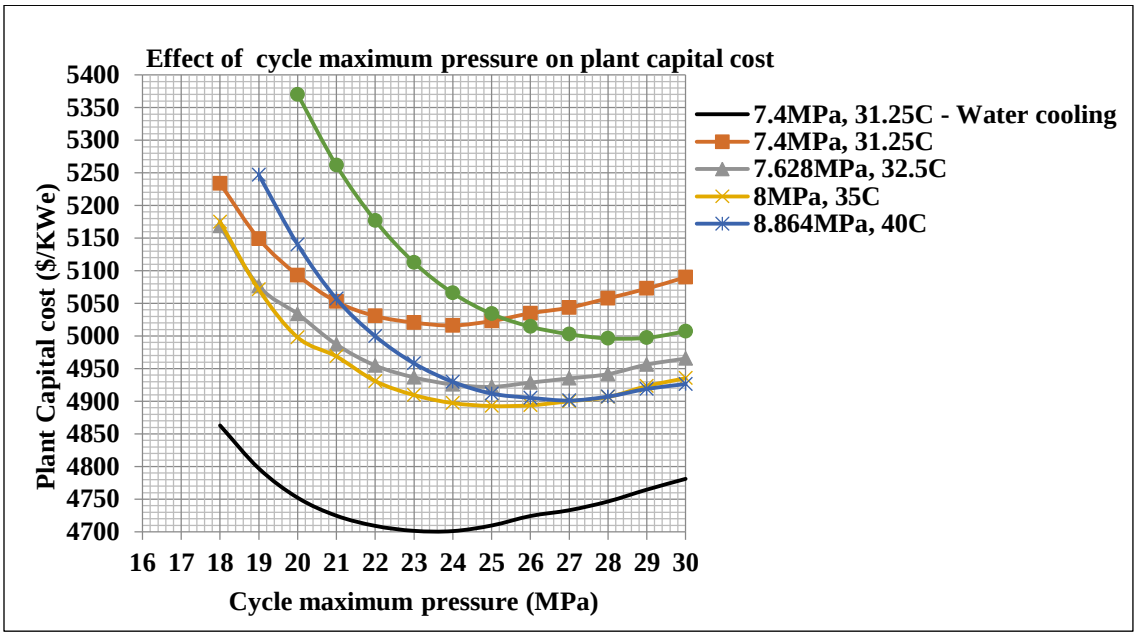

Figure 28: Effect of cycle maximum pressure on the plant $/kWe for fixed turbine efficiency

The optimum cycle conditions tend to shift to higher cycle maximum pressures which is expected due to an increase in the cycle efficiency. For example, the optimum cycle maximum pressure for 8.864 MPa, 40^{o}C case is 25 MPa and 27 MPa for the fixed turbomachinery inputs

case and the fixed turbine efficiency case respectively (see Figures 26 and 28). Unfortunately, neither of the calculations presented in the previous section or this section take into account the turbomachinery costs to conclude which of these calculations can be considered more accurate. We believe that if the turbomachinery costs are taken into account both of these calculations will yield similar results. For the fixed turbine efficiency case, the optimum cycle conditions are 8 MPa, 35^{o}C with maximum cycle pressure of 25 MPa. The plant capital cost for this case is 4893 $/kWe which is about 2.5% higher than that of the reference water cooled cycle (4780 $/kWe). In the future, when a proper cost estimation procedure for the turbomachinery components is developed, it is recommended to implement the design changes to the compressors and turbine and re-optimize the cycle to obtain more accurate results for the plant $/kWe.

Selection of cycle minimum pressure around the pseudo-critical pressure

In the previous section, the optimum plant $/kWe values for the cycle minimum temperatures of 32.5^{o}C, 35^{o}C, and 40^{o}C are very close to each other (less than 1% difference in Figure 28). In this section, the sensitivity of choice of cycle minimum pressure in the vicinity of pseudo-critical point is investigated for these three cases. These calculations will aid in proper selection of the cycle minimum pressure for a given minimum temperature. Figure 29 presents the plant efficiency and plant $/kWe calculations for the cycle minimum temperature of 32.5^{o}C for various minimum pressures. Please note that these results are obtained using the same cost-based optimization procedure described in previous chapter. The plot clearly indicates that the cycle benefits greatly (due to reduction in compressor work from increased fluid density) by selecting the cycle minimum pressure greater than the pseudo-critical pressure (7.628 MPa for 32.5^{o}C). As the cycle maximum pressure is increased, the plant efficiency for 7.7 MPa case is about 1% higher than that of the 7.628 MPa case. This increase in the plant efficiency is also reflected in the plant capital cost. By increasing the cycle minimum pressure from 7.628 MPa to 7.7 MPa the optimum plant capital cost can be reduced from 4922 $/kWe to 4894 $/kWe (about 0.5% reduction in the capital cost). Since, the results for 7.7 MPa and 7.8 MPa minimum pressures are almost identical, cycle minimum pressure of 7.7 MPa is chosen as the optimum for this case.

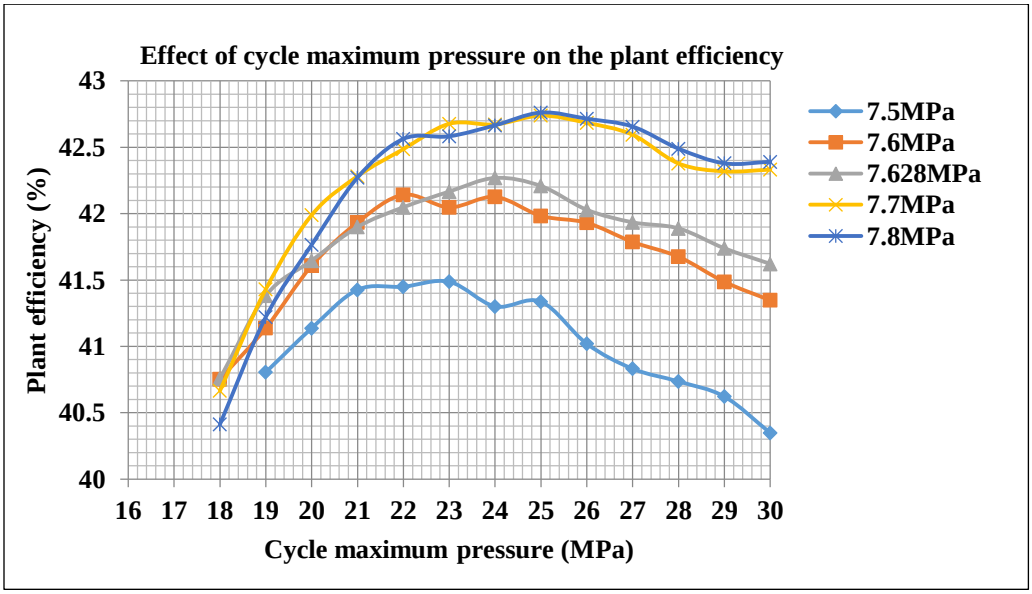

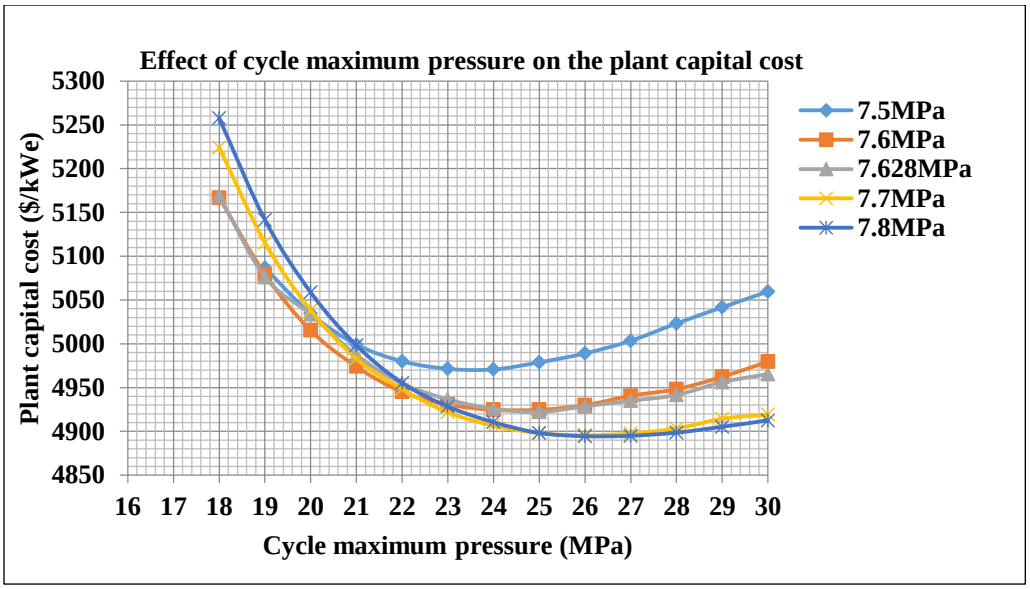

Figure 29: Effect of cycle maximum pressure on plant efficiency and $/kWe for cycle minimum temperature of 32.5°C, different cycle minimum pressures

Figure 30 presents the plant efficiency and plant capital cost calculations for the cycle minimum temperature of 35°C for different minimum pressures. Similar to the 32.5°C case, the cycle benefits from selecting the cycle minimum pressure greater than the pseudo-critical pressure (8.04 MPa for 35°C). Increasing the cycle minimum pressure from 8 MPa to 8.2 MPa, the optimum plant efficiency increases by roughly 0.8% but even a greater reduction in the plant capital cost is calculated. The plant capital cost decreased from 4893 $/kWe to 4832 $/kWe (about 1% reduction in the plant capital cost). To achieve this the cycle maximum pressure has to be increased from 25 MPa (optimum for 8 MPa case) to 28 MPa (optimum for 8.2 MPa case). However, even for cycle maximum pressure of 25 MPa, about 1% reduction in the plant capital cost can be achieved by increasing the cycle minimum pressure from 8 MPa to 8.2 MPa.

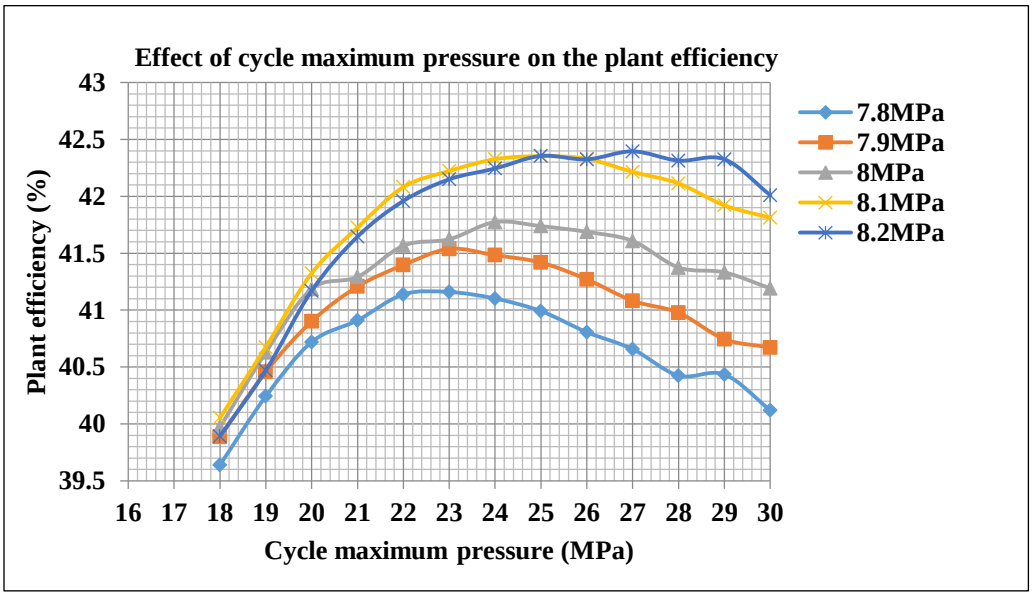

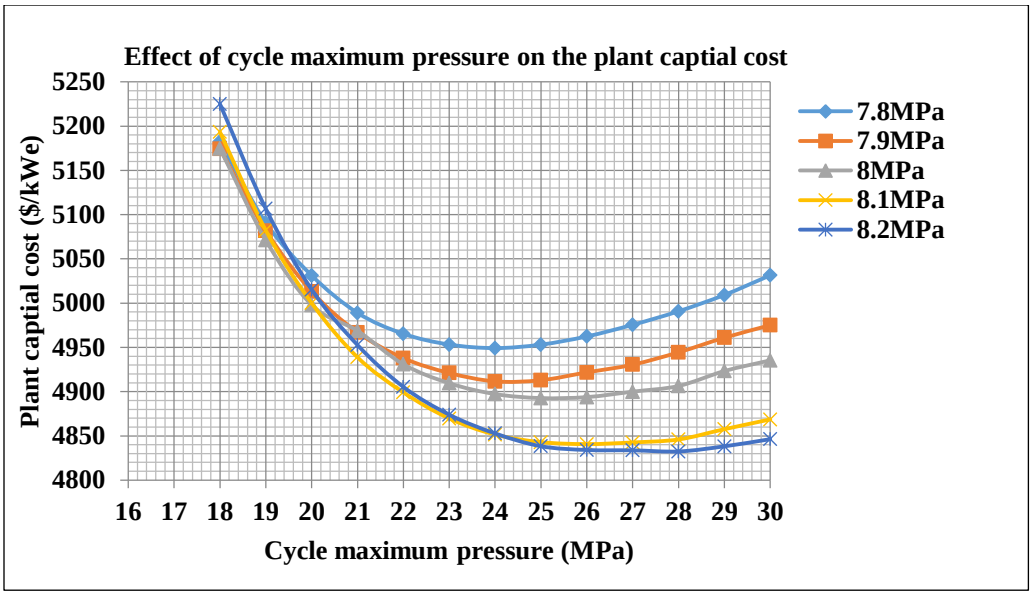

Figure 30: Effect of cycle maximum pressure on plant efficiency and $/kWe for cycle minimum temperature of 35°C, different cycle minimum pressures

The plant efficiency and the plant capital cost for the cycle minimum temperature of 40°C are plotted in Figure 31 for different minimum pressures. The effect of increasing the cycle minimum pressure on the plant capital cost for this particular case is not as significant as the other two cases. The optimum minimum pressure for this case is selected as 9.2 MPa. For a cycle maximum pressure of 28 MPa, the plant capital cost is 4872 $/kWe which is lower than the optimum value for the 32.5°C case but higher than optimum value of 35°C case. It is also interesting to note that as the cycle minimum temperature increases, it is required to increase the minimum pressure further above the pseudo-critical pressure to observe a noticeable reduction in the plant $/kWe values.

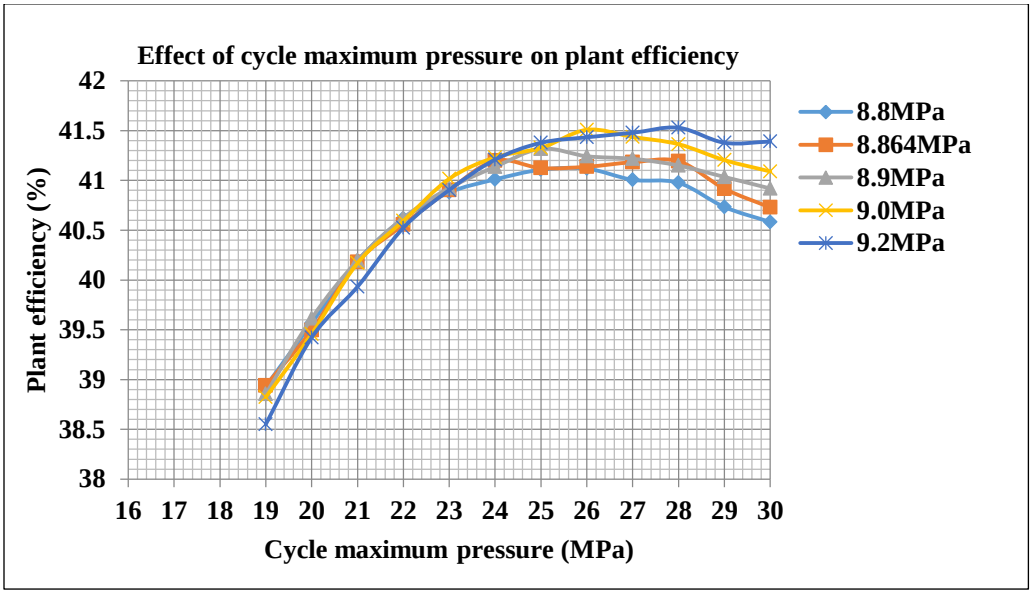

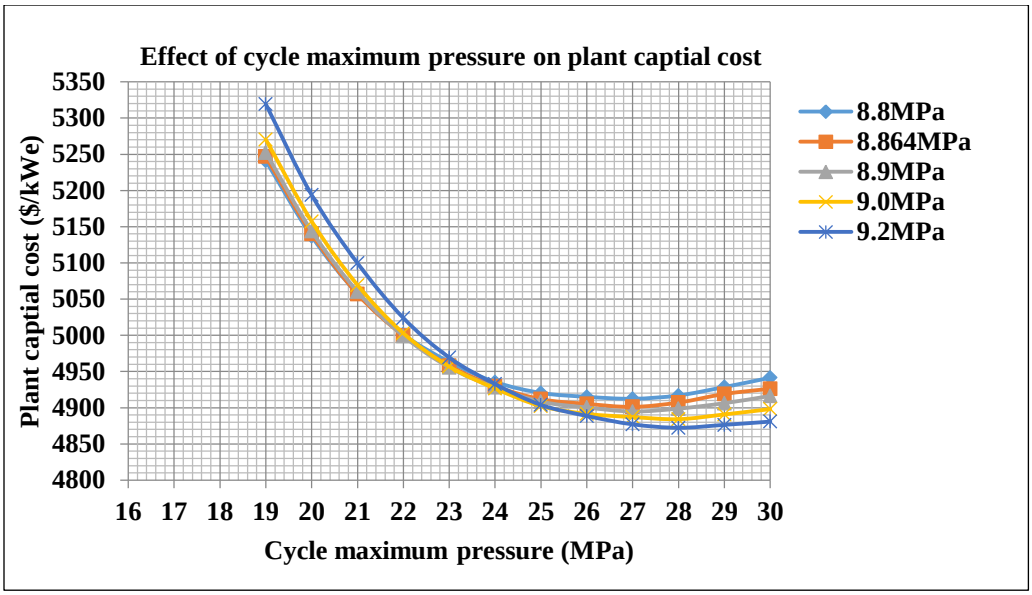

Figure 31: Effect of cycle maximum pressure on plant efficiency and $/kWe for cycle minimum temperature of 40°C, different cycle minimum pressures

Finally, the optimum cycle minimum pressures (resulting in the least $/kWe) for each of these minimum temperatures are selected and the results are plotted in Figure 32 for the final selection of the optimum cycle operating conditions. Strictly going by these plots, the optimum cycle conditions would be minimum pressure of 8.2 MPa, minimum temperature of 35°C, and maximum pressure of 28 MPa. However, the calculations presented in this report didn't account for lot of costs which are affected by increase in the cycle maximum pressure. For example, the 28 MPa valves can be significantly expensive than 25 MPa valves. Similarly, one should also keep in mind that the heat exchanger headers will have to be thicker and welding of the thick headers, and plant piping can be an expensive task.

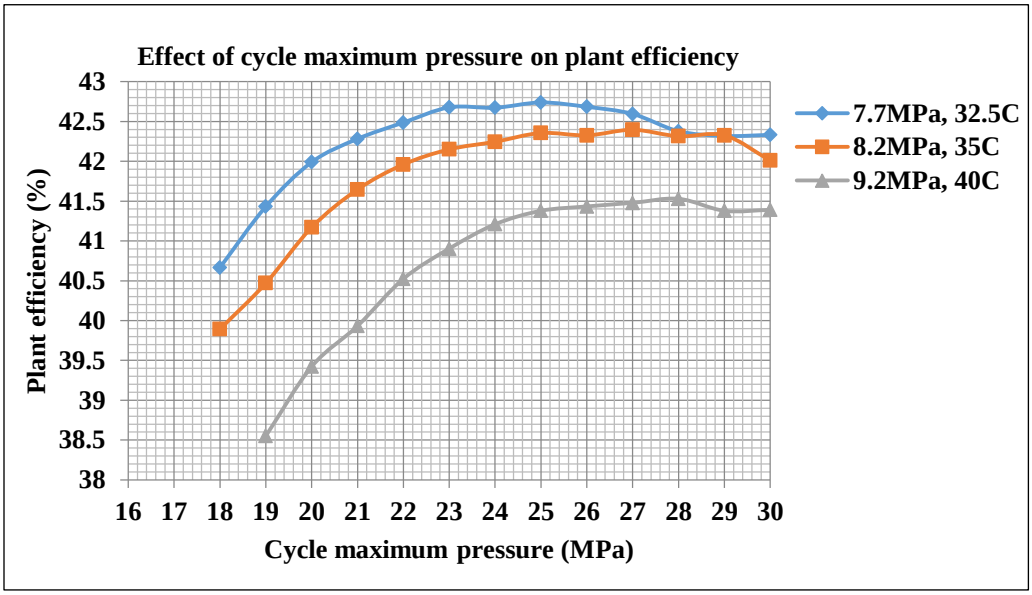

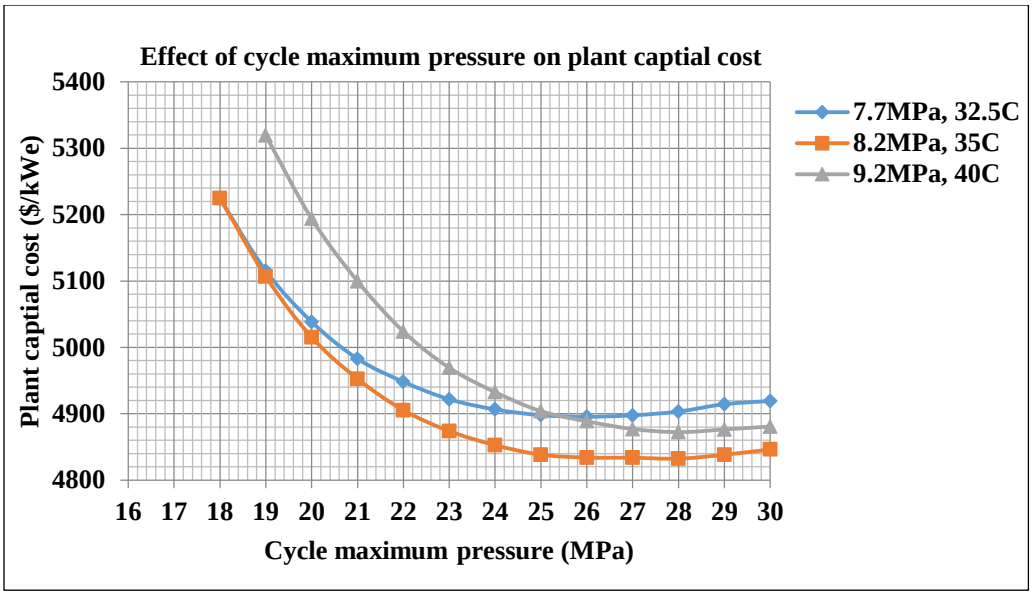

Figure 32: Effect of cycle maximum pressure on plant efficiency and $/kWe for the selected cycle minimum pressures and temperatures

Higher cycle pressure also means more safety concern and one should keep in mind the costs associated with the CO_2 leak in the heat exchangers (especially in the RHX, where CO_2 interacts with Na in the case of a leak), CO_2 leak into the turbine building etc. All these costs are hard to estimate and a proper engineering judgement has to be used while selecting the maximum pressure for the cycle. For the reasons stated above, the optimum maximum pressure is chosen as 25 MPa rather than 28 MPa (For minimum pressure, and minimum temperature of 8.2 MPa, and 35^{o}C respectively). Moreover, the plant $/kWe value for the maximum pressure of 28 MPa is not significantly lower than that of the 25 MPa case. Detailed cycle calculations for this optimum case are presented in Figure 33. Compared to the reference water cooled cycle in Figure 1, the cycle efficiency increased from 42.27% to 42.90%. The modified CO_2-to-air cooler design utilizes 68 cooler units (details of each unit are presented in previous section, refer to Figure 2) and consumes 1.4MW electrical power for operating the fans whereas the reference cycle consumes 0.84MW electrical power to operate the water pump. ***The capital cost of the optimized air cooled cycle is 4833 $/kWe. This corresponds to only about 1% increase in the plant capital cost compared to the reference water cooled cycle (4780 $/kWe)***. The detailed optimized designs of the RHX, HTR, and LTR are presented in Table 15.

Effect of ambient air temperature

All the calculations presented till now assumed that the ambient air temperature is 30^{o}C. This might not be true for all the power plant locations and it is important to investigate the effect of ambient air temperature on the plant $/kWe. In this section, the preliminary calculations performed for different ambient temperatures are presented. The maximum ambient air temperature is selected to be 40^{o}C. For an ambient temperature of 40^{o}C, the minimum temperature of the cycle has to be greater than 40^{o}C in order to perform the calculations. Therefore, cycle minimum temperature is selected as 45^{o}C and the corresponding cycle minimum pressure is chosen to be the pseudo-critical pressure (9.688 MPa for 45^{o}C). Figure 34 presents the calculations to show the effect of number of cooler units on the fan power

consumption and the plant capital cost. Please note that all the curves presented in Figure 34 are for the compressor inlet conditions of 9.688 MPa, and 45°C.

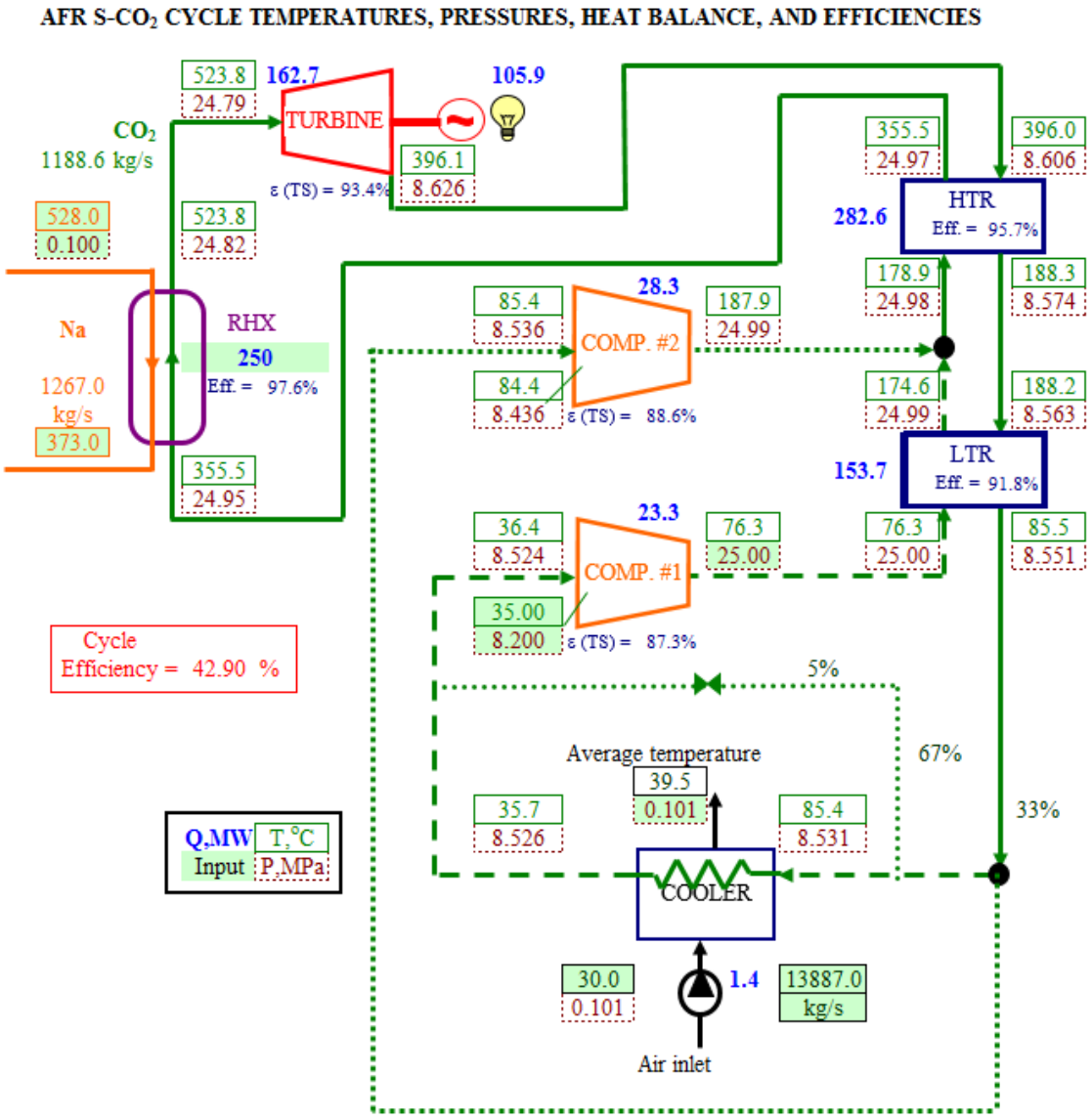

Figure 33: Cycle calculations after cost-based optimization using the CO_2-to-air cooler design

As expected, the air cooler fan power consumption increases with increase in the ambient air temperature because of the reduction in the cooler approach temperature (defined as the difference in CO_2 outlet temperature and air inlet temperature in the cooler). This is especially true for smaller number of the cooler units. As the number of cooler units increase to match the heat load, the fan power consumption becomes less dependent on the ambient air temperature. However, increasing the number of cooler units to match the heat load for different ambient air temperatures is not an economical option. Consequently, the optimum number of cooler units will have to be selected as a function of the ambient air temperature in order to minimize the plant $/kWe. The capital cost calculations presented in Figure 34 show that the optimum number

of cooler units increase as the ambient air temperature increases. For example, the optimum number of cooler units increases from 29 to 58 as the ambient air temperature increases from 30°C to 40°C (100% increase in the number of cooler units, and cooler cost). However, the corresponding plant capital cost increases only from 5072 $/kWe to 5180 $/kWe as the ambient air temperature increases from 30°C to 40°C (roughly about 2% increase in the plant capital cost). One important thing to be noted here is that the results presented in Figure 34 are based only on cost-based optimization technique applied to the CO_2-to-air cooler while other parameters (such as split fraction, RHX, HTR, and LTR designs) are kept constant. Therefore, cycle minimum pressure of 9.688 MPa might not be the optimum minimum pressure for any of these ambient air temperatures and the actual increase in the plant capital cost for different ambient air temperatures can be either higher or lower than the preliminary 2% increase calculated in this section.

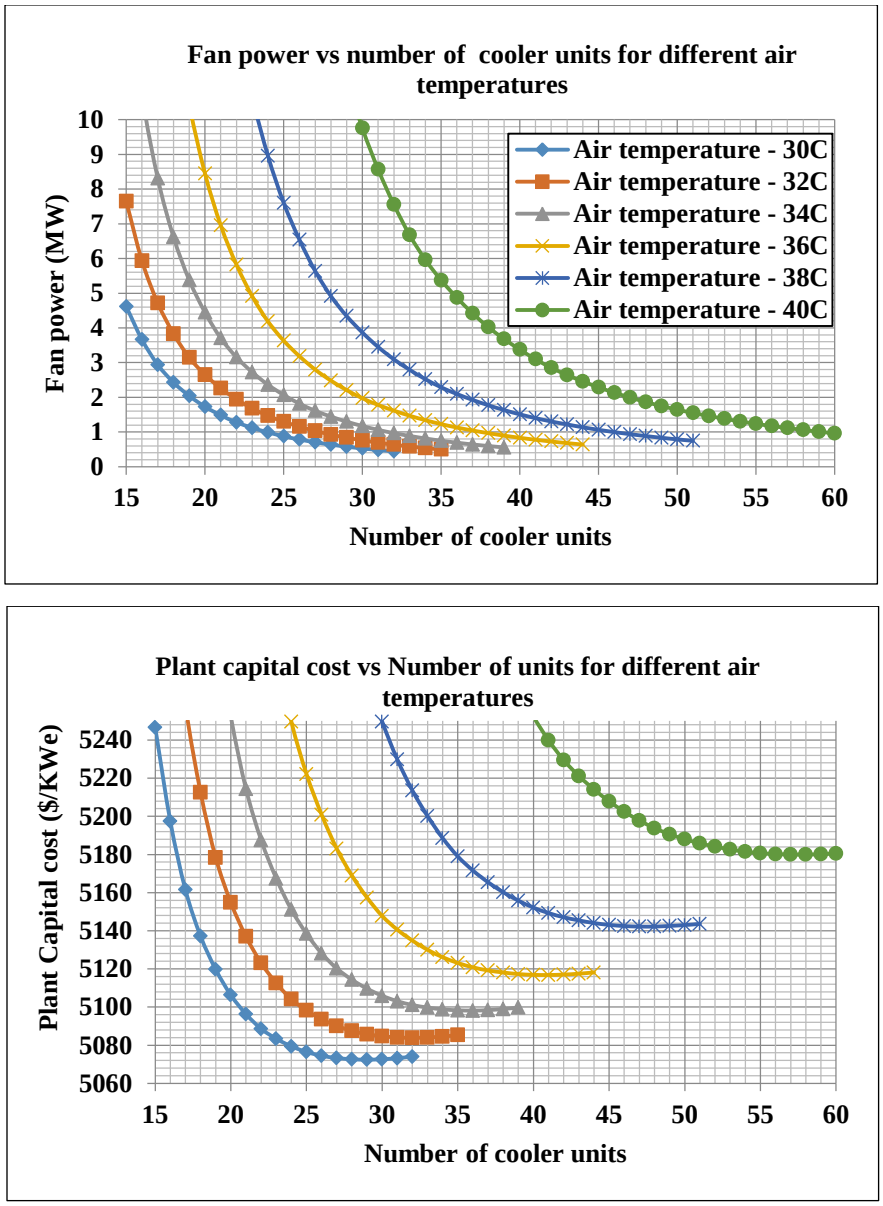

Figure 34: Effect of ambient air temperature on the required fan power and the plant $/kWe

Table 15: Modified heat exchangers design for the optimized cycle conditions

Optimized design of the RHX

Type	Z/I PCHE	
Number of units	84	All parameters below are per unit
Heat transfer capacity	2.98 MW_{th}	
Hot side fluid	Na	
Hot side temperature inlet	528^{o}C	
Hot side temperature outlet	373^{o}C	
Hot side pressure inlet	0.1 MPa	
Hot side pressure outlet	0.1 MPa	
Hot side flow rate	15.1 kg/s	
Hot side pressure drop	0.1 kPa	
Cold side fluid	CO_2	
Cold side temperature inlet	355.5^{o}C	
Cold side temperature outlet	523.8^{o}C	
Cold side pressure inlet	24.952 MPa	
Cold side pressure outlet	27.816 MPa	
Cold side flow rate	14.2 kg/s	
Cold side pressure drop	136.4 kPa	
Effectiveness	97.6%	
Heat transfer area	169.1 m^2	
Unit width	0.6 m	
Unit height	0.6 m	
Unit length	1.5 m	
Heat transfer length	1.5 m	
Number of plates	84	Each side
Hot side channel diameter	6.0 mm	Semi-Circular channel
Hot side channel pitch	6.5 mm	
Hot side plate thickness	5.1 mm	
Hot side number of channels	84	Per plate
Hot side channel angle	0^{o}	
Hot side channel length	1.5 m	
Cold side channel diameter	2.0 mm	Semi-Circular channel
Cold side channel pitch	2.8 mm	
Cold side plate thickness	1.6 mm	
Cold side number of channels	178	
Cold side channel angle	60^{o}	
Cold side channel length	1.732 m	
Void fraction	59.3%	From channels
Metal mass	1.751 tonnes	Dry
Properties		
Hot side – inlet		
Density	828.1 kg/m^3	
Specific heat	1260.1 J/kg-K	
Hot side – outlet		
Density	863.9 kg/m^3	
Specific heat	1289.1 J/kg-K	
Cold side – inlet		
Density	210.8 kg/m^3	
Specific heat	1257.2 J/kg-K	
Cold side – outlet		
Density	158.2 kg/m^3	
Specific heat	1250.8 J/kg-K	

Optimized design of the HTR

Type	PCHE	
Number of units	38	All parameters below are per unit
Heat transfer capacity	7.44 MW_{th}	
Hot side temperature inlet	396^{o}C	
Hot side temperature outlet	188.3^{o}C	
Hot side pressure inlet	8.606 MPa	
Hot side pressure outlet	8.574 MPa	
Hot side flow rate	31.3 kg/s	
Hot side pressure drop	32.3 kPa	
Cold side temperature inlet	178.9^{o}C	
Cold side temperature outlet	355.5^{o}C	
Cold side pressure inlet	24.981 MPa	
Cold side pressure outlet	24.970 MPa	
Cold side flow rate	31.3 kg/s	
Cold side pressure drop	10.7 kPa	
Effectiveness	95.7%	
Heat transfer area	281 m^2	
Unit width	1.5 m	
Unit height	0.6 m	
Unit length	0.6 m	
Heat transfer length	0.38 m	
Plate material	SS316	
Number of plates	268	Each side
Hot side channel diameter	1.3 mm	Semi-Circular channel
Hot side channel pitch	1.8 mm	
Hot side plate thickness	1.1 mm	
Hot side number of channels	715	Per plate
Hot side channel length	0.439 m	
Hot side channel angle	60^{o}	
Cold side channel diameter	1.3 mm	Semi-Circular channel
Cold side channel pitch	1.8 mm	
Cold side plate thickness	1.1 mm	
Cold side number of channels	715	
Cold side channel length	0.439 m	
Cold side channel angle	60^{o}	
Void fraction	34.6%	From channels
Metal mass	2.816 tonnes	Dry
Properties		
Hot side – inlet		
Density	68.3 kg/m^3	
Specific heat	1161.9 J/kg-K	
Hot side – outlet		
Density	107.2 kg/m^3	
Specific heat	1156 J/kg-K	
Cold side – inlet		
Density	357.3 kg/m^3	
Specific heat	1560.2 J/kg-K	
Cold side – outlet		
Density	210.9 kg/m^3	
Specific heat	1257.3 J/kg-K	

Optimized design of the LTR

Type	PCHE	
Number of units	48	All parameters below are per unit
Heat transfer capacity	3.20 MW_{th}	
Hot side temperature inlet	188.2^{o}C	
Hot side temperature outlet	85.5^{o}C	
Hot side pressure inlet	8.563 MPa	
Hot side pressure outlet	8.551 MPa	
Hot side flow rate	24.8 kg/s	
Hot side pressure drop	12.6 kPa	
Cold side temperature inlet	76.3^{o}C	
Cold side temperature outlet	174.6^{o}C	
Cold side pressure inlet	24.997 MPa	
Cold side pressure outlet	24.991 MPa	
Cold side flow rate	16.6 kg/s	
Cold side pressure drop	6.0 kPa	
Effectiveness	91.8%	
Heat transfer area	293.8 m^2	
Unit width	1.5 m	
Unit height	0.6 m	
Unit length	0.6 m	
Heat transfer length	0.38 m	
Plate material	SS316	
Number of plates	273	Each side
Hot side channel diameter	1.3 mm	Semi-Circular channel
Hot side channel pitch	1.7 mm	
Hot side plate thickness	1.0 mm	
Hot side number of channels	734	Per plate
Hot side channel length	0.439 m	
Hot side channel angle	60^{o}	
Cold side channel diameter	1.3 mm	Semi-Circular channel
Cold side channel pitch	1.7 mm	
Cold side plate thickness	1.0 mm	
Cold side number of channels	600	
Cold side channel length	0.537 m	
Cold side channel angle	90^{o}	
Void fraction	36.2%	From channels
Metal mass	2.747 tonnes	Dry
Properties		
Hot side – inlet		
Density	107.1 kg/m^3	
Specific heat	1155.8 J/kg-K	
Hot side – outlet		
Density	168.9 kg/m^3	
Specific heat	1515.4 J/kg-K	
Cold side – inlet		
Density	705.1 kg/m^3	
Specific heat	2251.4 J/kg-K	
Cold side – outlet		
Density	364.8 kg/m^3	
Specific heat	1583.3 J/kg-K	

Optimized design of the CO_2-to-air cooler

Parameter	Base Case	Optimal Case
Mass Flow	878.9 kg/s	819.2 kg/s
Inlet Temperature	89.6 C	94.56 C
Inlet Pressure	7.635 MPa	8.256 MPa
Outlet Temperature	32.657 C	36.207 C
Outlet Pressure	7.630 MPa	8.248 MPa
Number of Cooler Units	86	60
Total Heat Transfer	137.8 MW	135.1 MW
Total Fan Power	5.655 MW	1.165 MW
Average Air Outlet Temperature (peak)	34.92 C (50.54 C)	40.78 C (63.75 C)

Table 16 compares three different heat rejection methods for the sCO_2 Brayton cycles. It should be noted that the values tabulated for the cooling towers are obtained from the previous techno-economic analysis performed for the induced draft wet cooling towers for the sCO_2 Brayton cycle [10].

Table 16: Comparison of various heat rejection options for the sCO_2 Brayton cycle.

Heat rejection Method	Direct water cooling	Cooling Towers	Dry air cooling
Flow rate [kg/s]	6,000	1,500	13,887
Peak water consumption rate [kg/s]	6,000	150	-
Cooler Inlet temperature [^{0}C]	30	27	30
Cooler outlet temperature [^{0}C]	35.5	48.86	39.5
Compressor Inlet temperature [^{0}C]	31.25	31.25	35
Compressor Inlet pressure [MPa]	7.4	7.4	8.2
Cycle Efficiency [%]	42.27	42.27	42.90
Blower power [MWe]	-	0.36	1.4
Pump power [MWe]	0.84	0.16	-
Plant capital cost [$/KWe]	4,780	4,685	4,833

Summary and Conclusions

The purpose of the work described in this report is to investigate the techno-economic feasibility of dry air cooling to reject waste heat from the S-CO_2 Brayton cycle. The cycle developed for sodium cooled fast reactors (SFRs) small modular reactor AFR-100 is selected for the investigation. The previous work at ANL targeted at investigation of the possibility of using dry air cooling concluded that at least a 40% increase in the electricity price could be expected from implementation of air cooling [1]. The air cooler used in their study was based on the Heatric diffusion bonded technology and the cost of such a cooler is very high when using air as one of the heat transfer fluids. Also, the maximum cycle pressure in their study was limited to 20 MPa. Increasing this limit to higher values can regain part of the lost efficiency due to air cooling.

In an effort to reduce the cost of air cooler, an alternative air cooler option was found in the market and was chosen for the cost-based optimization study. The CO_2 undergoes three passes in each cooler module and flows inside stack of stainless steel tubes with aluminum fins to enhance the heat transfer. Each cooler module is equipped with three fans to distribute the air flow uniformly throughout the module in cross-flow arrangement. This is a very similar arrangement

to that of a car radiator. A quotation from the manufacturer (Harsco Industrial Air-X-Changers [4]) was obtained for the reference cycle conditions and a model for the cooler was developed independently in EES to confirm the manufacturer quoted specifications. The EES model calculations matched well with the vendor specifications. The plant capital cost per unit electrical output ($/kWe) for the reference cycle conditions using the new air cooler is calculated. ***The calculations showed about 6% increase in the capital cost compared to the water cooled cycle for reference conditions which is a significant improvement in the plant economics compared to the previous study [1]***.

For an air cooled cycle, the cycle minimum temperature is dictated by the ambient air temperature and it is important to investigate the plant capital cost for higher cycle minimum temperatures. Increasing the cycle minimum temperature will reduce the S-CO_2 cycle efficiency and in order to regain part of the lost efficiency, the cycle maximum pressure is also increased. Therefore, three parameters namely cycle minimum temperature, minimum pressure, and maximum pressure are chosen for the cost-based optimization of the plant. The cycle minimum pressure is selected close to the pseudo-critical pressure to exploit the high fluid density during the compression process. As the cycle maximum pressure is increased the cycle components (reactor heat exchanger, high temperature recuperator, low temperature recuperator, plant piping, and turbomachinery) design has to be modified to withstand the higher pressure differentials. Design modifications to these components, except the turbomachinery, is made as per the ASME guidelines and the cost changes associated with the modifications is taken into account during the cost-based optimization. No design modifications were made to the turbomachinery components.

For the cost-based optimization, all the heat exchangers designs are optimized individually in an effort to minimize the plant $/kWe for a given set of cycle parameters. This cost-based optimization technique is consistent with the previous optimization work at ANL. Optimization of the heat exchangers (excluding the CO_2-to-air cooler) is performed in Matlab using the ANL PDC for the cycle calculations and the final cooler conditions are exported to the EES air cooler model for selection of the optimum number of cooler units.

For the initial set of calculations, the turbine inputs to the PDC were left unchanged and a 4% drop in turbine efficiency was noticed by increasing the cycle maximum pressure from 18 MPa to 30 MPa. The cost-based optimization results showed that the optimum cycle conditions are minimum pressure of 8 MPa, minimum temperature of 35^{o}C, and maximum pressure of 24 MPa. *For this case, the plant capital cost ($/kWe) is about 3% higher that of the reference water cooled cycle*.

For the next set of calculations, the turbine design part of the PDC is skipped and a constant static-to-static turbine efficiency of 93.4% is assumed for the calculations. The cost-based optimization results showed that the optimum cycle maximum pressure shifts slightly towards the higher value due to an increase in the plant efficiency. However, these calculations didn't account for turbomachinery costs. If these cost are accounted for, it is believed that both these set of calculations should yield similar results. For the fixed turbine efficiency case, the optimum cycle conditions are minimum pressure of 8 MPa, minimum temperature of 35^{o}C, and maximum pressure of 24 MPa. *For this case, the plant capital cost ($/kWe) is about 2% higher than that of the reference water cooled cycle*.

In order to investigate any potential savings in the vicinity of the pseudo-critical pressure, three cases were selected (minimum temperatures of 32.5^{o}C, 35^{o}C, and 40^{o}C). For all three cases, the calculations showed the plant $/kWe can be reduced by selecting the cycle minimum pressure greater than the pseudo-critical pressure (this will increase the cooler cost slightly but gain in cycle efficiency outperforms the increase in the cooler cost). Out of all the cases investigated, the optimum cycle conditions are minimum pressure of 8.2 MPa, minimum temperature of 35^{o}C. For this case, strictly going by the obtained results, the optimum maximum pressure is 28 MPa. However, the calculations presented in this report didn't account for lot of cost changes associated with high pressure and engineering judgement was used to choose 25 MPa as optimum pressure. Moreover, the $/kWe values were not significantly different for the 28 MPa and 25 MPa cases. *For the optimum case, the plant capital cost ($/kWe) is only about 1% higher that of the reference water cooled cycle*. This of course doesn't include the increase in cost of turbine to achieve the static-to-static turbine efficiency of 93.4%.

Finally, the effect of ambient temperature on the plant capital cost was investigated. *The plant $/kWe increased by 2% as the ambient air temperature is increased from 30^{o}C to 40^{o}C*. These calculations were performed for the cycle minimum temperature of 45^{o}C and the cost-based optimization technique was applied only to the CO_2-to-air cooler while rest of the parameters are fixed. In order to calculate more accurate increase in the plant capital cost, the cycle minimum pressure has be to re-optimized for different ambient air temperatures.

Overall, the results of the present analysis of the dry air cooling for the S-CO_2 cycle using the new air cooler design are very promising. Even for a worst case scenario, less than 5% increase in the plant capital cost over the water cooled plant is calculated [11]. This has a significant impact on the applicability range of the S-CO_2 cycles.

References

[1] Moisseytsev, A., and Sienicki J. J., "Investigation of a dry air cooling option for an S-CO_2 cycle." *The 4th International Symposium – Supercritical CO_2 Power Cycles,* Pittsburgh, PA, September 9-10, 2014.

[2] Heatric Division of Meggitt (UK) Ltd., 2014, http://www.heatric.com/

[3] Moisseytsev, A. and Sienicki, J. J., "Cost-Based Optimization of Supercritical Carbon Dioxide Brayton Cycle Equipment," *Transactions of the American Nuclear Society,* American Nuclear Society 2011 Winter Meeting, Washington, DC, October 30-November 3, 2011.

[4] Kays, William Morrow, and Alexander Louis London. "Compact heat exchangers." (1984).

[5] Nellis, G., & Klein, S., *Heat Transfer*, Cambridge University Press, (2009).

[6] Zigrang, D. J., and N. D. Sylvester. "Explicit approximations to the solution of Colebrook's friction factor equation." *AIChE Journal* 28, no. 3 (1982): 514-515.

[7] Gnielinski, V. "Equations for calculating heat transfer in single tube rows and banks of tubes in transverse flow." *Int. Chem. Eng.; (United States)* 19, no. 3 (1979).

[8] Pierres, R. L., D. Southall, and S. Osborne. "Impact of mechanical design issues on printed circuit heat exchangers." In *SCO2 Power Cycle Symposium, University of Colorado, Boulder, CO*. 2011.

[9] Sienicki J. J., Moisseytsev, A., and Krajtl, L. "A Supercritical CO_2 Brayton cycle power converter for a sodium cooled fast reactor small modular reactor." In *Proceedings of ASME Power & Energy Conference 2015, San Diego, CA*. 2015.

[10] Pidaparti, Sandeep R., Anton Moisseytsev, James J. Sienicki, and Devesh Ranjan. "Counter flow induced draft cooling tower option for supercritical carbon dioxide Brayton cycle." *Nuclear Engineering and Design* 295 (2015): 549-558.

[11] Pidaparti, Sandeep R., Patrick J. Hruska, Anton Moisseytsev, James J. Sienicki, and Devesh Ranjan. "Technical and economic feasibility of Dry Air Cooling for the Supercritical CO2 Brayton cycle using existing technology." In *The 5th International Symposium-Supercritical CO2 Power Cycles*. 2016.